Protein aggregation in biomolecular condensates

Wojciech P. Lipiński

Protein aggregation in biomolecular condensates

Wojciech P. Lipiński

Protein aggregation in biomolecular condensates

Proefschrift ter verkrijging van de graad van doctor
aan de Radboud Universiteit Nijmegen
op gezag van de rector magnificus prof. dr. J.M. Sanders,
volgens besluit van het college voor promoties
in het openbaar te verdedigen op

woensdag 17 januari 2024
om 16.30 uur precies

door

Wojciech Paweł Lipiński
geboren op 7 mei 1995
te Łódź, Polen

Promotor
Prof. dr. W.T.S. Huck

Copromotor
Dr. E. Spruijt

Manuscriptcommissie
Prof. dr. R.P.A. Dullens
Prof. dr. ir. S. Otto (Rijksuniversiteit Groningen)
Prof. dr. R. Ulijn (The City University of New York, Verenigde Staten)

Paranimfen
Merlijn H.I. van Haren
Brent S. Visser

Protein aggregation in biomolecular condensates

Dissertation to obtain the degree of doctor
from Radboud University Nijmegen
on the authority of the Rector Magnificus prof. dr. J.M. Sanders,
according to the decision of the Doctorate Board
to be defended in public on

Wednesday, January 17, 2024
at 4.30 pm

by

Wojciech Paweł Lipiński
born on May 7, 1995
in Łódź, Poland

Contents

Summary

Protein aggregation, related to multiple neurodegenerative disorders, has been a topic of notable scientific interest for decades. However, only recently it has become clear that the aggregation process can be affected by another biologically important phenomenon - liquid-liquid phase separation, which underlies the formation of membraneless organelles. In this work, we investigate how the aggregation of proteins and peptides can be altered by the presence of biomolecular condensates by using simulations and experimental models in vitro.

In Chapter 1 we start by explaining the relevance of protein aggregation and liquid-liquid phase separation in the cellular context. We explain the physical basis of liquid-liquid phase separation, and show how different types of protein liquid-liquid phase separation can be qualitatively illustrated using phase diagrams. Then we look at the molecular background of both liquid-liquid phase separation and aggregation, and summarise our current knowledge about the liquid-to-solid transition of proteins. Finally, we discuss aggregation in host-guest systems, in which the aggregating protein does not undergo liquid-liquid phase separation on its own.

In Chapter 2 we introduce our first experimental model, based on small peptide derivatives, composed of two dipeptide moieties and a diamine linker. We show that some of them can undergo self-coacervation, mostly driven by hydrophobic forces. We explore the universality of the derivative design, changing the dipeptide moiety sequence and the linker, to conclude that liquid-liquid phase separation can occur for derivatives containing hydrophobic dipeptides (stickers) and flexible, hydrophilic linkers (spacers), analogously to phase-separating intrinsically disordered proteins. We also show that phase separation of derivatives containing a disulphide linker can be regulated by redox reactions and the condensates can accumulate various molecules.

In Chapter 3 we focus on the propensity of some of the derivatives introduced in Chapter 2 to undergo liquid-to-solid transition. We first examine the morphological changes of condensates at the microscopic level (using light microscopy) and on the nanoscopic level (using transmission electron microscopy and atomic force microscopy), showing that the transformation of liquid droplets into solid particles is linked to the formation of nanoscopic fibrillar structures. Subsequently, we provide a more detailed, molecular-level characterisation of the fibrils formed by the FFssFF derivative, by means of X-ray diffraction and solid-state NMR. NMR measurements combined with structure calculations allow the identification of two ladder structures that compose the fibrils.

In Chapter 4 we exploit the reversibility of the disulphide bond formation to chemically control and drive phase transitions of peptide derivatives with a disulphide linker. We select a range of peptide dimers with different propensities (completely soluble, liquid-liquid phase separating at high concentration, liquid-liquid phase separating with further liquid-to-solid transition, and phase separating directly into aggregate) and show, by means of simulations, that monomer exchange can drive phase-transitions. Then, we also provide experimental evidence that small changes in the condensate composition can result in liquid-to-solid transition or in the condensate dissolution. Finally, we show that monomer exchange can occur in multiple combinations of dimer-monomer.

In Chapter 5 we investigate the possible mechanisms of protein aggregation in host-guest two-phase systems. Building on the basic aggregation model, describing protein aggregation using 3 reactions (primary nucleation, elongation and secondary nucleation), we develop several ordinary differential equations-based models to describe multiple aspects of protein aggregation in the presence of liquid condensates. We discuss the influence of the partition coefficient and the condensate volume, sequestration of monomers by altered activity coefficient or reaction rate constants in the condensed phase, and the interface-catalysed nucleation of fibrils. At the end of the chapter, we also use a stochastic model of protein aggregation based on the Gillespie algorithm to investigate the influence of partitioning on the distribution of aggregation times and fibril lengths.

In Chapter 6 we attempt to prove experimentally our findings from Chapter 5, and show that model biomolecular condensates can affect the kinetics of α-synuclein aggregation. We study aggregation of 3 α-synuclein variants (full-length α-synuclein, truncated variant without the negatively charged C-terminal fragment and a short sequence from the β-sheet-forming fragment) in the presence of 3 model biomolecular condensates. We identify 3 aggregating protein-condensate interaction modes (partitioning, interfacial accumulation and exclusion) and show that these interactions can affect the kinetics of protein aggregation, as followed by the thioflavin T assay. Namely, partitioning can result in both accelerated and hampered aggregation, while interfacial accumulation results in substantial acceleration of aggregation. Similarly, partitioning or interfacial accumulation of insulin can also result in faster aggregation. Microscope-based assays with FRET-labelled α-synuclein and thioflavin T show that protein aggregation is most probably initiated at the interface of condensates, also in the case of protein partitioning into condensates.

The final Chapter 7 provides general conclusions of the findings described in Chapters 2-6. We also look at the most recent developments from the field of protein aggregation in the presence of liquid condensates. We end with suggestions for possible continuation of the work described in the thesis.

Streszczenie

Agregacja białek, powiązana z wieloma chorobami neurodegeneracyjnymi, od dziesiątek lat pozostaje tematem wzmożonego zainteresowania naukowców. Jednak dopiero stosunkowo niedawno odkryto, że na proces agregacji wpływać może inne zjawisko – separacja faz ciecz-ciecz [ang. *liquid-liquid phase separation*], która leży u podstawy powstawania organelli bezbłonowych [ang. *membraneless organelles*]. W tej pracy próbujemy wyjaśnić, poprzez wykorzystanie symulacji oraz modeli eksperymentalnych in vitro, jak na agregację białek i peptydów wpływać może obecność kondensatów biomolekularnych.

W Rozdziale 1 rozpoczynamy od opisania znaczenia agregacji białek i separacji fazowej ciecz-ciecz w kontekście komórkowym. Wyjaśniamy fizyczne podstawy separacji fazowej ciecz-ciecz i pokazujemy, jak różne rodzaje białkowej separacji fazowej ciecz-ciecz mogą być ilościowo zilustrowane za pomocą diagramów fazowych. Następnie przyglądamy się mechanizmowi separacji fazowej ciecz-ciecz i agregacji na poziomie cząsteczkowym i podsumowujemy obecny stan wiedzy na temat separacji fazowej ciecz-ciecz białek. Wreszcie omawiamy agregację w układach typu gospodarz-gość [ang. *host-guest*], w których agregujące białko nie ulega separacji fazowej ciecz-ciecz samoistnie.

W Rozdziale 2 przedstawiamy nasz pierwszy model eksperymentalny, oparty na małych pochodnych peptydów, złożonych z dwóch fragmentów dipeptydowych i łącznika diaminowego. Wykazujemy, że niektóre z tych pochodnych mogą ulegać samokoacerwacji [ang. *self-coacervation*], powodowanej głównie przez oddziaływania hydrofobowe. Badamy też, na ile uniwersalna jest konstrukcja badanych pochodnych, zmieniając łącznik i sekwencję fragmentu dipeptydowego, by dojść do wniosku, że separacji fazowej ciecz-ciecz ulegać mogą pochodne, w skład których wchodzą dipeptydy hydrofobowe (które pełnią rolę spajaczy [ang. *stickers*]) oraz giętkie, hydrofilowe łączniki (które pełnią rolę odstępników [ang. *spacers*]), podobnie do inherentnie nieuporządkowanych białek ulegających separacji fazowej. Następnie pokazujemy, że separacja fazowa pochodnych zawierających łączniki disiarczkowe może być regulowana przez reakcje redoks, a kondensaty mogą akumulować różne cząsteczki.

W Rozdziale 3 skupiamy się na skłonności niektórych pochodnych opisanych w Rozdziale 2 do przemiany z fazy ciekłej w fazę stałą [ang. *liquid-to-solid transition*]. W pierwszej kolejności badamy zmiany w morfologii kondensatów na poziomie mikroskopowym (z wykorzystaniem mikroskopii optycznej) oraz nanoskopowym (z wykorzystaniem transmisyjnej mikroskopii elektronowej oraz mikroskopii sił atomowych), wykazując, że przemiana ciekłych kropel w stałe cząstki powiązana jest z powstawaniem włóknistych struktur na poziomie nanoskopowym. Następnie przeprowadzamy bardziej szczegółową charakteryzację struktur tworzonych przez pochodną FFssFF na poziomie cząsteczkowym z wykorzystaniem dyfrakcji promieniowania rentgenowskiego oraz NMR ciała stałego. Pomiary NMR w połączeniu z obliczeniami strukturalnymi pozwalają zidentyfikować dwie struktury β o odmiennej geometrii, które tworzą włókna.

W Rozdziale 4 wykorzystujemy odwracalność tworzenia wiązań disiarczkowych do kierowania przemianami fazowymi pochodnych peptydów z łącznikiem disiarczkowym. Wybieramy grupę peptydowych dimerów o różnych właściwościach (całkowicie roztwarzalnych, ulegających separacji fazowej ciecz-ciecz przy wysokim stężeniu, ulegających se-

paracji fazowej ciecz-ciecz z dalszą przemianą z cieczy w ciało stałe oraz ulegających bezpośredniemu wydzieleniu z roztworu w formie stałych agregatów) i wykazujemy z pomocą symulacji komputerowych, że wymiana monomerów może napędzać przemiany fazowe. Następnie dowodzimy eksperymentalnie, że małe zmiany w składzie kondensatu prowadzić mogą do przemiany fazowej ciecz-ciało stałe lub do roztworzenia kondensatu. Wreszcie pokazujemy, że wymiana monomerów zachodzić może dla różnych kombinacji dimer-monomer.

W Rozdziale 5 analizujemy możliwe mechanizmy agregacji białek w dwufazowych systemach gospodarz-gość. Bazując na podstawowym modelu agregacji, opisującym agregację białek za pomocą 3 reakcji (nukleacja pierwotna [ang. *primary nucleation*], elongacja [ang. *elongation*] i nukleacja wtórna [ang. *secondary nucleation*]), opracowujemy kilka modeli opartych na równaniach różniczkowych zwyczajnych [ang. *ordinary differential equations*] w celu opisania wielu aspektów agregacji białek w obecności ciekłych kondensatów. Omawiamy wpływ współczynnika podziału oraz objętości kondensatu, sekwestrację monomerów poprzez zmieniony współczynnik aktywności lub stałą kinetyczną reakcji w fazie skondensowanej, a także nukleację włókien na granicy faz. Na końcu rozdziału wykorzystujemy również stochastyczny model agregacji białka oparty na algorytmie Gillespiego, w celu zbadania wpływu partycjonowania na rozkład czasów agregacji oraz długości włókien.

W Rozdziale 6 staramy się eksperymentalnie potwierdzić obserwacje z Rozdziału 5, wykazując, że modele kondensatów biomolekularnych mogą wpływać na kinetykę agregacji α-synukleiny. Badamy agregację 3 wariantów α-synukleiny (α-synukleiny pełnej długości, skróconego wariantu bez ujemnie naładowanego fragmentu C-końcowego i krótkiej sekwencji pochodzącej z fragmentu tworzącego β-kartkę) w obecności 3 eksperymentalnych modeli kondensatów biomolekularnych. Identyfikujemy 3 tryby interakcji białko-kondensat (akumulacja wewnątrz kondensatu, akumulacja na granicy faz oraz wykluczenie) i za pomocą testów z tioflawiną T pokazujemy, że te interakcje mogą w różnym stopniu wpływać na kinetykę agregacji białka. Mianowicie, akumulacja wewnątrz kondensatu może prowadzić zarówno do przyspieszonej, jak i spowolnionej agregacji, podczas gdy akumulacja na granicy faz prowadzi do znacznego przyspieszenia agregacji. Podobnie w przypadku insuliny – akumulacja wewnątrz lub na granicy faz przyspiesza agregację. Badania mikroskopowe z użyciem FRET-oznakowanej α-synukleiny oraz tioflawiny T pokazują, że agregacja białka najprawdopodobniej inicjowana jest na powierzchni kondensatów, także w przypadku akumulacji białka wewnątrz kondensatu.

W ostatnim Rozdziale 7 przedstawiamy ogólne wnioski z badań opisanych w Rozdziałach 2-6. Przyglądamy się także najnowszym osiągnięciom z obszaru agregacji białek w obecności ciekłych kondensatów. Na końcu sugerujemy możliwe kierunki rozwoju badań opisanych w pracy.

Samenvatting

Vertaald uit het Engels door Merlijn van Haren en Brent Visser

Eiwitaggregatie is al tientallen jaren een onderwerp van omvangrijke wetenschappelijke interesse en is frequent gerelateerd aan meerdere neurodegeneratieve aandoeningen. Het is echter pas recent duidelijk geworden dat het aggregatieproces beïnvloed kan worden door een ander belangrijk biologisch fenomeen:vloeistof-vloeistof fasescheiding, een proces dat ten grondslag ligt aan de vorming van membraanloze organellen. In dit werk onderzoeken we hoe de aggregatie van eiwitten en peptiden beïnvloed wordt door de aanwezigheid van biomoleculaire condensaten, via simulaties en experimentele modellen in vitro.

In Hoofdstuk 1 beginnen we met het uitleggen van de relevantie van eiwitaggregatie en vloeistof-vloeistof fasescheiding in een cellulaire context. We leggen de fysische basis van vloeistof-vloeistof fasescheiding en laten zien hoe verschillende soorten vloeistof-vloeistof fasescheiding van eiwitten kwalitatief kunnen worden geïllustreerd met behulp van fase-diagrammen. Vervolgens kijken we naar de moleculaire achtergrond van zowel vloeistof-vloeistof fasescheiding als aggregatie, en geven we een samenvatting over onze huidige kennis is van de vloeistof naar vaste stof overgang van eiwitten. Tot slot bespreken we aggregatie in host-guest systemen, waarin het aggregerende eiwit zelf geen vloeistof-vloeistof fasescheiding ondergaat.

In Hoofdstuk 2 introduceren we ons eerste experimentele model, gebaseerd op kleine peptidederivaten, bestaande uit twee dipeptidegroepen en een diaminelinker. We laten zien dat sommige van deze peptidenderivaten zelf-coacervatie kunnen ondergaan, voornamelijk aangedreven door hydrofobe interacties. We onderzoeken hoe algemeen het derivaatontwerp is door de sequentie van de dipeptidegroepen en de linker veranderen, om vervolgens te concluderen dat vloeistof-vloeistof fasescheiding kan optreden voor derivaten met hydrofobe dipeptiden (stickers) en flexibele, hydrofiele linkers (spacers), analoog aan fasescheidende intrinsiek ongestructureerde eiwitten. We laten ook zien dat fasescheiding van derivaten die een disulfide-linker bevatten gereguleerd kan worden door redoxreacties en dat de condensaten verschillende moleculen kunnen accumuleren.

In Hoofdstuk 3 richten we ons op de neiging van sommige van de derivaten, geïntroduceerd in Hoofdstuk 2, om de overgang van vloeistof naar vaste stof te ondergaan. We onderzoeken eerst de morfologische veranderingen van condensaten op microscopisch niveau (met lichtmicroscopie) en op nanoscopisch niveau (met een transmissie-elektronenmicroscoop en atoomkrachtmicroscopie), waarbij we laten zien dat de transformatie van vloeistofdruppels naar vaste deeltjes gekoppeld is aan de vorming van nanoscopische fibrillaire structuren. Vervolgens karakteriseren we op moleculair niveau de fibrillen die gevormd worden door het FFssFF-derivaat, door middel van röntgendiffractie en vaste stof NMR. De NMR-metingen gecombineerd met structuurberekeningen maken het mogelijk om twee ladderstructuren waaruit de fibrillen zijn opgebouwd te identificeren.

In Hoofdstuk 4 maken we gebruik van de omkeerbaarheid van de vorming van de disulfidebinding, om chemisch de faseovergangen van peptidederivaten met een disulfide-linker chemisch te controleren en aan te sturen. We selecteren een reeks van peptidedimeren met verschillende eigenschappen (volledig oplosbaar, vloeistof-vloeistof fase scheidend bij hoge concentratie, vloeistof-vloeistof fase scheidend met vervolgens vloeistof-naar-vaste

fase overgang, en fase scheidend direct als aggregaat) en laten door middel van simulaties zien dat monomeeruitwisseling faseovergangen kan aandrijven. Vervolgens leveren we ook experimenteel bewijs dat kleine veranderingen in de samenstelling van het condensaat kunnen resulteren in vloeistof-naar-vaste stof overgang, of in het oplossen van het condensaat. Tot slot laten we zien dat monomeeruitwisseling kan plaatsvinden in meerdere combinaties van dimeer-monomeer.

In Hoofdstuk 5 onderzoeken we de mogelijke mechanismen van eiwitaggregatie in host-guest tweefasensystemen. Op basis van het simpele aggregatiemodel, waarin eiwitaggregatie beschreven wordt met behulp van drie reacties (primaire nucleatie, verlenging en secundaire nucleatie), ontwikkelen we verschillende modellen gebaseerd op gewone differentiaalvergelijkingen om meerdere aspecten van eiwitaggregatie in de aanwezigheid van vloeibare condensaten te beschrijven. We bespreken de invloed van de verdelingscoëfficiënt en het condensaatvolume, inactieve opslag van monomeren door veranderde activiteitscoëfficiënt of reactiesnelheidsconstanten in de gecondenseerde fase, en de interface gekatalyseerde nucleatie van fibrillen. Aan het eind van het hoofdstuk gebruiken we ook een stochastisch model van eiwitaggregatie gebaseerd op het Gillespie-algoritme, om de invloed van de verdelingscoëfficiënt te onderzoeken op aggregatietijden en fibrillenlengtes.

In Hoofdstuk 6 proberen we de bevindingen uit Hoofdstuk 5 experimenteel te bewijzen en laten we zien dat model biomoleculaire condensaten de kinetiek van α-synucleïneaggregatie kunnen beïnvloeden. We bestuderen aggregatie van drie α-synucleïne varianten (het volledige α-synucleïne eiwit, een ingekorte variant zonder het negatief geladen C-terminale fragment, en een korte sequentie van het β-sheet-vormende fragment) in de aanwezigheid van drie model biomoleculaire condensaten. We identificeren 3 aggregerende eiwit-condensaat interactiemodi (partitionering, oppervlakteaccumulatie en uitsluiting) en laten zien dat deze interacties de kinetiek van eiwitaggregatie kunnen beïnvloeden door de aggregatie te volgen met thioflavine-T assays. Partitionering van α-synucleïne kan resulteren in zowel versnelde als vertraagde aggregatie, terwijl oppervlakteaccumulatie resulteert in een aanzienlijke versnelling van aggregatie. Op dezelfde manier kan partitionering of oppervlakte-accumulatie van insuline ook leiden tot snellere aggregatie. Microscoop-gebaseerde assays met FRET-gelabelde α-synucleïne en thioflavine-T laten zien dat eiwitaggregatie hoogstwaarschijnlijk wordt geïnitieerd op het grensvlak van condensaten en ook in het geval van eiwitpartitionering in condensaten.

Tenslotte geven we in het laatste Hoofdstuk 7 algemene conclusies van de bevindingen beschreven in de Hoofdstukken 2-6. We kijken ook naar de meest recente ontwikkelingen op het gebied van eiwitaggregatie in de aanwezigheid van vloeibare condensaten. We eindigen met suggesties voor mogelijke voortzetting van het werk beschreven in dit proefschrift.

Frequent acronyms

AD Alzheimer's disease
AFM atomic force microscopy
ALS amyotrophic lateral sclerosis
α**Syn** α-synuclein
α**Syn-108** truncated variant of α-synuclein, α-synuclein(1-108)

CP cross-polarisation

DARR dipolar assisted rotational resonance
Ddx4 DEAD-box helicase 4
DNA deoxyribonucleic acid
DREAM dipolar recoupling enhanced by amplitude modulation
DTT dithiothreitol

FF phenylalanyl-phenylalanine
FL-α**Syn** full-length α-synuclein
FRET fluorescence resonance energy transfer
FUS fused in sarcoma

HD Huntington's disease
HEPES 4-(2-hydroxyethyl)-1-piperazineethanesulfonic acid
hnRNPA1 heterogeneous nuclear ribonucleoprotein A1
HPLC high-performance liquid chromatography

IDP intrinsically disordered protein
IDR intrinsically disordered region

LCST lower critical solution temperature
LLPS liquid-liquid phase separation
LST liquid-to-solid transition
LUV large unilamellar vesicle

MLOs membraneless organelles
MS mass spectrometry

NACore non-amyloid-β component of α-synuclein, α-synuclein(68-78)
NMR nuclear magnetic resonance

ODE ordinary differential equation

PAIN proton-assisted insensitive nuclei cross-polarisation
PD Parkinson's disease
PEG poly(ethylene glycol)
PLL-g-PEG poly-L-lysine grafted with poly(ethylene glycol)
pLys/ATP coacervate formed by poly-L-lysine and adenosine triphosphate

pLys/pGlu coacervate formed by poly-D,L-lysine and poly-D,L-glutamate

RNA ribonucleic acid
RNP ribonucleoprotein
RP3/polyU coacervate formed by RRASLRRASLRRASL-NH$_2$ peptide with polyuridylic acid

SSA stochastic simulation algorithm
SUV small unilamellar vesicle

TCEP tris(2-carboxyethyl)phosphine
TDP-43 TAR DNA-binding protein 43
TEAB triethylammonium bicarbonate
TEM transmission electron microscopy
ThT thioflavin T
Tris tris(hydroxymethyl)aminomethane

UCST upper critical solution temperature

XRD X-ray diffraction

1

General introduction

1.1 Protein aggregation

With increasing life expectancy, neurodegenerative diseases involving pathological amyloid formation are becoming alarmingly common. Misfolded and aggregated proteins may accumulate during the lifetime of a cell when they are not refolded or cleared by protein quality control machinery. Formation of protein aggregates is one of the hallmarks of neurodegenerative diseases such as Alzheimer's Disease (AD), Parkinson's Disease (PD), Amyotrophic Lateral Sclerosis (ALS), frontotemporal lobar degeneration (FTLD) and Huntington's Disease (HD)[1–3]. Figure 1.1 depicts different aspects of four neurodegenerative diseases: FTLD, ALS, PD, and AD. Currently, there are around 50 known protein precursors related to amyloid disease, such as amyloid-β (related to AD), α-synuclein (PD), and huntingtin (HD).
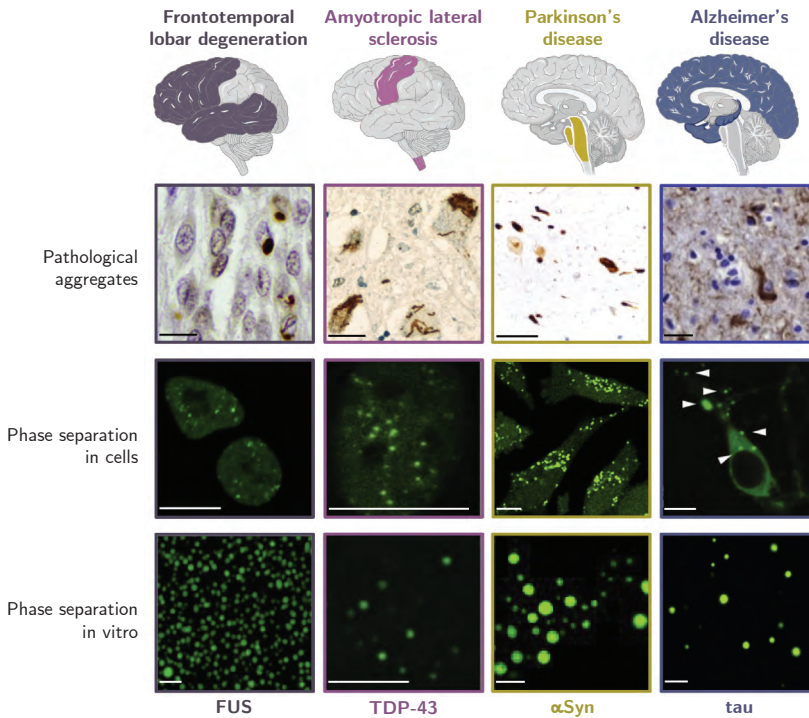
Figure 1.1: Proteins associated with neurodegenerative diseases and their LLPS behaviour. Schematic representation of brain areas containing pathological aggregates of FTD-associated FUS (purple), ALS-associated TDP-43 (pink), PD-associated α-synuclein (yellow), and AD-associated tau (blue). Second row: representative immunohistochemistry images of pathological aggregates found in postmortem brain samples from FUS and TDP-43, α-synuclein, and tau. Scale bar is 20 μm. Third and fourth row: phase-separated protein in cells and in vitro, respectively. Scale bar is 10 μm. Figure taken from[4].

For many years researchers have studied the origins, mechanism, and toxicity of pro-

tein aggregation to develop effective therapies. Still, many aspects of the mechanism of protein aggregation remain incompletely understood [5,6]. The quest for new therapies is impeded by the fact that processes inside cells take place in a complex environment that is difficult to reproduce in vitro [7]. By contrast, most protein aggregation studies are carried out with synthetic peptides or protein fragments in dilute, homogeneous, and well-mixed solutions [8,9]. However, the aggregation process can be significantly influenced by the inhomogeneities of the cell environment, including the biomolecular condensates formed upon liquid-liquid phase separation (LLPS).

In this thesis, we try to investigate the potential influences of liquid condensates on the aggregation process. We use a simplistic approach to model biological condensates with coacervates formed by much simpler molecules and study the basic principles governing LLPS followed by the transition from liquid to solid. We also look at the aggregation process in liquid-liquid phase separated systems in which the coacervates serve as hosts for the guest molecules of aggregating protein. We aim to understand better the mechanisms by which liquid condensates can affect aggregation in living cells.

This introduction chapter aims to explain the basic principles of LLPS and introduce some examples of liquid condensates, to further look at the mechanism of protein aggregation and the possible relations between the formation of condensed liquids and solid aggregates.

1.2 Liquid-liquid phase separation in living cells

In contrast to solutions typically used for experiments in vitro, the composition of living cells is far from homogeneous and diluted [10]. The presence of highly concentrated biomolecules results in high viscosity and molecular crowding that affect the reaction kinetics [11,12]. And the lack of homogeneity is caused by the cellular mechanisms of segregating its components into organelles, which provide spatiotemporal control over biochemical processes and stored material. This allows cells to maintain complex metabolic pathways and control various biochemical reactions at the same time [13]. As an example, the nucleus separating transcription from the translation process allowed eukaryotes to develop a complex system of posttranscriptional control, which is not possible in nucleus-less prokaryotes [14].

Nucleus, lysosomes, and endoplasmic reticulum are examples of classical, membrane-bound organelles. They are separated from the cytoplasm by a lipid bilayer. However, cells also contain a plethora of organelles that are not surrounded by a membrane, thus called membrane-less organelles (MLOs) (Figure 1.2). These are typically assemblies of mostly proteins and nucleic acids and examples of them include stress granules, processing bodies or the centriole in the cytoplasm, and nucleolus or nuclear speckles in the nucleus. While the coexistence of different compartments separated by a membrane is rather understandable, the presence of separated volumes without any (physical barrier) may be puzzling [13,15].

MLOs emerge as a result of LLPS and are a specific example of coacervates – liquid condensates formed when one or multiple water-soluble polymers[i] start forming two phases

---

[i]Typically LLPS involves polymers/macromolecules, but small molecules can also undergo LLPS.

– a dilute phase (diluted water solution of these polymers) and a condensed phase (phase with extremely high concentration of the polymers, still containing a significant amount of water). The condensed phase shows properties that are distinct from the dilute phase (and distinct from diluted water solutions in general) in terms of hydrophobicity, viscosity, and molecular crowding. This could have a significant influence on the biochemical processes occurring in the presence of condensed droplets, including the process of pathological protein aggregation[12].
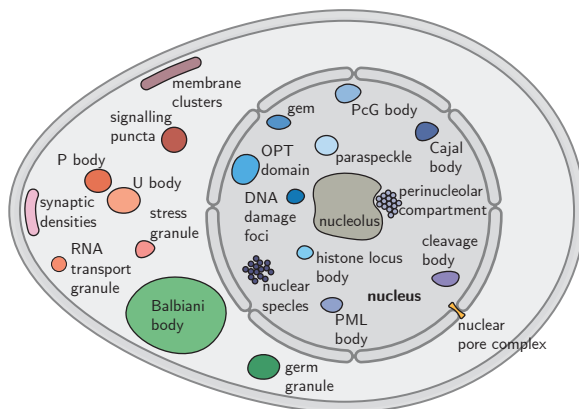
Figure 1.2: Schematic of MLOs in the nucleus, cytoplasm, and membranes of eukaryotic cells. Adapted from[13].

1.2.1 Basics of LLPS

Depending on the driving forces behind LLPS, it can be divided into three main types: (i) segregative, (ii) associative, and (iii) simple phase separation[16]. Segregative phase separation occurs when two water-soluble molecules do not mix and divide into two separated aqueous phases, each enriched in one of the solutes. This happens despite the favourable entropy of mixing, as a result of repulsive interactions between the components. An example of segregative phase separation is that of poly(ethylene glycol) (PEG) and dextran.

In associative phase separation, solutes end up in the same condensed phase, due to attractive interactions between them. This condensed phase is called a (complex) coacervate – it is enriched in both soluble molecules but still contains a significant amount of solvent (typically more than 50% w/w) and coexists with a dilute phase, depleted of both solutes (containing mostly solvent). A classical example of associative phase separation is that of two oppositely charged polymers – the attraction between positive and negative charges drives the formation of the dense phase.

Finally, simple phase separation occurs when the attractive interactions are present within the population of only one type of molecule. Single solutes can undergo LLPS as a result of changes in temperature, pH, or ionic strength (salt concentration). The condensed phase that is formed in such a case is called a simple coacervate, as it is

also enriched in the solute, it coexists with a dilute phase, and it has similar properties to the condensates formed upon complex coacervation. Many proteins with disordered regions have been found to undergo simple phase separation, as a result of π-π, cation-π, hydrogen bonding, dipole-dipole and charge interactions[17,18].

1.2.2 Flory-Huggins solution theory

A relatively simple approach to describe the thermodynamics of LLPS makes use of the Flory-Huggins solution theory (equation 1.1)[19]. The theory is based on a lattice model for a binary mixture of linear polymer molecules and solvent molecules Figure 1.3 and allows to calculate the free energy density change accompanying mixing at constant temperature and pressure.

$$\Delta F_{\mathrm{mix}} = \Delta U_{\mathrm{mix}} - T\Delta S_{\mathrm{mix}}$$
$$\Delta F_{\mathrm{mix}} = \Delta U_{\mathrm{mix}} + Tk_B \left[\frac{\phi}{N} \ln \phi + (1-\phi)\ln(1-\phi) \right]$$
$$\frac{\Delta U_{\mathrm{mix}}}{k_B T} = \chi \phi (1-\phi)$$

(1.1)

The change in free energy density (ΔF_{mix}) consists of (i) the heat term (ΔU_{mix}), which depends on the attractive or repulsive polymer-polymer interactions, solvent-polymer interactions and solvent-solvent interactions, and of (ii) the entropic term ($T\Delta S_{\mathrm{mix}}$), related to the increase of available polymer configurations in the lattice upon mixing[20,21]. The entropic term can be expanded as shown in the second row of equation 1.1, where N is the number of monomers in the polymer chain, ϕ is the volume fraction of the polymer in the mixture, k_B is the Boltzmann's constant and T is temperature. It is worth noting that the entropy of mixing is always negative and therefore always promotes mixing. Also, the absolute value of the term decreases with increasing number of monomers in the polymer chain. The heat term can be simplified by an interaction parameter χ that encompasses all interactions in the mixture.
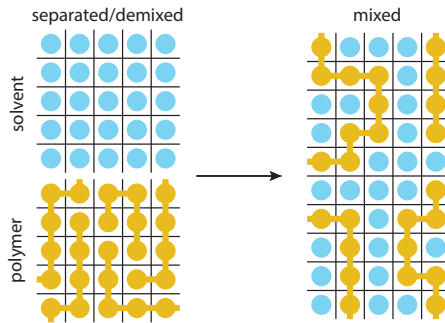
Figure 1.3: Schematic representation of the lattice model.

The mean field approach is very simplistic but it can help explain the driving forces be-

hind the demixing or LLPS of polymers forming simple coacervates when polymer-polymer interactions are stronger than the polymer-solvent interactions. One of its limitations is only taking into account the entropy gain from the redistribution of the molecules within the lattice, but not considering the changes in entropy related to the restricted conformation or orientation of molecules in the mixed or demixed state. This entropy change originating from the conformation/orientation of molecules can be included in the enthalpic term, and by making χ dependent on temperature, composition or other parameters it is even possible to model re-entrant phase transition. We show the importance of these additional entropy terms in Chapter 2 where we propose the design of a small phase-separating peptide, which LLPS is driven by hydrophobic interactions and non-mixing entropy gain.

1.2.3   Phase diagrams

The occurrence of LLPS and the composition of both phases is often summarised using a phase diagram Figure 1.4. In the case of segregative phase separation, the diagram depicts the range of concentrations of the two soluble molecules (and sometimes also temperature or pH) for which the mixed state (one-phase region) and the demixed state (two-phase region) are thermodynamically stable. The boundary between these regions is called the binodal. Each point on the binodal represents a possible composition of one of the phases formed upon phase separation and is connected to a second point corresponding to the coexisting phase via a tie line. The solution can remain supersaturated and not undergo LLPS upon crossing the binodal line when the nucleation energy barrier delays the demixing. The area of concentrations for which demixing occurs spontaneously and the solution cannot be supersaturated is bordered by the spinodal.
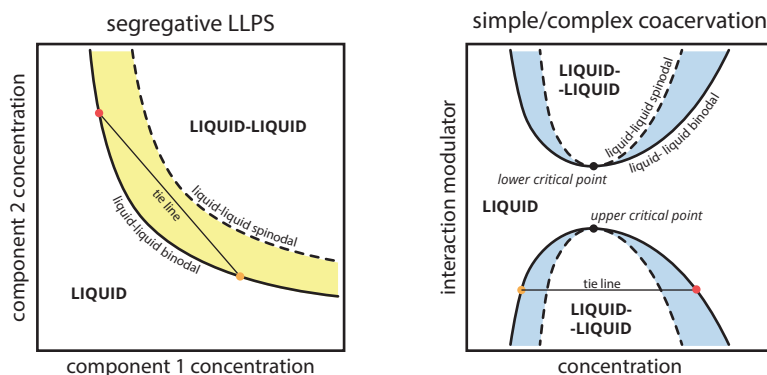
Figure 1.4: Schematic phase diagrams of segregative phase separation and of simple or complex coacervation.

Phase diagrams are most often constructed by preparing mixtures at different relative concentrations and reporting their state (mixed/demixed) after equilibration. The approximate binodal is then drawn as the line that separates the one- and two-phase regions. A more accurate approach is to measure the concentration of both molecules in the separate

phases (e.g., by absorbance, fluorescence, or NMR) for different overall compositions, to draw a series of tie lines and reconstruct the binodal by connecting these points[22].

A phase diagram of associative phase separation often depicts the one- and two-phase regions for a particular ratio between the two interacting molecules (e.g., equimolar, or 1:1 charge ratio), as a function of the concentration of one of them and a tuning parameter, such as temperature or salt concentration (Figure 1.4). As for segregative phase separation, the binodal separates the two regions, and tie lines connect two coexisting phases on the binodal. The tuning parameter can be used to increase or decrease the width of the two-phase region, and beyond a critical point no phase separation occurs. Depending on the tuning parameter, this could be an upper or lower critical solution temperature (UCST/LSCT) point or a critical salt concentration. Certain systems have both upper and lower critical solution points, which means there are two regions where LLPS occurs (as depicted in Figure 1.4). The transition from a two-phase region into a one-phase region and then into a two-phase region again, upon changing only one parameter (temperature or salt concentration), is called reentrant phase transition. Again, supersaturation due to the nucleation energy barrier can occur within the area bounded by the binodal and spinodal line. The phase diagram of simple coacervation is similar to the diagram for complex coacervate, but it considers the concentration of only one component instead of two at a fixed ratio.

1.3 Molecular determinants of coacervation and aggregation

The condensed phase formed upon coacervation (so either as a result of associative or simple LLPS) is stabilised by the weak and transient interactions between multivalent molecules. These are typically attractive interactions between oppositely charged moieties, dipole-dipole interactions (or mixed dipole-charge), hydrogen bonds, cation-π interactions or π-π interactions Figure 1.5. To keep the condensed phase dynamic, patches rich in the interacting moieties should be separated by typically flexible linkers, in a so-called sticker-spacer arrangement. The balance between sticker and spacer motifs should allow for intermolecular interactions strong enough to drive condensation, but should also allow for enough flexibility to prevent aggregation of phase-separating molecules.

In many cases, the condensed liquid is metastable, separated by an energy barrier from the thermodynamically preferred aggregate state (Figure 1.6). The energy barrier is typically linked to conformational rearrangements within the disordered linker segments. The left panel of Figure 1.6 shows a schematic phase diagram of a protein undergoing metastable LLSP with an upper critical point. The liquidus line corresponds to the concentration of the solution in equilibrium with protein crystals. Solidus corresponds to the concentration of protein in crystals. The yellow region represents the supersaturation region of solution-crystal demixing and the dashed line marks the border of the region of spontaneous demixing. Similarly to the phase diagram depicted in the left panel of Figure 1.4, also here there is a liquid-liquid region with an upper critical point. Within this region demixing into two liquid phases is thermodynamically preferred over homogeneous solution phase. Even though the formation of a solid phase is thermodynamically
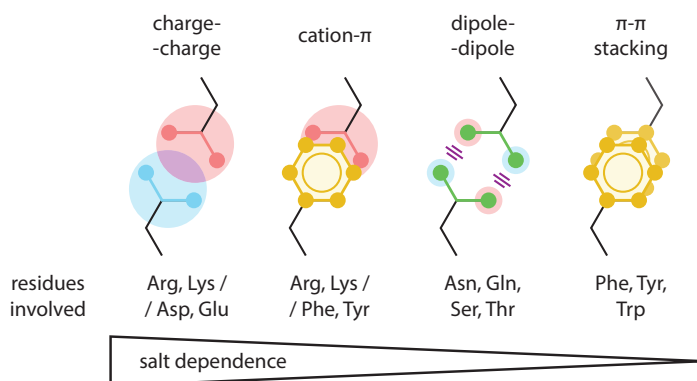
Figure 1.5: Possible interactions involved in the formation of peptide/protein-based coacervates. Based on [21].

preferred over the formation of dense liquid, protein mixture can demix into a metastable liquid-liquid phase due to the energy barrier (right panel of Figure 1.6). In some cases, protein can form also a solid-like gel phase, which, similarly to the condensed liquid phase, is metastable in respect to the crystal phase. Concentration in the gel phase is represented by the gelation line.

The design patterns described in the previous section apply also to proteins undergoing LLPS. Different protein systems can be called multivalent and have sticker-spacer type of structure. In the case of folded/globular protein stickers are the interaction domains located on the surface scaffold of the globular domain (spacer). Linear multivalent proteins contain typically folded interaction domains as stickers separated by disordered, flexible linkers. Finally, for intrinsically disordered proteins (IDPs) and proteins containing intrinsically disordered regions (IDRs), stickers are interacting with single residues or short disordered sequences separated by non-interacting linear motifs [23].

The last type of arrangement is very common for proteins undergoing LLPS. It is also very common for proteins that are prone to aggregate. While in a disordered state, the spacer motifs provide enough flexibility to keep the protein in a soluble or dense-liquid state, conformational changes allowing for stronger intermolecular interactions can drive transition into solid aggregates. These are often amyloid-like, rich in β-sheet structures and stabilised by hydrogen bonds.

Examples of aggregating proteins that share the disordered character include amyloid-β, tau and α-synuclein. Around 50 different proteins or peptides are known to form amyloid aggregates [24,25]. Aggregates of these proteins are stabilised by cross-β structures, but the structure of the fibrils can be complex. Different proteins can form amyloids with different structures and often even one protein can form different polymorphic fibrils. For example, amyloid-β(1-42) can form two polymorphic fibrils at different growth conditions [26,27] and amyloid-β(1-40) can form different polymorphs under the same growth conditions but when propagated from different seeds [28]. The common feature of different amyloid polymorphs is a ladder of β-strands oriented perpendicular to the fibril axis with peptide

chains separated by 4.7-4.8 Å. This spacing is determined by regular hydrogen bond distances between paired carbonyl and amide groups in adjacent β-strands[24]. These β-strands are stabilised by steric zippers - interactions between hydrophobic side groups of the aggregated polypeptide[29].

The ability to form various polymorphic aggregates under different conditions suggests that the aggregation mechanism can be dependent on the environment. This includes the temperature, pH or ionic strength of the solution, but also the presence of interfaces and dense liquid phase. Understanding the aggregation mechanisms, amyloid structures that they lead to and ultimately their relations with the disease is essential to develop new methods of diagnosing, delaying and hopefully also stopping the progression of the disease.
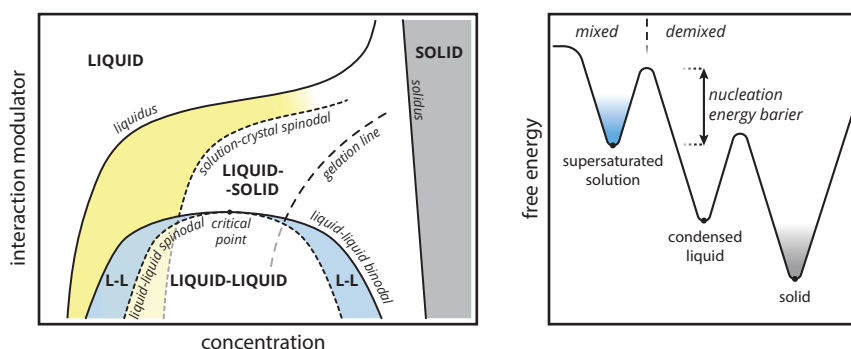
Figure 1.6: Schematic phase diagram and energy landscape diagram of a protein undergoing LLPS and LST. Based on[30].

1.4 Liquid-to-solid transition in protein condensates

Proteins that have the ability to form fibrillar aggregates, may not only be affected by partitioning into liquid condensates formed by other materials. They are very often undergoing LLPS on their own, and the condensed liquid state can be a transition state on the way to aggregates. It is commonly agreed that the formation of fibrils can be initiated in the dilute phase, as a combination of primary and secondary nucleation. Fibril formation within the liquid phase is an alternative pathway, and the condensed liquid phase can facilitate fibril formation by increasing the local concentration of the protein[31].

It is still not clear to what extent LLPS can be relevant in pathological aggregation – the two routes, nucleation in the dilute phase and liquid-to-solid transition, are not mutually exclusive and their significance may differ for different proteins and different contexts (e.g. in vitro vs. in living cells). The ability to undergo LLPS has been shown either in vivo or in vitro for proteins like FUS[32,33], hnRNPA1[34,35] and TDP-43[34], and for all of them it has been also observed that the neurodegenerative disease-related mutations within their low-complexity domains can promote LLPS[32,33,36,37]. In vitro

LLPS and further liquid-to-solid transition (LST) of pure amyloidogenic proteins is only a great simplification of the processes that occur in living cells. However, studying these processes in simple systems can still provide information about the general mechanisms of liquid-to-solid transition.

For example, recent work by S. Ray et al. shows that Parkinson's related protein α-synuclein (αSyn) undergoes LLPS on its own[38] and that the liquid condensates can serve as nucleation spots for amyloid aggregation[39] (Figure 1.7). This LST, or ageing of liquid droplets, is initiated primarily in the centre of the droplets (due to high local concentration). Upon fusion and Ostwald ripening fresh monomeric material gets transported from homogeneous liquid droplets to droplets containing the solid-like core. Interestingly, this transport seems to be arrested in condensates that underwent complete LST and formed solid particles[39].
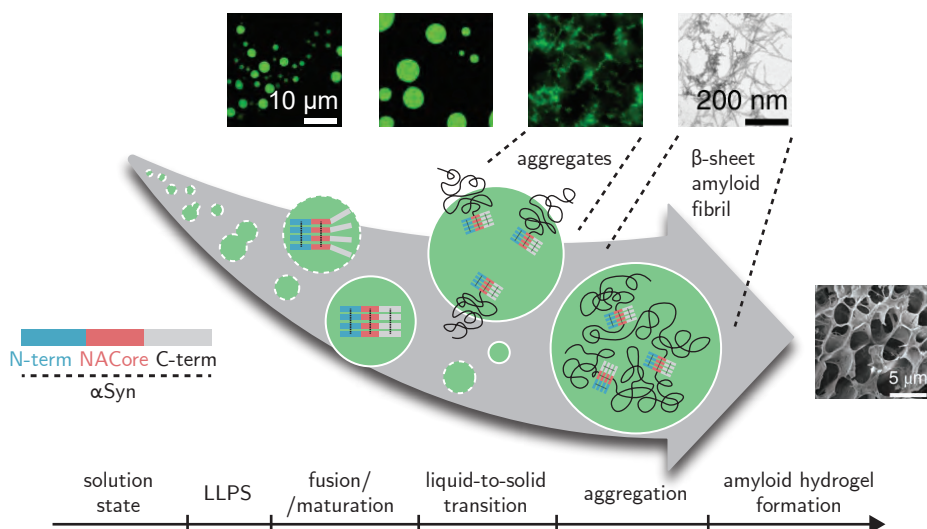
Figure 1.7: A scheme of αSyn aggregation via condensed liquid phase. The large grey arrow represents the timeline of LLPS and subsequent LST driven by the gradual rearrangement of molecules into cross-β structures. Liquid droplets and aggregates are visualised using fluorescence microscopy, amyloid fibrils are visualised using TEM and hydrogel is visualised using SEM. Adapted from[38].

Studies of tau protein, which plays a role in microtubule assembly and stabilisation, but can also form pathological aggregates, have shown that it has the propensity to undergo LLPS[40,41]. A more detailed investigation of the LST process occurring in tau condensates revealed that the environment of liquid droplets promotes extended protein conformation, facilitating intermolecular interactions, and further clustering and aggregation[42]. A simple, but elegant study by Boyko et al. has shown that while aggregation kinetics of phase-separating proteins should not be affected by the changes in concentration within the phase-separation regime (as the rate-determining concentration within liquid droplets

remains constant), it can be regulated upon the addition of non-aggregating mutants that colocalise in the dense-liquid phase[43]. This case of *diluted* tau, even though droplets are formed by mutants of the same protein, is effectively similar to host-guest systems where aggregating protein is only one of the components.

As mentioned, the direct connection between LLPS and LST of pure amyloidogenic proteins in vitro and the pathological LST (or aggregation in general) remains questionable, as condensation of pure proteins requires typically non-physiologically high concentration (either of the protein itself or of additives)[38,44]. Also in vivo studies are usually performed in systems in which proteins are overexpressed to reach very high concentrations[45]. However, it is well possible that small clusters with liquid-like properties, locally enriched in the aggregating proteins, emerge either within heterogeneous liquid droplets or at biological interfaces (like lipid-membranes or liquid-liquid interfaces)[46].

Interestingly, intracellular proteins that undergo LLPS share similarities with proteins forming biologically functional fibrils, such as elastin[47] or silk[48]. Multiple proteins and peptides, including FUS and Ded1 (RNA binding proteins from human and yeast cells), have been shown to undergo shear-mediated LST and fibril formation[49]. Authors suggested that the shear-driven LST and ageing of liquid biomolecular condensates have a common background, which is the formation of rigid hydrogen-bond-stabilised structures, mostly intermolecular β-sheets.

1.5   Aggregation of proteins in host-guest systems

The involvement of liquid condensates in protein aggregation is not limited to the situation when the aggregating protein undergoes LLPS on its own. An alternative scenario is an aggregation in the presence of liquid condensates formed by *inert* material, inert in the sense that it does not undergo aggregation. In the ideal host-guest system, guest material (aggregation-prone protein) does not change the properties of liquid condensates formed by the host (this is valid assuming the large excess of host molecules over guest molecules in the condensed phase). An ideal inert condensate system is also not affected by the emergence of aggregates within the droplets. While the concentrations of aggregating proteins within living cells may be too low to induce LLPS it is very probable that at even low concentrations aggregating proteins interact with condensates formed by other material, abundant in living cells.

The importance of this mechanism may be still underestimated. The influence of inert liquid condensates on the protein aggregation process has been theoretically studied by Weber and co-workers[50]. In this work, they show the effect of partitioning into inert condensates can have a profound influence on the aggregation kinetics, even for very low partition coefficients (K_P). The effect is driven by a positive feedback loop. Upon nucleation inside the condensed phase, aggregating monomers start to be quickly used in the elongation process. However, unlike in the homogeneous system, where this results in an also quick decrease in monomer concentration, in a two-phase system, the concentration of monomers gets replenished by partitioning of monomers from the outer phase (Figure 1.8). When the volume of the condensed phase is much smaller than the volume of the dilute phase, and when the transport of monomers between phases is much faster

than the aggregation reactions, the effective influence on the kinetics can be comparable to increasing the concentration in a corresponding homogeneous system K_P-times (of course the amount of aggregate formed remains the same). In a more realistic scenario, when the ratio of condensate versus dilute-phase volumes is not negligible, this value does not only have an influence on the kinetics but also on the number of aggregates (so also on their length), in addition to the reaction order indexes n_c and n_2.
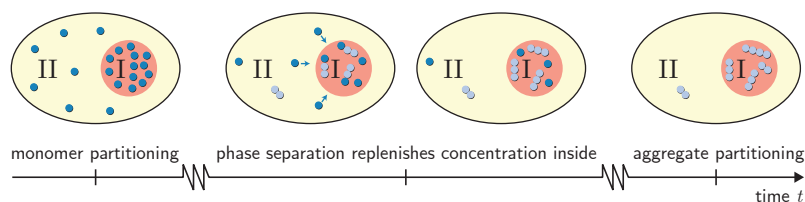
Figure 1.8: Scheme of aggregation kinetics in a two-phase system. Compartment II represents the dilute phase and compartment I represents the condensed phase. Left: Initially, monomers get enriched on short diffusive time scales due to the partitioning mediated by the phase-separated compartments. Centre: Monomers slowly aggregate. More aggregates nucleate and grow in compartment I due to the initial partitioning of monomers. This pronounced, initial aggregation causes a continuous monomer flux into compartment I, further promoting aggregation (positive feedback indicated by arrows). Right: Partitioning of monomers together with the positive feedback can cause a very pronounced accumulation of aggregates relative to compartment II. Adapted from [50].

A more realistic scenario takes into account that the condensate environment has a significantly distinct viscosity from the surrounding dilute phase. This can have a significant effect on the aggregation rates. It can be expected that increased viscosity slows down the aggregation process, simply due to decreased mobility of the molecules. A simple assay studying the kinetics of αSyn aggregation in solutions containing increasing amount of glycerol showed that the aggregation rates increased with increasing amount of glycerol for solutions containing up to 40% of glycerol [51]. For solutions containing above 40% of glycerol, the aggregation rate starts to decrease. The initial increase can be explained by the altered interactions between water and protein upon the addition of glycerol, or in other words, by stabilisation of the more aggregation-prone conformations of αSyn, probably as a result of increased hydrophobicity. The latter decrease reflects the actual effect of the increasing viscosity of the solvent. In a solution containing 50% aggregation happened still faster than in the control sample (no glycerol) but a solution containing 60% did not aggregate within the experiment time.

Apart from higher viscosity, the condensate environment is also characterised by high molecular crowding, meaning that a large fraction of the volume is occupied by macromolecules (molecular crowders). Other species (guest species, in the case of condensates) are excluded from the volume occupied by the crowders. The excluded volume is dependent on both the size of the crowder molecules and the size of guest species.

Finally, condensates are more hydrophobic than the surrounding solution. The relative permittivity, which is a measure of the polarisability of the medium, of complex coacervates has been estimated to be around 40-50 [52], significantly lower than the relative

permittivity of water, which is 78. This means that inside liquid condensates intermolecular interactions between hydrophobic moieties, like π-π stacking, are weaker than in water, while interactions between hydrophilic moieties, like ion pairing, are stronger than in water[53]. All in all, these effects can affect aggregation kinetics in liquid condensates beyond the simple local concentration increase.

1.6   Aim and outline of the thesis

Studying phase transitions of proteins in living cells proves to be difficult. The main challenge when investigating complex systems is to disentangle the influences of different factors on the liquid-liquid phase separation and liquid-to-solid transition processes. In this thesis we propose methods to study these processes in vitro, using simple model systems, that allow us to look at the basic driving forces of transformations in more detail.

In Chapter 2 we study the properties of small peptide derivatives that are able to undergo LLPS and LST. They can be considered a minimal system of phase transitions based on the sticker-and-spacer model, suggested previously for phase-separating proteins. Similarly to large proteins, these minimal derivatives form water-rich liquid condensates, that are responsive to pH (because of the presence of free amino groups) and reduction/oxidation (due to the presence of a disulphide moiety linking the stickers). We observe that the hydrophobicity of the sticker and the flexibility of the linker determine the propensity to form liquid condensates or solid aggregates.

In Chapter 3 we look closer at the LST of the short peptide derivatives. We observe that over the course of hours, liquid condensates of selected derivatives transform into solid, fibrillar aggregates. We follow the transition process using optical microscopy and TEM, and characterise the aggregates by means of solid-state NMR, XRD, TEM and AFM. Altogether, these show that LLPS is mostly driven by hydrophobic interactions between disordered molecules, but upon reorganisation into amyloid-like β-sheet structures liquid condensates transform into solid aggregates.

In Chapter 4 we describe a dynamic system based on redox-sensitive phase-separating small peptide derivatives. Upon disulphide exchange, these small peptide derivatives can undergo transformations from soluble to coacervating to aggregating (or in the other direction). We show that dynamic chemistry may be used to shape supramolecular assemblies and control phase transitions in protocell models.

In Chapter 5 we describe modelling methods to study the influence of liquid compartments on the aggregation process. Using ODEs we show that even small compartments that partition aggregating monomers can substantially accelerate the aggregation process and in certain cases slow it down. We also show that the interface of condensates can potentially serve as a heterogeneous nucleation spot, also increasing the aggregation rate. Using stochastic simulations, we look at the distribution of the aggregation times and the length of the fibrils, and on the influence of condensates on the noise in the aggregation process.

Finally, in Chapter 6, we provide experimental evidence that model coacervate systems can affect protein aggregation. We study aggregation of three different αSyn variants in the presence of three different complex coacervate systems and observe that the aggreg-

ation process can be accelerated and decelerated in the presence of condensates, by partitioning of protein monomers into condensates or by the accumulation of the monomers at the condensate interface. We suggest that these studies provide a new perspective on the early stages of protein aggregation in the complex cellular environment.

1.7 Contributions and acknowledgements

Manzar Abbas and Jiahua Wang co-wrote the original text for section 1.3. Brent Visser co-wrote the original text for section 1.4 and section 1.5.

Bibliography

[1] C. A. Ross and M. A. Poirier, "Protein aggregation and neurodegenerative disease," *Nat. Med.*, vol. 10, no. 7, p. S10, 2004.

[2] C. A. Brunello, M. Merezhko, R. L. Uronen, and H. J. Huttunen, "Mechanisms of secretion and spreading of pathological tau protein," *Cell. Mol. Life Sci.*, vol. 77, no. 9, pp. 1721–1744, 2020.

[3] D. J. Irwin, V. M. Lee, and J. Q. Trojanowski, "Parkinson's disease dementia: Convergence of α-synuclein, tau and amyloid-β pathologies," *Nat. Rev. Neurosci.*, vol. 14, no. 9, pp. 626–636, 2013.

[4] A. Zbinden, M. Pérez-Berlanga, P. De Rossi, and M. Polymenidou, "Phase Separation and Neurodegenerative Diseases: A Disturbance in the Force," *Dev. Cell*, vol. 55, no. 1, pp. 45–68, 2020.

[5] S. Linse, "Mechanism of amyloid protein aggregation and the role of inhibitors," *Pure Appl. Chem.*, vol. 91, no. 2, pp. 211–229, 2019.

[6] D. Willbold, B. Strodel, G. F. Schröder, W. Hoyer, and H. Heise, "Amyloid-type Protein Aggregation and Prion-like Properties of Amyloids," *Chem. Rev.*, vol. 121, no. 13, pp. 8285–8307, 2021.

[7] N. Laohakunakorn, L. Grasemann, B. Lavickova, G. Michielin, A. Shahein, Z. Swank, and S. J. Maerkl, "Bottom-Up Construction of Complex Biomolecular Systems With Cell-Free Synthetic Biology," *Front. Bioeng. Biotechnol.*, vol. 8, p. 213, 2020.

[8] L. W. Simpson, T. A. Good, and J. B. Leach, "Protein folding and assembly in confined environments: Implications for protein aggregation in hydrogels and tissues," *Biotechnol. Adv.*, vol. 42, p. 107573, 2020.

[9] D. Ami, A. Natalello, M. Lotti, and S. M. Doglia, "Why and how protein aggregation has to be studied in vivo," *Microb. Cell Fact.*, vol. 12, no. 1, p. 17, 2013.

[10] A. A. André and E. Spruijt, "Liquid–liquid phase separation in crowded environments," *Int. J. Mol. Sci.*, vol. 21, no. 16, pp. 1–20, 2020.

[11] D. Gomez and S. Klumpp, "Biochemical reactions in crowded environments: Revisiting the effects of volume exclusion with simulations," *Front. Phys.*, vol. 3, p. 45, 2015.

[12] J. S. Schreck, J. Bridstrup, and J. M. Yuan, "Investigating the Effects of Molecular Crowding on the Kinetics of Protein Aggregation," *J. Phys. Chem. B*, vol. 124, no. 44, pp. 9829–9839, 2020.

[13] S. F. Banani, H. O. Lee, A. A. Hyman, and M. K. Rosen, "Biomolecular condensates: Organizers of cellular biochemistry," *Nat. Rev. Mol. Cell Biol.*, vol. 18, no. 5, pp. 285–298, 2017.

[14] S. Boeynaems, S. Alberti, N. L. Fawzi, T. Mittag, M. Polymenidou, F. Rousseau, J. Schymkowitz, J. Shorter, B. Wolozin, L. Van Den Bosch, P. Tompa, and M. Fuxreiter, "Protein Phase Separation: A New Phase in Cell Biology," *Trends Cell Biol.*, vol. 28, no. 6, pp. 420–435, 2018.

[15] A. A. Hyman, C. A. Weber, and F. Jülicher, "Liquid-liquid phase separation in biology," *Annu. Rev. Cell Dev. Biol.*, vol. 30, no. 1, pp. 39–58, 2014.

[16] M. Abbas, W. P. Lipiński, J. Wang, and E. Spruijt, "Peptide-based coacervates as biomimetic protocells," *Chem. Soc. Rev.*, vol. 50, no. 6, pp. 3690–3705, 2021.

[17] B. Gabryelczyk, H. Cai, X. Shi, Y. Sun, P. J. Swinkels, S. Salentinig, K. Pervushin, and A. Miserez, "Hydrogen bond guidance and aromatic stacking drive liquid-liquid phase separation of intrinsically disordered histidine-rich peptides," *Nat. Commun.*, vol. 10, no. 1, p. 5465, 2019.

[18] G. C. Yeo, F. W. Keeley, and A. S. Weiss, "Coacervation of tropoelastin," *Adv. Colloid Interface Sci.*, vol. 167, no. 1-2, pp. 94–103, 2011.

[19] P. J. Flory, *Principles of Polymer Chemistry*. New York: Cornell University Press, 1953.

[20] A. Veis, "A review of the early development of the thermodynamics of the complex coacervation phase separation," *Adv. Colloid Interface Sci.*, vol. 167, no. 1-2, pp. 2–11, 2011.

[21] C. P. Brangwynne, P. Tompa, and R. V. Pappu, "Polymer physics of intracellular phase transitions," *Nat. Phys.*, vol. 11, no. 11, pp. 899–904, 2015.

[22] K. K. Nakashima, A. A. André, and E. Spruijt, "Enzymatic control over coacervation," *Methods Enzymol.*, vol. 646, pp. 353–389, 2021.

[23] J. M. Choi, A. S. Holehouse, and R. V. Pappu, "Physical Principles Underlying the Complex Biology of Intracellular Phase Transitions," *Annu. Rev. Biophys.*, vol. 49, no. 1, pp. 107–133, 2020.

[24] M. G. Iadanza, M. P. Jackson, E. W. Hewitt, N. A. Ranson, and S. E. Radford, "A new era for understanding amyloid structures and disease," *Nat. Rev. Mol. Cell Biol.*, vol. 19, no. 12, pp. 755–773, 2018.

[25] J. D. Sipe, M. D. Benson, J. N. Buxbaum, S. I. Ikeda, G. Merlini, M. J. Saraiva, and P. Westermark, "Amyloid fibril proteins and amyloidosis: chemical identification and clinical classification International Society of Amyloidosis 2016 Nomenclature Guidelines," *Amyloid*, vol. 23, no. 4, pp. 209–213, 2016.

[26] L. Gremer, D. Schölzel, C. Schenk, E. Reinartz, J. Labahn, R. B. Ravelli, M. Tusche, C. Lopez-Iglesias, W. Hoyer, H. Heise, D. Willbold, and G. F. Schröder, "Fibril structure of amyloid-$\beta(1–42)$ by cryo–electron microscopy," *Science*, vol. 358, pp. 6359, pp. 116–119, 2017.

[27] M. T. Colvin, R. Silvers, Q. Z. Ni, T. V. Can, I. Sergeyev, M. Rosay, K. J. Donovan, B. Michael, J. Wall, S. Linse, and R. G. Griffin, "Atomic Resolution Structure of Monomorphic Aβ42 Amyloid Fibrils," *J. Am. Chem. Soc.*, vol. 138, no. 30, pp. 9663–9674, 2016.

[28] A. K. Paravastu, R. D. Leapman, W. M. Yau, and R. Tycko, "Molecular structural basis for polymorphism in Alzheimer's β-amyloid fibrils," *Proc. Natl. Acad. Sci. U. S. A.*, vol. 105, no. 47, pp. 18349–18354, 2008.

[29] M. R. Sawaya, S. Sambashivan, R. Nelson, M. I. Ivanova, S. A. Sievers, M. I. Apostol, M. J. Thompson, M. Balbirnie, J. J. Wiltzius, H. T. McFarlane, A. Madsen, C. Riekel, and D. Eisenberg, "Atomic structures of amyloid cross-β spines reveal varied steric zippers," *Nature*, vol. 447, no. 7143, pp. 453–457, 2007.

[30] M. Sleutel, *Growth kinetics and mass transport phenomena during protein crystallization*. PhD thesis, Vrije Universiteit Brussel, Brussels, 2008.

[31] C. Mathieu, R. V. Pappu, and J. Paul Taylor, "Beyond aggregation: Pathological phase transitions in neurodegenerative disease," *Science*, vol. 370, no. 6512, pp. 56–60, 2020.

[32] A. Patel, H. O. Lee, L. Jawerth, S. Maharana, M. Jahnel, M. Y. Hein, S. Stoynov, J. Mahamid, S. Saha, T. M. Franzmann, A. Pozniakovski, I. Poser, N. Maghelli, L. A. Royer, M. Weigert, E. W. Myers, S. Grill, D. Drechsel, A. A. Hyman, and S. Alberti, "A Liquid-to-Solid Phase Transition of the ALS Protein FUS Accelerated by Disease Mutation," *Cell*, vol. 162, no. 5, pp. 1066–1077, 2015.

[33] T. Murakami, S. Qamar, J. Q. Lin, G. S. Schierle, E. Rees, A. Miyashita, A. R. Costa, R. B. Dodd, F. T. Chan, C. H. Michel, D. Kronenberg-Versteeg, Y. Li, S. P. Yang, Y. Wakutani, W. Meadows, R. R. Ferry, L. Dong, G. G. Tartaglia, G. Favrin, W. L. Lin, D. W. Dickson, M. Zhen, D. Ron, G. Schmitt-Ulms, P. E. Fraser, N. A. Shneider, C. Holt, M. Vendruscolo, C. F. Kaminski, and P. St George-Hyslop, "ALS/FTD Mutation-Induced Phase Transition of FUS Liquid Droplets and Reversible Hydrogels into Irreversible Hydrogels Impairs RNP Granule Function," *Neuron*, vol. 88, no. 4, pp. 678–690, 2015.

[34] A. Molliex, J. Temirov, J. Lee, M. Coughlin, A. P. Kanagaraj, H. J. Kim, T. Mittag, and J. P. Taylor, "Phase Separation by Low Complexity Domains Promotes Stress Granule Assembly and Drives Pathological Fibrillization," *Cell*, vol. 163, no. 1, pp. 123–133, 2015.

[35] Y. Lin, D. S. Protter, M. K. Rosen, and R. Parker, "Formation and Maturation of Phase-Separated Liquid Droplets by RNA-Binding Proteins," *Mol. Cell*, vol. 60, no. 2, pp. 208–219, 2015.

[36] H. J. Kim, N. C. Kim, Y. D. Wang, E. A. Scarborough, J. Moore, Z. Diaz, K. S. MacLea, B. Freibaum, S. Li, A. Molliex, A. P. Kanagaraj, R. Carter, K. B. Boylan, A. M. Wojtas, R. Rademakers, J. L. Pinkus, S. A. Greenberg, J. Q. Trojanowski, B. J. Traynor, B. N. Smith, S. Topp, A. S. Gkazi, J. Miller, C. E. Shaw, M. Kottlors, J. Kirschner, A. Pestronk, Y. R. Li, A. F. Ford, A. D. Gitler, M. Benatar, O. D. King, V. E. Kimonis, E. D. Ross, C. C. Weihl, J. Shorter, and J. P. Taylor, "Mutations in prion-like domains in hnRNPA2B1 and hnRNPA1 cause multisystem proteinopathy and ALS," *Nature*, vol. 495, no. 7442, pp. 467–473, 2013.

[37] A. E. Conicella, G. H. Zerze, J. Mittal, and N. L. Fawzi, "ALS Mutations Disrupt Phase Separation

Mediated by α-Helical Structure in the TDP-43 Low-Complexity C-Terminal Domain," *Structure*, vol. 24, no. 9, pp. 1537–1549, 2016.

[38] S. Ray, N. Singh, R. Kumar, K. Patel, S. Pandey, D. Datta, J. Mahato, R. Panigrahi, A. Navalkar, S. Mehra, L. Gadhe, D. Chatterjee, A. S. Sawner, S. Maiti, S. Bhatia, J. A. Gerez, A. Chowdhury, A. Kumar, R. Padinhateeri, R. Riek, G. Krishnamoorthy, and S. K. Maji, "α-Synuclein aggregation nucleates through liquid–liquid phase separation," *Nat. Chem.*, vol. 12, no. 8, pp. 705–716, 2020.

[39] S. Ray, D. Chatterjee, S. Mukherjee, K. Patel, and J. Mahato, "Spatiotemporal solidification of α-synuclein inside the liquid droplets," *bioRxiv*, 2021.

[40] S. Wegmann, B. Eftekharzadeh, K. Tepper, K. M. Zoltowska, R. E. Bennett, S. Dujardin, P. R. Laskowski, D. MacKenzie, T. Kamath, C. Commins, C. Vanderburg, A. D. Roe, Z. Fan, A. M. Molliex, A. Hernandez-Vega, D. Muller, A. A. Hyman, E. Mandelkow, J. P. Taylor, and B. T. Hyman, "Tau protein liquid–liquid phase separation can initiate tau aggregation," *EMBO J.*, vol. 37, no. 7, p. e98049, 2018.

[41] S. Boyko, X. Qi1, T. H. Chen, K. Surewicz, and W. K. Surewicz, "Liquid-liquid phase separation of tau protein: The crucial role of electrostatic interactions," *J. Biol. Chem.*, vol. 294, no. 29, pp. 11054–11059, 2019.

[42] J. Wen, L. Hong, G. Krainer, Q. Q. Yao, T. P. Knowles, S. Wu, and S. Perrett, "Conformational Expansion of Tau in Condensates Promotes Irreversible Aggregation," *J. Am. Chem. Soc.*, vol. 143, no. 33, pp. 13056–13064, 2021.

[43] S. Boyko, K. Surewicz, and W. K. Surewicz, "Regulatory mechanisms of tau protein fibrillation under the conditions of liquid-liquid phase separation," *Proc. Natl. Acad. Sci. U. S. A.*, vol. 117, no. 50, pp. 31882–31890, 2020.

[44] A. S. Sawner, S. Ray, P. Yadav, S. Mukherjee, R. Panigrahi, M. Poudyal, K. Patel, D. Ghosh, E. Kummerant, A. Kumar, R. Riek, and S. K. Maji, "Modulating α-Synuclein Liquid-Liquid Phase Separation," *Biochemistry*, vol. 60, no. 48, pp. 3676–3696, 2021.

[45] M. C. Hardenberg, T. Sinnige, S. Casford, S. T. Dada, C. Poudel, E. A. Robinson, M. Fuxreiter, C. F. Kaminksi, G. S. Kaminski Schierle, E. A. Nollen, C. M. Dobson, and M. Vendruscolo, "Observation of an α-synuclein liquid droplet state and its maturation into Lewy body-like assemblies," *J. Mol. Cell Biol.*, vol. 13, no. 4, pp. 282–294, 2021.

[46] S. Ray, T. O. Mason, L. Boyens-Thiele, A. Farzadfard, J. A. Larsen, R. K. Norrild, N. Jahnke, and A. K. Buell, "Mass photometric detection and quantification of nanoscale α-synuclein phase separation," *Nat. Chem.*, vol. 15, no. 9, pp. 1306–1316, 2023.

[47] A. Vidal Ceballos, J. A. Díaz, J. M. Preston, C. Vairamon, C. Shen, R. L. Koder, and S. Elbaum-Garfinkle, "Liquid to solid transition of elastin condensates," *Proc. Natl. Acad. Sci. U. S. A.*, vol. 119, no. 37, p. e2202240119, 2022.

[48] P. Mohammadi, A. S. Aranko, L. Lemetti, Z. Cenev, Q. Zhou, S. Virtanen, C. P. Landowski, M. Penttilä, W. J. Fischer, W. Wagermaier, and M. B. Linder, "Phase transitions as intermediate steps in the formation of molecularly engineered protein fibers," *Commun. Biol.*, vol. 1, no. 1, p. 86, 2018.

[49] Y. Shen, F. S. Ruggeri, D. Vigolo, A. Kamada, S. Qamar, A. Levin, C. Iserman, S. Alberti, P. S. George-Hyslop, and T. P. Knowles, "Biomolecular condensates undergo a generic shear-mediated liquid-to-solid transition," *Nat. Nanotechnol.*, vol. 15, no. 10, pp. 841–847, 2020.

[50] C. Weber, T. Michaels, and L. Mahadevan, "Spatial control of irreversible protein aggregation," *eLife*, vol. 8, p. e42315, 2019.

[51] L. A. Munishkina, E. M. Cooper, V. N. Uversky, and A. L. Fink, "The effect of macromolecular crowding on protein aggregation and amyloid fibril formation," *J. Mol. Recognit.*, vol. 17, no. 5, pp. 456–464, 2004.

[52] E. Spruijt, J. Sprakel, M. Lemmers, M. A. Stuart, and J. Van Der Gucht, "Relaxation dynamics at different time scales in electrostatic complexes: Time-salt superposition," *Phys. Rev. Lett.*, vol. 105, no. 20, p. 208301, 2010.

[53] N. A. Yewdall, A. A. André, T. Lu, and E. Spruijt, "Coacervates as models of membraneless organelles," *Curr. Opin. Colloid Interface Sci.*, vol. 52, p. 101416, 2021.

2

Phase separation of short peptide derivatives

2.1   Why small coacervating molecules?

Typically, coacervates are formed by relatively large polymeric molecules, either synthetic or natural. Simple coacervates are formed by one type of polymeric molecules, complex coacervates contain two types of charged polymers or one type of charged polymer and small counterions. There is a plain thermodynamic cause that usually prevents small molecules from LLPS. In short, the loss of entropy under condensation of a large number of small molecules (much larger than in the case of one polymeric molecule) cannot be compensated by the enthalpic gain (similar when condensing a number of small molecules or one polymeric molecule of similar size and with similar types of interactions)[i].

Access to small molecules with the ability to undergo liquid-liquid phase separation is desired for a multitude of reasons. One of them is being able to study phase transitions in an easy-to-modify and easy-to-characterise system. While the current methods already allow to study certain aspects of LLPS and aggregation of amyloidogenic proteins[1,2], studies of minimal model systems with similar properties can potentially provide a more detailed understanding of the basics of protein LLPS and LST.

Another reason motivating the search for small, simple molecules undergoing liquid-liquid phase separation is to find a system that is more prebiotically plausible. Coacervates have been proposed as potential means of compartmentalisation of the earliest form of life[3,4], but currently known natural phase-separating systems are too complex to form spontaneously from a mixture of chemicals present on the early Earth. Compartments formed by small molecules could have potentially emerged from this group of molecules and further drive the formation of more complex compounds.

In this chapter, we present a short peptide synthon for LLPS. The design was inspired by the sticker-and-spacer pattern identified as an important characteristic of many phase-separating proteins[5–7]. The molecules that we study are composed of two dipeptide motifs containing aliphatic or aromatic residues, and a flexible diamine linker. We show that within the class of these derivatives, there is a group of molecules able to reversibly form water-rich liquid condensates. These coacervates are responsive to pH, temperature and organic solutes. Introducing a disulphide moiety to the linker allows for a reversible formation and dissolution of the condensates by controlling the redox chemistry[8]. Condensates formed by the small peptide derivatives show the ability to partition different guest molecules, including single-stranded DNA, RNA, porphyrins and various organic dyes. Small RNA hairpins de-hybridise upon uptake, while rotationally dynamic dyes such as thioflavins partly lose their rotational freedom inside the coacervates. With this design, we propose a new class of condensates formed by single peptide species, a potential model system to obtain a fundamental insight into the intracellular protein phase transitions.

2.2   Self-coacervation of peptide derivatives

Aromatic residues are known to be important for self-assembly and phase separation of peptides and proteins[5,9,10]. The architecture of phase-separating proteins has been

---

[i]Also explained in subsection 1.2.2.

suggested to be subject to the sticker-and-spacer design principle, with interacting fragments, e.g. aromatic residues (stickers) separated by flexible regions of soluble linker fragments (spacers). So far, no small molecule featuring this architecture has been described to undergo LLPS. We hypothesised that linking two hydrophobic dipeptides together with a flexible, polar spacer could result in the formation of condensed liquid droplets. Phenylalanyl-phenylalanine (FF) dipeptide is widely known for being the minimal motif responsible for amyloid formation and for its ability to self-assemble into fibrils and hydrogels[11–14]. Using two FF moieties to drive the intermolecular interactions and joining them with a flexible and more hydrophilic linker creates a minimal motif composed of two stickers and a spacer that can undergo simple coacervation above the critical association concentration.
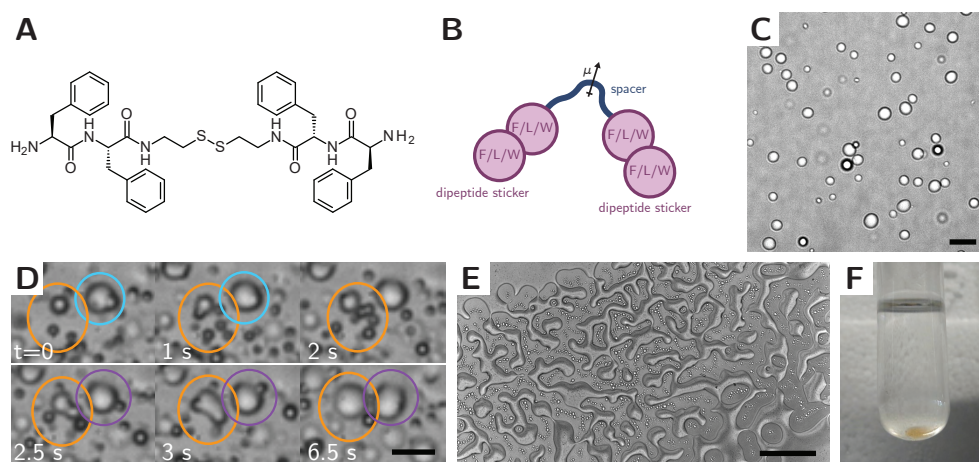
Figure 2.1: Liquid-liquid phase separation of cystamine-linked phenylalanine dipeptides. (A) Structure of FFssFF. (B) Schematic illustration of a synthon motif comprising two dipeptide stickers and a polar spacer. (C) Microscope image of droplets of FFssFF (1 mg/ml, pH 8) after 5 min incubation. (D) Fusion of FFssFF coacervate droplets (2 mg/ml, pH 8) (labels indicate time in seconds, coloured circles highlight fusion events). (E) Wetting patterns formed by FFssFF coacervates (2 mg/ml, pH 8) on a glass surface. (F) Bulk coacervate phase collected after centrifugation (3 mg/ml, pH 8, 4000 rcf). Scale bar in (C) and (D) is 10 μm and in (E) is 200 μm.

We first selected a cystamine moiety to link two L-phenylalanyl-L-phenylalanine dipeptides together via their C-termini (Figure 2.1A and B). The disulphide bond in the linker allows for dynamic control over the assembly through redox chemistry. Unlike FF dipeptide and most FF derivatives the cystamine-conjugated derivative bis(phenylalanylphenylalanyl) cystamine (FFssFF) is completely soluble in water below pH 6 up to 15 mg/ml. When the pH was increased to 7 or higher, the solution of FFssFF became turbid. Microscopic investigation revealed the formation of condensed droplets with a typical size of 1-10 μm (Figure 2.1C). These peptide-rich condensates are liquid, which is evident from their ability to fuse (Figure 2.1D), spread and deform (Figure 2.1E), and ultimately separate into a bulk phase after centrifugation (Figure 2.1F), just like coacervates of polyelectrolytes or

disordered proteins.

An important difference between these FFssFF droplets and other coacervates made of polyelectrolytes or proteins is the size of the constituent molecules. While synthetic polymers, RNA and intrinsically disordered proteins used to make coacervate droplets have a typical mass of more than 1000 Da, these peptide derivatives are small molecules with a molecular weight of less than 750 Da. Nonetheless, the droplets shown in Figure 2.1C are coacervates: they are condensed liquids containing the same solvent as the coexisting dilute phase (water) and enriched in at least one of the dissolved species (FFssFF)[15]. We determined the amount of water present in the coacervate droplets by separating them from the supernatant after centrifugation (Figure 2.1F), and found that they indeed contain a substantial amount of water (75$\pm$10% w/w at pH 8, see Experimental details). In addition, the droplets contain a very high peptide concentration, reaching 1000-times higher concentrations than the surrounding dilute solution (Figure 2.2A). Because of the high internal concentration, which results in a high viscosity and small capillary velocity (γ/η), coacervates of FFssFF do not coalesce easily, and the average droplet size of an emulsion of FFssFF coacervates increases only slowly over time (Figure 2.2B). Eventually, the coacervate droplets undergo complete fusion, indicating that the peptides remain sufficiently mobile, and the droplets are liquid. We estimated the inverse capillary velocity from the coalescence of pairs of droplets to be 0.44 s/µm (see Experimental details), which is slightly higher than previous reports for droplets of RGG IDRs[16], but lower than RNA-binding IDP Whi3[17], and suggests that FFssFF-based coacervates are comparable in viscosity to other IDPs.

A second difference between FFssFF coacervates and most other oligopeptide-based coacervate protocells studied so far[18] is that these types of peptide coacervates designed with a sticker-and-spacer architecture do not require combining two oppositely charged species, as is the case for complex coacervates[4,19,20]. The droplets shown in Figure 2.1C form as a result of homotypic interactions between the apolar side groups of FFssFF, and are therefore called simple coacervates[21]. Measurements of FFssFF coacervation at different salt concentrations confirm that the ionic strength has a very small effect on the coacervation transition (Figure 2.2C) and coacervate stability, while the phase transition is sensitive to pH and temperature (Figure 2.2A and D). This situation is similar to the phase separation of aromatic-rich disordered proteins such as FUS[9] and hnRNPA1[5], although segregation from other cytosolic components is believed to play a role in the phase separation of IDRs/IDPs[22]. Based on these similarities, the design shown in Figure 2.1B could be regarded as a minimal model of the sticker-and-spacer motifs required for phase separation.

On the other hand, the FFssFF coacervates are fundamentally different from oil droplets in water that have been studied as protocell models[23,24], even though hydrophobic interactions underlie the formation of both. Coacervates, like the FFssFF droplets in Figure 2.1, constitute a liquid phase that contains both peptides and water, which only exists when the peptide is dissolved in water. This situation is analogous to the formation of membraneless organelles from hydrated disordered proteins.
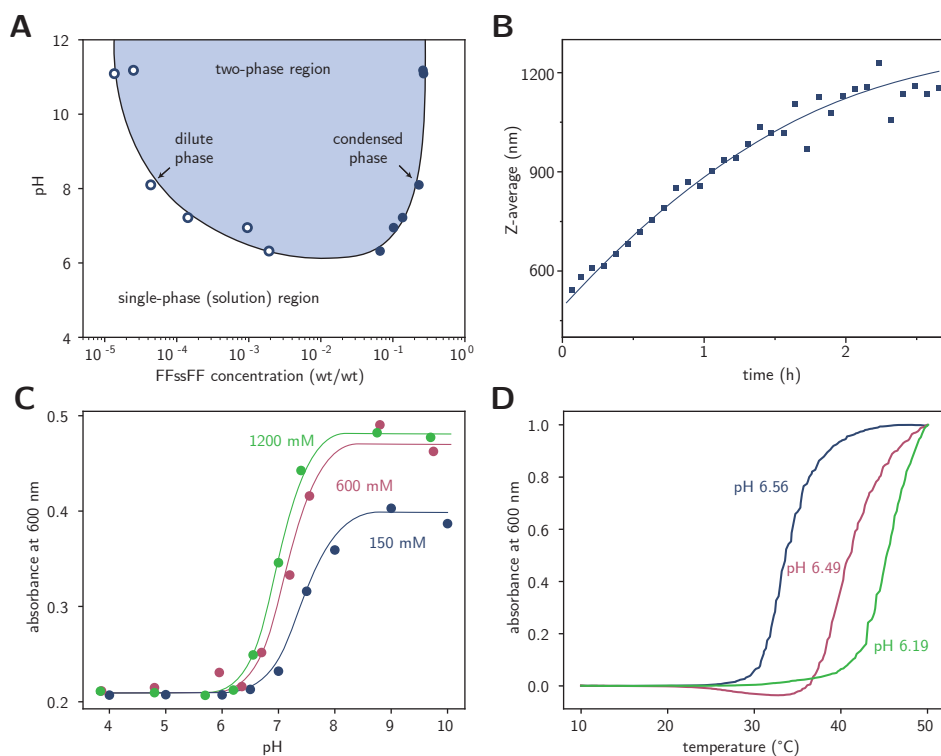
Figure 2.2: Liquid-liquid phase separation range of FFssFF. (A) Phase diagram of FFssFF. The shaded area is the two-phase region in which coacervates are formed and the solid boundary line is drawn to guide the eye. (B) Size of FFssFF coacervates (Z-average) over time monitored by DLS at 1 mg/ml concentration of FFssFF at pH 7. Line is drawn to guide the eye. (C) pH-triggered phase transition in FFssFF solutions (0.5 mg/ml) at different salt concentrations monitored by absorbance at 600 nm. Lines are drawn to guide the eye. (D) Normalised absorbance at 600 nm of FFssFF as a function of temperature at different pH conditions.

2.3   Exploring universality of the design

To explore the general nature of the design in Figure 2.1B, we synthesised variants with different hydrophobic dipeptides (stickers, Figure 2.3 and Figure 2.4) and different hydrophilic linkers (spacers, Figure 2.5 and Figure 2.6), including a cystine linker. Compounds with amino acids carrying less hydrophobic side chains such as leucine ($\Delta G_{\text{w-oct}}$ = -5.2 kJ/mol versus -7.1 kJ/mol for phenylalanine) formed clear liquid coacervate droplets, but required higher concentrations (Figure 2.4). Mixed compounds (FLssLF and LFssFL) had a critical coacervation concentration between the homodipeptide compounds LLssLL and FFssFF. For compounds with more hydrophobic side chains such as tryptophan ($\Delta G_{\text{w-oct}}$ = -8.7 kJ/mol) the associations became too strong, and solid aggregates were found for WWssWW and the mixed compounds WFssFW and FWssWF.
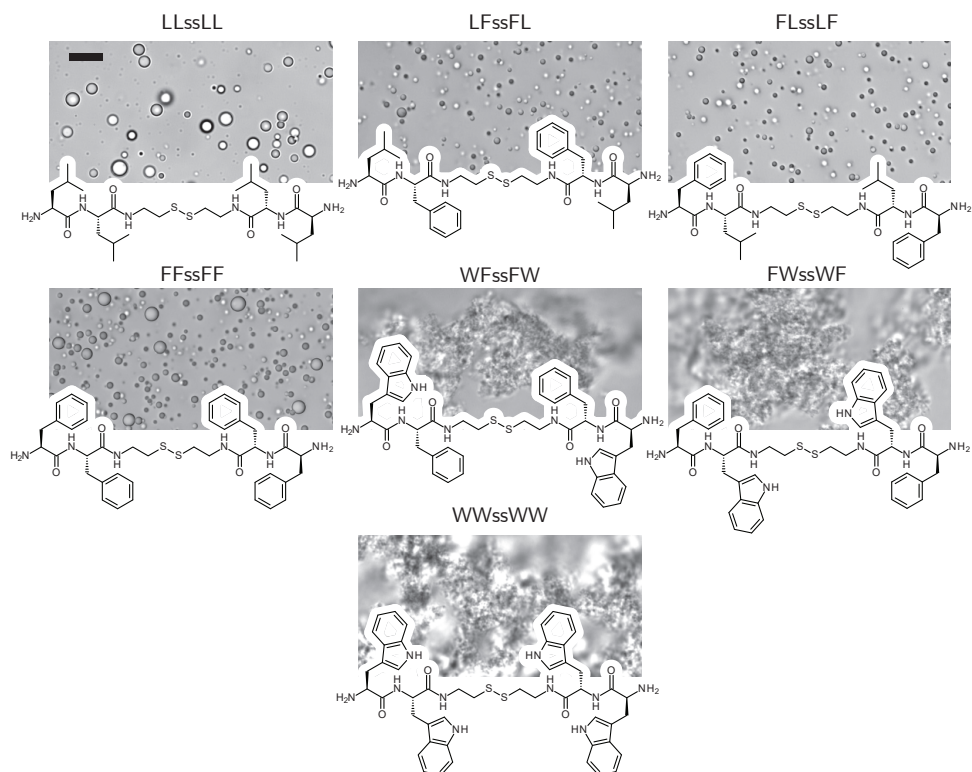
Figure 2.3: Self-coacervation of different hydrophobic dipeptide stickers connected with a disulphide spacer. Scale bar is 10 μm.
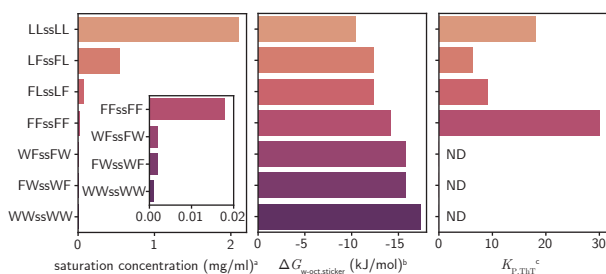
Figure 2.4: Physico-chemical properties of different hydrophobic dipeptide stickers connected with a disulphide spacer. [a]HPLC analysis. [b]Calculated as the sum of amino acid side chain transfer free energies. [c]Confocal fluorescence microscopy analysis.

Analysis of the condensation of different spacers revealed that polar and unstructured spacers with heteroatoms were all able to form coacervates (Figure 2.5). With the apolar 1,6-hexanediamine spacer, only aggregates were observed, while 2,2,4(2,4,4)-trimethyl-

1,6-hexanediamine appeared to be at the boundary between coacervate and aggregate, showing tiny solvated globules attached together in a fractal-like aggregate. Taking the spacer's free energy of solvation and dipole moment as indicators of their ability to solubilise the stickers and keep the condensates in a hydrated, liquid state, we find a clear boundary between polar spacers with a zero or negative solvation free energy, which give rise to coacervates, and apolar spacers with a positive solvation free energy and limited solubility, which give rise to aggregates (Figure 2.6). Finally, compounds with a cystine spacer did not form coacervates, in agreement with cystine's low solubility and the propensity of cystine-containing peptides to form highly structured aggregates through β-sheet hydrogen bonding [25].
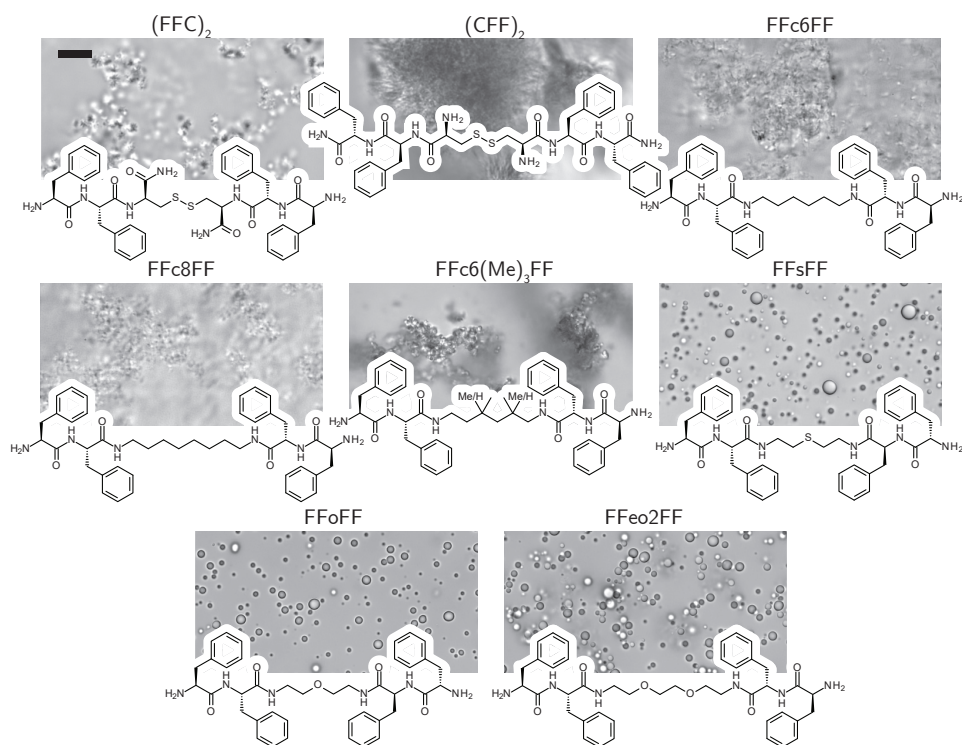
Figure 2.5: Self-coacervation of FF dipeptide stickers connected with different spacers. Scale bar is 10 μm.

Altogether, we find that phase separation is the result of a balance between the solubilising effect of one or more spacers, and the homotypic (hydrophobic) interactions between stickers. These guiding principles suggest that phase separation could be induced either by increasing the stickiness (hydrophobicity) of the stickers or decreasing the solvation free energy of the spacer. This is indeed what we observe for FFssFF solutions at pH 6.8 (Figure 2.2B): at this pH FFssFF has too high a net charge to undergo LLPS. By increasing the salt concentration to 1.2 M, the homotypic interaction strength between
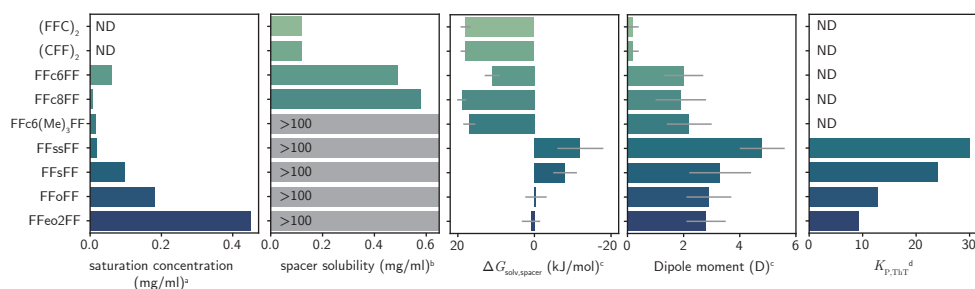
Figure 2.6: Physico-chemical properties of FF dipeptide stickers connected with different spacers. [a]HPLC analysis. [b]Information provided by the supplier. [c]PM3 calculations using MolCalc. [d]Confocal fluorescence microscopy analysis.

stickers can be increased[26] and the electrostatic repulsion screened enough to induce phase separation. In brief, hydrophobic dipeptide stickers linked by an unstructured, polar spacer are minimal motifs for simple coacervation.

2.4 Redox reversibility of phase separation

We selected the phenylalanyl–phenylalanine peptide derivatives with a cystamine linker (FFssFF) to investigate the properties that make these coacervates attractive proto-cells in more detail. The disulphide bond allows direct control over coacervate formation by redox chemistry. By reducing the disulphide bond in FFssFF with DTT or tris(2-carboxyethyl)phosphine (TCEP), the peptide derivative is converted into two free thiols that are soluble in water, even at pH >7, and a turbid dispersion of coacervate droplets is converted into a clear solution (Figure 2.7). This transition is completely reversible by oxidation of the free thiols using oxidising agents.

   We monitored the redox-controlled phase transition in more detail using a turbid-ity titration. Figure 2.7A shows the complete disappearance of turbidity in a 0.5 mg/ml dispersion of FFssFF coacervates within 10 min upon addition of DTT (19 mM final con-centration) Figure 2.7B shows the complete disappearance of turbidity in a 1.0 mg/ml dispersion of FFssFF coacervates within 10 min upon addition of TCEP (19 mM final concentration). Subsequent addition of H_2O_2 or $K_3Fe(CN)_6$ (45 mM final concentration) resulted in the formation of liquid droplets as before reduction and reappearance of tur-bidity over 15 min. These regenerated coacervates could be completely dissolved again by reduction with DTT or TCEP, indicating that they have the same redox sensitivity as the originally formed coacervates. The turbidity after oxidation did not reach the same level as before the first reduction because the rate of formation of the coacervating product. Initially, coacervates were formed very rapidly, within seconds, by increasing the pH of an acidic solution of FFssFF to 7. Coacervation by oxidation of thiols takes longer and some coacervates could have settled and adhered to the walls of the measuring chamber during that time. The same phenomenon is also observed when the turbidity decreases immediately after switching the pH (Figure 2.7A).

These results show that oxidation of small dipeptide-conjugated thiols, such as FFsH, under prebiotically relevant conditions can result in the efficient and spontaneous formation of protocellular compartments.
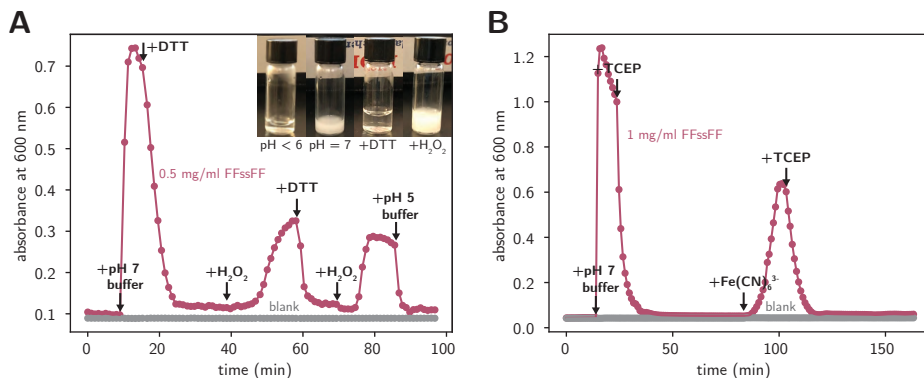
Figure 2.7: Reversible reduction and oxidation of FFssFF. (A) Kinetics of dissolution of FFssFF coacervates upon reduction with DTT, and formation of coacervates through condensation upon oxidation with H_2O_2, as monitored by absorbance at 600 nm. Inset: pictures of vials containing FFssFF (1 mg/ml) in various stages of the reduction and oxidation (dissolved at low pH, phase separated at pH 7, dissolved after reduction and phase separated after oxidation). (B) Same as (A) but using TCEP as reducing agent and $K_3Fe(CN)_6$ as oxidising agent.

2.5 Selective partitioning of RNA, DNA and small molecule guests

One of the most important characteristics of coacervates and an argument for their potential relevance in the emergence of life is their ability to take up a wide variety of guest molecules and concentrate them to potentially high enough concentrations to facilitate reactions[3,4,27]. We determined the ability of the FFssFF coacervates to concentrate different guest molecules by fluorescence microscopy, as shown in Figure 2.8. Aromatic fluorophores, including ThT (Figure 2.8B), 4',6-diamidino-2-phenylindole (DAPI, Figure 2.8C), methylene blue (Figure 2.8D) and SYBR Green (Figure 2.8F) all became concentrated inside FFssFF coacervates, with apparent partition coefficients ($K_P = c_{droplet}/c_{solution}$) of 30, 35, 21 and 56, respectively, due to the different polarity inside the coacervates. In the case of ThT, the strong fluorescence suggests that this fluorophore becomes rotationally restricted inside the coacervates by binding to the apolar peptide side groups, similar to its binding to β-sheet structures in proteins. The fluorescence intensity of ThT in LLssLL coacervates was slightly lower ($K_P = 18$), as expected based on the weaker preference of ThT for the aliphatic isobutyl side chains of leucine[28]. Fluorescein was also taken up and concentrated inside FFssFF coacervates but to a much smaller extent (Figure 2.8E, $K_P = 1.7$). The partition coefficients of these dyes are lower than in some polymeric

coercervates[29], but the fact that various small molecules can still be concentrated is evidence for the potential utility of these coacervates in a protocell context.
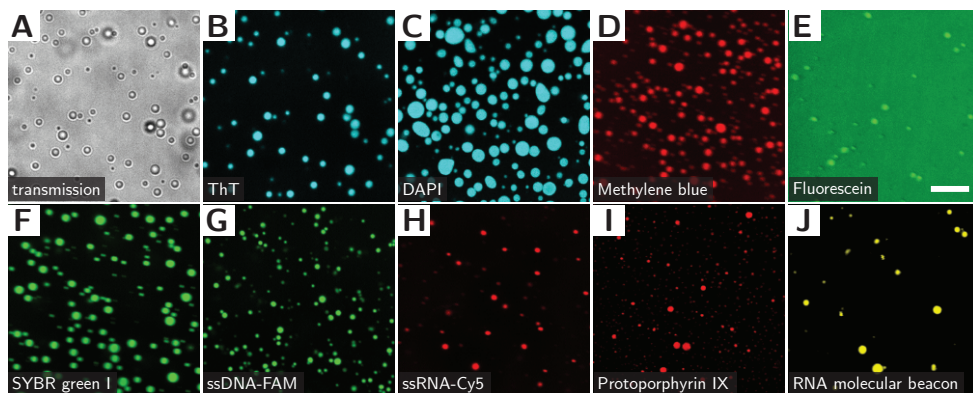
Figure 2.8: Partitioning of guest molecules in FFssFF coacervates. (A) Bright-field image of FFssFF coacervates incubated with ThT. (B) Confocal fluorescence image of ThT at the same position. (C-J) Confocal fluorescence image of FFssFF coacervates incubated with DAPI (C), methylene blue (D), 5(6)-carboxyfluorescein (E), SYBR Green I (F), fluorescein amine-labelled ssDNA (43 nt) (G), Cy5-labelled ssRNA (24 nt) (H), protoporphyrin IX (I), and RNA molecular beacon (J). Scale bar (shown in E) is 10 μm.
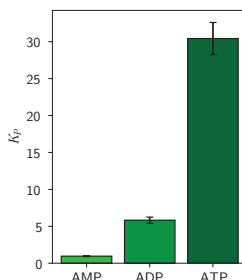
Figure 2.9: Partitioning of nucleotides in FFssFF coacervates. Partition coefficients calculated based on the HPLC analysis.

Apart from small-molecule fluorophores, these peptide-based coacervates also seque-ster longer nucleic acids. Figure 2.8G and H shows fluorescence microscope images of FFssFF coacervates that were incubated with 500 nM of ssDNA (43 nt) and ssRNA (24 nt), respectively. Both nucleic acids were concentrated and distributed evenly in the coacervate droplets ($K_P = 68$ and 75, respectively). This partitioning is weaker than in complex coacervates, where partial exchange with nucleotides inside the coacervates can lead to partition coefficients up to 10^5 [30]. To deduce the molecular basis of the par-titioning of nucleic acids, we determined the partitioning of adenosine mono-, di- and

triphosphate by HPLC (Figure 2.9). We found that the partition coefficient increases strongly with an increasing number of phosphates, and adenosine monophosphate exhibits no preferential partitioning ($K_P = 1$). Therefore, we conclude that the partitioning of nucleotides and nucleic acids is dominated by interactions between the negatively charged phosphate groups and the amine groups on FFssFF. Finally, protoporphyrin IX, a prototypical anionic tetrapyrrole macrocycle and a precursor for haemoglobin and chlorophyll, was also concentrated in the FFssFF coacervates (Figure 2.8I, $K_P = 35$).

2.6 Conclusion

We have developed a new class of short peptide derivatives, which represent a synthon for LLPS. When dissolved in water, these small-molecule compounds self-coacervate into stable liquid droplets that contain up to 75% w/w water upon increasing the temperature or pH. The peptide derivatives were designed after a recent sticker-and-spacer model for protein-phase separation[5] and represent the minimal motif required for phase separation. The derivatives consist of two hydrophobic dipeptide stickers, linked together by a flexible hydrophilic spacer. We have identified guidelines for sticker hydrophobicity and spacer polarity that define the boundary between dynamic liquids and aggregated solids. For intracellular protein condensates, precisely this boundary is believed to separate healthy organelles from disease states[31], and the minimal LLPS motif presented here could open the way for the development of model systems to systematically study the molecular principles underlying the liquid-to-solid transition. An important first step would be to use bioinformatics tools and computer-aided peptide design to identify minimal unstructured peptide sequences to replace the pseudopeptide linker in our synthon[32].

Moreover, the minimal sticker-and-spacer coacervates we created are attractive protocell models based on their structural simplicity and unique chemical properties. We have used FFssFF, a disulphide-linked derivative with two aromatic dipeptides, to show for the first time that a single small-molecule compound can form effective microcompartments by self-coacervation at submillimolar concentrations. We were able to control the formation of these protocells using redox chemistry, and to sequester and melt nucleic acids inside these coacervates.

2.7 Experimental details

2.7.1 Materials

N-(tert-Butoxycarbonyl)-L-phenylalanine (Boc-Phe-OH), 1-hydroxybenzotriazole (HOBt), 2-(1H-benzotriazole-1-yl)-1,1,3,3-tetramethyluronium tetra fluoroborate (TBTU), N,N-diisopropylethylamine (DIPEA) and 4 M hydrogen chloride solution in dioxane were obtained from Fluorochem. Cystamine dihydrochloride (CDC), methylene blue, 4′,6-diamidino-2-phenylindole (Dapi), SYBR green I, fluorescein, thioflavin T (ThT), protoporphyrin, potassium ferricyanide, tris(2- carboxyethyl) phosphine (TCEP), phenyalanine methyl ester (PheOMe) and hydrogen peroxide (35% w/w solution) were purchased from

Sigma Aldrich. All solvents and salts used were purchased from Sigma Aldrich. The nucleic acids (single-stranded DNA, single-stranded RNA, and RNA hairpin) were obtained from IDT Technologies. Their sequences are:
ssDNA: 5'-[FAM]-GCCTCGAATCACTCCACTGAACCATCCTCTTGATCTTGTGAAC-3'
ssRNA: 5'-[Cy5]-ACUGACUGACUGACUGACUGACUG-3'
RNA hairpin: 5'-[Alexa-647]-GCGCAAAUAAAUUUAAGGGUAAGCGC-[Iowa Black RQ]-3'
(all 2'-O-methylribonucleotides).

2.7.2   Synthesis of FFssFF

The synthesis of the peptide derivatives used for phase separation was completed in four steps (i-iv). The detailed procedure for FFssFF is given below as a typical example. The synthesis of all other derivatives was performed analogously. (i) Boc-Phe-OH (398 mg, 1.55 mmol), HBTU (557 mg, 1.47 mmol) and HOBt (199 mg, 1.47 mmol) were dissolved in DMF (3 ml) in a round-bottom flask and the mixture was stirred with a magnetic stirrer. DIPEA (1050 µl, 6.2 mmol), and CDC (158 mg, 0.7 mmol) were added with an interval of 1 min respectively and the reaction mixture was stirred for 24 h at room temperature. The reaction mixture was poured into 50 ml of water. White precipitate was collected by filtration and washed with water. The crude product was dried in a desiccator and characterised by LC-MS. (ii) The product from the first step (Boc-FssF-Boc) (327 mg, 0.51 mmol) was dissolved in 4:1 dioxane/DCM (1.5 ml) in a round bottom flask. To deprotect the intermediate product, 4 M hydrogen chloride solution in dioxane (3 ml) was added and the reaction mixture was stirred for 3 h. The solvent was evaporated on a rotary evaporator, yielding oily residue. Diethyl ether (40 ml) was added to the flask and the content was gently stirred. White precipitate was separated by centrifugation. The product was characterised by LC-MS. (iii) Boc-Phe-OH (297 mg, 1.12 mmol), HBTU (402 mg, 1.06 mmol) and HOBt (143 mg, 1.06 mmol) were dissolved in DMF (3 ml) in a round-bottom flask and the mixture was stirred with a magnetic stirrer. DIPEA (780 µl, 4.5 mmol), and product from the second step (FssF, 263 mg, 0.51 mmol) were added with an interval of 1 min respectively and the reaction mixture was stirred for 24 h at room temperature. The reaction mixture was poured into 50 ml of water. White precipitate was collected by filtration and washed with water. The crude product was purified by recrystallisation from EtOH/H$_2$O, dried and characterised by LC-MS. (iv) The product from the third step (Boc-FFssFF-Boc) (359 mg, 0.29 mmol) was dissolved in dioxane/DCM (1.5 ml) in a round bottom flask. 4 M hydrogen chloride solution in dioxane (3 ml) was added for deprotection and the reaction mixture was stirred for 3 h. The solvent was evaporated on a rotary evaporator, yielding oily residue. Diethyl ether (40 ml) was added to the flask and the content was gently stirred. White precipitate formed and was separated by centrifugation. The final product was obtained after freeze drying (yield 75%), and characterised by ^{1}H NMR, ^{13}C NMR, and LC-MS. The detailed analysis is available in the supporting information of the article[33].

2.7.3 Synthesis and characterisation of other dipeptide derivatives

The other derivatives were synthesised using analogous procedures and using Boc-protected L-leucine or L-tryptophan, and 1,6-hexanediamine, 2,2,4-trimethyl-1,6-hexanediamine, 2,2′-diaminoethyl sulphide, 2-(2-aminoethoxy)ethylamine, 2,2′-(ethylenedioxy)bis(ethylamine) and 1,4-bis(3-aminopropoxy)butane as linkers. Disulphide-linked homodimers of H_2N-CFF-OH and H_2N-FFC-OH were prepared by oxidation of purified tripeptides using DMSO, followed by purification using preparative HPLC. An overview of all synthesised derivatives is shown below. All final products were characterised by LC-MS and ^{1}H NMR and the corresponding spectra are provided in the supporting information of the article [33].

2.7.4 Coacervation

The lyophilised powder of dipeptide derivatives was dissolved in milliQ water. The pH of the homogeneous solution of peptide derivatives was in the range of 5-6 depending on the concentration of the peptide. The coacervation/aggregation was triggered by increasing the pH to 7 using 1 µl of 0.2 M NaOH solution or 5 µl of 100 mM phosphate/Tris/TEAB buffer for each 100 µl solution of peptide. The milky colour appeared immediately and coacervation was confirmed by bright-field microscopy (Olympus IX71 inverted microscope).

2.7.5 Turbidity

All turbidity-based titrations were performed on a Tecan Spark multimode plate reader with a built-in spectrophotometer and automated injector. We use turbidity as an indicator of LLPS for samples in which liquid droplets have been confirmed by optical microscopy. We used 600 nm as the wavelength for all turbidity measurements, and all measurements were performed at room temperature (21 ± 2 °C), unless stated otherwise. Titrations were carried out in triplicate and the titrant concentration was chosen such that the added volume did not exceed 10% of the original volume, except for acetonitrile and L-phenylalanine methyl ester (Phe-OMe) titrations. Turbidity was recorded after shaking the sample for 5 s following each addition. A well with the same volume of buffer was used as blank.

2.7.6 Phase diagram

To determine the phase diagram, samples of FFssFF (400 µl, 3 mg/ml) were titrated with different amounts of NaOH solution (1.0 M) to reach different pH. The final pH was measured using a pH-meter. The dispersions were centrifuged for 30 min at 4000 rcf and the supernatant (dilute phase) was carefully separated from the oily, brownish coacervate phase and stored in a separate tube. The last bit of the dilute phase was taken up with a piece of filter paper, and the coacervate phase was weighed using an analytical balance. To determine the amount of FFssFF in both phases, the coacervate phase was dissolved in acetonitrile (400 µl), and both the previously separated dilute phase and the diluted coacervate phase were analysed using HPLC with absorbance detection at 254 nm. The amount of FFssFF dissolved in each phase was determined by comparing the peak area with peak areas obtained for FFssFF calibration solutions with known concentrations.

Concentrations were converted to the mass fraction using the measured mass of the coacervate phase and assuming the mass of the dilute phase equals the mass of water used to prepare the initial solution. The error in the mass concentration was estimated based on a measurement uncertainty of 1 mg in determining the mass of the coacervate or solution phase, 0.1 mg in determining the mass of the peptide for the stock solution, and uncertainty in the HPLC signal integration of 100 units. A smoothed solid line that approximately connects the equilibrium concentrations was drawn to guide the eye.

2.7.7 Water content

To determine the water content of FFssFF and other coacervates, a solution of the respective peptide derivative (20 ml, 1 mg/ml) was prepared at pH 6. A clean, empty glass tube was weighed and then filled with 12 ml of the FFssFF solution, and titrated with 0.2 M NaOH to a pH of 8. The coacervate dispersion was left to equilibrate for 1 h on the bench. The glass tube was centrifuged inside a plastic Falcon tube with tissue paper added as padding at 3000 rcf for 1 h. After centrifugation, the supernatant was clear and the dense phase was collected as a semitransparent, slightly opaque liquid at the bottom (Figure 2.1F). The supernatant was removed by pipetting, and the last droplets were blotted with a piece of filter paper. The inside walls of the glass tube were blotted with filter paper, and the tube with coacervate was weighed again. Subsequently, the glass tube was placed inside a vacuum oven at 120 °C for 48 h to dry to constant weight. The coacervate was now a brownish, transparent film with clear cracks. Finally, the dried tube was weighed again, and the water content was calculated as: $Q_{\mathrm{w}} = (m_{\mathrm{coac}} - m_{\mathrm{dry}})/(m_{\mathrm{coac}} - m_{\mathrm{empty}})$. The uncertainty of the water content was estimated based on a 1 mg accuracy of the balance. Table 2.1 shows the water content of the derivatives for which it was determined.

derivative	water content (% w/w)
FFssFF	75±10
LFssFL	76±19
FLssLF	62±11
LLssLL	79±13
FFsFF	70±10
FFoFF	82±12

Table 2.1: Water content (weight %) of coacervates formed by different derivatives.

2.7.8 Capillary velocity

The inverse capillary velocity, defined as the ratio of viscosity to surface tension, governs the rate of fusion between separate coacervate droplets, assuming they behave as Newtonian liquids. To determine the capillary velocity, we analysed microscope videos of two individual coacervate droplets coalescing into a single droplet. For each coalescence event, we plotted the aspect ratio of the fusing droplets, defined as the long axis divided by the short (perpendicular) axis, as a function of time, and fitted the decay to a single exponential function $AR = a + be^{-t/\tau}$. We plotted the fusion time scales fitted τ as a

function of the fusion length scale (initial long axis) and determined the inverse capillary velocity from the linear slope of the resulting data.

2.7.9 Calculation of spacer properties

Solvation free energy and dipole moments of non-derivatised spacers (except cystine) were estimated from PM3 quantum chemical calculations using MolCalc [34] All structures were first optimised using GAMESS, and dipole moments and solvation surfaces were calculated using PM3 theory. The values reported are the average of 6 independent calculations. Electron density maps of several individual conformations are shown below. Cystine dipole moment was taken from Sawicka et al [35] (lowest energy structure), and the solubility and solvation free energy were taken from Carta and Tola [36].

2.7.10 Reversible oxidation and reduction of the coacervates

The reversible coacervation of peptides upon oxidation of free thiols and reduction of the disulphide-linked homodimer was monitored by turbidity measurements. An FFssFF solution (100 µl of 0.50 or 1.0 mg/ml, pH<6) was placed in a 96-well plate. 50 or 100 µl of milliQ water was used as blank. After collecting several data points for the initial solution (1 min interval between measurements), 5 µl of potassium phosphate buffer solution (1.0 M, pH 7) was added and an increase of turbidity could be observed. Turbidity was monitored for another 5 min. After that, 1 or 2 µl, depending on the concentration of FFssFF, of the reducing agent (DTT or TCEP, 1.0 M) was added and the turbidity decreased. When the turbidity reached a stable level, a total of 3 or 5 µl, depending on the concentration of FFssFF, of the oxidising agent (H_2O_2 or $K_3Fe(CN)_6$, 1.0 M) was added and the increase in turbidity was monitored until it reached a stable level. The reduction/oxidation cycle was repeated by adding first a double amount (2 or 4 µl) of the reducing agent (DTT or TCEP, 1.0 M). In some cases, the coacervates were formed again by subsequently adding 8 µl of the oxidising agent (H_2O_2 1.0 M). Finally, 10 µl of acetate buffer (1.0 M, pH 5) was added and the turbidity decreased almost to the initial level.

This experiment was run in parallel in test tubes and recorded with a camera. 200 µl of a clear 1 mg/ml FFssFF solution was placed in a glass vial (Figure 2.7A, inset). The pH was increased to 7 by adding 1 µl of NaOH (0.5 M). 300 µl of a 6 mM DTT solution was added and the mixture was incubated for 3 h at room temperature. Finally, 10 µl of H_2O_2 solution (30%) was added to the vial, resulting in an increase in turbidity.

2.7.11 Analysis of reduction and oxidation of FFssFF

Characterisation of all synthesised products and products from oxidation/reduction experiments was realised using analytical LC-MS (Shimadzu LC-20A). The system was equipped with a Gemini NX-C18 column (15 cm x 3 mm, 3 µm). A gradient method 5-90% of phase B in phase A during 15 min, (phase A: 100% H_2O with 0.1% formic acid, phase B: 100% acetonitrile with 0.1% formic acid) and flow rate 0.2 ml/min was used. The mass spectrum was acquired on a Thermo Finnigan LCQ Advantage max (ESI-Q) system.

2.7.12   Partitioning experiments

For partitioning of guest molecules we used a 1 mg/ml stock solution of FFssFF at pH<6. We prepared 1 mM stock solutions of the dye molecules, 10 µM stock solutions of ssDNA-FAM (140 ng/µl), ssRNA-Cy5 (85 ng/µl) and RNA hairpin (100 ng/µl), and a saturated solution of protoporphyrin IX in milli-Q water. Twenty microlitres of FFssFF stock solution was mixed with 2 µl of a 100 mM buffer solution pH 7.5 (Tris) to induce coacervation. After 1 min, 2 µl of the dye stock solutions or 1 µl of the nucleic acid stock solutions was added and mixed with the coacervates by pipetting. The mixtures were incubated for 30 min, and after incubation 10 µl of the mixture was applied on a cover glass (number 1.5H) and imaged directly using a CSU X-1 Yokogawa spinning disc confocal system on an Olympus IX81 inverted microscope, or a Leica TCS Sp8X confocal microscope (HC PL APO $\times$100/1.40 (oil) CS2 objective).

2.7.13   Determination of ATP, ADP and AMP partition coefficients

A stock solution of FFssFF (2 mg/ml) was mixed with a stock solution of ATP, ADP or AMP (13.9, 16.9 and 23.2 mM, determined by measuring absorbance at 254 nm) and a stock solution of HEPES buffer (1.0 M, pH 7.4) to achieve final concentrations of 1.8 mg/ml for FFssFF, 100 mM for HEPES and 0.1 mM for ATP, ADP or AMP in a final volume of 300 µl. Solutions were placed in tared 500 µl eppendorf tubes, and the total mass of solution was measured. Samples were then centrifuged at 3000 rcf for 30 minutes to separate the dense (coacervate) and the dilute phase, similar to the determination of the water content.

For each sample ca. 100 µl of the dilute phase was transferred to an HPLC vial equipped with a glass insert and the remaining dilute solution was carefully removed from the eppendorf tube with a pipette and finally the coacervate and eppendorf walls were blotted with a filter paper to remove remaining dilute phase. The mass of the eppendorf tubes with the condensed phase were measured. For each sample, the condensed phase was dissolved in 300 µl of 10 mM HCl solution and transferred into an HPLC vial. Subsequently, both samples (prepared from the dilute phase and the condensed phase) obtained for ATP, ADP and AMP were analysed using analytical HPLC (Shimadzu Nexera X3). The system was equipped with a Shim-pack WAX-1 column (5.0 cm x 4 mm, 3 µm). A gradient method 0-100% of phase B during 15 minutes (phase A: 20 mM KH_2PO_4/K_2HPO_4 buffer, pH 7.0; phase B: 480 mM KH_2PO_4/K_2HPO_4 buffer, pH 6.9) and flow rate 0.8 ml/min was used. The detection was performed by measuring absorbance at 254 nm. The ratio of ATP, ADP or AMP mass concentration in the condensed and the dilute phase (partitioning constant) was calculated using the following formula:

$$K_P = \frac{I_c}{I_d} \cdot \frac{m_t - m_c}{m_c} \tag{2.1}$$

where: I_c/I_d is the integrated peak area for the condensed/dilute phase, m_t is the total suspension mass (before separating the phases), m_c is the mass of the condensed phase. It was assumed that the total volume of the dilute phase and the condensed phase after dissolving in HCl solution was the same (300 µl).

2.8 Contributions and acknowledgements

Bibliography

[1] S. Ray, N. Singh, R. Kumar, K. Patel, S. Pandey, D. Datta, J. Mahato, R. Panigrahi, A. Navalkar, S. Mehra, L. Gadhe, D. Chatterjee, A. S. Sawner, S. Maiti, S. Bhatia, J. A. Gerez, A. Chowdhury, A. Kumar, R. Padinhateeri, R. Riek, G. Krishnamoorthy, and S. K. Maji, "α-Synuclein aggregation nucleates through liquid–liquid phase separation," *Nat. Chem.*, vol. 12, no. 8, pp. 705–716, 2020.

[2] S. Jonchhe, W. Pan, P. Pokhrel, and H. Mao, "Small Molecules Modulate Liquid-to-Solid Transitions in Phase-Separated Tau Condensates," *Angew. Chemie - Int. Ed.*, vol. 61, no. 23, p. e202113156, 2022.

[3] R. R. Poudyal, F. Pir Cakmak, C. D. Keating, and P. C. Bevilacqua, "Physical Principles and Extant Biology Reveal Roles for RNA-Containing Membraneless Compartments in Origins of Life Chemistry," *Biochemistry*, vol. 57, no. 17, pp. 2509–2519, 2018.

[4] S. Koga, D. S. Williams, A. W. Perriman, and S. Mann, "Peptide-nucleotide microdroplets as a step towards a membrane-free protocell model," *Nat. Chem.*, vol. 3, no. 9, pp. 720–724, 2011.

[5] E. W. Martin, A. S. Holehouse, I. Peran, M. Farag, J. J. Incicco, A. Bremer, C. R. Grace, A. Soranno, R. V. Pappu, and T. Mittag, "Valence and patterning of aromatic residues determine the phase behavior of prion-like domains," *Science*, vol. 367, no. 6478, pp. 694–699, 2020.

[6] J. Wang, J. M. Choi, A. S. Holehouse, H. O. Lee, X. Zhang, M. Jahnel, S. Maharana, R. Lemaitre, A. Pozniakovsky, D. Drechsel, I. Poser, R. V. Pappu, S. Alberti, and A. A. Hyman, "A Molecular Grammar Governing the Driving Forces for Phase Separation of Prion-like RNA Binding Proteins," *Cell*, vol. 174, no. 3, pp. 688–699.e16, 2018.

[7] J. M. Choi, A. S. Holehouse, and R. V. Pappu, "Physical Principles Underlying the Complex Biology of Intracellular Phase Transitions," *Annu. Rev. Biophys.*, vol. 49, no. 1, pp. 107–133, 2020.

[8] X. Zhang, S. Malhotra, M. Molina, and R. Haag, "Micro- and nanogels with labile crosslinks-from synthesis to biomedical applications," *Chem. Soc. Rev.*, vol. 44, no. 7, pp. 1948–1973, 2015.

[9] A. C. Murthy, G. L. Dignon, Y. Kan, G. H. Zerze, S. H. Parekh, J. Mittal, and N. L. Fawzi, "Molecular interactions underlying liquid-liquid phase separation of the FUS low-complexity domain," *Nat. Struct. Mol. Biol.*, vol. 26, no. 7, pp. 637–648, 2019.

[10] J. P. Brady, P. J. Farber, A. Sekhar, Y. H. Lin, R. Huang, A. Bah, T. J. Nott, H. S. Chan, A. J. Baldwin, J. D. Forman-Kay, and L. E. Kay, "Structural and hydrodynamic properties of an intrinsically disordered region of a germ cell-specific protein on phase separation," *Proc. Natl. Acad. Sci. U. S. A.*, vol. 114, no. 39, pp. E8194–E8203, 2017.

[11] M. Reches and E. Gazit, "Formation of closed-cage nanostructures by self-assembly of aromatic dipeptides," *Nano Lett.*, vol. 4, no. 4, pp. 581–585, 2004.

[12] L. Adler-Abramovich and E. Gazit, "The physical properties of supramolecular peptide assemblies: From building block association to technological applications," *Chem. Soc. Rev.*, vol. 43, no. 20, pp. 6881–6893, 2014.

[13] C. Chen, K. Liu, J. Li, and X. Yan, "Functional architectures based on self-assembly of bio-inspired dipeptides: Structure modulation and its photoelectronic applications," *Adv. Colloid Interface Sci.*, vol. 225, pp. 177–193, 2015.

[14] C. Yuan, A. Levin, W. Chen, R. Xing, Q. Zou, T. W. Herling, P. K. Challa, T. P. Knowles, and X. Yan, "Nucleation and Growth of Amino Acid and Peptide Supramolecular Polymers through Liquid–Liquid Phase Separation," *Angew. Chemie - Int. Ed.*, vol. 58, no. 50, pp. 18116–18123, 2019.

[15] H. G. Bungenberg de Jong and H. R. Kruyt, "Coacervation (partial miscibility in colloid systems)," *Proc.Acad.Sci Amsterdam*, vol. 32, no. 1927, pp. 849–856, 1929.

[16] B. S. Schuster, G. L. Dignon, W. S. Tang, F. M. Kelley, A. K. Ranganath, C. N. Jahnke, A. G.

Simpkins, R. M. Regy, D. A. Hammer, M. C. Good, and J. Mittal, "Identifying sequence perturbations to an intrinsically disordered protein that determine its phase-separation behavior," *Proc. Natl. Acad. Sci. U. S. A.*, vol. 117, no. 21, pp. 11421–11431, 2020.

[17] H. Zhang, S. Elbaum-Garfinkle, E. M. Langdon, N. Taylor, P. Occhipinti, A. A. Bridges, C. P. Brangwynne, and A. S. Gladfelter, "RNA Controls PolyQ Protein Phase Transitions," *Mol. Cell*, vol. 60, no. 2, pp. 220–230, 2015.

[18] M. Abbas, W. P. Lipiński, J. Wang, and E. Spruijt, "Peptide-based coacervates as biomimetic protocells," *Chem. Soc. Rev.*, vol. 50, no. 6, pp. 3690–3705, 2021.

[19] S. L. Perry, L. Leon, K. Q. Hoffmann, M. J. Kade, D. Priftis, K. A. Black, D. Wong, R. A. Klein, C. F. Pierce, K. O. Margossian, J. K. Whitmer, J. Qin, J. J. De Pablo, and M. Tirrell, "Chirality-selected phase behaviour in ionic polypeptide complexes," *Nat. Commun.*, vol. 6, no. 1, p. 6052, 2015.

[20] W. M. Aumiller and C. D. Keating, "Phosphorylation-mediated RNA/peptide complex coacervation as a model for intracellular liquid organelles," *Nat. Chem.*, vol. 8, no. 2, pp. 129–137, 2016.

[21] I. Kaminker, W. Wei, A. M. Schrader, Y. Talmon, M. T. Valentine, J. N. Israelachvili, J. H. Waite, and S. Han, "Simple peptide coacervates adapted for rapid pressure-sensitive wet adhesion," *Soft Matter*, vol. 13, no. 48, pp. 9122–9131, 2017.

[22] A. A. André and E. Spruijt, "Liquid–liquid phase separation in crowded environments," *Int. J. Mol. Sci.*, vol. 21, no. 16, pp. 1–20, 2020.

[23] J. M. P. Gutierrez, T. Hinkley, J. W. Taylor, K. Yanev, and L. Cronin, "Evolution of oil droplets in a chemorobotic platform," *Nat. Commun.*, vol. 5, no. 1, p. 5571, 2014.

[24] M. Tena-Solsona, C. Wanzke, B. Riess, A. R. Bausch, and J. Boekhoven, "Self-selection of dissipative assemblies driven by primitive chemical reaction networks," *Nat. Commun.*, vol. 9, no. 1, p. 2044, 2018.

[25] T. J. Cashman and B. R. Linton, "β-Sheet hydrogen bonding patterns in cystine peptides," *Org. Lett.*, vol. 9, no. 26, pp. 5457–5460, 2007.

[26] M. Makowski and M. Bogunia, "Influence of ionic strength on hydrophobic interactions in water: Dependence on solute size and shape," *J. Phys. Chem. B*, vol. 124, no. 46, pp. 10326–10336, 2020.

[27] C. Love, J. Steinkühler, D. T. Gonzales, N. Yandrapalli, T. Robinson, R. Dimova, and T. Y. Tang, "Reversible pH-Responsive Coacervate Formation in Lipid Vesicles Activates Dormant Enzymatic Reactions," *Angew. Chemie - Int. Ed.*, vol. 59, no. 15, pp. 5950–5957, 2020.

[28] M. Biancalana, K. Makabe, A. Koide, and S. Koide, "Molecular Mechanism of Thioflavin-T Binding to the Surface of β-Rich Peptide Self-Assemblies," *J. Mol. Biol.*, vol. 385, no. 4, pp. 1052–1063, 2009.

[29] M. Zhao, S. A. Eghtesadi, M. B. Dawadi, C. Wang, S. Huang, A. E. Seymore, B. D. Vogt, D. A. Modarelli, T. Liu, and N. S. Zacharia, "Partitioning of Small Molecules in Hydrogen-Bonding Complex Coacervates of Poly(acrylic acid) and Poly(ethylene glycol) or Pluronic Block Copolymer," *Macromolecules*, vol. 50, no. 10, pp. 3818–3830, 2017.

[30] F. P. Cakmak, S. Choi, M. C. Meyer, P. C. Bevilacqua, and C. D. Keating, "Prebiotically-relevant low polyion multivalency can improve functionality of membraneless compartments," *Nat. Commun.*, vol. 11, no. 1, p. 5949, 2020.

[31] Y. Shin and C. P. Brangwynne, "Liquid phase condensation in cell physiology and disease," *Science*, vol. 357, no. 6357, p. eaaf4382, 2017.

[32] P. W. Frederix, G. G. Scott, Y. M. Abul-Haija, D. Kalafatovic, C. G. Pappas, N. Javid, N. T. Hunt, R. V. Ulijn, and T. Tuttle, "Exploring the sequence space for (tri-)peptide self-assembly to design and discover new hydrogels," *Nat. Chem.*, vol. 7, no. 1, pp. 30–37, 2015.

[33] M. Abbas, W. P. Lipiński, K. K. Nakashima, W. T. Huck, and E. Spruijt, "A short peptide synthon for liquid–liquid phase separation," *Nat. Chem.*, vol. 13, no. 11, pp. 1046–1054, 2021.

[34] J. H. Jensen and J. C. Kromann, "The molecule calculator: A web application for fast quantum mechanics-based estimation of molecular properties," *J. Chem. Educ.*, vol. 90, no. 8, pp. 1093–1095, 2013.

[35] A. Sawicka, P. Skurski, and J. Simons, "Excess electron attachment to disulfide-bridged L,L-cystine. An ab initio study," *J. Phys. Chem. A*, vol. 108, no. 19, pp. 4261–4268, 2004.

[36] R. Carta and G. Tola, "Solubilities of L-cystine, L-tyrosine, L-leucine, and glycine in aqueous solutions at various pHs and NaCl concentrations," *J. Chem. Eng. Data*, vol. 41, no. 3, pp. 414–417, 1996.

Liquid-to-solid transition of short peptide derivatives

3.1 Expanding the versatility of short phase-separating peptide derivatives

Many different proteins have been recently shown to participate in liquid-liquid phase separation (LLPS), both in vitro and in vivo. In living cells, liquid condensates, also referred to as membraneless organelles (MLOs), can fulfil various biological functions [1–4]. While MLOs are often recognised for their dynamic state [5], it has been reported that many protein-based condensates may gradually transform into gel-like or even entirely solid aggregates. In certain cases, such a transition is required for the function of the organelle, e.g. in Balbiani bodies [6] or in heterochromatin assembly [7]. However, most MLOs depend on a dynamic interior for their natural function, and the appearance of solid or gel-like states has been linked to pathological conditions [8]. Several proteins involved in liquid-to-solid transition (LST) of MLOs belong to the class of RNA-binding proteins and are linked with neurodegenerative diseases [9], such as amyotrophic lateral sclerosis (ALS) [10]. In addition, mutations in intrinsically disordered regions (IDRs) of proteins that undergo LLPS can accelerate the maturation of initially liquid droplets into gels or solid aggregates. Examples of proteins that can undergo LLPS but that can also form solid-like aggregates include fused in sarcoma (FUS) [11], tau [12] and heterogeneous nuclear ribonucleoprotein A1 (hnRNPA1) [13].

Despite the widespread occurrence of condensate maturation and solidification, it remains elusive how the molecular properties of molecules undergoing LLPS affect LST and the structural characteristics of gel or solid aggregates. Multivalency has been proposed as a requirement for the formation of MLOs through LLPS [5,14]. Weak, noncovalent interactions (e.g., charge-charge, π-π or cation-π interactions, as well as hydrogen bonding) within IDRs in a protein have been shown to drive LLPS, but these interactions can also promote the self-assembly process into cross-β structures very similar to those observed in amyloid fibrils [6,11–13,15–18]. In recent work, the importance of noncovalent interactions in LLPS has been outlined, and in particular cation-π interactions between tyrosine and positively charged arginine sidechains were identified as possible drivers of both LLPS and assembly into ordered filaments [19]. In solution or in condensates that remain stable as liquid droplets, stretches of polar residues provide enough separation between the (mostly) aromatic residues that are involved in the association to prevent aggregation. This is commonly described as the sticker-and-spacer model [20]. However, we currently lack the molecular understanding of LST and structural models of the different states of assembly, since model systems in which the chemical nature and position of stickers and spacers can be readily changed are missing.

Here, we study the behaviour of small synthetic peptide derivatives that are able to undergo LLPS and LST. They represent a minimal model of phase-separating proteins based on the sticker-and-spacer motif. We show that these simple derivatives can recapitulate the broad scope of phases found in IDR-containing proteins, ranging from the formation of stable liquid droplets, maturation and transformation into arrays of ordered solid fibrils, to immediate solid precipitation. Solid-state NMR under magic-angle spinning (MAS) is the method of choice to study protein samples in macroscopically condensed phases and has been particularly successful in determining the structures of a variety of amyloid fib-

rils [21–26]. It has also recently been employed in the context of phase separation [27–32]. A particular strength of NMR is the possibility to distinguish different polymorphs, which are often observed in the context of amyloid fibrils [21,33,34] and may be of relevance in the context of LST. We performed structural solid-state NMR studies, complemented with transmission electron microscopy (TEM), atomic-force microscopy (AFM) and X-ray diffraction, of several model peptide derivatives with an XXssXX motif, in which two dipeptide sticker moieties (XX) are linked together via a flexible disulphide bond. Using specifically $^{13}C/^{15}N$ labelled samples, we derive a structural model for the formed fibril state highlighting the role of intermolecular π-π interactions in phase separation. Better understanding of the molecular structure of the dense liquid and fibril-like states, and of the interactions stabilising both phases, will provide insight also into the pathological transitions of proteins, which is crucial to develop new methods of preventing and curing aggregation-related diseases.

3.2 Small peptide derivatives are model systems that can undergo LLPS and LST

In the previous chapter, we have described the properties of FFssFF and similar derivatives. These derivatives are typically soluble in acidic conditions (pH below 6.5), but undergo LLPS above pH 7. Derivatives of dipeptides containing phenylalanine and/or leucine amino acids and a linker with one or two sulphur atoms, like FFssFF, LLssLL, LFssFL, FLssLF and FFsFF, were all found to undergo LLPS above a characteristic saturation concentration [35]. Derivatives containing tryptophan residues (WWssWW) formed solid aggregates directly in the solution at room temperature. We have previously shown that the condensates formed by FFssFF and other derivatives have characteristics of coacervates: they form spherical droplets containing 50-70% w/w water that undergo fusion, wet the glass surface, and recover after photobleaching, while aggregates formed by WWssWW are not dynamic and show no fluorescence recovery. These findings could be rationalised in terms of the relative hydrophobicity of the sticker residues that underlie LLPS: when the interaction between stickers is too strong, stacking interactions and limited backbone flexibility in derivatives containing tryptophan residues prevent the dynamic exchange inside condensates, which results in an arrested, solid-like state.

   Interestingly, we observed that the liquid droplets formed by derivatives with phenylalanine (and mixed F and L) could undergo LST upon incubation at elevated temperatures. We also observed that this transition can be induced by mechanical shear, similarly to LST described more generally for proteins and peptides undergoing LLPS [36]. LST of our peptide derivatives typically occurred within 2-5 hours when concentrated samples (10 mg/ml) were agitated during incubation at 37 °C. In optical microscopy images, this is manifested by condensates that acquired irregular shapes (the average circularity decreased) and show non-homogeneous light transmission (upper row of Figure 3.1 and Figure S3.1 in the Supplementary Information at the end of this chapter). TEM of samples collected at different incubation times shows a gradual transition from homogeneous, droplet-like condensates into fibrils (lower row of Figure 3.1). The TEM images suggest that fibril formation is nucleated inside the droplets or at their interface, the latter has
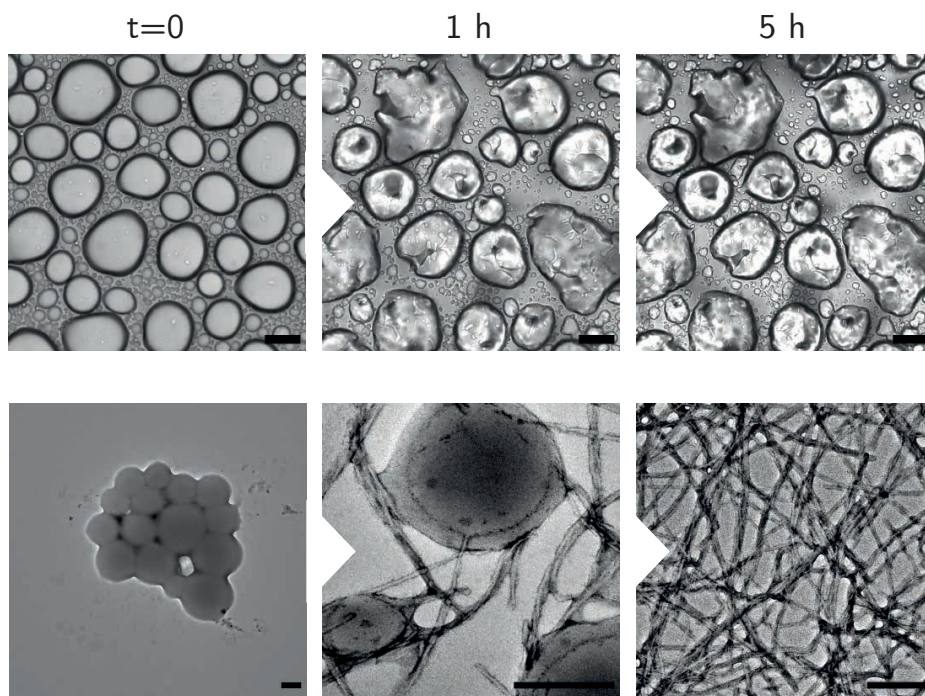
Figure 3.1: Liquid-to-solid transition of FFssFF condensates. Followed over time under optical microscope (upper row, 10 mg/ml FFssFF concentration, scale bar is 20 µm) and under TEM (lower row, 1 mg/ml concentration, scale bar is 200 nm).
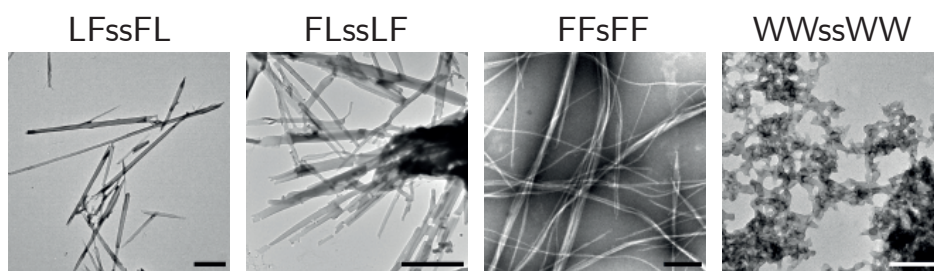
Figure 3.2: TEM images of aggregates formed by different derivatives. From left to right: LFssFL, FLssLF, FFsFF and WWssWW after incubation for 24 h at 37 °C (scale bar is 2 µm for LFssFL and FLssLF, 200 nm for FFsFF and WWsWW).

been reported for instance very recently in the context of the hnRNPA1 protein [37].

The investigation by TEM shows that all solid aggregates formed through LST have a fibrillar structure, although the fibrils appear to have different morphology for different

derivatives (Figure 3.2). This is in contrast to solid aggregates that form upon immediate precipitation from solution by WWssWW, as these aggregates appear amorphous. It is possible that the amorphous solid aggregate is a kinetically trapped form of WWssWW, which unlike liquid condensates of FFssFF cannot undergo transition into fibrils, due to a higher energy barrier. Interestingly, the appearance of condensates formed by derivatives with relatively weak stickers (LLssLL) did not change even after 36 hours of incubation, suggesting that these derivatives do not undergo LST (Figure S3.2).

3.3 Structural information of the solid aggregates is accessible by solid-state NMR

To obtain more insight into the physical state and molecular structure of these different condensates, we focused on maturated condensates of four small peptide derivatives that show distinct phase behaviour: after 24 hours of incubation at 37 °C, FFssFF and FFsFF could undergo LLPS and a LST yielding ordered fibrils, WWssWW precipitated immediately into amorphous solid aggregates, and LLssLL could also undergo LLPS, but not LST. We studied maturated samples of all four derivatives by solid-state NMR.

Figure 3.3A shows the ^{13}C,^{1}H cross-polarisation (CP) spectra measured at 278 K of the compounds without any isotope labelling. In such CP spectra, only the immobilised species is detected. Broad ^{13}C resonances are detected for WWssWW, much narrower resonances for FFsFF and particularly for FFssFF, whereas for LLssLL, except for the side-chain resonances, only broad resonances with rather low intensity are observed. We attribute the different ^{13}C linewidths to the tendency of the corresponding peptide derivatives to form well-ordered fibril structures as judged from the TEM images of the samples (Figure 3.3B), which show well-defined fibrils for FFssFF and FFsFF in agreement with the narrowest ^{13}C resonances observed, unstructured aggregates for WWssWW and spherical deposits from liquid droplets for LLssLL. Although LLssLL only showed liquid-like coacervates by optical microscopy, a weak CP signal was measured pointing to some fraction of less mobile peptide in these coacervates. The high resolution and the good signal-to-noise ratio of the ^{13}C spectrum of FFssFF motivated us to continue with a more detailed examination of the fibrils formed by this derivative.

3.4 FFssFF forms homogeneous fibrils through LST

TEM images of FFssFF aggregates formed by incubation at basic pH reveal the formation of fibrils with a width of around 32 nm (Figure 3.4A). The same sample was also analysed using AFM and the average height of the fibrils was determined to be 6.4 nm (Figure 3.4B). The height and the width of the fibrils suggest that each fibril contains several protofilaments (layers of FFssFF molecules stacked together). The X-ray diffraction (XRD) pattern of a freeze-dried fibril sample (Figure 3.5) points to the formation of a structure with cross-β like arrangement since the pattern resembles that of other amyloid fibrils[38]. The reflexes at 4.8 Å are characteristic of the spacing between two β-strands across the β-sheets along the fibril axis and 11.7 Å is indicative for the spacing
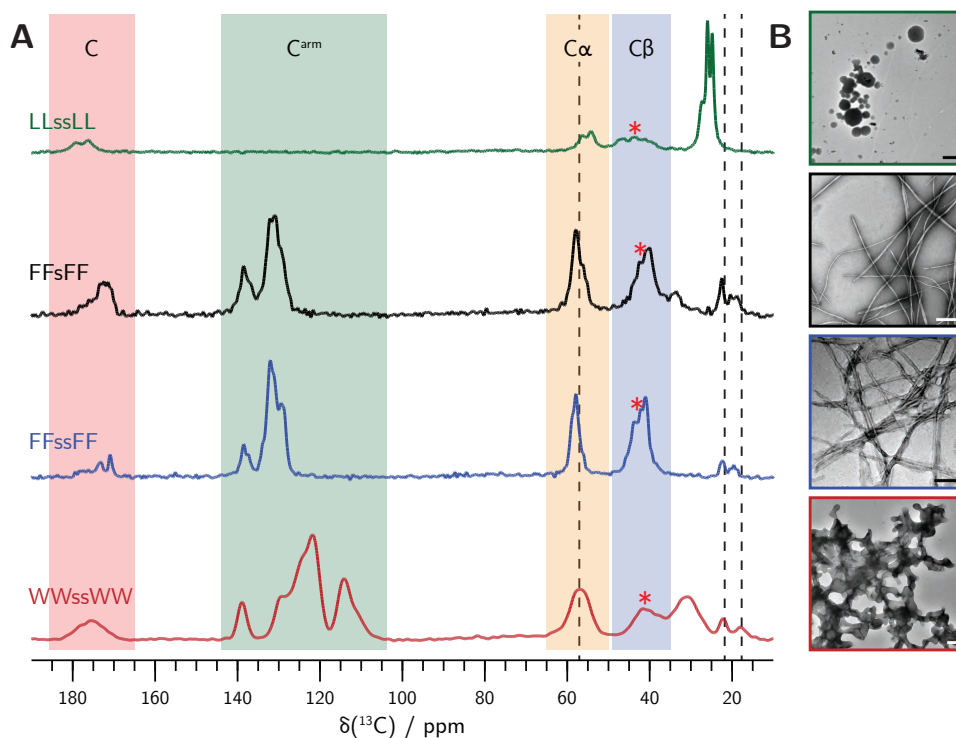
Figure 3.3: Immobilised species are detected in ^{13}C CP-MAS NMR spectra. (A) ^{13}C,[1]H CP-MAS spectra of maturated natural abundance WWssWW (red), FFssFF (blue), FFsFF (black) and LLssLL (green) condensates. All spectra were recorded at 11.7 T and 17 kHz MAS. Black dashed lines indicate sodium trimethylsilylpropanesulfonate (DSS) resonances used for referencing. Red asterisks show the ^{13}C resonances of the disulphide bridge linker (for LLssLL, FFssFF and WWssWW) or the thioeter linker (for FFsFF). (B) TEM images of the samples (scale bar is 2 μm for LLssLL, 200 nm for FFsFF, FFssFF and WWssWW).

perpendicular to the fibril axis [39].

For a more detailed, atomic-level structural model of the fibrils formed by LST, we investigated the samples further by various solid-state NMR techniques. Our goal was to derive a model of the FFssFF fibrils using distance restraints extracted from solid-state NMR spectra in a structure calculation. We used ^{13}C/^{15}N labelled samples in which the phenylalanine residues were isotopically labelled, but the cystamine linker was not. Figure 3.6 shows the 2D MAS ^{13}C-^{13}C 20 ms dipolar assisted rotational resonance (DARR) spectrum [40,41] in which typically intra-residue correlations are detected. The spectrum reveals four phenylalanine Cα/Cβ correlation peaks in an approximate 1:1:1:1 intensity ratio (Figure S3.3) and the observed spectral resolution points to a rather homogeneous sample (which is supported by ^{13}C linewidths, expressed as full width at half maximum, of ⩽1 ppm). The mentioned intensity ratio was preserved in different samples, thus ruling out the effect of polymorphism on the intensity ratio of such resonances (Figure S3.3).
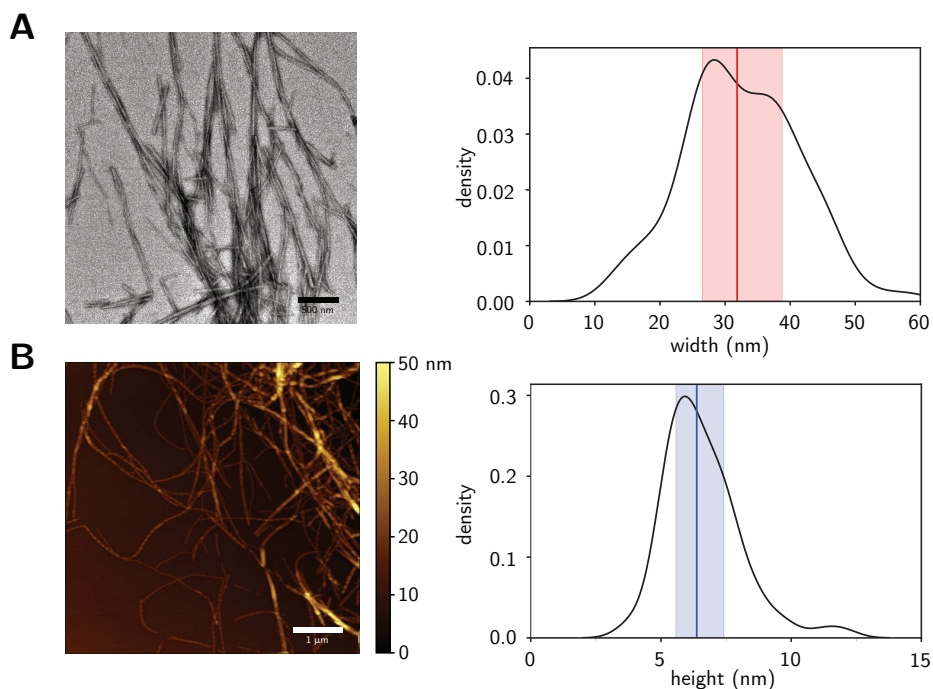
Figure 3.4: Microscopic characterisation of FFssFF fibrils. (A) Representative TEM image of FFssFF fibrils and distribution (kernel density plot, n = 192) of fibril width measured from 4 TEM images. The red line indicates the median (32 nm) and the shaded area corresponds to the range between the 1st and 3rd quartile. (B) AFM height image of FFssFF fibrils and distribution (kernel density plot, n = 75) of fibril height measured from the AFM image. The blue line indicates the median (6.4 nm) and the shaded area corresponds to the range between the 1st and 3rd quartile.

Negligible polymorphism is however observed and reflected in three sets of resonances with the major polymorph strongly dominating (occurrence of more than 90%).

3.5 Two FF pairs can be sequentially assigned

As a first step towards a structure determination, the backbone resonances were assigned using 2D DARR, NCA and NCO spectra (Figure 3.6 and Figure 3.7), the phenylalanaine sidechains were assigned by 2D dipolar recoupling enhanced by amplitude modulation (DREAM)[42] and 3D NCACX spectra (Figure S3.4). A near-complete assignment for two FF pairs was achieved (Figure 3.8A). Note that the linker fragment is not ^{13}C labelled and leads to rather large distances between F2 and F3 (ca. 4 Å between Cα atoms of F1 and F2 vs. ca. 14 Å between Cα atoms of F2 and F3 assuming a linear FFssFF structure) rendering polarisation transfer between F2 and F3 impossible (vide infra). At this stage,
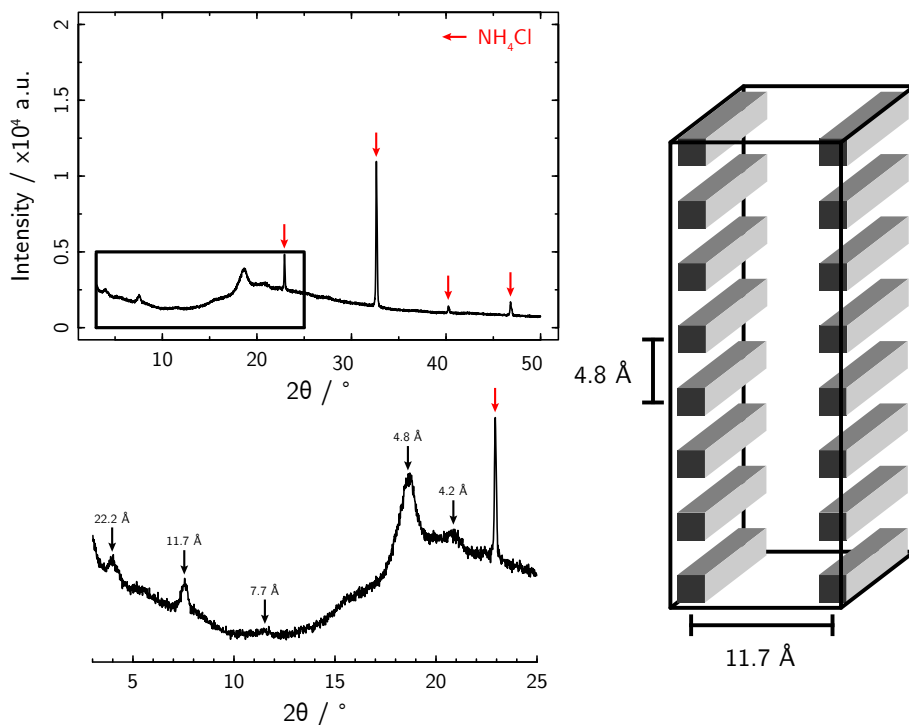
Figure 3.5: X-ray diffraction characterisation of FFssFF fibrils. X-ray diffraction pattern revealing distances of 4.8 Å and 11.7 Å as expected for a fibrillar arrangement as shown schematically on the right. Red arrows indicate NH_4Cl reflexes.

we can only speculate that: (i) the four resonances can be assigned to a FFssFF molecule in which the structural symmetry between the two halves is broken, e.g. by intermolecular packing interactions[43–45]; or (ii) that they can be assigned to two FFssFF molecules (each of them possessing a local C2 symmetry) that are structurally distinct[46–48]. The latter hypothesis seems reasonable in light of the several layers of FFssFF molecules that are present as judged from the TEM data, and that structurally distinct molecules with corresponding peak splitting in NMR spectra have also been reported in the context of amyloid fibrils[47,48]. In the following sections we, therefore, chose to label the residues of the (C2-symmetric) molecules 1 and 2 by F1/F4 and F2/F3 or F1'/F4' and F2'/F3', respectively (Figure 3.6, Figure 3.7 and Figure 3.8). However, we note that a definite answer remains elusive by our solid-state NMR studies.

Figure 3.6: Dipolar assisted rotational resonance (DARR) spectrum of a uniformly-labelled sample. 2D ^{13}C-^{13}C 20 ms DARR (orange and cyan dots with error bars indicate the average Cα/Cβ chemical-shift values for Phe in α-helices and β-sheets, respectively)[49].

Figure 3.7: NCO, NCA and DREAM characterisation of the UL sample. (A) ^{15}N-^{13}C NCO. (B) ^{15}N-^{13}C NCA. (C) ^{13}C-^{13}C DREAM spectrum showing the aromatic region (negative contour levels are plotted in grey, positive contour levels in yellow).

3.6 Backbone secondary chemical shifts point to β-strand-like conformation

The conformation of the peptide backbone can be assessed by solid-state NMR due to the dependence of the Cα/Cβ chemical-shift values on dihedral angles[50,51]. Figure 3.8B

shows the secondary chemical-shift analysis for FFssFF fibrils. Although, strictly speaking, more than three residues downstream of a reference residue with negative secondary chemical shifts are required to identify a sequence as β-strand[51], we conclude that the negative secondary chemical shift values observed here for all phenylalanine residues point to a backbone conformation in the FFssFF molecules that is *β-strand-like*, in good agreement with the XRD analysis (Figure 3.5). This is further supported by plotting the statistical distribution of averaged Phe ^{13}C Cα/Cβ chemical-shift values for the different secondary structure elements on the spectrum (Figure 3.6).51 Based on the secondary chemical-shift analysis, we assume typical dihedral angles of β-strand for F2/F3 and F2'/F3' ($\phi = 140°$ and $\psi = -125°$) in the structure calculations (vide infra). Interestingly, the results for the terminal phenylalanine residues (either in the same or in two different molecules) are quite different (secondary chemical shifts of -4 ppm compared to -1.5 ppm). A similar observation is made in ^{1}H-detected hNH spectra using an MAS frequency of 40 kHz (Figure 3.8C). The primary amine (-NH$_2$) proton chemical-shift values of F1/F4 and F1'/F4' differ by around 2 ppm whose origin remains currently unclear.
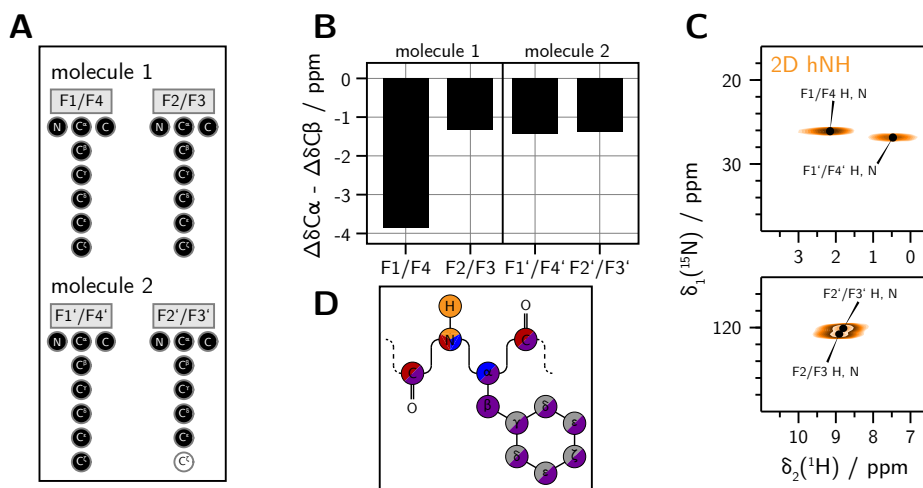
Figure 3.8: Resonance assignment and secondary chemical-shift analysis. (A) Resonance assignment graph. (B) Secondary chemical-shift analysis (chemical shifts of the random coil conformation are taken from[49]). (C) ^{15}N,^{1}H hNH spectrum. (D) Schematic representation of phenylalanine resonances and their appearance in the solid-state NMR spectra using the colour-coding used for the individual spectra.

3.7 Long-range distance restraints for structural modelling

We next determined the long-range distance restraints required for the structure calculation. Such restraints were obtained from a uniformly-labelled sample (using 150

ms DARR and 400 μs spin-diffusion based CHHC experiments[52]) and a ^{13}C:^{15}N 1:1 mixed-labelled sample (using NCA, NCO, 6 ms proton-assisted insensitive nuclei cross-polarisation (PAIN)[53], 500 μs NHHC[52], 150 ms DARR and 400 μs CHHC experiments, see Figure S3.5 and Figure S3.6). Unfortunately, a diluted sample (^{13}C-labelled peptide diluted in ^{15}N-labelled peptide with a ratio of 1:2.5) required for unambiguously distinguishing intra- and intermolecular correlations observed in uniformly-labelled samples yielded another polymorph in several efforts (see Figure S3.7).

Of particular importance are the 2D NCA and NCO spectra performed on the mixed-labelled sample, which probe ^{13}C,^{15}N intermolecular contacts (Figure S3.6C and D). We observe strong intermolecular correlations in the 2D NCA spectrum between backbone nitrogen and Cα atoms of the same residue ($i{\rightarrow}i$) pointing to rather short intermolecular contacts and already suggesting a top-on-top alignment of the molecules, which in amyloid fibrils is often denoted as *in-register* parallel stacking. This is further supported by intermolecular $i{\rightarrow}i{+}1$ backbone nitrogen and CO correlations observed in the NCO spectrum (Figure S3.6D). We also recorded a ^{13}C,^{15}N PAIN[53] spectrum on the mixed-labelled sample, which is typically used in amyloid fibrils to probe intermolecular interactions along the fibril axis[54] (Figure 3.9A, pale red spectrum) and compared it with the NCA spectrum of the unifor mly labelled sample (Figure 3.9A, blue spectrum), in which intense intraresidual correlations are detected. If the peak positions of the NCA and PAIN spectra match, the residues are stacked directly on top of each other, which is indeed observed in the present case (Figure 3.9). Note that in the PAIN spectrum also intermolecular $i{\rightarrow}i{+}1$ contacts are observed. Finally, it is important to mention that in all spectra no intermolecular long-range correlations between the two sets of resonances can be observed (e.g. no contacts between F1/F4 and F1'/F4').

3.8 Phenylalanine sidechain π-π interactions are involved in phase separation and fibril formation

As a consecutive step, we performed a structure calculation with CYANA[55,56] using six FFssFF molecules and the determined distance restraints for the two C2-symmetric molecules 1 and 2 (108 and 112 in total, see Figure S3.8). For the calculation, we assume scenario (ii), a C2 symmetry within the molecule, which we implemented in the calculation by mirroring the distance restraints for the two halves of the molecule. All distance restraints can be fulfilled, which leads to small values of the CYANA target function (0.06 and 0.59 Å^2 for ladders formed of molecules 1 and 2, respectively).

The resulting structural models for the two FFssFF ladders are shown in Figure 3.10 and clearly show a parallel alignment of molecules along the fibril axis. Interestingly, in the energetically most favoured state, the arrangement of the phenylalanine rings suggests π-π stacking interactions between them (note that no intermolecular restraints between the aromatic rings were explicitly used in the calculations). It is reasonable to assume that these noncovalent interactions stabilize the fibrilar aggregates of FFssFF, in agreement with our previous findings that LLssLL does not display LST under studied conditions. It is plausible that a lower degree of π-π stacking interactions initially drives LLPS, which can subsequently be rearranged in the dense liquid droplets leading to nucleation and
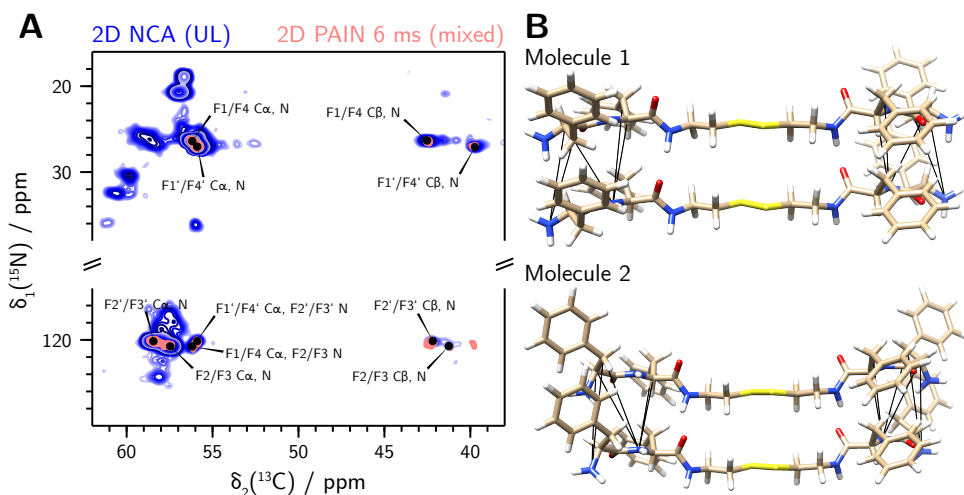
Figure 3.9: Structural model of FFssFF fibrils from solid-state NMR distance constraints. (A) Superposition of the NCA spectrum of UL ^{13}C,^{15}N-labelled fibrils (blue) and the PAIN spectrum of mixed ^{13}C- and ^{15}N-labelled fibrils (pale red). The superposition of cross peaks indicates a parallel alignment of the molecules along the fibril axis. (B) Parallel alignment of FFssFF molecules with the distance restraints determined from the PAIN spectrum for both molecules.

growth of ordered fibrils. The fact that under studied conditions LLPS can precede fibril formation in these and other systems is likely due to the fact that some of the aromatic groups are more spatially restricted than others, and have a higher energy barrier. The liquid condensed state represents a highly concentrated environment in which nucleation of amyloid-like fibrils is more likely [11,12,57–59]. These results pinpoint to the important role of π-π interactions and steric effects in both LLPS and LST [19,30].
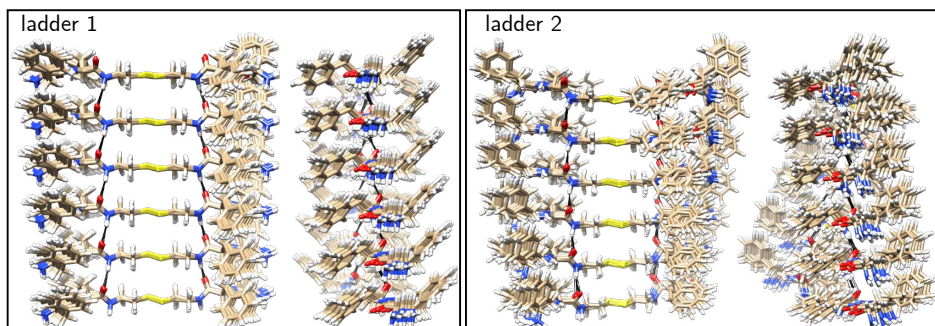
Figure 3.10: Lowest energy structure bundles for FFssFF ladders. Shown in two different orientations, obtained by CYANA calculations.

3.9 Conclusion

By means of NMR, microscopy and XRD we investigated the structures of solid and liquid condensates formed by several short peptide derivatives. NMR experiments showed that while in the condensed liquid phase molecules remain disordered, LLPS may facilitate the formation of ordered supramolecular structures. Derivatives precipitating immediately into solid aggregates exhibit a disordered amorphous structure, while derivatives undergoing LLPS form liquid-like droplets that can further transform into solid, fibrillar aggregates with well-defined, amyloid-like structure. TEM images show that fibrils emerge from condensed droplets, suggesting that they are nucleated inside the droplets or at their interface. The fibrils are relatively thick (ca. 32 nm in diameter), pointing to several protofilaments within the fibril, in agreement with previous reports for fibrillar structures of similar short peptides[60,61]. NMR and XRD experiments showed that the molecules are oriented top-on-top (*in-register*) along the fibril axis. Polymorphism, a common phenomenon in the amyloid fibril formation[54], has been observed as well, but we found that one polymorph was always strongly dominating, pointing to a highly directive LST process. Interestingly, NMR experiments suggest the presence of four chemically distinct phenylalanine residues, appearing always with a fixed intensity ratio of 1:1:1:1. This can be explained by: (i) self-assembly of FFssFF into fibrils resulting in breaking of the molecular C2-symmetry; or (ii) self-assembly into two FFssFF ladders, in which the molecular C2-symmetry is preserved for the two molecules, but which are chemically distinct from each other due to their arrangement within the fibril. Structural modelling of FFssFF based on the collected solid-state NMR distance restraints confirms the top-to-top alignment of molecules along the fibril axis, with peptide backbone angles resembling that of β-sheets in larger peptides. In the energetically most favoured state, a geometry favouring π-π stacking of the phenylalanine rings is observed in both calculated models for the two FFssFF ladders detected, which suggests that these interactions stabilise the fibril structure and might be the driving force for the LST process as well as LLPS[19,20,62–65]. Since the FFssFF molecule design is based on the simplified sticker-spacer model typical for proteins undergoing LLPS and the structure of fibrils resembles amyloids, our results may suggest that similar stabilisation through π-π interactions may be also responsible for the LST of membraneless organelles in cells.

3.10 Experimental details

3.10.1 Materials and synthesis

Unless specified otherwise, reagents were obtained from Sigma Aldrich. All peptide derivatives studied here (FFssFF, FFsFF, LLssLL and WWssWW) were synthesised in solution using Boc/HATU chemistry as described in Chapter 2. Isotopically labelled variants of FFssFF were synthesised according to the same protocol, using ^{15}N-, ^{13}C- and double ^{13}C/^{15}N-labelled Boc-Phe-OH. Isotopically labelled Boc-Phe-OH was obtained from L-phenylalanine with a minimal isotopic purity of 98% purchased from Sigma Aldrich, using di-tert-butyl dicarbonate, according to the protocol described elsewhere[66]. For the 1:1

mixed-labelled sample, ^{13}C-labelled FFssFF was mixed with ^{15}N-labelled FFssFF in a 1:1 molar ratio. For the ^{13}C-diluted sample, ^{13}C-labelled FFssFF was mixed with ^{15}N-labelled FFssFF in a 1:2.5 molar ratio.

3.10.2 Sample preparation

Samples for the NMR studies were prepared by dissolving peptide derivatives at a concentration of 10 mg/ml (experiment with derivatives containing different amino acids) or at 6 mg/ml (experiments with different labelled FFssFF samples), filtering the solution (cellulose acetate filter, 0.45 μm pore size), precipitating by adding 0.4 M or 1 M NaOH to the final concentration of 16 or 12 mM (respectively for 10 mg/ml and 6 mg/ml solutions) and subsequent incubation in a thermoshaker for 24 h (37 °C, orbital shaking at 600 rpm). Samples for TEM and AFM were prepared by dissolving peptide derivatives at a concentration of 1 mg/ml, filtering the solution (cellulose acetate filter, 0.45 μm pore size), precipitating by adding 1 M NaOH to the final concentration of 2 mM and subsequent incubation in a thermoshaker for 24 h (37 °C, orbital shaking at 600 rpm). Samples for optical microscopy were prepared by dissolving peptide derivatives at a concentration of 10 mg/ml, filtering the solution (cellulose acetate filter, 0.45 μm pore size), precipitating by adding 1 M NaOH to the final concentration of 12 mM and subsequent incubation in a thermoshaker for 24 h (37 °C, orbital shaking at 600 rpm).

3.10.3 NMR sample preparation

All peptide derivative solutions were sedimented [67–70] in the MAS-NMR rotor (16 h at 4 °C at 210 000×g) using home-built tools [71]. A summary of the samples is given in Table 3.1.

sample	isotope labeling scheme	rotor diameter / mm
LLssLL	NA	3.2
FFsFF	NA	3.2
FFssFF	NA	3.2
WWssWW	NA	3.2
FFssFF	UL	1.9
FFssFF	Mixed (^{13}C:^{15}N = 1:1)	1.9
FFssFF	Diluted (^{13}C:^{15}N = 1:2.5)	1.9

Table 3.1: Summary of the prepared solid-state NMR samples. NA: natural abundance. UL: uniformly-labelled.

3.10.4 Solid-state NMR

[1]H- and ^{13}C-detected solid-state NMR spectra were acquired at 11.7 and 20.0 T static magnetic field strength using 1.9 and 3.2 mm Bruker Biospin probes. The MAS frequency was set to 17 and 40 kHz. The sample temperature was set to 278 and 304 K using the water line as an internal reference for the measurements in 3.2 and 1.9 mm

rotors, respectively [71]. The spectra were processed with the software TOPSPIN (version 3.5, Bruker Biospin) with a shifted (2.5 to 5.0) squared cosine apodisation function and automated baseline correction in the indirect and direct dimensions. An overview of the experimental parameters for all NMR spectra is available in the Supplementary Information of [72]. Spectra were analysed with the software CcpNmr (version: 2.4.2) [73–75] and referenced to 4,4-dimethyl-4-silapentane-1-sulfonic acid (DSS).

3.10.5   CYANA calculation

All structure calculations were performed with CYANA (version 3.98.13) [55,56]. The residue library was expanded by the molecule construct for FFss. This molecule has been created with the program Avogadro (version 1.2) [76]. For each CYANA calculation, two molecule constructs of FFss are needed to generate a full FFssFF molecule. The two constructs are connected with each other by overlaying corresponding atoms in the S–S linker. A C2-symmetry is used to generate a highly symmetric molecule along the fibril axis. The used distance restraints with their upper distance limits [21,23] are summarised in the Supplementary Information of [72]. The CYANA code and the residue library of FFss are given in the Supplementary Information of [72].

3.10.6   X-ray diffraction

The diffractograms were measured on a Panalytical Empyrean diffractometer in Debye-Scherrer transmission geometry (capillary mode) using monochromatic Cu Kα radiation (1.541 Å) from a sealed LFF tube (operating voltage of 45 kV, current 40 mA), a focusing X-ray mirror (elliptic, W/Si) and a PIXcel3D 1x1 detector. A continuous scan was made in the 2°< 2θ < 35° range with a step size of 0.013°. A freeze-dried sample of FFssFF fibrils was placed in a 0.5 mm soda lime glass capillary and sealed hermetically using super glue.

3.10.7   TEM measurements

Post incubation, suspension of the phase-separated sample (5 µl) was transferred onto a TEM grid (EM-Tec carbon support film on copper, 300 square mesh, Micro to Nano, the Netherlands). Samples were blotted with filter paper, stained with 5 µl of 2% w/w sodium phosphotungstate solution (adjusted to pH 7.4), washed with 5 µl of water and left to dry overnight. Imagining was performed using JEOL JEM-1400 FLASH. For the time-resolved liquid-to-solid transition experiment, samples were collected at specified time points during incubation.

3.10.8   AFM measurements

Post incubation, suspension of the phase-separated sample (10 µl) was transferred onto a mica disc (Nano-Tec V-1 grade muscovite mica discs, Micro to Nano, the Netherlands), blotted with filter paper, washed with 10 µl of milliQ water and left to dry overnight. AFM

images were collected in tapping mode on a Veeco Dimension 3000 AFM, using SSS-NCHR-SPL silicon tips (Nanosensors, Switzerland). Images were analyzed in Gwyddion 2.56.

3.11   Contributions and acknowledgements

Johannes Zehnder performed all the NMR experiments and carried out the CYANA calculations with Peter Güntert. Manzar Abbas contributed to the original synthesis and microscopy investigation. Thomas Wiegand, Evan Spruijt and other authors analysed the data and contributed to the writing of the original text.

We would like to thank Paul Tinnemans (Radboud University) for performing the X-ray diffraction measurements and for helping with their interpretation. We also thank Geert-Jan Janssen (Radboud University) for helping with the TEM measurements and Ettore Bartalucci (MPI CEC, Mülheim) for providing the script to analyse the secondary chemical shift values.

3.12   Supplementary information
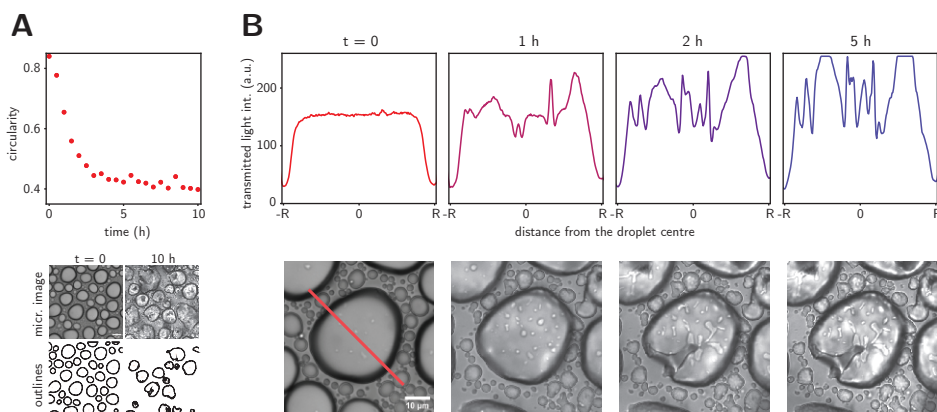
Figure S3.1: LST of FFssFF condensates followed over time. (A) Circularity of FFssFF condensates over time, average value for condensates from one time series, outlines of condensates were determined by automatic intensity thresholding. (B) Intensity profiles (transmitted light) for a selected condensate over time.
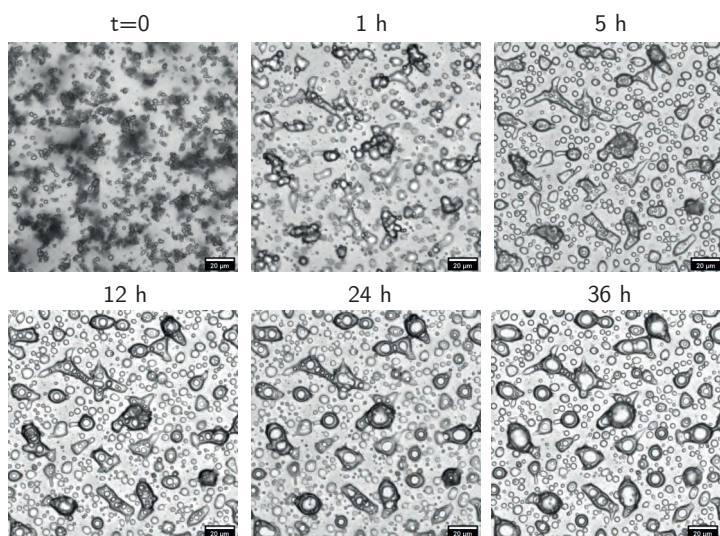
Figure S3.2: LLssLL liquid condensates observed under the optical microscope at different time points after sample preparation.
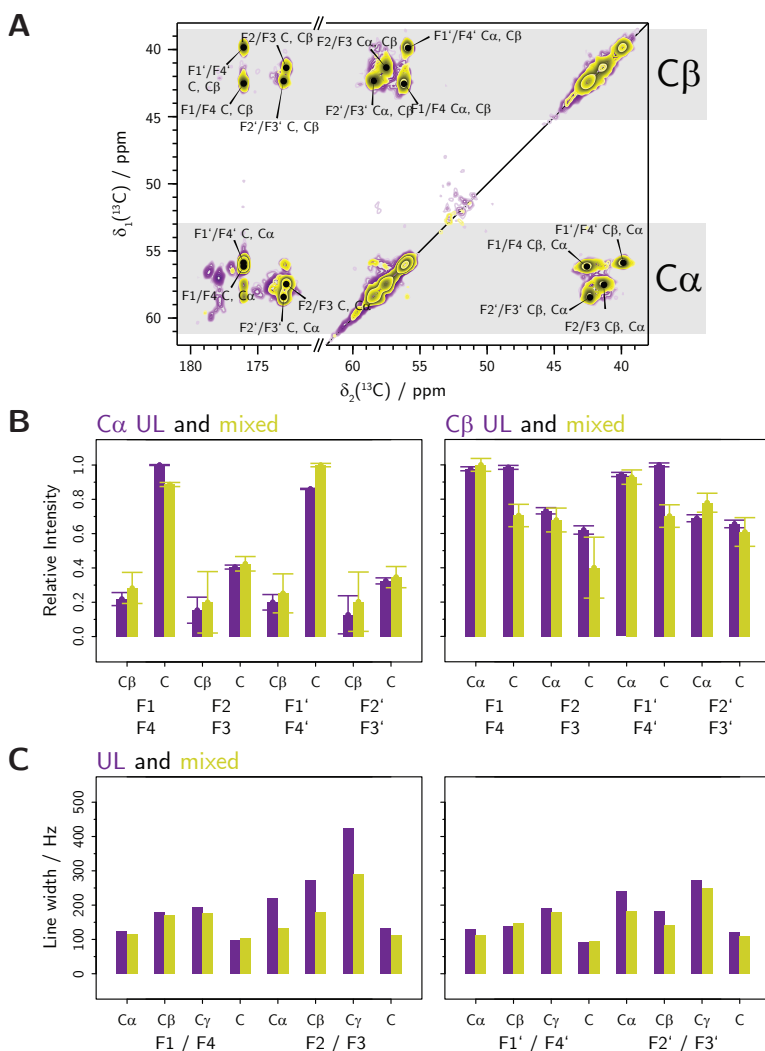
Figure S3.3: Comparison of intensities and linewidths observed in ^{13}C-^{13}C 20 ms DARR spectra between UL and mixed-labelled samples. (A) Overlay of ^{13}C-^{13}C 20 ms DARR spectra recorded on UL (purple) and mixed-labelled FFssFF (yellow). (B) Comparison of cross-peak intensities and (C) line widths of Cα, Cβ, Cγ and C from the spectra shown in (A).

Figure S3.4: 2D and 3D assignment of backbone and side-chain resonances. (A) Example for the sequential walk along the peptide backbone by using ^{13}C-^{13}C 20 ms DARR, ^{15}N-^{13}C NCA and ^{15}N-^{13}C NCO spectra. (B) Side-chain assignment for both molecules employing a 3D NCACX spectrum. Four 2D planes along the four backbone ^{15}N frequencies are shown.
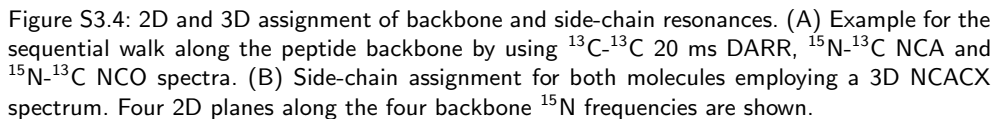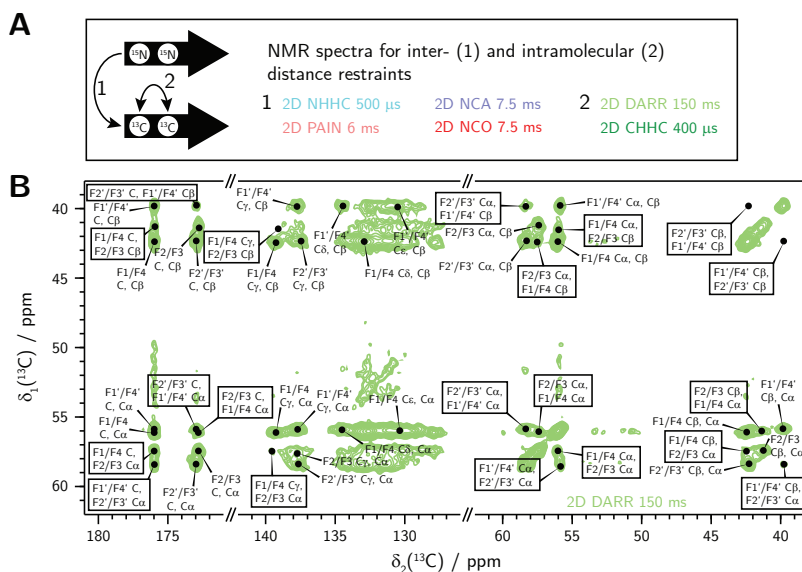
Figure S3.5: Long-range distance restraints and molecular packing revealed by solid-state NMR using a mixed-labelled FFsFF sample (I). (A) Overview of performed NMR experiments to determine intra- and intermolecular distance restraints, (B) ^{13}C-^{13}C 150 ms DARR spectrum.
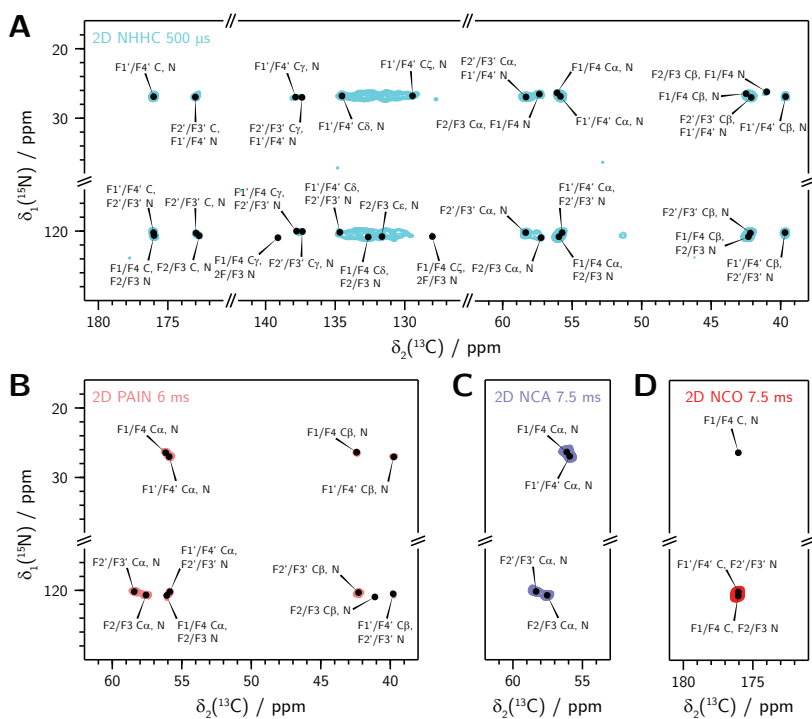
Figure S3.6: Long-range distance restraints and molecular packing revealed by solid-state NMR using a mixed-labelled FFssFF sample (II). (A) 500 µs NHHC spectrum, (B) ^{15}N-^{13}C 6 ms PAIN spectrum, (C) ^{15}N-^{13}C NCA 7.5 ms spectrum and (D) ^{15}N-^{13}C NCO 7.5 ms spectrum.
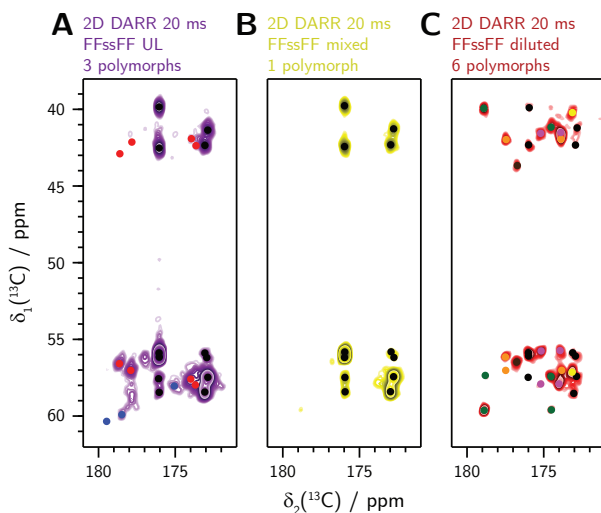
Figure S3.7: Polymorphism in different sample preparations of FFssFF. (A) UL FFssFF shows one major polymorph (black) and two minor polymorphs (red and blue) in the aromatic region of a 20 ms ^{13}C-^{13}C DARR correlation spectrum. (B) Mixed-labelled (^{13}C:^{15}N 1:1) FFssFF shows the major polymorph (black). (C) Diluted (^{13}C:^{15}N 1:2.5) FFssFF sample shows in total six polymorphs. The dots represent the resonances of the different polymorphs, the black polymorph dominating in the UL and mixed-labelled samples.

Molecule 1

DARR 150 ms

	ω₁	ω₂
F1/F4 - F2/F3	C	C
	C	Cα
	C	Cβ
	Cα	C
	Cα	Cα
	Cα	Cβ
	Cβ	C
	Cβ	Cα
	Cγ	Cα
	Cγ	Cβ
F2/F3 - F1/F4	C	C
	C	Cα
	Cα	C
	Cα	Cα
	Cα	Cβ
	Cβ	Cα

2D CHHC 400 µs

	ω₁	ω₂
F1/F4 - F2/F3	C	C
	C	Cα
	C	Cβ
	Cα	C
	Cα	Cα
	Cα	Cβ
	Cβ	Cα
F2/F3 - F1/F4	C	C
	C	Cα
	Cα	C
	Cα	Cβ
	Cβ	C
	Cβ	Cα

2D NHHC 500 µs

	ω₁	ω₂
F1/F4 - F1/F4	Cα	N
	Cβ	N
F1/F4 - F2/F3	C	N
	Cα	N
	Cβ	N
	Cγ	N
	Cδ	N
	Cζ	N
F2/F3 - F1/F4	Cα	N
	Cβ	N
F2/F3 - F2/F3	C	N
	Cα	N
	Cε	N

2D PAIN 6 ms

	ω₁	ω₂
F1/F4 - F1/F4	Cα	N
	Cβ	N
F1/F4 - F2/F3	Cα	N
F2/F3 - F2/F3	Cα	N
	Cβ	N

2D NCA 7.5 ms

	ω₁	ω₂
F1/F4 - F1/F4	Cα	N
F2/F3 - F2/F3	Cα	N

2D NCA 12.5 ms

	ω₁	ω₂
F1/F4 - F1/F4	Cα	N
F2/F3 - F2/F3	Cα	N

2D NC 7.5 ms

	ω₁	ω₂
F1/F4 - F1/F4	C	N
F2/F3 - F2/F3	C	N

Molecule 2

DARR 150 ms

	ω₁	ω₂
F1'/F4' - F2'/F3'	C	C
	C	Cα
	Cα	C
	Cα	Cα
	Cβ	C
	Cβ	Cβ
F2'/F3' - F3'/F4'	C	C
	C	Cβ
	Cα	C
	Cα	Cα
	Cβ	Cβ

2D CHHC 400 µs

	ω₁	ω₂
F1'/F4' - F2'/F3'	C	C
	Cα	C
	Cα	Cα
	Cβ	Cα
	Cβ	Cβ
F2'/F3' - F1'/F4'	C	C
	C	Cα
	Cα	C
	Cα	Cα
	Cα	Cβ
	Cβ	Cβ

2D NCA 7.5 ms

	ω₁	ω₂
F1'/F4' - F1'/F4'	Cα	N
F2'/F3' - F2'/F3'	Cα	N

2D NCO 7.5 ms

	ω₁	ω₂
F1'/F4' - F2'/F3'	C	N

2D NHHC 500 µs

	ω₁	ω₂
F1'/F4' - F1'/F4'	C	N
	Cα	N
	Cβ	N
	Cγ	N
	Cδ	N
	Cζ	N
F1'/F4' - F2'/F3'	C	N
	Cα	N
	Cβ	N
	Cγ	N
	Cδ	N
F2'/F3' - F1'/F4'	C	N
	Cα	N
	Cβ	N
	Cγ	N
F2'/F3' - F2'/F3'	C	N
	Cα	N
	Cβ	N
	Cγ	N

2D PAIN 6 ms

	ω₁	ω₂
F1'/F4' - F1'/F4'	Cα	N
	Cβ	N
F1'/F4' - F2'/F3'	Cα	N
	Cβ	N
F2'/F3' - F2'/F3'	Cα	N
	Cβ	N

2D NCA 12.5 ms

	ω₁	ω₂
F1'/F4' - F1'/F4'	Cα	N
F1'/F4' - F2'/F3'	Cα	N
F2'/F3' - F2'/F3'	Cα	N

Figure S3.8: Collection of distance restraints. Separated dataset for molecules 1 and 2. Details of the corresponding distance limits are summarised in the Supplementary Information of [72].

Bibliography

[1] D. M. Mitrea and R. W. Kriwacki, "Phase separation in biology; Functional organization of a higher order Short linear motifs - The unexplored frontier of the eukaryotic proteome," *Cell Commun. Signal.*, vol. 14, no. 1, p. 1, 2016.

[2] E. Gomes and J. Shorter, "The molecular language of membraneless organelles," *J. Biol. Chem.*, vol. 294, no. 18, pp. 7115–7127, 2019.

[3] C. Greening and T. Lithgow, "Formation and function of bacterial organelles," *Nat. Rev. Microbiol.*, vol. 18, no. 12, pp. 677–689, 2020.

[4] C. A. Azaldegui, A. G. Vecchiarelli, and J. S. Biteen, "The emergence of phase separation as an organizing principle in bacteria," *Biophys. J.*, vol. 120, no. 7, pp. 1123–1138, 2021.

[5] A. A. Hyman, C. A. Weber, and F. Jülicher, "Liquid-liquid phase separation in biology," *Annu. Rev. Cell Dev. Biol.*, vol. 30, no. 1, pp. 39–58, 2014.

[6] E. Boke, M. Ruer, M. Wühr, M. Coughlin, R. Lemaitre, S. P. Gygi, S. Alberti, D. Drechsel, A. A. Hyman, and T. J. Mitchison, "Amyloid-like Self-Assembly of a Cellular Compartment," *Cell*, vol. 166, no. 3, pp. 637–650, 2016.

[7] M. Falk, Y. Feodorova, N. Naumova, M. Imakaev, B. R. Lajoie, H. Leonhardt, B. Joffe, J. Dekker, G. Fudenberg, I. Solovei, and L. A. Mirny, "Heterochromatin drives compartmentalization of inverted and conventional nuclei," *Nature*, vol. 570, no. 7761, pp. 395–399, 2019.

[8] S. Alberti and S. Carra, "Quality Control of Membraneless Organelles," *J. Mol. Biol.*, vol. 430, no. 23, pp. 4711–4729, 2018.

[9] W. M. Babinchak and W. K. Surewicz, "Liquid–Liquid Phase Separation and Its Mechanistic Role in Pathological Protein Aggregation," *J. Mol. Biol.*, vol. 432, no. 7, pp. 1910–1925, 2020.

[10] S. C. Ling, M. Polymenidou, and D. W. Cleveland, "Converging mechanisms in als and FTD: Disrupted RNA and protein homeostasis," *Neuron*, vol. 79, no. 3, pp. 416–438, 2013.

[11] A. Patel, H. O. Lee, L. Jawerth, S. Maharana, M. Jahnel, M. Y. Hein, S. Stoynov, J. Mahamid, S. Saha, T. M. Franzmann, A. Pozniakovski, I. Poser, N. Maghelli, L. A. Royer, M. Weigert, E. W.

Myers, S. Grill, D. Drechsel, A. A. Hyman, and S. Alberti, "A Liquid-to-Solid Phase Transition of the ALS Protein FUS Accelerated by Disease Mutation," *Cell*, vol. 162, no. 5, pp. 1066–1077, 2015.

[12] S. Wegmann, B. Eftekharzadeh, K. Tepper, K. M. Zoltowska, R. E. Bennett, S. Dujardin, P. R. Laskowski, D. MacKenzie, T. Kamath, C. Commins, C. Vanderburg, A. D. Roe, Z. Fan, A. M. Molliex, A. Hernandez-Vega, D. Muller, A. A. Hyman, E. Mandelkow, J. P. Taylor, and B. T. Hyman, "Tau protein liquid–liquid phase separation can initiate tau aggregation," *EMBO J.*, vol. 37, no. 7, p. e98049, 2018.

[13] A. Molliex, J. Temirov, J. Lee, M. Coughlin, A. P. Kanagaraj, H. J. Kim, T. Mittag, and J. P. Taylor, "Phase Separation by Low Complexity Domains Promotes Stress Granule Assembly and Drives Pathological Fibrillization," *Cell*, vol. 163, no. 1, pp. 123–133, 2015.

[14] P. Li, S. Banjade, H. C. Cheng, S. Kim, B. Chen, L. Guo, M. Llaguno, J. V. Hollingsworth, D. S. King, S. F. Banani, P. S. Russo, Q. X. Jiang, B. T. Nixon, and M. K. Rosen, "Phase transitions in the assembly of multivalent signalling proteins," *Nature*, vol. 483, no. 7389, pp. 336–340, 2012.

[15] M. Kato, T. W. Han, S. Xie, K. Shi, X. Du, L. C. Wu, H. Mirzaei, E. J. Goldsmith, J. Longgood, J. Pei, N. V. Grishin, D. E. Frantz, J. W. Schneider, S. Chen, L. Li, M. R. Sawaya, D. Eisenberg, R. Tycko, and S. L. McKnight, "Cell-free formation of RNA granules: Low complexity sequence domains form dynamic fibers within hydrogels," *Cell*, vol. 149, no. 4, pp. 753–767, 2012.

[16] H. Zhang, S. Elbaum-Garfinkle, E. M. Langdon, N. Taylor, P. Occhipinti, A. A. Bridges, C. P. Brangwynne, and A. S. Gladfelter, "RNA Controls PolyQ Protein Phase Transitions," *Mol. Cell*, vol. 60, no. 2, pp. 220–230, 2015.

[17] Y. Shin and C. P. Brangwynne, "Liquid phase condensation in cell physiology and disease," *Science*, vol. 357, no. 6357, p. eaaf4382, 2017.

[18] S. F. Banani, H. O. Lee, A. A. Hyman, and M. K. Rosen, "Biomolecular condensates: Organizers of cellular biochemistry," *Nat. Rev. Mol. Cell Biol.*, vol. 18, no. 5, pp. 285–298, 2017.

[19] J. Wang, J. M. Choi, A. S. Holehouse, H. O. Lee, X. Zhang, M. Jahnel, S. Maharana, R. Lemaitre, A. Pozniakovsky, D. Drechsel, I. Poser, R. V. Pappu, S. Alberti, and A. A. Hyman, "A Molecular Grammar Governing the Driving Forces for Phase Separation of Prion-like RNA Binding Proteins," *Cell*, vol. 174, no. 3, pp. 688–699.e16, 2018.

[20] E. W. Martin, A. S. Holehouse, I. Peran, M. Farag, J. J. Incicco, A. Bremer, C. R. Grace, A. Soranno, R. V. Pappu, and T. Mittag, "Valence and patterning of aromatic residues determine the phase behavior of prion-like domains," *Science*, vol. 367, no. 6478, pp. 694–699, 2020.

[21] M. A. Wälti, F. Ravotti, H. Arai, C. G. Glabe, J. S. Wall, A. Böckmann, P. Güntert, B. H. Meier, and R. Riek, "Atomic-resolution structure of a disease-relevant Aβ(1-42) amyloid fibril," *Proc. Natl. Acad. Sci. U. S. A.*, vol. 113, no. 34, pp. E4976–E4984, 2016.

[22] M. T. Colvin, R. Silvers, Q. Z. Ni, T. V. Can, I. Sergeyev, M. Rosay, K. J. Donovan, B. Michael, J. Wall, S. Linse, and R. G. Griffin, "Atomic Resolution Structure of Monomorphic Aβ42 Amyloid Fibrils," *J. Am. Chem. Soc.*, vol. 138, no. 30, pp. 9663–9674, 2016.

[23] H. Van Melckebeke, C. Wasmer, A. Lange, E. Ab, A. Loquet, A. Böckmann, and B. H. Meier, "Atomic-resolution three-dimensional structure of HET-s(218-289) amyloid fibrils by solid-state nmr spectroscopy," *J. Am. Chem. Soc.*, vol. 132, no. 39, pp. 13765–13775, 2010.

[24] D. T. Murray, M. Kato, Y. Lin, K. R. Thurber, I. Hung, S. L. McKnight, and R. Tycko, "Structure of FUS Protein Fibrils and Its Relevance to Self-Assembly and Phase Separation of Low-Complexity Domains," *Cell*, vol. 171, no. 3, pp. 615–627.e16, 2017.

[25] C. Seuring, J. Verasdonck, J. Gath, D. Ghosh, N. Nespovitaya, M. A. Wälti, S. K. Maji, R. Cadalbert, P. Güntert, B. H. Meier, and R. Riek, "The three-dimensional structure of human β-endorphin amyloid fibrils," *Nat. Struct. Mol. Biol.*, vol. 27, no. 12, pp. 1178–1184, 2020.

[26] A. K. Schütz, T. Vagt, M. Huber, O. Y. Ovchinnikova, R. Cadalbert, J. Wall, P. Güntert, A. Böckmann, R. Glockshuber, and B. H. Meier, "Atomic-resolution three-dimensional structure of amyloid b fibrils bearing the osaka mutation," *Angew. Chemie - Int. Ed.*, vol. 54, no. 1, pp. 331–335, 2015.

[27] R. F. Berkeley, M. Kashefi, and G. T. Debelouchina, "Real-time observation of structure and dynamics during the liquid-to-solid transition of FUS LC," *Biophys. J.*, vol. 120, no. 7, pp. 1276–1287, 2021.

[28] R. Damman, S. Schütz, Y. Luo, M. Weingarth, R. Sprangers, and M. Baldus, "Atomic-level insight into mRNA processing bodies by combining solid and solution-state NMR spectroscopy," *Nat. Commun.*, vol. 10, no. 1, p. 4536, 2019.

[29] S. E. Reichheld, L. D. Muiznieks, F. W. Keeley, and S. Sharpe, "Direct observation of structure

and dynamics during phase separation of an elastomeric protein," *Proc. Natl. Acad. Sci. U. S. A.*, vol. 114, no. 22, pp. E4408–E4415, 2017.

[30] B. Gabryelczyk, H. Cai, X. Shi, Y. Sun, P. J. Swinkels, S. Salentinig, K. Pervushin, and A. Miserez, "Hydrogen bond guidance and aromatic stacking drive liquid-liquid phase separation of intrinsically disordered histidine-rich peptides," *Nat. Commun.*, vol. 10, no. 1, p. 5465, 2019.

[31] E. Gibbs, B. Perrone, A. Hassan, R. Kümmerle, and R. Kriwacki, "NPM1 exhibits structural and dynamic heterogeneity upon phase separation with the p14ARF tumor suppressor," *J. Magn. Reson.*, vol. 310, p. 106646, 2020.

[32] A. C. Murthy and N. L. Fawzi, "The (un)structural biology of biomolecular liquid-liquid phase separation using NMR spectroscopy," *J. Biol. Chem.*, vol. 295, no. 8, pp. 2375–2384, 2020.

[33] J. Gath, L. Bousset, B. Habenstein, R. Melki, A. Böckmann, and B. H. Meier, "Unlike twins: An NMR comparison of two α-synuclein polymorphs featuring different toxicity," *PLoS One*, vol. 9, no. 3, p. e90659, 2014.

[34] C. Wasmer, A. Soragni, R. Sabaté, A. Lange, R. Riek, and B. H. Meier, "Infectious and noninfectious amyloids of the HET-s(218-289) prion have different NMR spectra," *Angew. Chemie - Int. Ed.*, vol. 47, no. 31, pp. 5839–5841, 2008.

[35] M. Abbas, W. P. Lipiński, K. K. Nakashima, W. T. Huck, and E. Spruijt, "A short peptide synthon for liquid–liquid phase separation," *Nat. Chem.*, vol. 13, no. 11, pp. 1046–1054, 2021.

[36] Y. Shen, F. S. Ruggeri, D. Vigolo, A. Kamada, S. Qamar, A. Levin, C. Iserman, S. Alberti, P. S. George-Hyslop, and T. P. Knowles, "Biomolecular condensates undergo a generic shear-mediated liquid-to-solid transition," *Nat. Nanotechnol.*, vol. 15, no. 10, pp. 841–847, 2020.

[37] M. Linsenmeier, L. Faltova, U. C. Palmiero, C. Seiffert, A. M. Küffner, D. Pinotsi, J. Zhou, R. Mezzenga, and P. Arosio, "The interface of condensates of the hnRNPA1 low-complexity domain promotes formation of amyloid fibrils," *Nat. Chem.*, vol. 15, no. 10, pp. 1340–1349, 2023.

[38] M. Sunde, L. C. Serpell, M. Bartlam, P. E. Fraser, M. B. Pepys, and C. C. Blake, "Common core structure of amyloid fibrils by synchrotron X-ray diffraction," *J. Mol. Biol.*, vol. 273, no. 3, pp. 729–739, 1997.

[39] A. W. Fitzpatrick, G. T. Debelouchina, M. J. Bayro, D. K. Clare, M. A. Caporini, V. S. Bajaj, C. P. Jaroniec, L. Wang, V. Ladizhansky, S. A. Müller, C. E. MacPhee, C. A. Waudby, H. R. Mott, A. De Simone, T. P. Knowles, H. R. Saibil, M. Vendruscolo, E. V. Orlova, R. G. Griffin, and C. M. Dobson, "Atomic structure and hierarchical assembly of a cross-β amyloid fibril," *Proc. Natl. Acad. Sci. U. S. A.*, vol. 110, no. 14, pp. 5468–5473, 2013.

[40] K. Takegoshi, S. Nakamura, and T. Terao, "13C–13C polarization transfer by resonant interference recoupling under magic-angle spinning in solid-state NMR," *Chem. Phys. Lett.*, vol. 307, no. 5-6, pp. 295–302, 1999.

[41] K. Takegoshi, S. Nakamura, and T. Terao, "13C-1H dipolar-assisted rotational resonance in magic-angle spinning NMR," *Chem. Phys. Lett.*, vol. 344, no. 5-6, pp. 631–637, 2001.

[42] R. Verel, M. Ernst, and B. H. Meier, "Adiabatic dipolar recoupling in solid-state NMR: The DREAM scheme," *J. Magn. Reson.*, vol. 150, no. 1, pp. 81–99, 2001.

[43] K. Ziach and J. Jurczak, "Mirror symmetry breaking upon spontaneous crystallization from a dynamic combinatorial library of macrocyclic imines," *Chem. Commun.*, vol. 51, no. 20, pp. 4306–4309, 2015.

[44] T. Matsuura and H. Koshima, "Introduction to chiral crystallization of achiral organic compounds: Spontaneous generation of chirality," *J. Photochem. Photobiol. C Photochem. Rev.*, vol. 6, no. 1, pp. 7–24, 2005.

[45] V. Sagar and G. Wistow, "Acquired Disorder and Asymmetry in a Domain-Swapped Model for γ-Crystallin Aggregation: Acquired asymmetry and disorder in a crystallin," *J. Mol. Biol.*, vol. 434, no. 9, p. 167559, 2022.

[46] J. T. Nielsen, M. Bjerring, M. D. Jeppesen, R. O. Pedersen, J. M. Pedersen, K. L. Hein, T. Vosegaard, T. Skrydstrup, D. E. Otzen, and N. C. Nielsen, "Unique Identification of Supramolecular Structures in Amyloid Fibrils by Solid-State NMR Spectroscopy," *Angew. Chemie*, vol. 121, no. 12, pp. 2152–2155, 2009.

[47] C. Sachse, M. Fändrich, and N. Grigorieff, "Paired β-sheet structure of an Aβ(1-40) amyloid fibril revealed by electron microscopy," *Proc. Natl. Acad. Sci. U. S. A.*, vol. 105, no. 21, pp. 7462–7466, 2008.

[48] J. M. Lopez Del Amo, M. Schmidt, U. Fink, M. Dasari, M. Fändrich, and B. Reif, "An asymmetric dimer as the basic subunit in Alzheimer's disease amyloid β fibrils," *Angew. Chemie - Int. Ed.*, vol. 51, no. 25, pp. 6136–6139, 2012.

[49] Y. Wang, "Probability-based protein secondary structure identification using combined NMR chemical-shift data," *Protein Sci.*, vol. 11, no. 4, pp. 852–861, 2002.

[50] S. Spera and A. Bax, "Empirical Correlation between Protein Backbone Conformation and Cα and Cβ 13C Nuclear Magnetic Resonance Chemical Shifts," *J. Am. Chem. Soc.*, vol. 113, no. 14, pp. 5490–5492, 1991.

[51] Y. Shen, F. Delaglio, G. Cornilescu, and A. Bax, "TALOS+: A hybrid method for predicting protein backbone torsion angles from NMR chemical shifts," *J. Biomol. NMR*, vol. 44, no. 4, pp. 213–223, 2009.

[52] A. Lange, S. Luca, and M. Baldus, "Structural constraints from proton-mediated rare-spin correlation spectroscopy in rotating solids," *J. Am. Chem. Soc.*, vol. 124, no. 33, pp. 9704–9705, 2002.

[53] J. R. Lewandowski, G. De Paëpe, and R. G. Griffin, "Proton assisted insensitive nuclei cross polarization," *J. Am. Chem. Soc.*, vol. 129, no. 4, pp. 728–729, 2007.

[54] L. Lecoq, T. Wiegand, F. J. Rodriguez-Alvarez, R. Cadalbert, G. A. Herrera, L. del Pozo-Yauner, B. H. Meier, and A. Böckmann, "A Substantial Structural Conversion of the Native Monomer Leads to in-Register Parallel Amyloid Fibril Formation in Light-Chain Amyloidosis," *ChemBioChem*, vol. 20, no. 8, pp. 1027–1031, 2019.

[55] P. Güntert, C. Mumenthaler, and K. Wüthrich, "Torsion angle dynamics for NMR structure calculation with the new program DYANA," *J. Mol. Biol.*, vol. 273, no. 1, pp. 283–298, 1997.

[56] P. Güntert and L. Buchner, "Combined automated NOE assignment and structure calculation with CYANA," *J. Biomol. NMR*, vol. 62, no. 4, pp. 453–471, 2015.

[57] W. M. Babinchak, R. Haider, B. K. Dumm, P. Sarkar, K. Surewicz, J. K. Choi, and W. K. Surewicz, "The role of liquid-liquid phase separation in aggregation of the TDP-43 low-complexity domain," *J. Biol. Chem.*, vol. 294, no. 16, pp. 6306–6317, 2019.

[58] S. Ray, N. Singh, R. Kumar, K. Patel, S. Pandey, D. Datta, J. Mahato, R. Panigrahi, A. Navalkar, S. Mehra, L. Gadhe, D. Chatterjee, A. S. Sawner, S. Maiti, S. Bhatia, J. A. Gerez, A. Chowdhury, A. Kumar, R. Padinhateeri, R. Riek, G. Krishnamoorthy, and S. K. Maji, "α-Synuclein aggregation nucleates through liquid–liquid phase separation," *Nat. Chem.*, vol. 12, no. 8, pp. 705–716, 2020.

[59] S. Ray, D. Chatterjee, S. Mukherjee, K. Patel, and J. Mahato, "Spatiotemporal solidification of α-synuclein inside the liquid droplets," *bioRxiv*, 2021.

[60] D. Matthes, V. Daebel, K. Meyenberg, D. Riedel, G. Heim, U. Diederichsen, A. Lange, and B. L. De Groot, "Spontaneous aggregation of the insulin-derived steric zipper peptide VEALYL results in different aggregation forms with common features," *J. Mol. Biol.*, vol. 426, no. 2, pp. 362–376, 2014.

[61] S. Chen, V. Berthelier, J. B. Hamilton, B. O'Nuallain, and R. Wetzel, "Amyloid-like features of polyglutamine aggregates and their assembly kinetics," *Biochemistry*, vol. 41, no. 23, pp. 7391–7399, 2002.

[62] C. Ma, J. Sun, B. Li, Y. Feng, Y. Sun, L. Xiang, B. Wu, L. Xiao, B. Liu, V. S. Petrovskii, Bin Liu, J. Zhang, Z. Wang, H. Li, L. Zhang, J. Li, F. Wang, R. Göstl, I. I. Potemkin, D. Chen, H. Zeng, H. Zhang, K. Liu, and A. Herrmann, "Ultra-strong bio-glue from genetically engineered polypeptides," *Nat. Commun.*, vol. 12, no. 1, p. 3613, 2021.

[63] R. M. C. Vernon, P. A. Chong, B. Tsang, T. H. Kim, A. Bah, P. Farber, H. Lin, and J. D. Forman-Kay, "Pi-Pi contacts are an overlooked protein feature relevant to phase separation," *eLife*, vol. 7, p. e31486, 2018.

[64] G. Kim, S. E. Lee, S. Jeong, J. Lee, D. Park, and S. Chang, "Multivalent electrostatic pi–cation interaction between synaptophysin and synapsin is responsible for the coacervation," *Mol. Brain*, vol. 14, no. 1, p. 137, 2021.

[65] K. Kamagata, R. Chiba, I. Kawahata, N. Iwaki, S. Kanbayashi, K. Maeda, H. Takahashi, A. Hirano, K. Fukunaga, K. Ikeda, and T. Kameda, "Characterization of design grammar of peptides for regulating liquid droplets and aggregates of FUS," *Sci. Rep.*, vol. 11, no. 1, p. 6643, 2021.

[66] M. Bodanszky and A. Bodanszky, *The practice of peptide synthesis*. Berlin: Springer-Verlag, 1 ed., 1984.

[67] I. Bertini, C. Luchinat, G. Parigi, E. Ravera, B. Reif, and P. Turano, "Solid-state NMR of proteins sedimented by ultracentrifugation," *Proc. Natl. Acad. Sci. U. S. A.*, vol. 108, no. 26, pp. 10396–10399, 2011.

[68] C. Gardiennet, A. K. Schütz, A. Hunkeler, B. Kunert, L. Terradot, A. Böckmann, and B. H. Meier, "A sedimented sample of a 59 kDa dodecameric helicase yields high-resolution solid-state NMR spectra," *Angew. Chemie - Int. Ed.*, vol. 51, no. 31, pp. 7855–7858, 2012.

[69] T. Wiegand, D. Lacabanne, A. Torosyan, J. Boudet, R. Cadalbert, F. H. Allain, B. H. Meier, and A. Böckmann, "Sedimentation Yields Long-Term Stable Protein Samples as Shown by Solid-State NMR," *Front. Mol. Biosci.*, vol. 7, p. 17, 2020.

[70] C. Gardiennet, T. Wiegand, A. Bazin, R. Cadalbert, B. Kunert, D. Lacabanne, I. Gutsche, L. Terradot, B. H. Meier, and A. Böckmann, "Solid-state NMR chemical-shift perturbations indicate domain reorientation of the DnaG primase in the primosome of Helicobacter pylori," *J. Biomol. NMR*, vol. 64, no. 3, pp. 189–195, 2016.

[71] A. Böckmann, C. Gardiennet, R. Verel, A. Hunkeler, A. Loquet, G. Pintacuda, L. Emsley, B. H. Meier, and A. Lesage, "Characterization of different water pools in solid-state NMR protein samples," *J. Biomol. NMR*, vol. 45, no. 3, pp. 319–327, 2009.

[72] W. P. Lipiński, J. Zehnder, M. Abbas, P. Güntert, E. Spruijt, and T. Wiegand, "Fibrils Emerging from Droplets: Molecular Guiding Principles behind Phase Transitions of a Short Peptide-Based Condensate Studied by Solid-State NMR," *Chem. - A Eur. J.*, vol. 29, no. 50, 2023.

[73] R. Fogh, J. Ionides, E. Ulrich, W. Boucher, W. Vranken, J. P. Linge, M. Habeck, W. Rieping, T. N. Bhat, J. Westbrook, K. Henrick, G. Gilliland, H. Berman, J. Thornton, M. Nilges, J. Markley, and E. Laue, "The ccpn project: An interim report on a data model for the nmr community," *Nat. Struct. Biol.*, vol. 9, no. 6, pp. 416–418, 2002.

[74] W. F. Vranken, W. Boucher, T. J. Stevens, R. H. Fogh, A. Pajon, M. Llinas, E. L. Ulrich, J. L. Markley, J. Ionides, and E. D. Laue, "The CCPN data model for NMR spectroscopy: Development of a software pipeline," *Proteins Struct. Funct. Genet.*, vol. 59, no. 4, pp. 687–696, 2005.

[75] T. J. Stevens, R. H. Fogh, W. Boucher, V. A. Higman, F. Eisenmenger, B. Bardiaux, B. J. Van Rossum, H. Oschkinat, and E. D. Laue, "A software framework for analysing solid-state MAS NMR data," *J. Biomol. NMR*, vol. 51, no. 4, pp. 437–447, 2011.

[76] M. D. Hanwell, D. E. Curtis, D. C. Lonie, T. Vandermeerschd, E. Zurek, and G. R. Hutchison, "Avogadro: An advanced semantic chemical editor, visualization, and analysis platform," *J. Cheminform.*, vol. 4, no. 8, p. 17, 2012.

4

**Disulphide
exchange-driven
phase transitions
of small peptide
derivatives**

4.1 On the way to dynamic and reversible phase transitions

Liquid-liquid phase separation is widely believed to underlie the formation of biomolecular condensates, also called membraneless organelles (MLOs)[1–4]. These condensates are mostly composed of proteins, often combined with nucleic acids. MLOs have a variety of biological functions, including storage of biomolecules, and spatial and temporal control over reactions[5]. Under normal conditions, these are liquid-like droplets, that can exchange constituents with the surrounding solution, and they can be reversibly formed and dissolved[6]. It has been observed that proteins that can undergo liquid-liquid phase separation (LLPS) in cells can also undergo liquid-to-solid transition (LST), irreversibly forming aggregates[7]. LST can be pathological when it is linked to neurodegenerative diseases but can also be functional, e.g. when forming elastin or silk fibrils. Phase transitions of proteins require usually complex enzymatic machinery driving folding and or post-translational modifications of proteins and are often difficult to reproduce in vitro. The development of systems inspired by the biological protein phase transitions but based on simpler chemistry is very interesting from the perspective of creating synthetic protocells and in general synthetic systems with controllable phase transitions.

Liquid condensates and solid aggregates formed by proteins are stabilised by similar types of intermolecular interactions, including interactions between oppositely charged residues, π-π, or cation-π interactions. In most cases LST requires only conformational changes within the protein chain, resulting in the formation of very stable β-sheet structures[8–11]. We have shown that the transition can happen also in a very simple phase-separating system formed by a small peptide derivative, FFssFF (Chapter 2). FFssFF undergoes simple coacervation, meaning that it can separate from water solution without any additional solutes. Water-rich condensates of FFssFF are stabilised by hydrophobic interactions of the phenyl rings and they can remain liquid-like for hours, as the flexible cystamine linker keeps the molecules in a disordered conformation. However, this state appears to be metastable – over time condensates transform into solid aggregates and this is a result of the reorganisation of FFssFF molecules into stable β-sheets stabilised by hydrogen bonds and π-π interactions (Chapter 3). Similarly to this minimal system, LST of large proteins has been mostly attributed to conformational changes of the backbone, allowing for stacking of the protein chains into stable aggregates.

Multiple synthetic systems that mimic protein LLPS have been proposed so far. Many of them are based on polymers forming complex coacervates, for example, arginine-rich peptides with RNA[12–14], unstructured polypeptides like poly-lysine with poly-glutamate[15] or poly-/oligopeptides with small charged molecules[16–18]. Also several phase-separating systems based on small molecules have been proposed, mostly based on peptides[19–21]. Phase separation of these small molecules can be controlled using relatively simple reactions. Disulphide formation and disulphide exchange are particularly interesting - it is easily reversible and can drive LLPS[22,23], and the exchange reactions offer the possibility of transient behaviours[24] and competition between products[25,26]. So far none of these simple systems could undergo chemical reaction-controlled reversible phase transitions between solution, condensed liquid and solid phases. Reversible LST is particu-

larly challenging as the solid phase is typically much more thermodynamically stable than the solution and the condensed liquid phases, however, controlling LST can allow for the formation of synthetic phase-separating systems with new functionalities, e.g. emerging catalytic properties, adjustable viscosity or even self-division.

In this chapter, we look at the possibility of controlling phase transitions of small peptide derivatives with chemical reactions. Presence of the disulphide linkage within the molecule allows for a dynamic exchange of monomers in basic conditions. We use a small library of peptide derivatives that undergo LLPS, aggregate or remain soluble, even at high concentrations. Partitioning of monomers into the condensed phase and high local concentration of substrates drives fast exchange yielding mixed dimers with different properties and can drive phase transitions. We use an experimental model system of dipeptide dimers linked together via a disulphide bond to prove that monomer exchange and the formation of mixed dimers can drive phase transitions. We verify the exchange reactions by HPLC and show that the monomers are mostly present in the supernatant, while the homo- and heterodimers are mostly localised in the liquid or solid-like condensates. We also model the mass-action kinetics in two coexisting phases to show how phase transitions affect the kinetics and the equilibrium state of dynamic covalent chemical reactions.
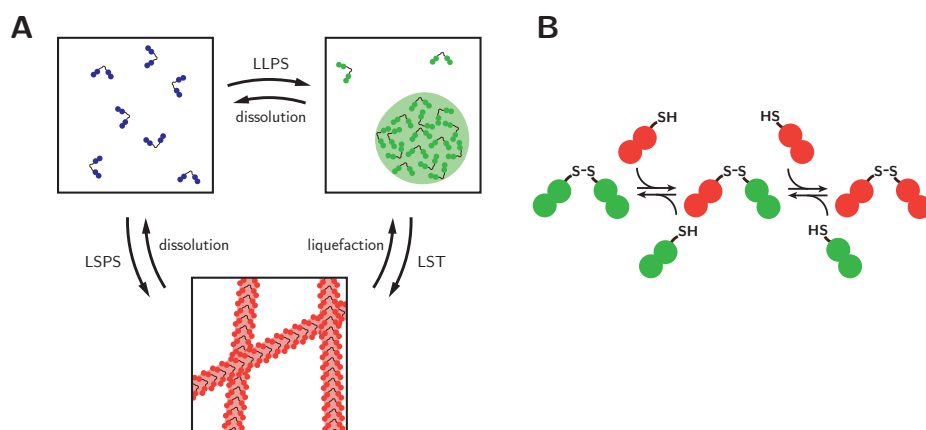
Figure 4.1: Schematic representation of disulphide exchange-driven phase transition. (A) Scheme of phase transitions driven by exchange reactions leading to the formation of soluble, liquid-liquid phase separating or aggregating dimers. (B) Scheme of disulphide exchange reaction. Reversible exchange should allow for the coexistence of homo- and heterodimers.

4.2   Phase transitions of small peptide derivatives

We propose that phase transitions of small peptide derivatives (Figure 4.1A) can be driven by a chemical reaction that changes the properties of the derivatives. Their dimeric structure and the presence of a disulphide linkage allow for disulphide exchange reactions (Figure 4.1B). We hypothesize that the exchange of a dipeptide monomer (i.e., one half

of the disulphide-bonded dimer) for a monomer containing more hydrophobic residues will allow for LLPS, liquid-solid phase separation, or for LST. Exchange for a monomer containing more hydrophilic residues will allow for the dissolution of liquid condensates or solid aggregates or for the liquefaction of aggregates into liquid condensates.

These transitions are only possible when having access to different dimers and monomers that have different properties under the same conditions. We have synthesised four dimers and their corresponding monomers, all comprising a cystamine linker (cysteamine modified C-terminus in the case of monomers) and two dipeptide moieties: valynyl-valine (abbreviated VVssVV and VVsH for the dimer and monomer respectively), leucyl-leucine (LLssLL/LLsH), phenylalanyl-phenylalanine (FFssFF/FFsH) and tryptophanyl-tryptophan (WWssWW/WWsH) (Figure 4.2). Under basic conditions (pH 10) VVssVV forms clear solutions even at high concentrations (higher than 10 mg/ml), LLssLL undergoes LLPS for concentrations above 2.1 mg/ml, FFssFF undergoes LLPS even at very low concentrations (as low as 0.02 mg/ml), and WWssWW forms solid aggregates even at low concentrations (as low as 0.001 mg/ml)[22]. FFssFF undergoes gradual LST which can be triggered or accelerated by shear forces. When incubated overnight at room temperature, an emulsion of FFssFF coacervates transforms into solid- or gel-like aggregates (Figure 4.2). In Chapter 3, we have shown that these aggregates have amyloid-like fibrillar structure[27].
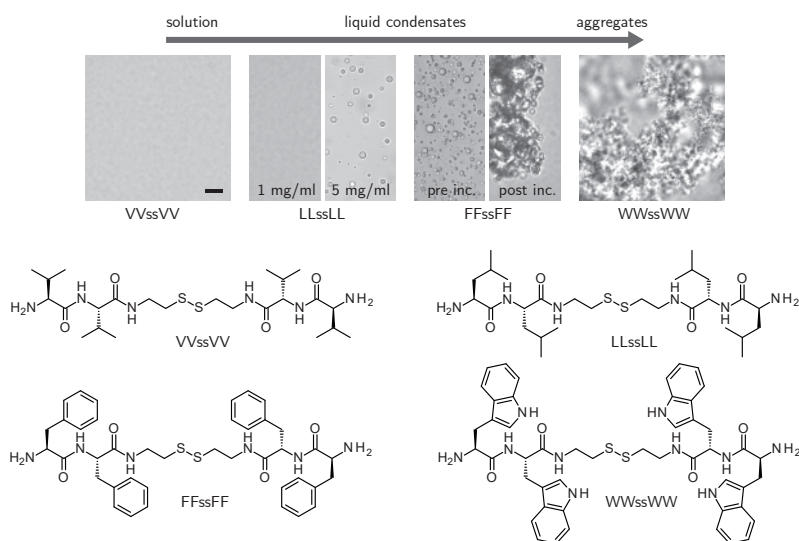
Figure 4.2: Optical microscope images of condensates formed by different XXssXX dimers. VVssVV is soluble even at high concentrations (above 10 mg/ml), LLssLL forms clear solutions at concentrations below ca. 2 mg/ml and liquid-liquid phase separates at higher concentrations, FFssFF forms liquid condensates even at low concentrations (as low as 0.02 mg/ml) and undergoes liquid-to-solid transition over time, WWssWW forms solid aggregates even at low concentrations. Scale bar is 10 μm. Below are the chemical structures of the dimers.

4.3   Modelling the disulphide exchange reaction

We first decided to theoretically analyse the possibility of disulphide exchange-driven (or monomer exchange-driven in general) phase transitions. Our aim was to develop a model that would take into account the influence of reactions on phase transitions (formation and dissolution of the condensed phase) and that would also include the influence of partitioning into the condensed phase on the reaction kinetics. Therefore, we set up a mass action kinetic model in two coexisting phases, and investigated how phase transitions affect the kinetics of the disulphide oxidation/reduction/exchange reactions. We based our model on the established experimental setup, with water-soluble monomers and phase-separating dimers. We assume that one of the homodimers can undergo LLPS and monomers and other dimers can partition into the condensed phase with different partition coefficients (K_P). To simplify the calculations, we assume immediate transport between the dilute and condensed phases (LLPS and partitioning are always equilibrated). We also assume constant volume change upon transport of a single molecule from the dilute to the condensed phase or from the condensed phase to the dilute phase. Finally, we assume that oxidant concentrations (e.g., oxygen or H_2O_2) are the same in the condensed and dilute phase (i.e. $K_P = 1$), and that the rate constants of all reactions are the same in the dilute and in the condensed phase.
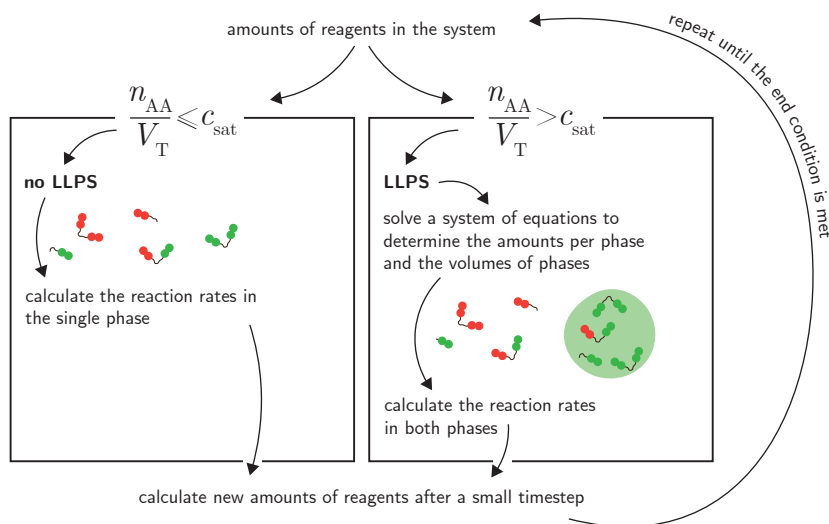
Figure 4.3: Schematic representation of the numerical procedure behind the LLPS-reaction model.

The model was designed to take into account LLPS upon crossing the saturation concentration of the phase-separating component. This is realised by recalculating the distribution of all components at the beginning of every iteration of the numerical method solving the system of ODEs, based on the saturation concentration of the phase-separating component and on the partition coefficients of the other components. The procedure is

schematically depicted in Figure 4.3, and the Python script with the model is available from a GitHub repository (https://github.com/wlipinski/Thesis).

The procedure begins with the evaluation of whether with the current amount of the phase separating component system is mixed (one phase) or demixed (two phases): Provided that the following inequality is fulfilled:

$$\frac{n_{\mathrm{AA}}}{V_{\mathrm{T}}} > c_{\mathrm{sat}} \tag{4.1a}$$

where n_{AA} is the total amount of dimer AA, V_{T} is the total volume of the system and c_{sat} is the saturation concentration, then, the amount of AA dimer in the condensed phase is determined as follows:

$$n_{\mathrm{AA}}^{\mathrm{C}} = \frac{n_{\mathrm{AA}} - c_{\mathrm{sat}} V_{\mathrm{T}}}{1 - c_{\mathrm{sat}} v_{\mathrm{mol}}} \tag{4.2a}$$

where $n_{\mathrm{AA}}^{\mathrm{C}}$ is the amount of dimer AA in the condensed phase, and v_{mol} is the molar volume of AA in the condensed phase (by this we mean that if 1 mole of AA phase separates, it forms v_{mol} of the condensed phase). Otherwise, the system is mixed so there is no condensed phase $n_{\mathrm{AA}}^{\mathrm{C}} = 0$.

If the demixing condition is met, the amounts of other components in the condensed phase are determined using a function which solves a system of equations:

$$\frac{n_{\mathrm{A}}^{\mathrm{C}}}{V_{\mathrm{C}}} = K_{\mathrm{P,A}} \frac{n_{\mathrm{A}} - n_{\mathrm{A}}^{\mathrm{C}}}{V_{\mathrm{T}} - V_{\mathrm{C}}} \tag{4.3a}$$

$$\frac{n_{\mathrm{B}}^{\mathrm{C}}}{V_{\mathrm{C}}} = K_{\mathrm{P,B}} \frac{n_{\mathrm{B}} - n_{\mathrm{B}}^{\mathrm{C}}}{V_{\mathrm{T}} - V_{\mathrm{C}}} \tag{4.3b}$$

$$\frac{n_{\mathrm{BB}}^{\mathrm{C}}}{V_{\mathrm{C}}} = K_{\mathrm{P,BB}} \frac{n_{\mathrm{BB}} - n_{\mathrm{BB}}^{\mathrm{C}}}{V_{\mathrm{T}} - V_{\mathrm{C}}} \tag{4.3c}$$

$$\frac{n_{\mathrm{AB}}^{\mathrm{C}}}{V_{\mathrm{C}}} = K_{\mathrm{P,AB}} \frac{n_{\mathrm{AB}} - n_{\mathrm{AB}}^{\mathrm{C}}}{V_{\mathrm{T}} - V_{\mathrm{C}}} \tag{4.3d}$$

where n_{A}, n_{B}, n_{BB}, n_{AB} are the total amounts of components A, B, BB and AB, $n_{\mathrm{A}}^{\mathrm{C}}$, $n_{\mathrm{B}}^{\mathrm{C}}$, $n_{\mathrm{BB}}^{\mathrm{C}}$, $n_{\mathrm{AB}}^{\mathrm{C}}$ are their amounts in the condensed phase, $K_{\mathrm{P,A}}$, $K_{\mathrm{P,B}}$, $K_{\mathrm{P,BB}}$ and $K_{\mathrm{P,AB}}$ are the partition coefficients of A, B, BB and AB, and V_{C} is the volume of the condensed phase, determined as the sum of volumes of each component in the condensed phase:

$$v_{\mathrm{AA}}^{\mathrm{C}} = n_{\mathrm{AA}}^{\mathrm{C}} v_{\mathrm{mol}} \tag{4.4a}$$

$$v_{\mathrm{A}}^{\mathrm{C}} = \frac{n_{\mathrm{A}}^{\mathrm{C}} v_{\mathrm{mol}}}{2} \tag{4.4b}$$

$$v_{\mathrm{B}}^{\mathrm{C}} = \frac{n_{\mathrm{B}}^{\mathrm{C}} v_{\mathrm{mol}}}{2} \tag{4.4c}$$

$$v_{\mathrm{BB}}^{\mathrm{C}} = n_{\mathrm{BB}}^{\mathrm{C}} v_{\mathrm{mol}} \tag{4.4d}$$

$$v_{\mathrm{AB}}^{\mathrm{C}} = n_{\mathrm{AB}}^{\mathrm{C}} v_{\mathrm{mol}} \tag{4.4e}$$

$$V_{\mathrm{C}} = v_{\mathrm{AA}}^{\mathrm{C}} + v_{\mathrm{A}}^{\mathrm{C}} + v_{\mathrm{B}}^{\mathrm{C}} + v_{\mathrm{BB}}^{\mathrm{C}} + v_{\mathrm{AB}}^{\mathrm{C}} \tag{4.4f}$$

Molar volumes of monomers in the condensed phase are assumed to be half of the volumes of dimers. If the demixing condition is not met (one phase system), the amounts of all components in the condensed phase equal 0.

Subsequently, the amounts of all reagents in the dilute phase (n_{AA}^D, n_A^D, n_B^D, n_{BB}^D and n_{AB}^D) can be determined by subtracting the amounts in the condensed phase from the total amounts:

$$n_{AA}^D = n_{AA} - n_{AA}^C \tag{4.5a}$$

$$n_A^D = n_A - n_A^C \tag{4.5b}$$

$$n_B^D = n_B - n_B^C \tag{4.5c}$$

$$n_{BB}^D = n_{BB} - n_{BB}^C \tag{4.5d}$$

$$n_{AB}^D = n_{AB} - n_{AB}^C \tag{4.5e}$$

The volume of the condensed phase V_C can be determined as in Equation 4.3, and the volume of the dilute phase is determined by subtracting V_C from the total volume V_T. Knowing the volumes of the phases and the amounts of each component per phase, concentration per phase can be determined (c_{AA}^C, c_{AA}^D etc. for other components) and these are used in the set of ODEs describing the reaction kinetics of the system:

$$\frac{dn_{AA}^D}{dt} = V_D \left(k_{AA}^d \left(c_A^D\right)^2 - k_{AA}^r c_{AA}^D - 2k_{BAA}^e c_B^D c_{AA}^D + k_{AAB}^e c_A^D c_{AB}^D \right) \tag{4.6a}$$

$$\frac{dn_A^D}{dt} = V_D \Big(-2k_{AA}^d \left(c_A^D\right)^2 - k_{AB}^d c_A^D c_B^D + 2k_{AA}^r c_{AA}^D + k_{AB}^r c_{AB}^D +$$
$$-2k_{ABB}^e c_A^D c_{BB}^D + k_{BAB}^e c_B^D c_{AB}^D + 2k_{BAA}^e c_B^D c_{AA}^D - k_{AAB}^e c_A^D c_{AB}^D \Big) \tag{4.6b}$$

$$\frac{dn_{BB}^D}{dt} = V_D \left(k_{BB}^d \left(c_B^D\right)^2 - k_{BB}^r c_{BB}^D - 2k_{ABB}^e c_A^D c_{BB}^D + k_{BAB}^e c_B^D c_{AB}^D \right) \tag{4.6c}$$

$$\frac{dn_B^D}{dt} = V_D \Big(-2k_{BB}^d \left(c_B^D\right)^2 - k_{AB}^d c_A^D c_B^D + 2k_{BB}^r c_{BB}^D + k_{AB}^r c_{AB}^D +$$
$$+2k_{ABB}^e c_A^D c_{BB}^D - k_{BAB}^e c_B^D c_{AB}^D - 2k_{BAA}^e c_B^D c_{AA}^D + k_{AAB}^e c_A^D c_{AB}^D \Big) \tag{4.6d}$$

$$\frac{dn_{AB}^D}{dt} = V_D \Big(k_{AB}^d c_A^D c_B^D - k_{AB}^r c_{AB}^D$$
$$+2k_{ABB}^e c_A^D c_{BB}^D - k_{BAB}^e c_B^D c_{AB}^D + 2k_{BAA}^e c_B^D c_{AA}^D - k_{AAB}^e c_A^D c_{AB}^D \Big) \tag{4.6e}$$

where k_{XX}^d are the dimerisation rate constants, k_{XX}^r are the reduction rate constants, and k_{XXX}^e are the exchange rate constants.

The concentration of the oxidating agent can be omitted, since we assumed it remains constant (it can be therefore included in the rate constant k_{XX}^d) The same set of equations can be formulated for the condensed phase (replacing the amounts, volume and concentrations with the corresponding values for the condensed phase). Then the total

change in the amount of each component can be determined as a sum of the change in the amount for the dilute phase and for the condensed phase:

$$\frac{dn_{\text{AA}}}{dt} = \frac{dn_{\text{AA}}^{\text{D}}}{dt} + \frac{dn_{\text{AA}}^{\text{C}}}{dt} \tag{4.7a}$$

$$\frac{dn_{\text{A}}}{dt} = \frac{dn_{\text{A}}^{\text{D}}}{dt} + \frac{dn_{\text{A}}^{\text{C}}}{dt} \tag{4.7b}$$

$$\frac{dn_{\text{BB}}}{dt} = \frac{dn_{\text{BB}}^{\text{D}}}{dt} + \frac{dn_{\text{BB}}^{\text{C}}}{dt} \tag{4.7c}$$

$$\frac{dn_{\text{B}}}{dt} = \frac{dn_{\text{B}}^{\text{D}}}{dt} + \frac{dn_{\text{B}}^{\text{C}}}{dt} \tag{4.7d}$$

$$\frac{dn_{\text{AB}}}{dt} = \frac{dn_{\text{AB}}^{\text{D}}}{dt} + \frac{dn_{\text{AB}}^{\text{C}}}{dt} \tag{4.7e}$$

and these constitute the set of ODEs used to compute the amounts and concentrations of components in the selected time range.
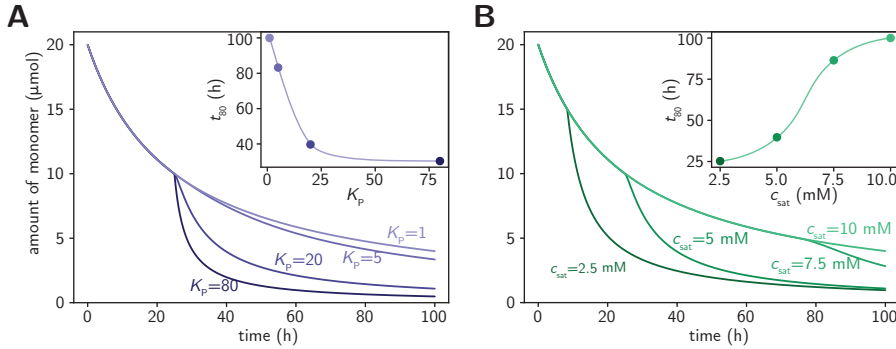

Figure 4.4: Simulation of an oxidation reaction in a phase separating system. (A) Amount of A monomer over time in a system with oxidation reaction of A to AA and with different K_{P} values. Inset graph shows the influence of changing K_{P} on the 80% conversion time. Line is drawn to guide the eye. Simulation parameters: $c_{\text{A}}^{0} = 20$ mM, $k_{\text{AA}}^{\text{d}} = 0.001$ mM^{-1}h^{-1}, $c_{\text{sat}} = 5$ mM, $v_{\text{mol}} = 1$ µl/µmol. (B) Amount of A monomer over time in a system with oxidation reaction of A to AA and with different c_{sat} values. Inset graph shows the influence of changing c_{sat} on the 80% conversion time. Line is drawn to guide the eye. Simulation parameters: $c_{\text{A}}^{0} = 20$ mM, $k_{\text{AA}}^{\text{d}} = 0.001$ mM^{-1}h^{-1}, $K_{\text{P}} = 20$, $v_{\text{mol}} = 1$ µl/µmol.

We first looked at a basic system composed of only one type of monomers at the starting point (Figure 4.4). In such a system, in the presence of an oxidant, monomers (XXsH, here called A and B form simplicity) are converted into dimers (XXssXX, here called AA, AB and BB), which subsequently undergo LLPS after crossing the critical concentration threshold. This does not affect the oxidation reaction (provided it is irreversible), unless the monomers can also partition into the condensed phase. In the latter case, partitioning can result in an increase in the local concentration of monomers and thus in a locally

faster oxidation reaction. As can be expected, in a system with partitioning, the overall kinetics of the monomer conversion depends not only on the initial concentration of the monomers and the reaction rate constant, but also on the partition coefficient (K_P, Figure 4.4A) of the monomers and on the critical phase-separation concentration (c_{sat}, Figure 4.4B) of the dimer. The lower K_P or the higher c_{sat}, the less prevalent is the acceleration effect observed in the monomer conversion upon LLPS. Inset plots in Figure 4.4 present the influence of these two parameters on the 80% conversion times (t_{80}). These trends depend also on other parameters of the system, but in general, these simulations show that even low K_P can have a substantial influence on the reaction kinetics. In the case of c_{sat}, the earlier the onset of LLPS (the lower the c_{sat}), the more pronounced the instant acceleration of the dimerisation reaction.
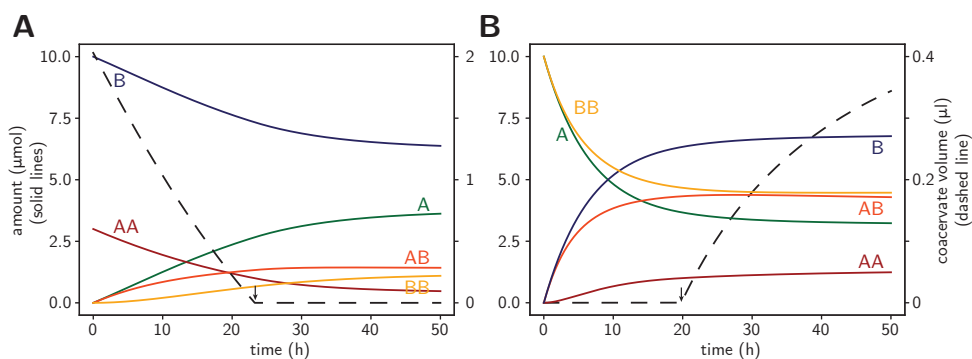

Figure 4.5: Simulation of dissolution and formation of the condensed phase driven by exchange reaction. (A) Dissolution of the condensed phase: amounts of reactants over time in a multi-component system with exchange reactions and with phase separation, starting with AA and B (left axis), and condensed phase volume (right axis). Simulation parameters: $c_{AA}^0 = 3$ mM, $c_B^0 = 10$ mM, $k_{ABB}^d = 0.005$ mM^{-1}h^{-1}, $k_{BAB}^d = 0.005$ mM^{-1}h^{-1}, $k_{BAA}^d = 0.005$ mM^{-1}h^{-1}, $k_{AAB}^d = 0.005$ mM^{-1}h^{-1}, $K_{P,A} = 5$, $K_{P,B} = 0.1$, $K_{P,BB} = 0.1$, $K_{P,AA} = 5$, $c_{sat} = 1$ mM, $v_{mol} = 1$ µl/µmol, $V_T = 1$ ml. Small black arrow indicates the moment of complete dissolution of the condensed phase. (B) Formation of the condensed phase: amounts of reactants over time in a multi-component system with exchange reactions and with phase separation, starting with BB and A (left axis), and condensed phase volume (right axis). Simulation parameters: $c_{BB}^0 = 10$ mM, $c_A^0 = 10$ mM, other parameters the same as in (A). Small black arrow indicates the moment when the condensed phase starts to form.

Upon adding another monomer B, the oxidation reaction results in the formation of AA, AB and BB. We assumed that the oxidation reaction does not favour the formation of any of the dimers, meaning that the ratio AA:AB:BB in the system where only oxidation occurs is 1:2:1. However, because partitioning of the monomers and dimers is not the same, local increased formation and accumulation of a certain type of dimers is possible.

We thus modelled situations where the exchange of monomers either drives the formation or the removal of phase-separating dimers AA from the system, resulting in the emergence or dissolution of the condensed phase, respectively (Figure 4.5). Figure 4.5A shows a situation where the starting concentration of phase-separating AA is above c_{sat}.

The mixture is spiked with monomeric B which can replace A in the AA dimer. Consequently, AB and BB dimers, and A monomers are formed, and the amount of AA decreases resulting in a complete dissolution of the condensed phase. Another scenario is presented in Figure 4.5B. In this case, the condensed phase is not present at time 0, when the mixture contains only BB and A. Due to exchange, even in the absence of oxidation, AB and AA dimers are formed and the concentration of AA exceeds c_{sat} at some point. Since moderate K_{P} values were used for all components (0.1 to 5, see the caption under Figure 4.5), the presence of the condensed phase does not have a substantial effect on the reaction kinetics in this case.
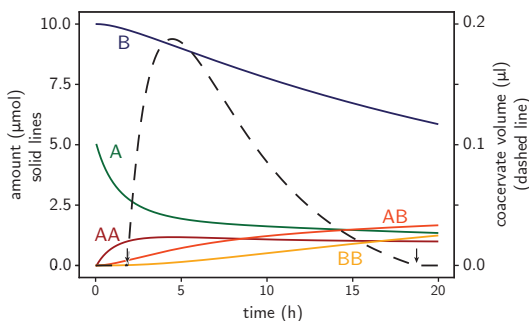

Figure 4.6: Simulation of transient LLPS. Amounts of reactants (left axis), and condensed phase volume (right axis) over time. Simulation parameters: $c_{\mathrm{A}}^0 = 5$ mM, $c_{\mathrm{B}}^0 = 10$ mM, $k_{\mathrm{ABB}}^{\mathrm{d}} = 0.01$ mM^{-1}h^{-1}, $k_{\mathrm{BAB}}^{\mathrm{d}} = 0.01$ mM^{-1}h^{-1}, $k_{\mathrm{BAA}}^{\mathrm{d}} = 0.01$ mM^{-1}h^{-1}, $k_{\mathrm{AAB}}^{\mathrm{d}} = 0.01$ mM^{-1}h^{-1}, $K_{\mathrm{P,A}} = 1$, $K_{\mathrm{P,B}} = 1$, $K_{\mathrm{P,BB}} = 1$, $K_{\mathrm{P,AA}} = 1$, $c_{\mathrm{sat}} = 1$ mM, $v_{\mathrm{mol}} = 1$ µl/µmol, $V_{\mathrm{T}} = 1$ ml. Small black arrows indicate the moments when the condensed phase starts to form and when it dissolves again.

Finally, we modelled a situation where oxidation of A monomers to phase-separating AA dimers and subsequent exchange with B monomers results in the transient formation of the condensed phase. In this case, the transient LLPS relies on fast A to AA oxidation and halted B oxidation (B can only undergo exchange reactions) Figure 4.6. Reversible phase separation based on disulphide chemistry has been shown recently, but it required subsequent addition of oxidating and reducing agents[22,23]. Our simulations show that, at least theoretically, the emergence and dissolution of the liquid phase can be kinetically driven without the addition of reagents during the process.

4.4 Liquid-to-solid and solid-to-liquid transition

We then set out to study whether the findings from the simulations can be reproduced experimentally. To show that disulphide exchange reactions and conversion of homodimers into heterodimers or more hydrophilic homodimers can potentially result in morphological changes of the condensates, we looked at the condensed phases formed by mixtures of liquid-liquid phase separating FFssFF and aggregating WWssWW. At 1 mg/ml total concentration, the mixtures form liquid-like condensates above pH 7 when the content of

WWssWW is sufficiently low (10% w/w or lower), gel-like condensates when the content of WWssWW is 20% and solid aggregates when the content of WWssWW reaches 50% (Figure 4.7A).

We have shown previously that the cystamine linker of the dimers can be reduced and subsequently oxidised resulting in the dissolution and formation of the condensed phase[22]. We looked at the morphological changes of the condensed phase upon the addition of the reducing agent. We used FFssFF fibrous aggregates prepared by incubating FFssFF condensates overnight and added an excess amount of DTT as the reducing agent. Interestingly, we observed that the solid particles undergo a transition into a liquid phase that wets the microscopy slide (Figure 4.7B). Subsequently, this liquid condensed phase dissolves to form a clear solution. This gradual transition is caused by the fact that FFsH monomers which are formed upon reduction of FFssFF by DTT, even though they are soluble on their own, can partition into the FFssFF condensed phase, presumably increasing its hydrophilicity and reversing the liquid to solid transition (i.e., liquefaction or solid to liquid transition) of the FFssFF aggregates. Reduction of even more FFssFF results in the complete dissolution of the condensed phase.
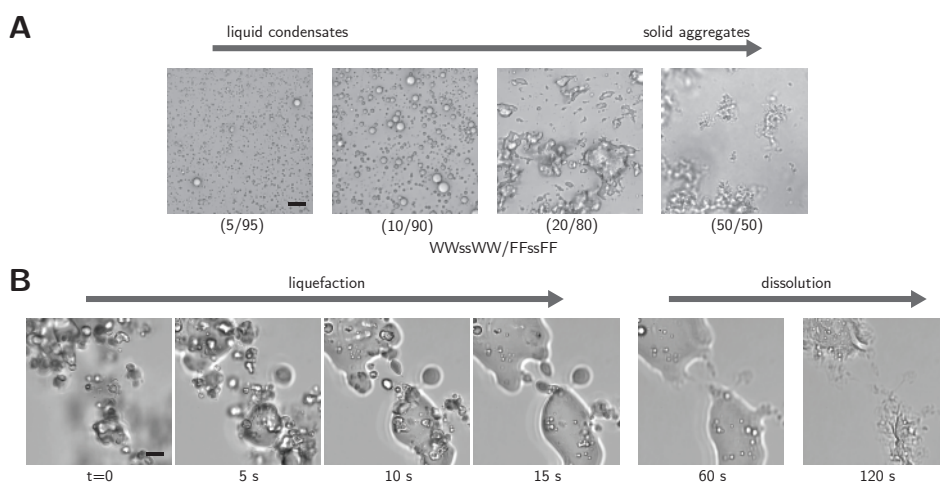

Figure 4.7: Composition change- and reaction-driven phase transitions. (A) Microscope images of condensates formed in the WWssWW/FFssFF mixtures with different content of WWssWW. Increasing the amount of WWssWW changes the morphology from liquid condensates (5% and 10% w/w WWssWW) through gel-like condensates (20% WWssWW) to solid aggregates (50% WWssWW). Scale bar is 10 μm. (B) FFssFF aggregates undergo liquefaction upon reduction with DTT and subsequent dissolution. Scale bar is 10 μm.

4.5 Disulphide exchange reactions in phase-separating systems

We used HPLC to quantify the disulphide exchange reaction. We first determined the retention times of all different monomers and dimers that were used as starting materials or as exchange reagents (Table S4.1 in the Supplementary Information at the end of this chapter). We prepared various dimer-monomer mixtures at a final concentration of 1 mg/ml of each (or 5 mg/ml when LLssLL was used as the dimer, since c_{sat} of LLssLL is ca. 2.5 mg/ml) and increased the pH to ca. 10 with 1 M NaOH solution. We incubated the mixtures in a thermoshaker at 20 °C for 12 h and separated the dilute phases (supernatants) from the condensed phases by centrifugation. The condensed phases were dissolved in 30/70 acetonitrile-water mixture and both the dilute and the condensed phases were analysed by HPLC.
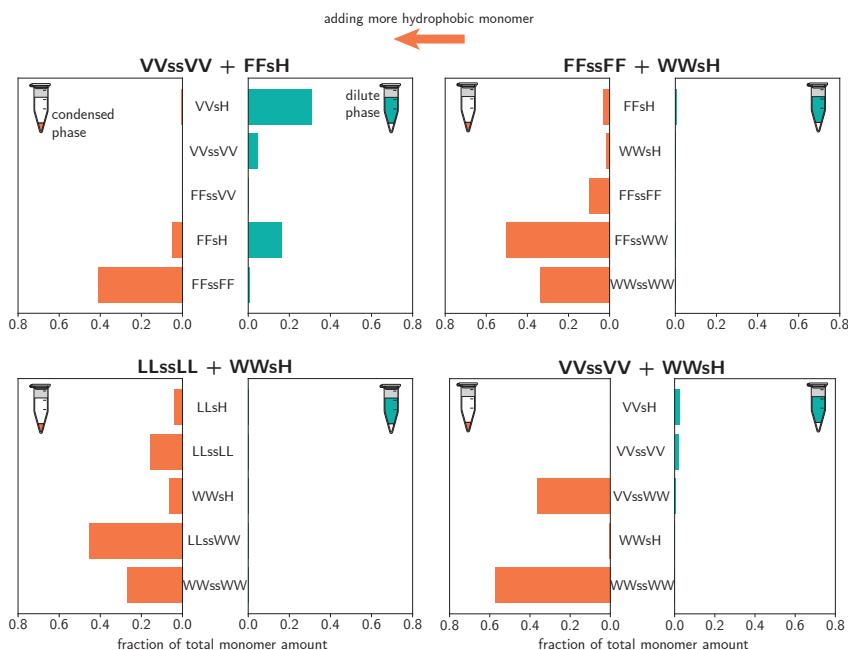

Figure 4.8: Distribution of monomers after exchange reaction, after adding more hydrophobic monomer. Staring composition: VVssVV (1 mg/ml) + FFsH (1 mg/ml), LLssLL (5 mg/ml) + WWsH (5 mg/ml), FFssFF (1 mg/ml) + WWsH (1 mg/ml) and VVssVV (1 mg/ml) + WWsH (1 mg/ml).

We tested the following combinations: (a) VVssVV + FFsH, (b) LLssLL + WWsH, (c) FFssFF + WWsH, (d) VVssVV + WWsH, (e) LLssLL + VVsH, (f) FFssFF + VVsH, (g) WWssWW + VVsH and (h) WWssWW + LLsH. In all of these combinations, we could observe the formation of heterodimers and new homodimers, indicating the disulphide

exchange (Figure S4.1 and Figure S4.2). We could also see that the monomers and hydrophilic dimers were enriched in the dilute phase, while the hydrophobic dimers were enriched in the condensed phase. In Figure 4.8 and Figure 4.9 we present the distribution of the total monomer amount post-reaction, determined by HPLC. The amounts presented in the figure are quantified by comparing the peak areas in the reaction mixture with the peak areas of the calibration samples containing known amounts of pure compounds. For mixed dimers, which were not obtained in the pure form, we assumed that the coefficient relating peak area to a known amount equals the average of areas for homodimers of the same monomers (so the coefficient of AB equals the average of coefficients for AA and BB).
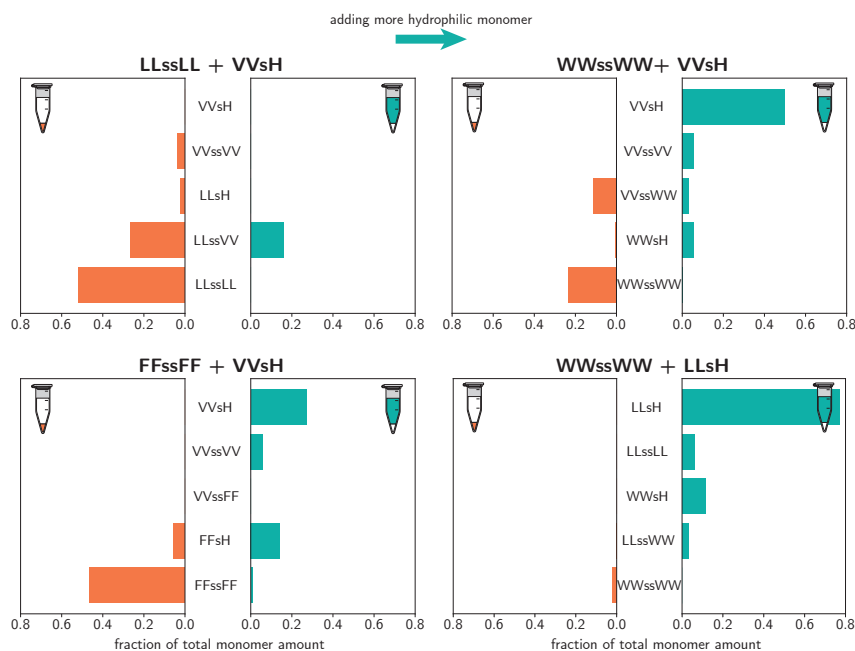

Figure 4.9: Distribution of monomers after exchange reaction, after adding more hydrophilic monomer. Starting composition LLssLL (5 mg/ml) + VVsH (5 mg/ml), FFssFF (1 mg/ml) + VVsH (1 mg/ml), WWssWW (1 mg/ml) + VVsH (1 mg/ml) and WWssWW (1 mg/ml) + LLsH (1 mg/ml).

Figure 4.8 presents the mixtures where a dimer of a more hydrophilic monomer was mixed with a more hydrophobic monomer. Figure 4.9 presents the mixtures where a dimer of a more hydrophobic monomer was mixed with a more hydrophilic monomer. In general, the addition of a more hydrophobic monomer resulted in the formation of more hydrophobic homo- and heterodimers, partitioning mostly to the condensed phase (in all 4 cases solid aggregates were present in the reaction tube after the reaction). The addition of a more hydrophilic monomer resulted in the formation of more hydrophilic homo- and heterodimers, partitioning mostly to the dilute phase. Interestingly, while in the case

of adding more hydrophobic monomer, low amounts of the hydrophobic monomer were detected post-reaction, in the case of adding more hydrophilic monomer, a large fraction of the monomer was still present in the mixture post-reaction. This suggests that the exchange reaction happens mostly in solution and is faster when the dimer has higher solubility, or that the reaction does not occur easily in systems where the dimer is initially aggregated. In particular, a large fraction of unreacted monomer was detected in samples WWssWW+VVsH and WWssWW+LLsH (in the last one, the amount of WWssWW or the mixed dimer is underestimated, probably due to incomplete condensed phase separation and dissolution for analysis). What is also worth noting, the final composition of sample VVssVV+FFsH is very similar to sample FFssFF+VVsH and that VVsH in sample LLssLL+VVsH appeared to be completely reacted, suggesting that under phase separating conditions reaction can still occur if the condensed phase is liquid.

4.6 Conclusion

Simple dimer molecules with sticker-and-spacer architecture and a linker allowing for the dynamic exchange of stickers offer access to a dynamic system in which phase transitions can be driven by disulphide exchange reactions. Since the sticker motif is based on a dipeptide moiety, it is easy to change its properties by synthesising derivatives with different amino acids. We have shown that, depending on the hydrophobicity of the stickers, the dimers can be water-soluble, undergo LLPS or aggregation. Using simulations, we confirm that the monomer exchange can potentially drive phase transitions, but also show that the presence of liquid condensates can affect reaction kinetics or result in a preferential formation of phase-separating products. These findings were at least partially confirmed by experiments, showing that the conversion of the dimers can result in morphological changes of the condensates, in particular liquid-to-solid transition or liquefaction and dissolution. Even dimers trapped in liquid condensates can undergo exchange with the soluble monomers (dimers trapped in solid aggregates undergo exchange but at much lower rate). This combination of systems chemistry and phase separation can lead to interesting dynamic behaviours, like transient LLPS. And since the formation of liquid compartments is dependent on a simple chemical reaction, it is particularly interesting from the protocell perspective.

4.7 Experimental details

4.7.1 Materials and synthesis

Unless specified otherwise, reagents were obtained from Sigma Aldrich. Most of the peptide derivatives studied here (FFssFF, FFsFF, LLssLL, WWssWW and IIssII) were synthesised in solution using Boc/HATU chemistry as described in Chapter 2 and before in [22]. VVssVV was synthesised in the monomeric form on solid phase using cysteamine 2-chlorotrityl resin and standard Fmoc/HATU chemistry and subsequently oxidised with iodine: VVsH was dissolved in water at 10 mg/ml concentration; solution of iodine in MeOH (0.06 M) was added dropwise under rapid stirring until the solution had a slight

yellow colour; excess iodine was quenched with 1 M ascorbic acid and the product was separated by HPLC. Monomers of other derivatives (FFsH, LLsH and WWsH) were obtained by reducing the corresponding dimers with TCEP: 20-30 mg of the dimer was dissolved in water; 85 mg of TCEP was dissolved in 1 ml of water and added to the dimer solution; the mixture was stirred for two hours and the product was separated by HPLC.

4.7.2   Preparation of condensates

Phase separation of the dimers was induced by adding 2 µl of 1 M NaOH solution to 100 µl of 1 mg/ml solution of the dimer (or 5 mg/ml in the case of LLssLL condensates), final pH was around 10 (pH paper). Mixed condensates were prepared by mixing 1 mg/ml stock solutions of corresponding dimers and then adding 2 µl of 1 M NaOH solution to 100 µl of solution. FFssFF aggregates were prepared by adding 2 µl of 1 M NaOH solution to 100 µl of 1 mg/ml solution of FFssFF and incubating in a thermoshaker for 12 h (at 20 °C and 600 rpm). Condensates were imaged in chambered glass slides (Ibidi 18-well µ-slide) using Olympus IX83 inverted microscope with 100x objective.

4.7.3   Reduction experiment

100 µl of suspension of pre-formed FFssFF aggregates was added to a chamber of a glass slide. Aggregates were allowed to sediment onto the glass slide for 5 min. Subsequently, 10 µl of 1 M solution of dithiothreitol (DTT) in water was added. Changes in morphology were followed immediately after adding DTT using Olympus IX83 inverted microscope with 100x objective.

4.7.4   Exchange experiment

For each experiment 50 µl of 2 mg/ml monomer stock solution was mixed with 50 µl of 2 mg/ml dimer stock solution. 2 µl of 1 M NaOH solution was added and the mixture was incubated in a thermoshaker for 12 h (at 20 °C and 600 rpm). The dilute phase was separated from the condensed phase by centrifugation for 30 min at 6700 rcf. The supernatants were carefully removed with a pipette and the condensed phase was dissolved in 30/70 v/v acetonitrile-water mixture with 0.1% TFA v/v. Both the dilute phase and the dissolved condensed phase were analysed using analytical HPLC, performed on a Shimadzu LC-20A system, equipped with a Gemini NX-C18 column (15 cm x 3 mm, 3 µm). A gradient programme was used, 5-100% of phase B in phase A during 30 min (phase A: 100% H2O + 0.1% TFA, phase B: 100% acetonitrile+ 0.1% TFA), flow 0.4 ml/min. Amounts of the monomers and dimers in both phases were determined by comparing the peak area with a reference sample of known concentration, and then by multiplying by the sample volume (it was assumed that the volume of the supernatant equals the initial sample volume and the condensed phase was dissolved in a known volume of acetonitrile-water mixture).

4.8 Contributions and acknowledgements

Work presented in this chapter started as a master's internship project of Stijn Jue. Stijn performed a large part of the synthesis work and the initial characterisation of the products. He also made the initial version of the simulation script.

4.9 Supplementary information

	RT (min)			RT (min)
VVsH	2.5		VVssWW	17.1
VVssVV	13.8		WWsH	17.7
LLsH	14.1		LLssWW	18.2
FFssVV	14.8		FFssFF	18.3
LLssVV	15.6		FFssWW	18.8
FFsH	16.5		WWssWW	19.2
LLssLL	17.0			

Table S4.1: Retention times of monomers and dimers.

Figure S4.1: Chromatograms of exchange reaction mixtures after adding more hydrophobic monomer. Chromatograms of the dilute phase (left panel) and the condensed phase (right panel) for different mixtures after 24 hour-incubation at room temperature. (A) VVssVV (1 mg/ml) + FFsH (1/mg/ml). (B) LLssLL (5 mg/ml) + WWsH (5 mg/ml). (C) FFssFF (1 mg/ml) + WWsH (1 mg/ml). (D) VVssVV (1 mg/ml) + WWsH (1 mg/ml). Monomers and dimers formed upon reaction are highlighted in bold.
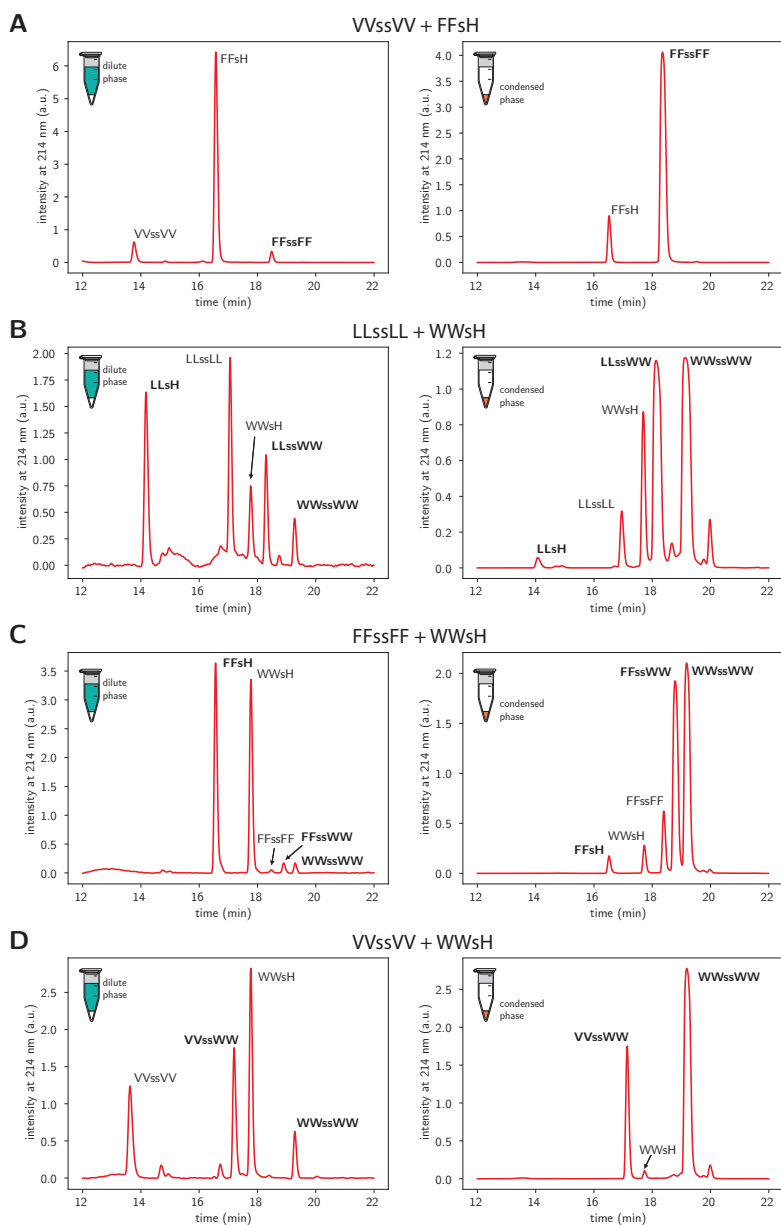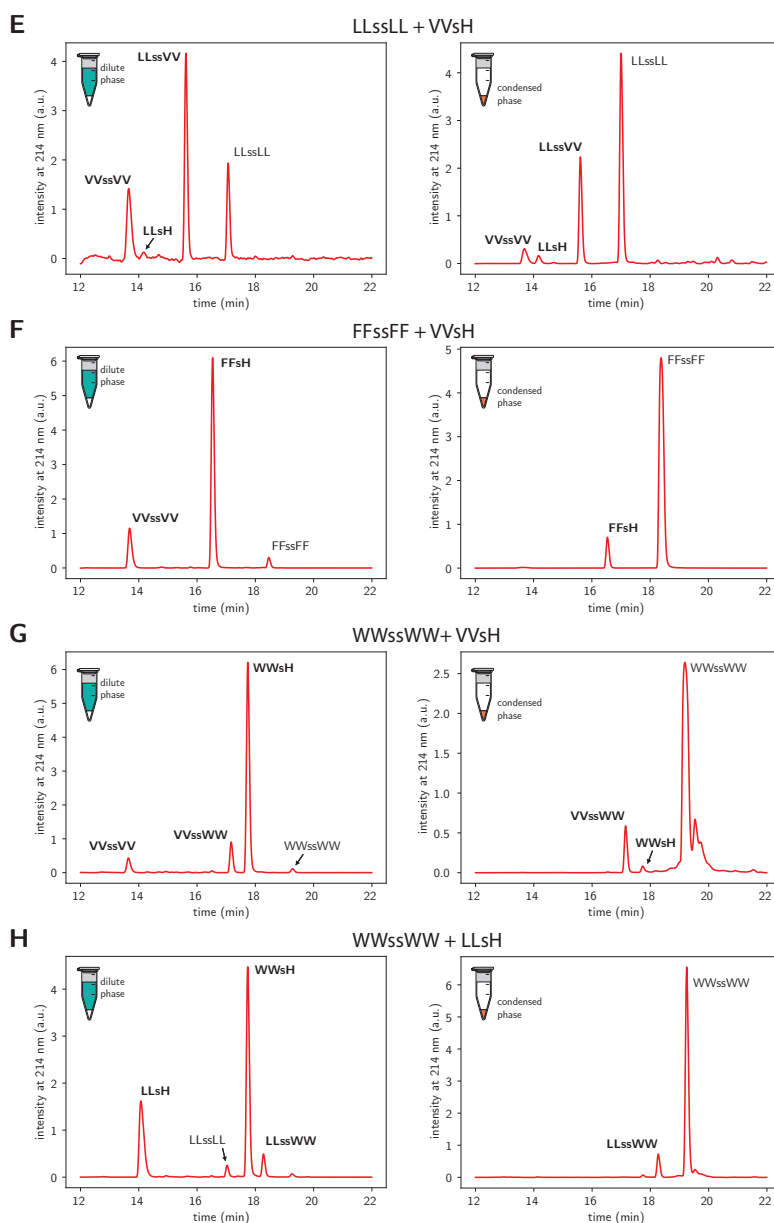
Figure S4.2: Chromatograms of exchange reaction mixtures after adding more hydrophilic monomer. Chromatograms of the dilute phase (left panel) and the condensed phase (right panel) for different mixtures after 24 hour-incubation at room temperature. (E) LLssLL (5 mg/ml) + VVsH (5 mg/ml). (F) FFssFF (1 mg/ml) + VVsH (1 mg/ml). (G) WWssWW (1 mg/ml) + VVsH (1 mg/ml). (H) WWssWW (1 mg/ml) + LLsH (1 mg/ml). Monomers and dimers formed upon reaction are highlighted in bold.

Bibliography

[1] D. M. Mitrea and R. W. Kriwacki, "Phase separation in biology; Functional organization of a higher order Short linear motifs - The unexplored frontier of the eukaryotic proteome," *Cell Commun. Signal.*, vol. 14, no. 1, p. 1, 2016.

[2] E. Gomes and J. Shorter, "The molecular language of membraneless organelles," *J. Biol. Chem.*, vol. 294, no. 18, pp. 7115–7127, 2019.

[3] C. Greening and T. Lithgow, "Formation and function of bacterial organelles," *Nat. Rev. Microbiol.*, vol. 18, no. 12, pp. 677–689, 2020.

[4] C. A. Azaldegui, A. G. Vecchiarelli, and J. S. Biteen, "The emergence of phase separation as an organizing principle in bacteria," *Biophys. J.*, vol. 120, no. 7, pp. 1123–1138, 2021.

[5] K. K. Nakashima, M. A. Vibhute, and E. Spruijt, "Biomolecular chemistry in liquid phase separated compartments," *Front. Mol. Biosci.*, vol. 6, p. 21, 2019.

[6] A. A. Hyman, C. A. Weber, and F. Jülicher, "Liquid-liquid phase separation in biology," *Annu. Rev. Cell Dev. Biol.*, vol. 30, no. 1, pp. 39–58, 2014.

[7] S. Alberti and S. Carra, "Quality Control of Membraneless Organelles," *J. Mol. Biol.*, vol. 430, no. 23, pp. 4711–4729, 2018.

[8] E. Boke, M. Ruer, M. Wühr, M. Coughlin, R. Lemaitre, S. P. Gygi, S. Alberti, D. Drechsel, A. A. Hyman, and T. J. Mitchison, "Amyloid-like Self-Assembly of a Cellular Compartment," *Cell*, vol. 166, no. 3, pp. 637–650, 2016.

[9] A. Patel, H. O. Lee, L. Jawerth, S. Maharana, M. Jahnel, M. Y. Hein, S. Stoynov, J. Mahamid, S. Saha, T. M. Franzmann, A. Pozniakovski, I. Poser, N. Maghelli, L. A. Royer, M. Weigert, E. W. Myers, S. Grill, D. Drechsel, A. A. Hyman, and S. Alberti, "A Liquid-to-Solid Phase Transition of the ALS Protein FUS Accelerated by Disease Mutation," *Cell*, vol. 162, no. 5, pp. 1066–1077, 2015.

[10] S. Wegmann, B. Eftekharzadeh, K. Tepper, K. M. Zoltowska, R. E. Bennett, S. Dujardin, P. R. Laskowski, D. MacKenzie, T. Kamath, C. Commins, C. Vanderburg, A. D. Roe, Z. Fan, A. M. Molliex, A. Hernandez-Vega, D. Muller, A. A. Hyman, E. Mandelkow, J. P. Taylor, and B. T. Hyman, "Tau protein liquid–liquid phase separation can initiate tau aggregation," *EMBO J.*, vol. 37, no. 7, p. e98049, 2018.

[11] A. Molliex, J. Temirov, J. Lee, M. Coughlin, A. P. Kanagaraj, H. J. Kim, T. Mittag, and J. P. Taylor, "Phase Separation by Low Complexity Domains Promotes Stress Granule Assembly and Drives Pathological Fibrillization," *Cell*, vol. 163, no. 1, pp. 123–133, 2015.

[12] W. M. Aumiller and C. D. Keating, "Phosphorylation-mediated RNA/peptide complex coacervation as a model for intracellular liquid organelles," *Nat. Chem.*, vol. 8, no. 2, pp. 129–137, 2016.

[13] T. Ukmar-Godec, S. Hutten, M. P. Grieshop, N. Rezaei-Ghaleh, M. S. Cima-Omori, J. Biernat, E. Mandelkow, J. Söding, D. Dormann, and M. Zweckstetter, "Lysine/RNA-interactions drive and regulate biomolecular condensation," *Nat. Commun.*, vol. 10, no. 1, p. 2909, 2019.

[14] I. Alshareedah, M. M. Moosa, M. Raju, D. A. Potoyan, and P. R. Banerjee, "Phase transition of RNA-protein complexes into ordered hollow condensates," *Proc. Natl. Acad. Sci. U. S. A.*, vol. 117, no. 27, pp. 15650–15658, 2020.

[15] S. L. Perry, L. Leon, K. Q. Hoffmann, M. J. Kade, D. Priftis, K. A. Black, D. Wong, R. A. Klein, C. F. Pierce, K. O. Margossian, J. K. Whitmer, J. Qin, J. J. De Pablo, and M. Tirrell, "Chirality-selected phase behaviour in ionic polypeptide complexes," *Nat. Commun.*, vol. 6, no. 1, p. 6052, 2015.

[16] S. Koga, D. S. Williams, A. W. Perriman, and S. Mann, "Peptide-nucleotide microdroplets as a step towards a membrane-free protocell model," *Nat. Chem.*, vol. 3, no. 9, pp. 720–724, 2011.

[17] K. K. Nakashima, J. F. Baaij, and E. Spruijt, "Reversible generation of coacervate droplets in an enzymatic network," *Soft Matter*, vol. 14, no. 3, pp. 361–367, 2018.

[18] I. B. A. Smokers, M. H. I. van Haren, T. Lu, and E. Spruijt, "Complex Coacervation and Compartmentalized Conversion of Prebiotically Relevant Metabolites," *ChemSystemsChem*, vol. 4, no. 4, 2022.

[19] M. Abbas, W. P. Lipiński, J. Wang, and E. Spruijt, "Peptide-based coacervates as biomimetic protocells," *Chem. Soc. Rev.*, vol. 50, no. 6, pp. 3690–3705, 2021.

[20] C. Yuan, A. Levin, W. Chen, R. Xing, Q. Zou, T. W. Herling, P. K. Challa, T. P. Knowles, and X. Yan, "Nucleation and Growth of Amino Acid and Peptide Supramolecular Polymers through Liquid–Liquid Phase Separation," *Angew. Chemie - Int. Ed.*, vol. 58, no. 50, pp. 18116–18123, 2019.

[21] Y. Tang, S. Bera, Y. Yao, J. Zeng, Z. Lao, X. Dong, E. Gazit, and G. Wei, "Prediction and characterization of liquid-liquid phase separation of minimalistic peptides," *Cell Reports Phys. Sci.*, vol. 2, no. 9, p. 100579, 2021.

[22] M. Abbas, W. P. Lipiński, K. K. Nakashima, W. T. Huck, and E. Spruijt, "A short peptide synthon for liquid–liquid phase separation," *Nat. Chem.*, vol. 13, no. 11, pp. 1046–1054, 2021.

[23] S. Chowdhuri, S. Das, R. Kushwaha, T. Das, B. K. Das, and D. Das, "Cumulative Effect of pH and Redox Triggers on Highly Adaptive Transient Coacervates," *Chem. - A Eur. J.*, vol. 29, no. 24, 2023.

[24] S. M. Morrow, I. Colomer, and S. P. Fletcher, "A chemically fuelled self-replicator," *Nat. Commun.*, vol. 10, no. 1, p. 1011, 2019.

[25] M. Colomb-Delsuc, E. Mattia, J. W. Sadownik, and S. Otto, "Exponential self-replication enabled through a fibre elongation/breakage mechanism," *Nat. Commun.*, vol. 6, no. 1, p. 7427, 2015.

[26] B. Liu, J. Wu, M. Geerts, O. Markovitch, C. G. Pappas, K. Liu, and S. Otto, "Out-of-Equilibrium Self-Replication Allows Selection for Dynamic Kinetic Stability in a System of Competing Replicators," *Angew. Chemie - Int. Ed.*, vol. 61, no. 18, 2022.

[27] W. P. Lipiński, J. Zehnder, M. Abbas, P. Güntert, E. Spruijt, and T. Wiegand, "Fibrils Emerging from Droplets: Molecular Guiding Principles behind Phase Transitions of a Short Peptide-Based Condensate Studied by Solid-State NMR," *Chem. - A Eur. J.*, vol. 29, no. 50, 2023.

5

Modelling protein aggregation in a two-phase system

5.1 Presence of liquid condensates affects aggregation kinetics

One of the most notable features that distinguish the complex intracellular environment from the protein solutions often used in vitro is the presence of condensates formed by liquid-liquid phase separation (LLPS) of biomolecules into so-called membraneless organelles (MLOs)[1–4]. These compartments are usually liquid-like, highly concentrated droplets of proteins and nucleic acids. Examples of such organelles include nucleoli[5] and Cajal bodies[6] in the nucleus, and stress granules in the cytoplasm[7]. The main difference between MLOs and membrane-bound compartments is the lack of a physical barrier between the organelle and the surrounding solution. This results in the ability to exchange components with the environment, to undergo fusion and to respond to the environmental changes by rapid formation/dissolution[8].

Knowing that MLOs contain proteins at very high concentrations and that proteins that undergo LLPS and proteins that partition into liquid droplets often feature low-complexity domains[2,9], a characteristic that is also common for amyloidogenic proteins, it becomes evident that the presence of biological condensates could drastically affect protein aggregation. For various phase-separating proteins, it has been suggested that prior condensation into liquid droplets can promote conformational changes within the disordered region, leading to the formation of gel-like structures or amyloid-like aggregates. Such a process has been observed, for instance, for hnRNPA1[7], FUS[10] or Tau[11,12]. Recently, it has been shown that also α-synuclein (αSyn), one of the archetypical amyloid-forming proteins, can undergo LLPS under PEG-based crowded conditions and that the condensed αSyn droplets may facilitate aggregation[13–16]. However, it remains unclear whether LLPS of αSyn is also likely to happen in living cells, as αSyn is known to interact with many components inside the cell, including membranes, the cytoskeleton and other proteins[17,18], which may suppress the concentration of free αSyn and prevent the formation of homotypic αSyn condensates.

Nonetheless, there is also another, more general way by which LLPS can affect protein aggregation, which is also relevant for proteins that are present in cells at low concentrations. Condensates can concentrate guest biomolecules, including amyloidogenic proteins, by partitioning or interfacial adsorption, and provide a distinct chemical environment in which the stability and reactivity of biomolecules may be affected. This can alter the kinetics of protein aggregation in multiple ways[2,19,20]. An enhanced local concentration of amyloidogenic proteins may result in the acceleration of the aggregation process, according to the law of mass action[21]. However, one has to take into account that the local environment of the condensed liquid may promote protein conformations that do not undergo aggregation as readily as ones dominating in the surrounding solution. This has been observed for amyloid-β(1-42)[22] and may occur also for other amyloidogenic proteins. Last, aggregating proteins could accumulate at the interface between condensate and the surrounding cytosol, potentially resulting in alternative, interfacial aggregation pathways, analogous to what has been observed for lipid vesicles and solid surfaces[23]. In general, the accumulation of amyloidogenic proteins at an interface can alter the kinetics of aggregation in two ways: an increased local concentration leads to faster aggregation,

and an altered conformation of molecules bound to the interface can either stabilize free monomers or promote their transformation into fibrils.

Accumulation of αSyn at the interface has been reported to accelerate aggregation, e.g. for exosomes and small unilamellar vesicles (SUVs)[24]. By contrast, aggregation was slowed down when SUVs were present in large excess over αSyn and most protein monomers were trapped in a stable configuration at the surface of SUVs and there was no free monomeric αSyn in solution[25]. Similar effects have been observed for SUVs and large unilamellar vesicles (LUVs) composed of mixtures of anionic, cationic and neutral lipids[26]. The effect of lipid membranes on αSyn is largely dependent not only on the lipid/protein ratio, but also on the chemical structure of lipid, mutations in the protein chain and probably also on the size (and thus the curvature) of the vesicles or surface defects associated with curvature[27]. It has been suggested that the presence of membranes can even induce fibril dissociation, by stabilising monomers and depleting the solution of free protein[28].

While there is ample evidence that biomolecular condensates can fundamentally alter protein distributions in vitro and in living cells by concentration, exclusion or interfacial localisation, a systematic investigation of the effects that pre-existing condensates have on protein aggregation is lacking. In this chapter, we computationally study the potential influence of liquid condensates on protein aggregation kinetics. We use models based on ordinary differential equations (ODEs) and on Gillespie's stochastic simulation algorithm (SSA) to simulate the effect of liquid condensates on the aggregation kinetics and on the distribution of aggregation times and fibril lengths. Similarly to the previous studies[21], we find that even low partition coefficient can result in accelerated aggregation and accumulation of fibrils inside liquid condensates, but we also look at the influence of condensates in a broader sense, showing that accumulation at their interface can also substantially affect the aggregation kinetics, and that partitioning of aggregating protein can affect the distribution of the aggregation times and of fibril lengths when aggregation is treated as a stochastic process.

5.2   Basic aggregation model

Typically for many amyloidogenic proteins, the aggregation process of αSyn may be considered an autocatalytic process. Our simple yet accurate model of αSyn aggregation is based on the secondary nucleation model proposed by Ferrone et al.[29] and involves 3 basic reactions: (i) primary nucleation of fibrils from αSyn monomers, (ii) elongation of fibrils by attaching monomers to one of the fibril ends, (iii) secondary nucleation catalysed by fibrils:

$$r_{\text{primary nucleation}} = k_n \, [S]^n \tag{5.1a}$$

$$r_{\text{elongation}} = 2k_+ \, [S] \, [P] \tag{5.1b}$$

$$r_{\text{secondary nucleation}} = k_2 \, [S]^{n_2} \, [M] \tag{5.1c}$$

where: k_n, k_+, k_2 are the reaction rate constants of the corresponding reactions, n and n_2 are the nucleation numbers of primary and secondary nucleation (the lowest number

of oligomers required to form a fibril nucleus), and $[S]$, $[P]$ and $[M]$ are the concentration of monomers, concentration of fibrils (so $2[P]$ reflects the concentration of fibril ends) and concentration of monomeric units incorporated in fibrils (proportional to fibril mass concentration and the surface available for secondary nucleation catalysis). Figure 5.1 shows a schematic representation of these reactions.
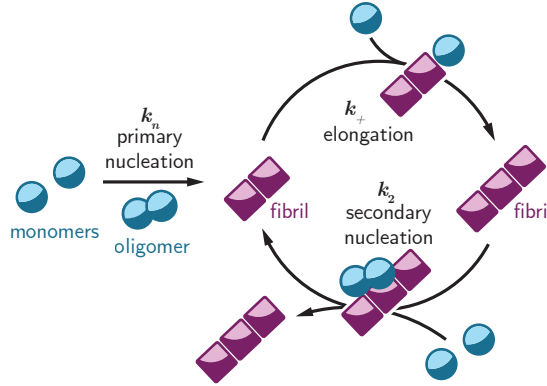

Figure 5.1: Scheme of the basic (primary nucleation/elongation/secondary nucleation) aggregation model.

From this a set of differential equations describing concentration changes in the system can be derived:

$$\frac{d[S]}{dt} = -nk_n[S]^n - 2k_+[S][P] - n_2k_2[S]^{n_2}[M] \tag{5.2a}$$

$$\frac{d[P]}{dt} = k_n[S]^n + k_2[S]^{n_2}[M] \tag{5.2b}$$

$$\frac{d[M]}{dt} = nk_n[S]^n + 2k_+[S][P] + n_2k_2[S]^{n_2}[M] \tag{5.2c}$$

Solving this set of equations provides a kinetic trace of the aggregation process Figure 5.2A. Fitting the solution to the experimentally measured concentration of one of the species provides information about the protein aggregation rates. The ratio of the nucleation and elongation rates determines not only the shape of the aggregation curve (concentration of protein in the fibril form $[M]$, Figure 5.2B), but also the number (concentration) of fibrils formed ($[P]$), thus also their final length (Figure 5.2C).

To ease the quantitative comparison of the aggregation kinetics we use parameters that can be determined from both simulated and experimental results: lag time, (t_{lag}, which is predominantly determined by the primary nucleation rate), and the maximum slope of the aggregation curves (v_{max}, which is mostly determined by the elongation and secondary nucleation rate). The lag time is in our case determined as the intersection of the line going through the max slope point and the baseline (x-axis in case of simulations).
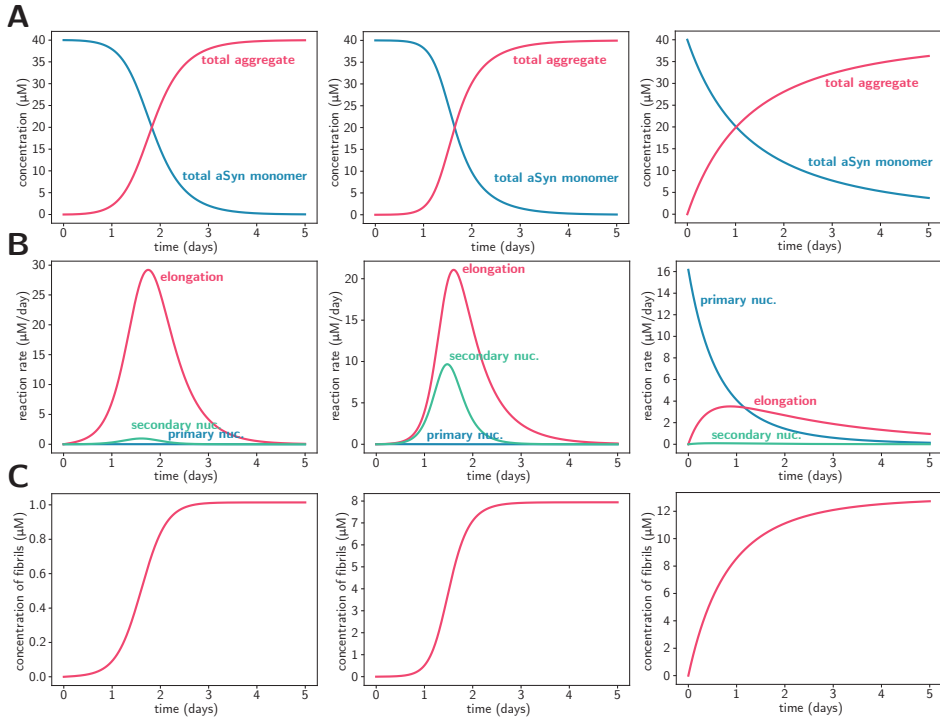
Figure 5.2: Aggregation traces simulated for the simple model for 3 different regimes: left column - elongation-dominated aggregation (parameters: $k_n = 10^{-5}$ µM^{-1}day^{-1}, $k_+ = 1$ µM^{-1}day^{-1}, $k_2 = 10^{-4}$ µM^{-2}day^{-1}, $[S]_0 = 40$ µM, $n = 2$, $n_2 = 2$); middle column - elongation/secondary nucleation-dominated aggregation (parameters: $k_n = 10^{-5}$ µM^{-1}day^{-1}, $k_+ = 0.1$ µM^{-1}day^{-1}, $k_2 = 10^{-3}$ µM^{-2}day^{-1}, $[S]_0 = 40$ µM, $n = 2$, $n_2 = 2$); right column - primary nucleation-dominated aggregation (parameters: $k_n = 0.01$ µM^{-1}day^{-1}, $k_+ = 0.01$ µM^{-1}day^{-1}, $k_2 = 10^{-5}$ µM^{-2}day^{-1}, $[S]_0 = 40$ µM, $n = 2$, $n_2 = 2$). (A) Concentration of monomeric ($[S]$) and fibril-bound ($[M]$) protein over time. (B) Reaction rates for primary nucleation, elongation and secondary nucleation reactions over time. (C) Concentration of fibrils $[P]$ over time.

5.3 ODE model of aggregation inside condensates

In the case of partitioning into the coacervate droplets, the concentrations of monomer in the dilute and in the condensed phase is determined by the partition coefficient:

$$K_{\mathrm{P}} = \frac{[S]_{\mathrm{cond}}}{[S]_{\mathrm{dil}}} \tag{5.3}$$

where K_{P} is the partition coefficient and $[S]_{\mathrm{cond}}$ and $[S]_{\mathrm{dil}}$ are the concentrations of the monomer in the condensed and the dilute phase respectively. Taking into account the equation describing the mass balance of monomers in the system:

$$[S]_{\text{tot}} = [S]_{\text{dil}} \frac{R}{1+R} + [S]_{\text{cond}} \frac{1}{1+R} \tag{5.4}$$

where R is the ratio of the dilute phase volume to the condensed phase volume, we can write equations describing the concentrations of the monomers in the dilute and in the condensed phase:

$$[S]_{\text{dil}} = \frac{1+R}{R+K_{\text{P}}} [S]_{\text{tot}} = \xi [S]_{\text{tot}} \tag{5.5a}$$

$$[S]_{\text{cond}} = K_{\text{P}} \frac{1+R}{R+K_{\text{P}}} [S]_{\text{tot}} = K_{\text{P}} \xi [S]_{\text{tot}} \tag{5.5b}$$

$$\xi = \frac{1+R}{R+K_{\text{P}}} \tag{5.5c}$$

We assume the transport/partitioning process to be much faster than aggregation and to simplify the kinetic equations we assume further that the partitioning remains at equilibrium at every timepoint of the aggregation reaction. This leads to a set of differential equations describing the aggregation process in the coacervate system with monomer partitioning:

$$\begin{aligned}
\frac{d[S]_{\text{tot}}}{dt} &= \left(\frac{R}{1+R} \right) \left[-nk_n \left(\xi [S]_{\text{tot}} \right)^n - 2k_+ \xi [S]_{\text{tot}} [P]_{\text{dil}} - \right.\\
&\quad \left. -n_2 k_2 \left(\xi [S]_{\text{tot}} \right)^{n_2} [M]_{\text{dil}} \right] +\\
&\quad + \left(\frac{1}{1+R} \right) \left[-nk_{n_{\text{cond}}} \left(K_{\text{P}} \xi [S]_{\text{tot}} \right)^n - 2k_{+_{\text{cond}}} K_{\text{P}} \xi [S]_{\text{tot}} [P]_{\text{cond}} + \right.\\
&\quad \left. -n_2 k_{2_{\text{cond}}} \left(K_{\text{P}} \xi [S]_{\text{tot}} \right)^{n_2} [M]_{\text{cond}} \right]
\end{aligned} \tag{5.6a}$$

$$\frac{d[P]_{\text{dil}}}{dt} = k_n \left(\xi [S]_{\text{tot}} \right)^n + k_2 \left(\xi [S]_{\text{tot}} \right)^{n_2} [M]_{\text{dil}} \tag{5.6b}$$

$$\frac{d[M]_{\text{dil}}}{dt} = nk_n \left(\xi [S]_{\text{tot}} \right)^n + 2k_+ \xi [S]_{\text{tot}} [P]_{\text{dil}} + n_2 k_2 \left(\xi [S]_{\text{tot}} \right)^{n_2} [M]_{\text{dil}} \tag{5.6c}$$

$$\frac{d[P]_{\text{cond}}}{dt} = k_{n_{\text{cond}}} \left(K_{\text{P}} \xi [S]_{\text{tot}} \right)^n + k_{2_{\text{cond}}} \left(K_{\text{P}} \xi [S]_{\text{tot}} \right)^{n_2} [M]_{\text{cond}} \tag{5.6d}$$

$$\begin{aligned}
\frac{d[M]_{\text{cond}}}{dt} &= nk_{n_{\text{cond}}} \left(K_{\text{P}} \xi [S]_{\text{tot}} \right)^n + 2k_{+_{\text{cond}}} K_{\text{P}} \xi [S]_{\text{tot}} [P]_{\text{cond}}\\
&\quad + n_2 k_{2_{\text{cond}}} \left(K_{\text{P}} \xi [S]_{\text{tot}} \right)^{n_2} [M]_{\text{cond}}
\end{aligned} \tag{5.6e}$$

Again, similarly to the simpler case of aggregation in a homogeneous solution, solving the equations yields aggregation kinetic trace for both the dilute and the condensed phase. The proposed model is similar to the model previously described by Weber et al. [21], with the following main differences: we allow for different rate constants in the condensed and dilute phase, and we assume that the exchange of material between the droplet and the solution is infinitely fast. A schematic representation of the described model is presented in Figure 5.3.
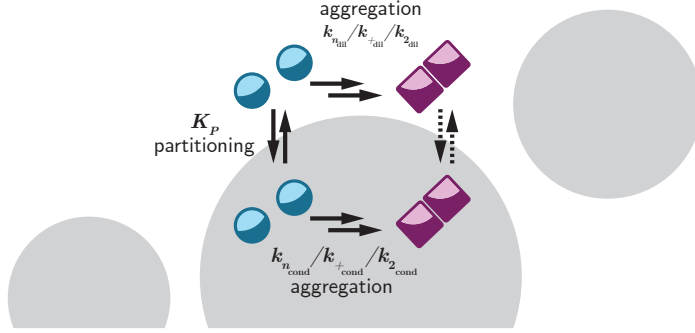
Figure 5.3: Scheme of the aggregation model with partitioning.

5.3.1 Influence of the partition coefficient and condensate size

Weber et al. have already shown that the presence of liquid compartments that accumulate monomers of the aggregating protein can substantially affect the aggregation kinetics[21]. The analytical solution derived there has the advantage over the modelling solution presented in this chapter in that it allows to follow trends related to the condensate size and partition coefficient. Therefore, we will only present some major findings and focus on other parameters later.
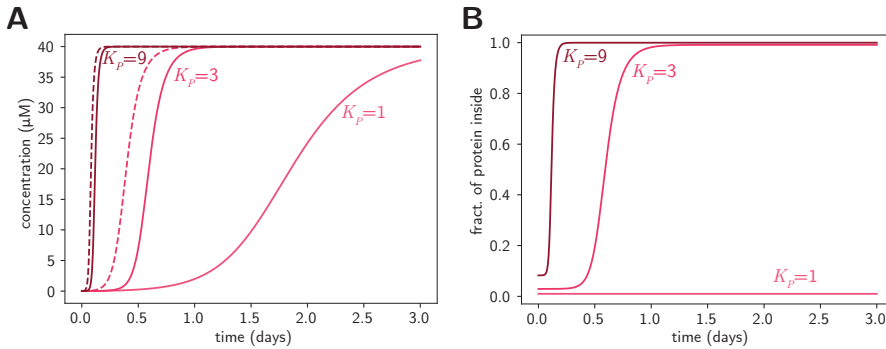

Figure 5.4: Aggregation traces simulated for partitioning model for 3 different partition coefficients (other parameters: $k_n = 10^{-5}$ µM^{-1}day^{-1}, $k_+ = 1$ µM^{-1}day^{-1}, $k_2 = 10^{-4}$ µM^{-2}day^{-1}, $[S]_0 = 40$ µM, $n = 2$, $n_2 = 2$, $R = 100$). (A) Concentration of monomeric ($[S]_{\text{tot}}$) and fibril-bound ($[M]_{\text{tot}}$) protein over time. Dashed lines in the middle and right column represent traces for a homogeneous system with K_{P}-times higher concentration, normalised by K_{P}. (B) Fraction of total protein amount in the condensed phase.

As shown in Figure 5.4 even low partition coefficients can substantially influence the aggregation kinetics and the spatial distribution of aggregates. This is because of the positive feedback loop effect - when monomers inside the condensate get depleted due to

the aggregation process, they are immediately replenished by monomers transported from the surrounding solution. Potentially this effect can be reduced by decreasing the transport rates, we assumed that the monomer transport rate is much faster than the aggregation rates and that the transport is instant. The effect on the aggregation kinetics is lower than the effect of increasing concentration of monomers K_P-times in a homogeneous system (Figure 5.4A) - this is because of two reasons: (i) unless the compartment is infinitely small ($R \to \infty$), the concentration inside is never reaching $K_P[S]_{tot}$ (as shown in Equation 5.5); (ii) even if aggregation reactions reach rates almost as high as in the homogeneous system with K_P-times higher concentrations, they occur in a small fraction of the total volume ($\frac{1}{1+R}$).
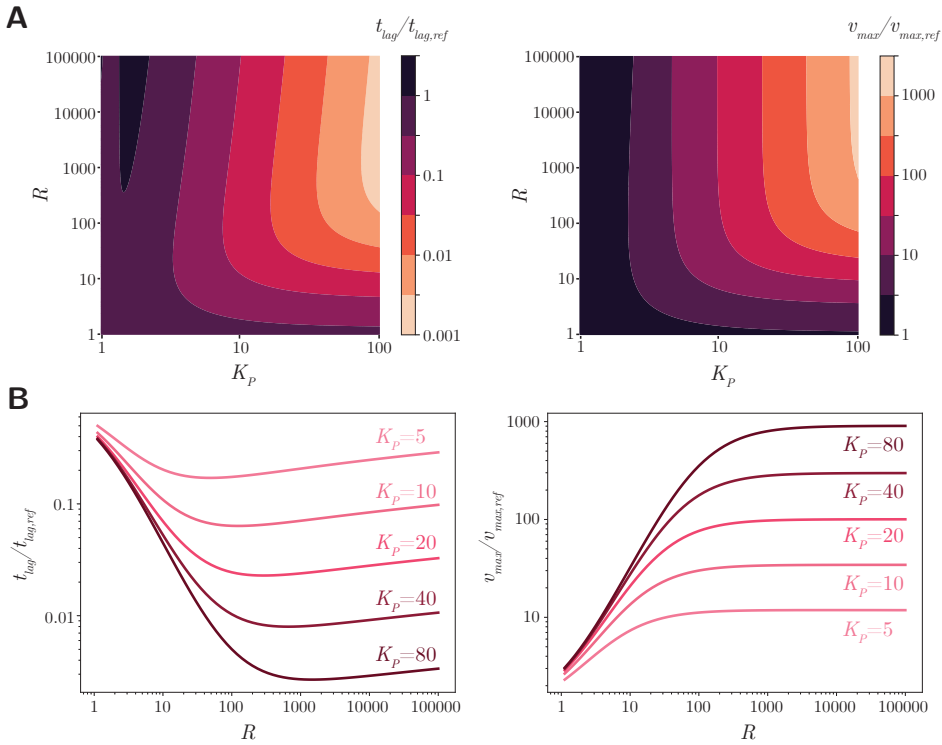

Figure 5.5: Aggregation parameters simulated for a range of condensate sizes and partition coefficients. (A) Contour maps of relative (normalised by values for the homogeneous system with the same aggregation kinetic rate constants) t_{lag} and v_{max} for a range of R and K_P (other parameters: $k_n = 10^{-5}$ µM^{-1}day^{-1}, $k_+ = 1$ µM^{-1}day^{-1}, $k_2 = 10^{-4}$ µM^{-2}day^{-1}, $[S]_0 = 40$ µM, $n = 2$, $n_2 = 2$). (B) Relative t_{lag} and v_{max} in the function of R for fixed K_P values, other parameters as in (A).

Increasing K_P in a system where aggregation rate constants and protein activity inside and outside the condensate are the same, will always accelerate the aggregation reaction. Changing the relative volume of the condensed phase does not result in an obvious trend

in the aggregation kinetics, as increasing the volume increases the volume in which the reaction happens faster, but at the same time decreases the concentration (Equation 5.5) in the condensed phase. Figure 5.5 shows the influence of changing R on the aggregation traces and the t_{lag} and v_{max} for different R and K_{P} combinations. As can be seen in Figure 5.5B, shortest t_{lag} and highest v_{max} are obtained for different R values, indicating that changing volume has a different effect on the nucleation and elongation kinetics.

5.3.2 Introducing varied activity inside condensates

So far, we have assumed that the activity of monomers and fibrils is proportional to the concentration. This is true for dilute aqueous solutions, but can be different when moving to the condensed phase. It can be expected that the crowded, viscous and more hydrophobic environment of the condensate influences the kinetics of aggregation. These properties affect the diffusion and conformation of protein molecules. For a more detailed study of the influence of crowding and viscosity on the aggregation kinetics, we refer to the previous work [30–33]. Since the overall influence of the coacervate environment on the aggregation kinetics is very complex, here we look only at the effect of altered monomer and fibril activity inside the condensates and in the following section we discuss some basic relations between viscosity and reaction kinetics.

In Equation 5.6 we presented a set of equations for the partitioning model that assumes that activity inside condensates and in the dilute solution is identical and proportional to the concentration. In this subsection we look at the system where the activity of all re-agents in the dilute phase and in the condensed phase is proportional to the concentration but with a proportionality coefficient (activity coefficient, γ) different from 1. For simplicity, we considered only the situation where all reactants have the same activity coefficient in the condensed phase, but a situation with a different activity coefficient for every re-actant could also be considered. In general, the activity factor-dependent reaction rates can be described by the following equations:

$$r_{\mathrm{primary\ nucleation}} = k_n \left(\gamma\left[S\right]\right)^n \tag{5.7a}$$

$$r_{\mathrm{elongation}} = 2k_+ \gamma\left[S\right] \gamma\left[P\right] \tag{5.7b}$$

$$r_{\mathrm{secondary\ nucleation}} = k_2 \left(\gamma\left[S\right]\right)^{n_2} \gamma\left[M\right] \tag{5.7c}$$

We assume that the activity factor in the dilute phase equals 1 and the activity factor γ is only used to describe the activity in the condensed phase, e.g. the differential equation for the monomer concentration change, presented for the general partitioning model in Equation 5.6 can be described including the activity factors in the condensed phase as following:

$$\frac{d\,[S]_{\text{tot}}}{dt} = \left(\frac{R}{1+R}\right)\left[-nk_n\left(\xi\,[S]_{\text{tot}}\right)^n - 2k_+\xi\,[S]_{\text{tot}}\,[P]_{\text{dil}} - n_2k_2\left(\xi\,[S]_{\text{tot}}\right)^{n_2}[M]_{\text{dil}}\right] +$$

$$+ \left(\frac{1}{1+R}\right)\left[-nk_{n_{\text{cond}}}\left(\gamma K_{\text{P}}\xi\,[S]_{\text{tot}}\right)^n - 2k_{+_{\text{cond}}}\gamma K_{\text{P}}\xi\,[S]_{\text{tot}}\,\gamma\,[P]_{\text{cond}} +$$

$$-n_2k_{2_{\text{cond}}}\left(\gamma K_{\text{P}}\xi\,[S]_{\text{tot}}\right)^{n_2}\gamma\,[M]_{\text{cond}}\right]$$

$$(5.8)$$

We simulated the aggregation reaction for a range of activity factors and a range of partition coefficients. The results show that low activity factors can reduce the accelerating propensity of condensates and, in the situation of high partition coefficient and low activity factor, condensates can even reduce the aggregation rates, due to the sequestration of monomers (Figure 5.6).
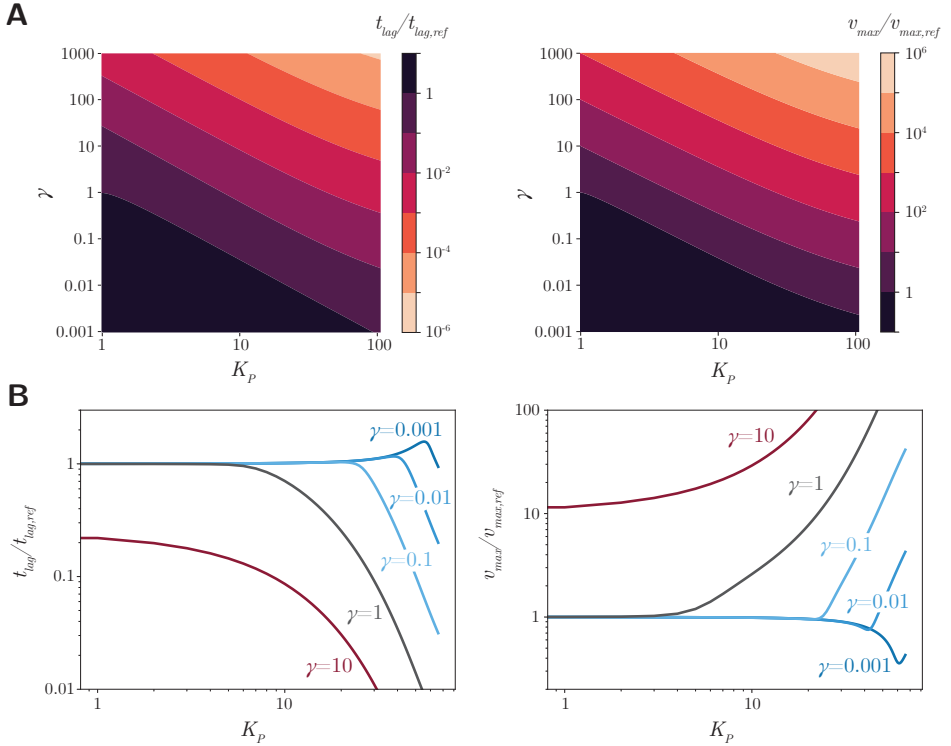

Figure 5.6: Aggregation parameters simulated for a range of activity factors and partition coefficients. (A) Contour maps of relative (normalised by values for the homogeneous system with the same aggregation kinetic rate constants) t_{lag} and v_{max} for a range of γ and K_{P} (other parameters: $k_n = 10^{-5}$ µM^{-1}day^{-1}, $k_+ = 1$ µM^{-1}day^{-1}, $k_2 = 10^{-4}$ µM^{-2}day^{-1}, $[S]_0 = 40$ µM, $n = 2$, $n_2 = 2$, $R = 100$). (B) Relative t_{lag} and v_{max} in the function of K_{P} for fixed γ values, other parameters as in (A).

5.3.3 Different reaction rate constants in the condensed phase

While the activity factor is a very simplistic method of modelling varied conformation or interactions with condensate material that can limit the availability of the reactive species, varying the reaction rate constants allows for modelling altered viscosity or activation energy barrier inside the condensate phase. To model the diffusion dependence of the reaction rate constants we could use the simplified relation:

$$k = \frac{k_D k_r}{k_D + k_r} \tag{5.9}$$

where k is the effective/observed reaction rate constant, k_D is the diffusion-limited rate constant and k_r is the inherent reaction rate constant. In the limit of the k_D to k_r ratio being infinitely large (fast diffusion, slow activation), the effective constant becomes equal to k_r (the reaction is purely activation-controlled). In the limit of the k_r to k_D ratio being infinitely large (fast activation, slow diffusion), the effective constant becomes equal to k_D (the reaction is purely diffusion-controlled).

The value of k_D can be estimated, given the viscosity of the solvent (η):

$$k_D = \frac{8RT}{3\eta} \tag{5.10}$$

In the case of water $\eta = 8.9 \cdot 10^{-3}$ Pa·s and $k_D = 7.42 \cdot 10^9$ 1/(M·s) at 25 °C. To observe differences in the effective kinetic rate constant with increasing viscosity, the value of the effective reaction rate constant should be comparable to k_D. Values reported in literature for the elongation reaction (the fastest reaction in the system) are typically within 10^2 to 10^6 1/(M·s) range [30], which means that the influence of limited diffusion could be only observed for fast elongating aggregation processes and extremely high viscosity values. This is not completely improbable, since the viscosity of the coacervate phase can presumably reach values 10^5 times higher than the value of water [34–36], but the effect would be observed only for extreme situations, therefore we will not discuss it further here.

It is also possible that the coacervate environment affects the activation barrier of the reaction, thus changing the k_r counterpart. It is difficult to predict a priori the influence of the coacervate environment on the activation energy. Therefore in Chapter 6, we use experimental data to fit the aggregation traces in the condensed and the dilute and thereby determine the effective k values for each of the aggregation reactions.

5.4   ODE model of aggregation at the interface

Another model was developed for a case where aggregation-prone protein accumulates in the coacervate-dilute phase interface (Figure 5.7). Binding of monomers to the coacervate interface can be described by the equation:

$$K_{\mathrm{B}} = \frac{[S]_{\mathrm{int}}}{[S]_{\mathrm{dil}} [I]} \tag{5.11}$$

where K_{B} is the binding constant, $[S]_{\mathrm{int}}$ is the concentration of interface-bound monomers and $[I]$ is the concentration of available binding sites ($[I] = [I]_{\mathrm{tot}} - [S]_{\mathrm{int}}$).

Again, taking into account the mass balance equation for monomers, we can write equations describing the concentration of free and surface-bound monomers. Since the aggregation reaction occurs now only in the dilute phase (or in the interface, which is treated as a part of the dilute phase), we can omit the change of volume:

$$[S]_{\text{dil}} = \frac{-1 - K_{\text{B}} [I]_{\text{tot}} + [S]_{\text{tot}} K_{\text{B}} + \sqrt{[1 + K_{\text{B}} ([I]_{\text{tot}} - [S]_{\text{tot}})]^2 + 4K_{\text{B}} [S]_{\text{tot}}}}{2K_{\text{B}}}$$

(5.12a)

$$[S]_{\text{int}} = \frac{K_{\text{B}} [I]_{\text{tot}} [S]_{\text{dil}}}{1 + K_{\text{B}} [S]_{\text{dil}}}$$
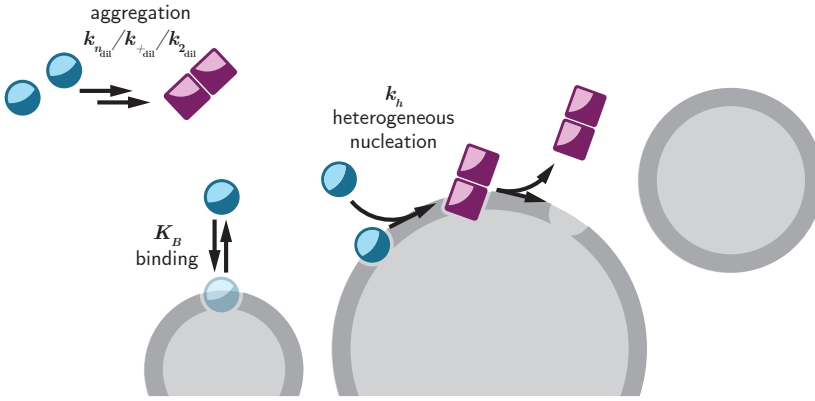
(5.12b)

Figure 5.7: Scheme of the aggregation model with heterogeneous nucleation at the interface and fibril detachment.

We assume that the surface can act as a nucleation site, requiring one monomer from the surface and one monomer from the solution to react. We further assume that the fibrils formed at the interface detach from the condensate and move to the dilute phase. This system can be described by the following set of equations:

$$\frac{d [S]_{\text{tot}}}{dt} = -nk_n [S]_{\text{dil}}^n - 2k_+ [S]_{\text{dil}} [P] - n_2 k_2 [S]_{\text{dil}}^{n_2} [M] - 2k_{\text{h}} [S]_{\text{dil}} [S]_{\text{int}}$$

(5.13a)

$$\frac{d [P]}{dt} = k_n [S]_{\text{dil}}^n + k_2 [S]_{\text{dil}}^{n_2} [M] + k_{\text{h}} [S]_{\text{dil}} [S]_{\text{int}}$$

(5.13b)

$$\frac{d [M]}{dt} = nk_n [S]_{\text{dil}}^n + 2k_+ [S]_{\text{dil}} [P] + n_2 k_2 [S]_{\text{dil}}^{n_2} [M] + 2k_{\text{h}} [S]_{\text{dil}} [S]_{\text{int}}$$

(5.13c)

where k_h is the reaction rate constant of the interface-catalysed nucleation and, for clarity, $[S]_{\text{dil}}$ and $[S]_{\text{int}}$ symbols were used instead of full equations dependent on $[S]_{\text{tot}}$.

5.4.1   Aggregation at the interface under saturation and no-saturation regimes

To illustrate the influence of the interfaces on the aggregation kinetics we simulated the aggregation process under 2 regimes: (i) saturation regime, in which protein fully or almost fully occupies the binding sites at the interface; (ii) no-saturation regime, in which surface is not completely covered by the aggregating monomers. In the first regime, assuming that the heterogeneous nucleation reaction is dominating, the aggregation rate shows stronger dependence on the amount of binding sites (so on the amount of available interface), and less pronounced dependence on the protein concentration (Figure 5.8).
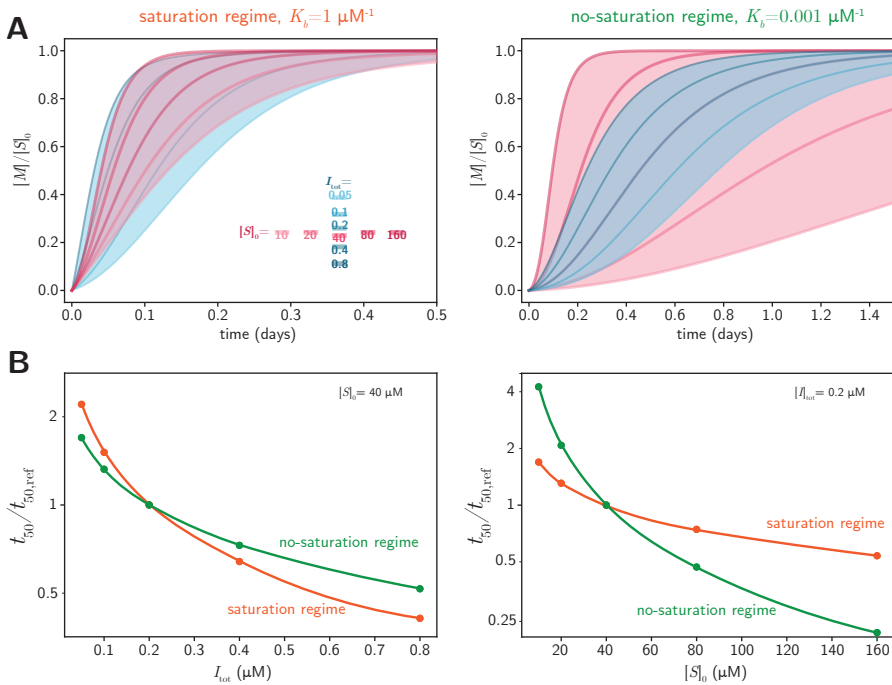

Figure 5.8: Aggregation traces and kinetic parameters simulated for the interface-aggregation model under different regimes. (A) Relative (normalised by $[S]_0$) concentration of fibril-bound ($[M]$) protein over time, simulated for a range of $[S]_0$ and I_{tot}. Left panel - under saturation regime ($K_B = 1$ µM^{-1}); right panel - under no-saturation regime ($K_B = 0.001$ µM^{-1}; other other parameters, same for left and right panel: $k_n = 10^{-5}$ µM^{-1}day^{-1}, $k_+ = 1$ µM^{-1}day^{-1}, $k_2 = 10^{-4}$ µM^{-2}day^{-1}, $k_h = 10$ µM^{-1}day^{-1}, $n = 2$, $n_2 = 2$. (B) Left panel - relative (normalised by values for the homogeneous system with the same aggregation kinetic rate constants) t_{50} in the function of I_{tot} for the saturation and no-saturation regimes; right panel - relative t_{50} in the function of $[S]_0$ for the saturation and no-saturation regimes; other parameters as in (A). Lines in (B) are drawn to guide the eye.

In the second regime, also in the case of dominating heterogeneous nucleation, the amount of surface is less relevant, but the amount of monomers has a more substantial

influence on the kinetics (Figure 5.8). In this case, we used aggregation half-time t_{50} (time until 50% of monomers are converted into aggregate), as nucleation-dominated reactions often do not have a clearly distinguishable lag phase.

5.4.2 Aggregation at the interface with non-detaching fibrils

Finally, we decided to model also the situation where protein fibrils do not detach from the interface (schematically shown in Figure 5.9A). This means that the number of fibrils formed at the interface needs to be subtracted from the amount of available binding sites at the interfaces to obtain the amount of effectively available binding sites (Equation 5.14). As a result, the amount of sites decreases during the progression of the surface-catalysed aggregation and the heterogeneous nucleation rate decreases, slowing the aggregation kinetics overall (Figure 5.9B). This model can also include different elongation and secondary nucleation rates for the reaction occurring at the interface, as shown in Equation 5.15.

$$[I]_{\text{eff}} = [I]_{\text{tot}} - [P]_{\text{int}} \tag{5.14a}$$

$$[S]_{\text{dil}} = \frac{-1 - K_{\text{B}} [I]_{\text{eff}} + [S]_{\text{tot}} K_{\text{B}} + \sqrt{\left[1 + K_{\text{B}} \left([I]_{\text{eff}} - [S]_{\text{tot}}\right)\right]^2 + 4 K_{\text{B}} [S]_{\text{tot}}}}{2 K_{\text{B}}} \tag{5.14b}$$

$$[S]_{\text{int}} = \frac{K_{\text{B}} [I]_{\text{eff}} [S]_{\text{dil}}}{1 + K_{\text{B}} [S]_{\text{dil}}} \tag{5.14c}$$

$$\frac{d[S]_{\text{tot}}}{dt} = -n k_n [S]_{\text{dil}}^n - 2 k_+ [S]_{\text{dil}} [P]_{\text{dil}} - n_2 k_2 [S]_{\text{dil}}^{n_2} [M]_{\text{dil}} - 2 k_{\text{h}} [S]_{\text{dil}} [S]_{\text{int}} + \\ - k_{+_{\text{int}}} [S]_{\text{dil}} [P]_{\text{int}} - n_2 k_{2_{\text{int}}} [S]_{\text{dil}}^{n_2} [M]_{\text{int}} \tag{5.15a}$$

$$\frac{d[P]_{\text{dil}}}{dt} = k_n [S]_{\text{dil}}^n + k_2 [S]_{\text{dil}}^{n_2} [M]_{\text{dil}} + k_{2_{\text{int}}} [S]_{\text{dil}}^{n_2} [M]_{\text{int}} \tag{5.15b}$$

$$\frac{d[M]_{\text{dil}}}{dt} = n k_n [S]_{\text{dil}}^n + 2 k_+ [S]_{\text{dil}} [P]_{\text{dil}} + n_2 k_2 [S]_{\text{dil}}^{n_2} [M]_{\text{dil}} + n_2 k_{2_{\text{int}}} [S]_{\text{dil}}^{n_2} [M]_{\text{int}} \tag{5.15c}$$

$$\frac{d[P]_{\text{int}}}{dt} = k_{\text{h}} [S]_{\text{dil}} [S]_{\text{int}} \tag{5.15d}$$

$$\frac{d[M]_{\text{int}}}{dt} = 2 k_{\text{h}} [S]_{\text{dil}} [S]_{\text{int}} + k_{+_{\text{int}}} [S]_{\text{dil}} [P]_{\text{int}} \tag{5.15e}$$

When all kinetic parameters are kept the same in solution and at the interface, the model with detaching fibrils yields faster aggregation than the model with non-detaching fibrils (Figure 5.9B), caused by the exhaustion of the binding sites upon nucleation at the interface. With changing kinetic parameters for the interface, the model with non-detaching fibrils allows for more flexibility and modelling of situations where the coacervate interface provides a distinct aggregation environment rather than a mere surface for nucleation.
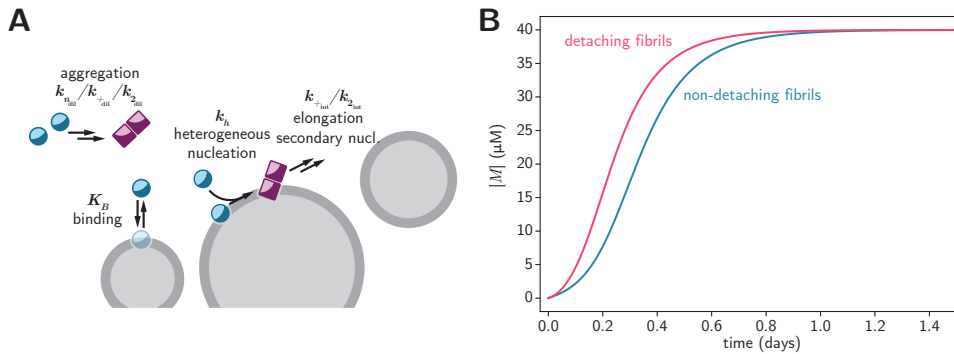
Figure 5.9: Aggregation model with heterogeneous nucleation at the interface with non-detaching fibrils. (A) Scheme of the model. (B) Aggregation traces simulated for the models with detaching and non-detaching fibrils (parameters: $k_n = 2 \cdot 10^{-4}$ µM^{-1}day^{-1}, $k_+ = 1$ µM^{-1}day^{-1}, $k_2 = 10^{-3}$ µM^{-2}day^{-1}, $k_h = 10$ µM^{-1}day^{-1}, $I_{\text{tot}} = 0.4$ µM, $K_{\text{B}} = 10^{-3}$, $[S]_0 = 40$ µM, $n = 2$, $n_2 = 2$ for both models; and $k_{+\text{int}} = 1$ µM^{-1}day^{-1}, $k_{2\text{int}} = 10^{-3}$ µM^{-2}day^{-1} for the non-detaching model).

5.5 Stochastic model of aggregation inside condensates

ODE-based models have several advantages, most importantly, they are fast to compute, thus allowing for screening of large ranges of parameters. However, they also possess a major limitation: it is not possible to simulate the randomness of chemical reactions and to study the distribution in the kinetics and in the final composition of the reaction system. Protein aggregation, like all autocatalytic processes, is strongly dependent on small fluctuations in the fibril concentration and this results in large variations in the concentration of aggregates at later times. This cannot be captured using ODE-based models because they are deterministic in nature. Therefore ODE-based models do not provide information about the influence of the condensed phase on the noise in the aggregation reaction and on the distribution of fibril length.

Therefore, to study the influence of liquid condensates on the noise in the protein aggregation process, we developed an SSA model of protein aggregation in the presence of liquid condensates. In brief, the SSA allows the simulation of single samples from the solution of the corresponding master equation[37] and running the simulation multiple times allows to determine the distribution in the kinetics and in the final state.

In general, SSA includes the following steps:

1. Setting the initial population of species (related to the concentrations and number of molecules/volume of the system).

2. Calculating the propensity function p_i for each of the J possible reactions.

3. Setting the total transition rate $Q = \sum_{i=1}^{J} p_i$.

4. Generating two pseudorandom numbers r_1 and r_2 on [0,1].

5. Setting $\Delta t = \frac{1}{Q} \ln \left(\frac{1}{r_1} \right)$.

6. Finding $\mu \in [1, ..., J]$ such that $\sum_{i=1}^{\mu-1} p_i < r_2 Q \leqslant \sum_{i=1}^{\mu} p_i$.

7. Setting $t = t + \Delta t$ and updating molecular species based on reaction μ.

8. Returning to step 2 and repeating until the end condition is met.

Calculation of the reaction propensity function is related to the kinetic rate. Equation 5.16 shows how the propensities of nucleation, elongation and secondary nucleation are calculated. Please note that the elongation reaction propensity refers to the elongation of fibrils of a particular length l (which means that elongation reaction propensity is calculated separately for each population of fibrils sharing the same length).

$$p_{\text{primary nucleation}} = k_n \frac{[S]_0}{N_{S,0}} N_{S,t} (N_{S,t} - 1) \tag{5.16a}$$

$$p_{\text{secondary nucleation}} = k_2 \left(\frac{[S]_0}{N_{S,0}} \right)^2 N_{S,t} (N_{S,t} - 1) N_{M,t} \tag{5.16b}$$

$$p_{\text{elongation}_{l \to l+1}} = 2k_+ \frac{[S]_0}{N_{S,0}} N_{P_l,t} N_{S,t} \tag{5.16c}$$

where: k_n, k_2 and k_+ are the kinetic rate constants, $[S]_0$ is the initial monomer concentration and $N_{S,0}$ is the initial number of monomer molecules, and $N_{S,t}$, $N_{M,t}$, $N_{P_l,t}$ are the number of monomer molecules, total number of monomer units in fibrils and number of fibrils of length l at time t.

In the case of protein aggregation as simulated here, we looked at the distribution of relative t_{50} and the fibril lengths after the aggregation process was completed in 95% (95% of monomer was converted into aggregate). The general aggregation equations used in the ODE-based model (Equation 5.2) allow determining the average fibril length (from the $[M]/[P]$ ratio), but do not allow determining the distribution of lengths. The stochastic model still uses the same kinetic equations (Equation 5.1), but allows following the number of fibrils of each specific length (and also treats the fibrils of different lengths individually when determining the reaction rates).

As measures of noise, we chose to use the coefficient of variation (CV) and the index of dispersion, also called the Fano factor (ID).

$$CV = \frac{\sigma}{\mu} \tag{5.17a}$$

$$ID = \frac{\sigma^2}{\mu} \tag{5.17b}$$

where σ is the standard deviation and μ is the mean. Both indicators can be useful in different situations. CV determines the ratio of the standard deviation and the mean and is a measure of the relative noisiness of the system. ID is a measure of how much a distribution differs from a Poisson distribution. In the case of Poissonian distribution, ID is 1.

5.5.1 Comparison of the influence of localised and homogeneous concentration increase on the noise in the aggregation kinetics

We first focused on the influence of the partitioning of the monomer into the condensed phase on the noise in the aggregation kinetics. As we have already shown using the ODE-based model, partitioning into the condensed phase can result in accelerated aggregation, purely due to increased local concentration of the monomer (subsection 5.3.1). The noise in the aggregation kinetics, as measured using CV can be expected to decrease with increasing the number of molecules. The left panel of Figure 5.10 shows the distribution of relative t_{50} (normalised by the value for the no-coacervate system) for increasing the number of molecules without increasing the concentration (scaling-up the system).
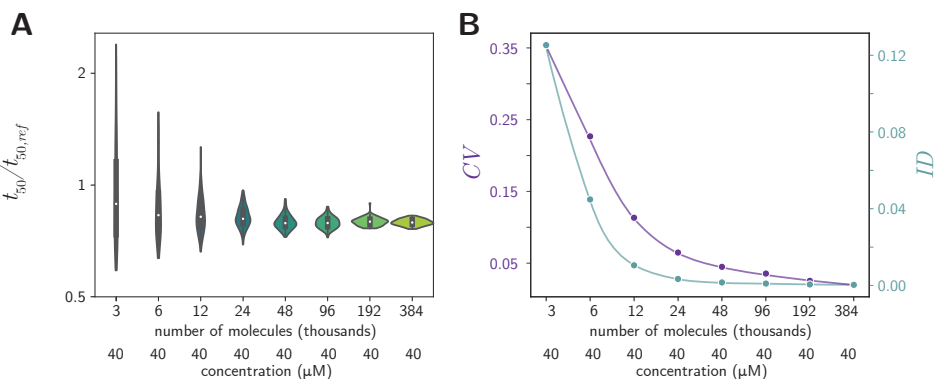

Figure 5.10: Concentration- and molecule number-dependent distribution of aggregation times (I). Changing the number of molecules at a constant concentration (scaling up the system). (A) Distribution of relative t_{50} (normalised by the average value for the system with 3000 molecules at 40 µM). (B) CV and ID. Parameters: $k_n = 10^{-5}$ µM^{-1}day^{-1}, $k_+ = 1$ µM^{-1}day^{-1}, $k_2 = 10^{-4}$ µM^{-2}day^{-1}. Distribution from 100 simulation runs. Lines in (B) are drawn to guide the eye.

The distribution becomes narrower while the mean value remains constant, which means decreasing CV and decreasing noise. On the other hand, increasing concentration without changing the number of molecules (decreasing the volume), results in an increase in noise (Figure 5.11). Finally, when both the concentration and the number of molecules increase (increasing the amount of reactant without changing the volume), the noise decreases (Figure 5.12). In all three situations, ID is always below 1 and decreases with an increasing number of molecules and with increasing concentration, indicating a sub-Poissonian distribution (a distribution that has a smaller variance than a Poisson distribution with the same mean).
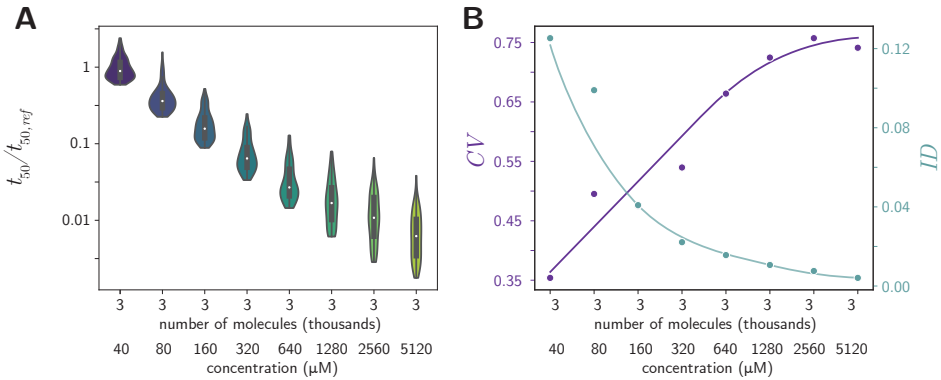
A

B

Figure 5.11: Concentration- and molecule number-dependent distribution of aggregation times (II). Changing the concentration at a constant number of molecules (decreasing the system volume). (A) Distribution of relative t_{50} (normalised by the average value for the system with 3000 molecules at 40 μM). (B) CV and ID. Simulation parameters same as in Figure 5.10. Distribution from 100 simulation runs. Lines in (B) are drawn to guide the eye.
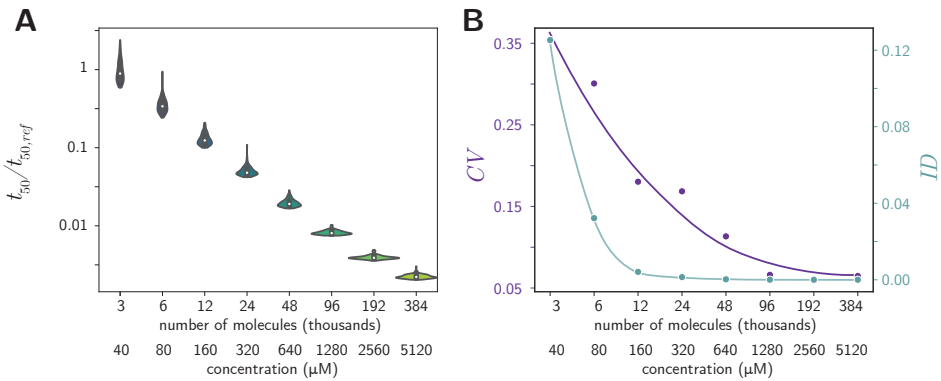
A

B

Figure 5.12: Concentration- and molecule number-dependent distribution of aggregation times (III). Changing the number of molecules and concentration (increasing the amount of reactant) (A) Distribution of relative t_{50} (normalised by the average value for the system with 3000 molecules at 40 μM). (B) CV and ID. Simulation parameters same as in Figure 5.10. Distribution from 100 simulation runs. Lines in (B) are drawn to guide the eye.

When the concentration is only increased locally, due to the partitioning of monomers into a condensate of small volume, the effect on noise in kinetics is different (Figure 5.13A and B). While CV increases with increasing K_{P}, similarly to the situation of increasing concentration without changing the number of molecules, ID initially increases above the values observed in a homogeneous systems and then starts to decrease for K_{P} values above 4. This trend in ID and also the generally higher CV values (compared to the homogeneous system) can be explained by the fact that only a small number of molecules partition into the condensed phase and undergoes reaction at a faster rate due to high local

concentration (and a lower number of molecules results in higher noise). Upon reaching the threshold partition coefficient value, the width of the distribution start to decrease, as both the number of molecules and the concentration in the condensed phase increase (Figure 5.13B).
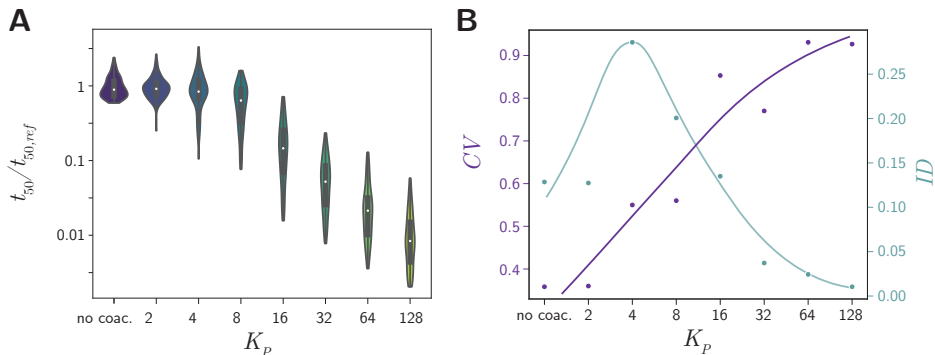

Figure 5.13: Partition coefficient-dependent distribution of aggregation times. (A) Distribution of relative t_{50} (normalised by the average value for the system without coacervates). (B) CV and ID. Parameters: $k_n = 10^{-5}$ µM⁻¹day⁻¹... $k_+ = 1$ µM⁻¹day⁻¹, $k_2 = 10^{-4}$ µM⁻²day⁻¹, $k_{out} = 10$ day⁻¹, $[S]_0 = 40$ µM, number of molecules= 3000, $R = 100$. Distribution from 100 simulation runs. Lines in (B) are drawn to guide the eye.

5.5.2 Variations in noise and fibril length

As explained at the beginning of this section, our stochastic aggregation model allows us to follow the distribution of fibril length at any timepoint of the aggregation reaction.

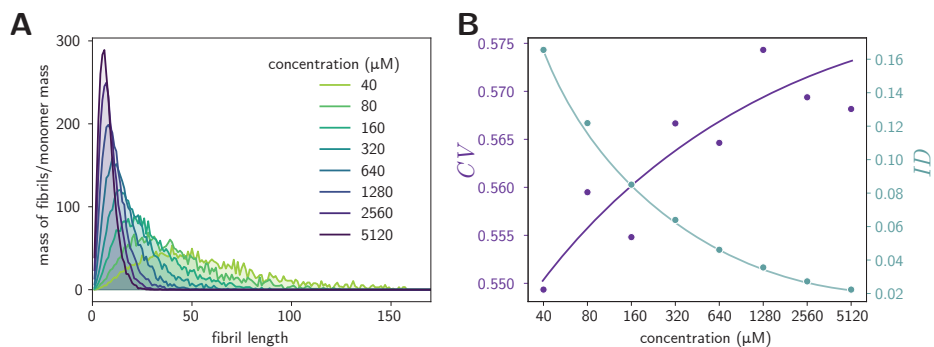Figure 5.14: Concentration-dependent distribution of fibril mass over length. (A) Distribution of fibril mass over length. (B) CV and ID of the fibril mass distribution. Parameters: $k_n = 10^{-5}$ µM⁻¹day⁻¹, $k_+ = 1$ µM⁻¹day⁻¹, $k_2 = 10^{-4}$ µM⁻²day⁻¹, $[S]_0 = 40$ µM, number of molecules= 3000. Average distribution from 100 simulation runs (per concentration). Lines in (B) are drawn to guide the eye.

We chose to compare the distributions at the point when aggregation is almost complete, so after 95% of monomers were converted into aggregate. As for the t_{50} distribution determination, for each set of conditions, we ran 100 simulation runs and took the average mass distribution (number of fibrils multiplied by length) over the length of the fibrils. From this, we determined again CV and ID.
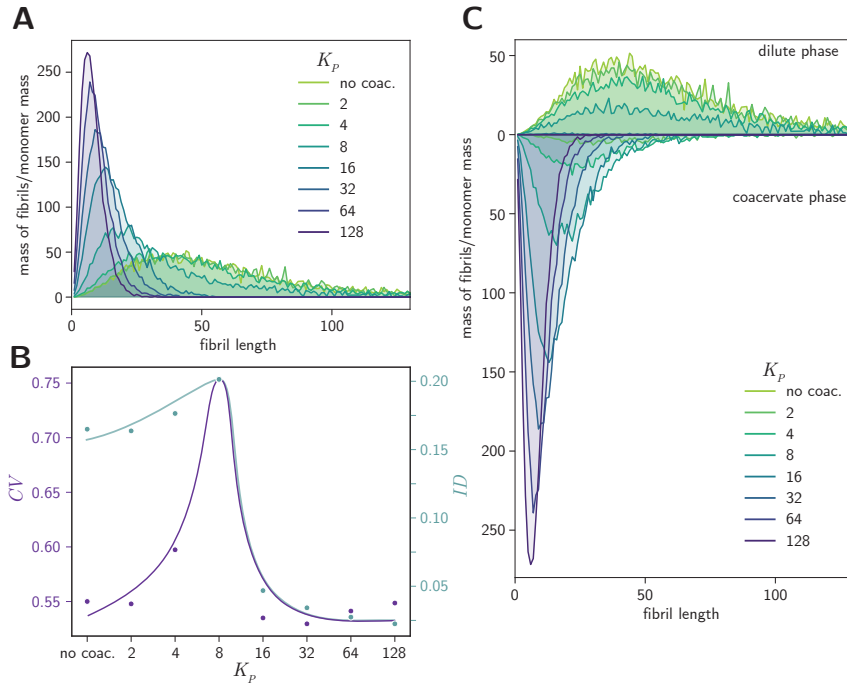

Figure 5.15: Partition coefficient-dependent distribution of fibril mass over length. (A) Distribution of total (dilute phase+coacervate phase) fibril mass over length. (B) CV and ID of the fibril mass distribution. (C) Distribution of fibril mass per phase. Parameters: $k_n = 10^{-5}$ µM^{-1}day^{-1}, $k_+ = 1$ µM^{-1}day^{-1}, $k_2 = 10^{-4}$ µM^{-2}day^{-1}, $k_{out} = 10$ day^{-1}, $[S]_0 = 40$ µM, number of molecules= 3000, $R = 100$. Average distribution from 100 simulation runs (per concentration). Lines in (B) are drawn to guide the eye.

As a benchmark, we looked at the distribution of fibril mass over length for different concentrations in a homogeneous system (with a constant number of molecules, Figure 5.14A). While the distribution becomes narrower for higher concentration (as measured by ID), the noisiness, measured by CV increases Figure 5.14B. Please note that a logarithmic scale was used to visualise the distribution of t_{50} (Figure 5.13) and a linear scale was used to visualise the distribution of fibril mass. The logarithmic scale allows for easier comparison of CV values, while the linear scale allows for easier comparison of ID values.

Again, we next looked at the situation when concentration is increased locally, by partitioning to the condensed phase (Figure 5.15A). In this case, the noise and the width

of fibril mass distribution increase until reaching a certain K_P value (Figure 5.15B). Similarly to the trend observed for the distribution of aggregation half-times, noise in the fibril mass distribution is dependent on both the number of molecules in the condensed phase and the local concentration, eventually decreasing for high K_P values. Higher K_P values result also in localisation of the fibrils mass in the condensed phase, as can be seen from Figure 5.15C).

5.6 Conclusion

This chapter presents how to theoretically predict the influence of the condensed phase on the aggregation kinetics and the noise in the aggregation process. We propose that in general condensates can have two distinct mechanisms of affecting protein aggregation: (i) partitioning of the aggregating protein in the condensed phase, which can result in both accelerated and sequestered aggregation, (ii) accumulation and heterogeneous nucleation at the interface of the condensed phase. We show that liquid condensates can have a non-obvious (when compared to simple concentration increase) influence on the noise/distribution of the aggregation half-times and fibrils mass. In Chapter 6, we present an experimental system that allows us to investigate the predicted trends in practice and use the proposed model to explain the influence of model coacervate systems on the aggregation of αSyn.

5.7 Experimental details

Python scripts with models used in this chapter are available from a GitHub repository (https://github.com/wlipinski/Thesis).

5.8 Contributions and acknowledgements

Work presented in this chapter started as a part of a master's internship project of Brent Visser. Brent participated in writing the first versions of the scripts used in the chapter and helped with the conceptualisation. We thank Bob van Sluijs for help with the SSA script.

Bibliography

[1] D. M. Mitrea and R. W. Kriwacki, "Phase separation in biology; Functional organization of a higher order Short linear motifs - The unexplored frontier of the eukaryotic proteome," *Cell Commun. Signal.*, vol. 14, no. 1, p. 1, 2016.

[2] E. Gomes and J. Shorter, "The molecular language of membraneless organelles," *J. Biol. Chem.*, vol. 294, no. 18, pp. 7115–7127, 2019.

[3] C. Greening and T. Lithgow, "Formation and function of bacterial organelles," *Nat. Rev. Microbiol.*, vol. 18, no. 12, pp. 677–689, 2020.

[4] C. A. Azaldegui, A. G. Vecchiarelli, and J. S. Biteen, "The emergence of phase separation as an organizing principle in bacteria," *Biophys. J.*, vol. 120, no. 7, pp. 1123–1138, 2021.

[5] M. Feric, N. Vaidya, T. S. Harmon, D. M. Mitrea, L. Zhu, T. M. Richardson, R. W. Kriwacki, R. V. Pappu, and C. P. Brangwynne, "Coexisting Liquid Phases Underlie Nucleolar Subcompartments," *Cell*, vol. 165, no. 7, pp. 1686–1697, 2016.

[6] T. E. Kaiser, R. V. Intine, and M. Dundr, "De novo formation of a subnuclear body," *Science*, vol. 322, no. 5908, pp. 1713–1717, 2008.

[7] A. Molliex, J. Temirov, J. Lee, M. Coughlin, A. P. Kanagaraj, H. J. Kim, T. Mittag, and J. P. Taylor, "Phase Separation by Low Complexity Domains Promotes Stress Granule Assembly and Drives Pathological Fibrillization," *Cell*, vol. 163, no. 1, pp. 123–133, 2015.

[8] A. A. Hyman, C. A. Weber, and F. Jülicher, "Liquid-liquid phase separation in biology," *Annu. Rev. Cell Dev. Biol.*, vol. 30, no. 1, pp. 39–58, 2014.

[9] T. J. Nott, T. D. Craggs, and A. J. Baldwin, "Membraneless organelles can melt nucleic acid duplexes and act as biomolecular filters," *Nat. Chem.*, vol. 8, no. 6, pp. 569–575, 2016.

[10] A. Patel, H. O. Lee, L. Jawerth, S. Maharana, M. Jahnel, M. Y. Hein, S. Stoynov, J. Mahamid, S. Saha, T. M. Franzmann, A. Pozniakovski, I. Poser, N. Maghelli, L. A. Royer, M. Weigert, E. W. Myers, S. Grill, D. Drechsel, A. A. Hyman, and S. Alberti, "A Liquid-to-Solid Phase Transition of the ALS Protein FUS Accelerated by Disease Mutation," *Cell*, vol. 162, no. 5, pp. 1066–1077, 2015.

[11] S. Wegmann, B. Eftekharzadeh, K. Tepper, K. M. Zoltowska, R. E. Bennett, S. Dujardin, P. R. Laskowski, D. MacKenzie, T. Kamath, C. Commins, C. Vanderburg, A. D. Roe, Z. Fan, A. M. Molliex, A. Hernandez-Vega, D. Muller, A. A. Hyman, E. Mandelkow, J. P. Taylor, and B. T. Hyman, "Tau protein liquid–liquid phase separation can initiate tau aggregation," *EMBO J.*, vol. 37, no. 7, p. e98049, 2018.

[12] J. Wen, L. Hong, G. Krainer, Q. Q. Yao, T. P. Knowles, S. Wu, and S. Perrett, "Conformational Expansion of Tau in Condensates Promotes Irreversible Aggregation," *J. Am. Chem. Soc.*, vol. 143, no. 33, pp. 13056–13064, 2021.

[13] S. Ray, N. Singh, R. Kumar, K. Patel, S. Pandey, D. Datta, J. Mahato, R. Panigrahi, A. Navalkar, S. Mehra, L. Gadhe, D. Chatterjee, A. S. Sawner, S. Maiti, S. Bhatia, J. A. Gerez, A. Chowdhury, A. Kumar, R. Padinhateeri, R. Riek, G. Krishnamoorthy, and S. K. Maji, "α-Synuclein aggregation nucleates through liquid–liquid phase separation," *Nat. Chem.*, vol. 12, no. 8, pp. 705–716, 2020.

[14] A. S. Sawner, S. Ray, P. Yadav, S. Mukherjee, R. Panigrahi, M. Poudyal, K. Patel, D. Ghosh, E. Kummerant, A. Kumar, R. Riek, and S. K. Maji, "Modulating α-Synuclein Liquid-Liquid Phase Separation," *Biochemistry*, vol. 60, no. 48, pp. 3676–3696, 2021.

[15] S. Ray, D. Chatterjee, S. Mukherjee, K. Patel, and J. Mahato, "Spatiotemporal solidification of α-synuclein inside the liquid droplets," *bioRxiv*, 2021.

[16] S. Ray, T. O. Mason, L. Boyens-Thiele, A. Farzadfard, J. A. Larsen, R. K. Norrild, N. Jahnke, and A. K. Buell, "Mass photometric detection and quantification of nanoscale α-synuclein phase separation," *Nat. Chem.*, vol. 15, no. 9, pp. 1306–1316, 2023.

[17] W. S. Woods, J. M. Boettcher, D. H. Zhou, K. D. Kloepper, K. L. Hartman, D. T. Ladror, Z. Qi, C. M. Rienstra, and J. M. George, "Conformation-specific binding of α-synuclein to novel protein partners detected by phage display and NMR spectroscopy," *J. Biol. Chem.*, vol. 282, no. 47, pp. 34555–34567, 2007.

[18] A. Esposito, C. P. Dohm, P. Kermer, M. Bähr, and F. S. Wouters, "α-Synuclein and its disease-related mutants interact differentially with the microtubule protein tau and associate with the actin cytoskeleton," *Neurobiol. Dis.*, vol. 26, no. 3, pp. 521–531, 2007.

[19] S. F. Banani, H. O. Lee, A. A. Hyman, and M. K. Rosen, "Biomolecular condensates: Organizers of cellular biochemistry," *Nat. Rev. Mol. Cell Biol.*, vol. 18, no. 5, pp. 285–298, 2017.

[20] K. K. Nakashima, M. A. Vibhute, and E. Spruijt, "Biomolecular chemistry in liquid phase separated compartments," *Front. Mol. Biosci.*, vol. 6, p. 21, 2019.

[21] C. Weber, T. Michaels, and L. Mahadevan, "Spatial control of irreversible protein aggregation," *eLife*, vol. 8, p. e42315, 2019.

[22] A. M. Küffner, M. Linsenmeier, F. Grigolato, M. Prodan, R. Zuccarini, U. Capasso Palmiero, L. Faltova, and P. Arosio, "Sequestration within biomolecular condensates inhibits Aβ-42 amyloid formation," *Chem. Sci.*, vol. 12, no. 12, pp. 4373–4382, 2021.

[23] F. Grigolato and P. Arosio, "The role of surfaces on amyloid formation," *Biophys. Chem.*, vol. 270, p. 106533, 2021.

[24] G. Marie, C. J. Dunning, R. Gaspar, C. Grey, P. Brundin, E. Sparr, and S. Linse, "Acceleration of α-synuclein aggregation by exosomes," *J. Biol. Chem.*, vol. 290, no. 5, pp. 2969–2982, 2015.

[25] C. Galvagnion, A. K. Buell, G. Meisl, T. C. Michaels, M. Vendruscolo, T. P. Knowles, and C. M.

Dobson, "Lipid vesicles trigger α-synuclein aggregation by stimulating primary nucleation," *Nat. Chem. Biol.*, vol. 11, no. 3, pp. 229–234, 2015.

[26] M. Zhu, J. Li, and A. L. Fink, "The association of α-synuclein with membranes affects bilayer structure, stability, and fibril formation," *J. Biol. Chem.*, vol. 278, no. 41, pp. 40186–40197, 2003.

[27] S. Rocha, R. Kumar, I. Horvath, and P. Wittung-Stafshede, "Synaptic vesicle mimics affect the aggregation of wild-type and A53T α-synuclein variants differently albeit similar membrane affinity," *Protein Eng. Des. Sel.*, vol. 32, no. 2, pp. 59–66, 2019.

[28] A. S. Kurochka, D. A. Yushchenko, P. Bouř, and V. V. Shvadchak, "Influence of lipid membranes on α-synuclein aggregation," *ACS Chem. Neurosci.*, vol. 12, no. 5, pp. 825–830, 2021.

[29] F. A. Ferrone, J. Hofrichter, and W. A. Eaton, "Kinetics of sickle hemoglobin polymerization. II. A double nucleation mechanism," *J. Mol. Biol.*, vol. 183, no. 4, pp. 611–631, 1985.

[30] J. S. Schreck, J. Bridstrup, and J. M. Yuan, "Investigating the Effects of Molecular Crowding on the Kinetics of Protein Aggregation," *J. Phys. Chem. B*, vol. 124, no. 44, pp. 9829–9839, 2020.

[31] S. Sukenik, R. Politi, L. Ziserman, D. Danino, A. Friedler, and D. Harries, "Crowding alone cannot account for cosolute effect on amyloid aggregation," *PLoS One*, vol. 6, no. 1, p. e15608, 2011.

[32] M. Kuragano, S. Yamanaka, and K. Tokuraku, "Kinetics of amyloid accumulation in physiological viscosity," *Colloids Surfaces B Biointerfaces*, vol. 214, p. 112449, 2022.

[33] L. A. Munishkina, E. M. Cooper, V. N. Uversky, and A. L. Fink, "The effect of macromolecular crowding on protein aggregation and amyloid fibril formation," *J. Mol. Recognit.*, vol. 17, no. 5, pp. 456–464, 2004.

[34] M. T. Wei, S. Elbaum-Garfinkle, A. S. Holehouse, C. C. H. Chen, M. Feric, C. B. Arnold, R. D. Priestley, R. V. Pappu, and C. P. Brangwynne, "Phase behaviour of disordered proteins underlying low density and high permeability of liquid organelles," *Nat. Chem.*, vol. 9, no. 11, pp. 1118–1125, 2017.

[35] D. M. Mitrea, B. Chandra, M. C. Ferrolino, E. B. Gibbs, M. Tolbert, M. R. White, and R. W. Kriwacki, "Methods for Physical Characterization of Phase-Separated Bodies and Membrane-less Organelles," *J. Mol. Biol.*, vol. 430, no. 23, pp. 4773–4805, 2018.

[36] N. A. Yewdall, A. A. André, T. Lu, and E. Spruijt, "Coacervates as models of membraneless organelles," *Curr. Opin. Colloid Interface Sci.*, vol. 52, p. 101416, 2021.

[37] D. T. Gillespie, "A general method for numerically simulating the stochastic time evolution of coupled chemical reactions," *J. Comput. Phys.*, vol. 22, no. 4, pp. 403–434, 1976.

6

Studying the influence of biomolecular condensates on αSyn aggregation

6.1 Basic experimental model to study protein aggregation kinetics in the presence of liquid condensates

In Chapter 5, by means of computer simulations, we show that liquid condensates can potentially affect protein aggregation kinetics. In this follow-up chapter, we present an experimental system to support the theoretical findings. Here, we study the influence of *inert* model condensates (coacervates) on the aggregation of α-synunclein (αSyn) as a key amyloid-forming protein (supplemented with experiments using insulin). Our model condensates are inert in the sense that they are not composed of, or dependent on, the aggregating protein, and they do not undergo any form of liquid-to-solid transition themselves. The goal of using these model condensates is to investigate whether pre-existing biomolecular condensates can have a generic effect on protein aggregation, by means of concentration, exclusion or stabilisation of disordered confirmations.

In the experiments, we use full-length αSyn (FL-αSyn) and two truncated variants to understand better which protein domains are responsible for specific behaviours. Three different coacervates were investigated as model condensates, and their selection was guided by well-defined coacervate models reported in literature of RNP granules containing RNA and arginine-rich peptides[1–3], heterotypic condensates containing unstructured polypeptides[4], and active droplets containing small molecules[5,6]. We show that depending on the composition of the condensed phase, amyloidogenic protein can partition into the droplets, remain excluded or accumulate at the interface. We find that FL-αSyn accumulates and aggregates preferentially inside two of the complex coacervate droplets and accumulates and aggregates at the interface of another type. Accumulation of FL-αSyn either inside or at the interface of coacervates always leads to enhanced aggregation compared to a homogeneous solution. Truncated variants of αSyn were typically excluded from the coacervate droplets and aggregated at a comparable rate or slower than in a homogeneous solution. The shortest variant, which only contains the β-sheet forming region and which normally has the fastest maximum rate of aggregation, is also accumulated inside two coacervates, but aggregates significantly slower than in solution. This demonstrates that sequestration of amyloidogenic proteins inside condensates can speed up aggregation by enhancing local concentrations in some condensates, but slow it down in others due to a stabilisation of the monomeric form of the protein.

6.2 Properties of selected αSyn variants

We selected three αSyn variants with different net charge and length of the intrinsically disordered region Figure 6.1A: wild-type, full-length αSyn (FL-αSyn), a truncated variant depleted of the negatively charged, disordered C-terminal domain (αSyn-108) and a relatively hydrophobic short peptide from the non-amyloid-β component of the protein, which is the part that is responsible for β-sheet formation in aggregates (NACore peptide, αSyn-68-78). While having different physicochemical properties, these variants are all able to aggregate into amyloids, and the kinetics of their aggregation can be described by a
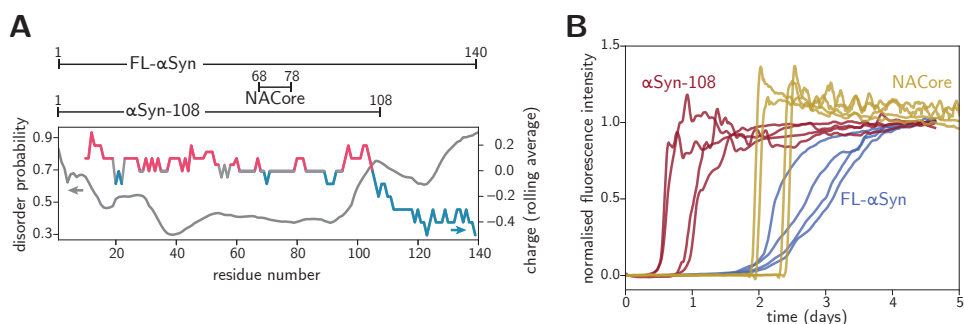
Figure 6.1: Amyloidogenic αSyn variants used in this study. (A) Variants of αSyn used in the study and predicted disorder along the protein chain (PrDOS, in gray)[7] and distribution of charged residues (in colour). (B) Aggregation traces (normalised ThT fluorescence intensity) for various αSyn variants (recorded for 40 μM concentration of FL-αSyn αSyn-108 and for 160 μM concentration of NACore), without coacervates.

classical nucleation and growth model[8] (Figure 6.1B), including primary and secondary nucleation and elongation (see Figure 5.1 for the schematic). All variants form fibrillar aggregates, as confirmed by transmission electron microscopy (TEM) (Figure 6.2A). For each variant, we determined the concentration at which complete aggregation, defined as reaching plateau of thioflavin T (ThT) intensity, was reached in less than five days, and these concentrations were used in further experiments unless stated otherwise (40 μM for FL-αSyn and αSyn-108, and 160 μM for NACore).
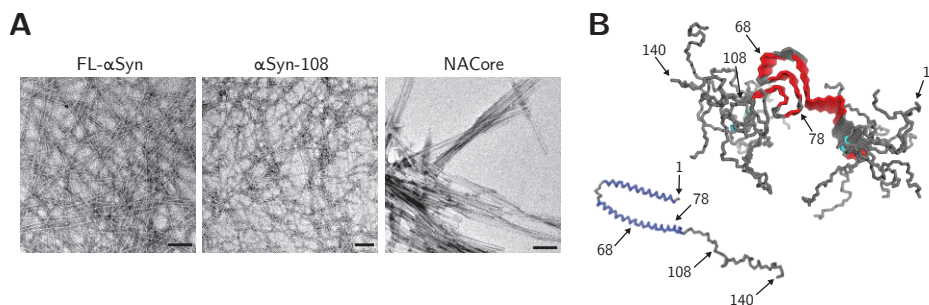
Figure 6.2: (A) TEM images of fibrils formed by studied variants. Scale bars are 200 nm. (B) FL-αSyn conformation when bound to lipids (bottom-left, Protein Data Bank (PDB) ID: 1XQ8) and stacked in amyloid fibrils (top-right, PDB ID: 2N0A); relevant residues are indicated.

6.3 Partitioning of αSyn into coacervate droplets

We investigated the localisation of selected αSyn variants in 3 coacervate systems, which may serve as very basic models of biological condensates: (i) (RRASL)$_3$ peptide/polyur-

idylic acid (RP3/polyU)[1,8], (ii) poly-D,L-lysine/poly-D,L-glutamate (pLys/pGlu)[4], and (iii) poly-L-lysine/adenosine triphosphate (pLys/ATP)[5,6] (Figure 6.3). All these systems phase separate upon mixing the (poly)cationic component with the (poly)anionic component and form micrometre-size droplets that fuse into larger droplets over time, but remain liquid over the course of several days.
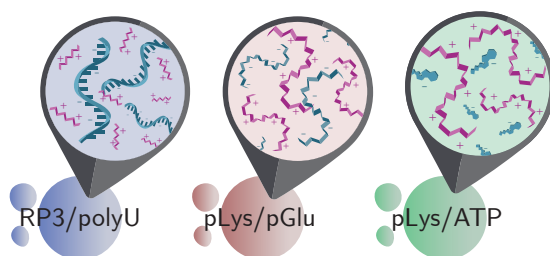

Figure 6.3: Schematic depiction of coacervate systems used in the study.

In addition, all droplets have been shown to take up or exclude a wide range of biomolecules and complexes[1,9–11], and are thus expected to influence the aggregation of αSyn. RP3/polyU coacervates (system i) have been suggested as a model for RNP granules, which are typically composed of RNA and arginine-rich peptides or proteins[12]. Our model system (i) contains a relatively short cationic component (RP3 peptide) and a long anionic component (polyU RNA), and is thus expected to have a negative surface potential[13] and interact weakly with negatively charged guest molecules. pLys/pGlu coacervates (system ii) are composed of large, unstructured cationic and anionic peptides, and have relevance for biomolecular condensates whose formation is known to be driven by proteins bearing charge patches, such as LAF-1 and Ddx4[14,15]. Last, pLys/ATP coacervates (system iii), which contain the biologically relevant small molecule and hydrotrope ATP[16], are of relevance within the context of biomolecular condensates that bind ATP to tune their properties and composition[17,18]. Moreover, these coacervates have been used as active droplet mimics[6], which makes understanding their influence on protein aggregation and fibrillisation also relevant from a protocell perspective. Unlike RP3/polyU coacervates, pLys/ATP coacervates contain a long cationic and a short anionic component, typically resulting in a positive surface potential when prepared at 1:1 charge ratio charge[19], and a strong interaction with negatively charged guest molecules. These three different model systems were selected to cover a variety of different condensate compositions and properties, for which we expected different interactions with the αSyn variants. Together, these model systems may yield generalisable, physicochemical insight into the influence of condensed aqueous droplets on protein aggregation.

To determine whether variants of αSyn partition into coacervate droplets or remain excluded, Alexa Fluor-647-labelled variants of αSyn were added to the coacervate emulsions and placed in a chambered glass slide to visualize them with confocal microscopy. Distinct partitioning could be observed for different combinations of labelled protein and coacervates (Figure 6.4 and Figure 6.5A). FL-αSyn accumulated at the interface of the coacervate droplets and the solution phase for pLys/pGlu and pLys/ATP systems (Figure 6.4B).
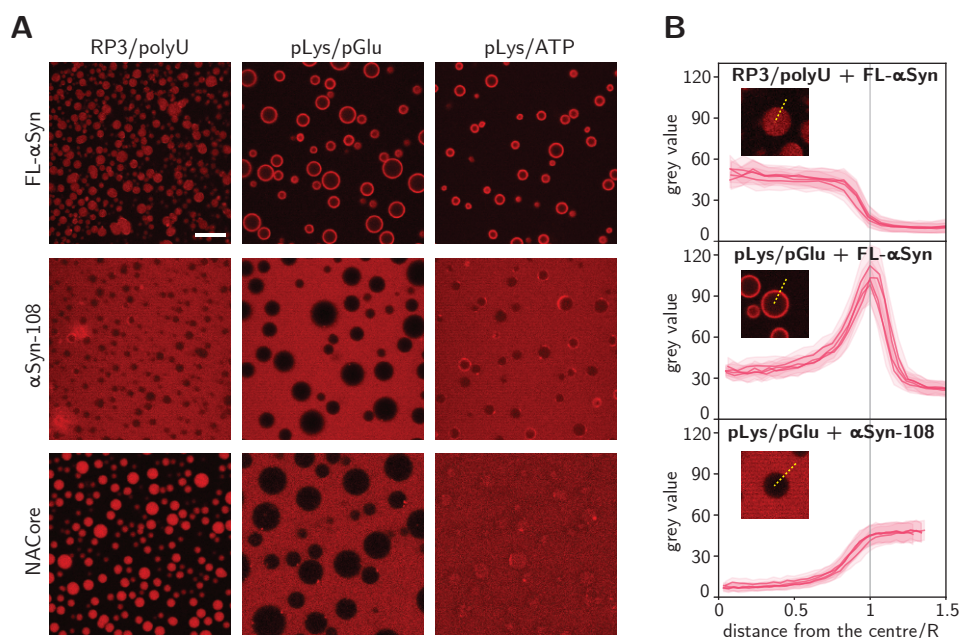
Figure 6.4: Interactions of coacervate systems with αSyn variants. (A) Confocal microscopy images of coacervate systems with labelled αSyn variants (Alexa Fluor 647–labelled S9C-FL-αSyn and S9C-αSyn-108, and TAMRA–labelled NACore). Scale bar is 20 µm. (B) Grey value profiles (angular averaging) of coacervate droplets from selected systems.

For all coacervates, the average fluorescence inside the droplets (excluding the interface) was higher than in the surrounding dilute phase (Figure 6.5A). The truncated variant αSyn-108 remained excluded from all coacervate droplets, and particularly for pLys/pGlu system for which the ratio of concentration inside/outside was lowest (Figure 6.4B). Finally, the NACore fragment partitioned into RP3/polyU droplets, and very weakly into pLys/ATP droplets, but remained excluded from coacervates formed by pLys/pGlu.

The tendency of FL-αSyn to localize to the interface of coacervate droplets may stem from the fact that its disordered chain includes both charged/hydrophilic and hydrophobic regions. Both large, negatively charged RNAs and small, hydrophobic dyes, have been found to partition into pLys/ATP coacervates[5,6]. However, in an amphiphilic molecule, such as FL-αSyn, not all regions are preferentially taken up by the coacervate environment, resulting in a strong localisation at the interface. Previous studies on partially unfolded proteins have also shown similar interfacial localisation[20]. Interfacial localisation seems to be strongest for coacervates with relatively low molecular weight anionic components, such as ATP in pLys/ATP and pGlu in pLys/pGlu. Displacing these small anions with FL-αSyn in the coacervates results in a larger gain in entropy than displacing the large polyU in RP3/polyU coacervates. Some uptake of FL-αSyn inside the coacervates is possible for all coacervates tested (Figure 6.5A), and can be explained by an overall favourable interaction between FL-αSyn and one of the components in the coacervates[20–23]. The
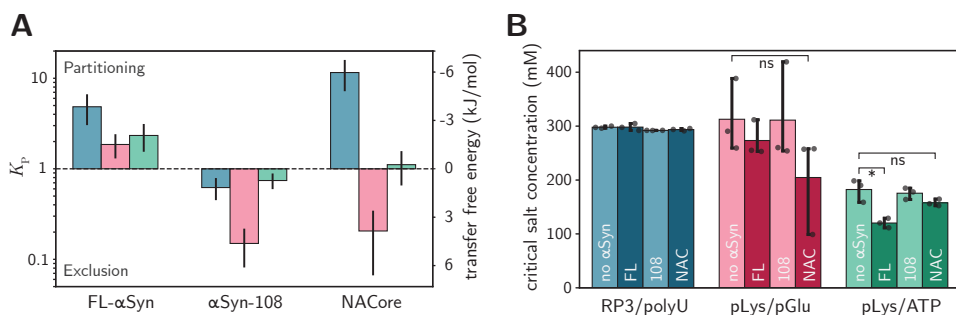
Figure 6.5: Partition coefficient and critical salt concentration of coacervate systems with αSyn variants. (A) Partition coefficient and transfer free energy (dilute phase-coacervate) determined from microscopy experiments. (B) Critical salt concentration of coacervate systems without and with αSyn variants. All coacervate systems were tested with FL-αSyn, αSyn-108 and NACore. Differences between selected samples were tested for statistical significance (Student's t-test) in coacervate droplets–supernatant control pairs. *ns* indicates values above 0.05, single asterisk indicates $\alpha < 0.05$.

negatively charged C-terminal domain appears crucial for both the uptake and the interfacial localisation: the truncated αSyn-108 was systematically excluded from the droplets. The NACore does not show any interfacial localisation, presumably because it only contains the relatively hydrophobic core region of the protein. Instead, it is either sequestered and distributed homogeneously inside the coacervates or excluded, reflecting the favourable interactions between NACore and RP3, and the unfavourable interactions with pGlu most likely.

We note that the quantification of local concentrations by fluorescence (e.g., Figure 6.5A) is dependent on the assumption that the fluorescence intensity of a dye is proportional to its concentration under all different circumstances. High concentrations of labelled αSyn, particularly at the interface of the droplets, could potentially result in self-quenching of the dye and underestimating of the local αSyn concentration. However, the Alexa Fluor dyes we used here were selected for their resistance to self-quenching and photobleaching. Moreover, the experiments shown in Figure 6.4, from which we extract local concentrations for later use, were always performed at very low concentrations of labelled αSyn (1 μM, which is orders of magnitude lower than typical aggregation conditions), and therefore, we assume that our estimates of the local αSyn concentrations inside the droplets were not affected by these effects.

6.4 Aggregation kinetics in the presence of coacervates

Upon phase separation most coacervate-forming material (peptides and RNA in our case) is condensed into droplets, which are in equilibrium with the surrounding dilute phase (supernatant). We used thioflavin T (ThT) assay[24,25] to study the aggregation kinetics

of the αSyn variants in the presence of the coacervate droplets. We verified that addition of the different αSyn variants does not affect the stability of the coacervate droplets (Figure 6.5B). The supernatant usually contains very low, but not negligible concentrations of the coacervate components. To distinguish the influence of coacervate droplets from the soluble components in the supernatant, we performed experiments in the presence of droplets and control experiments with only the supernatant (separated from coacervate droplets by centrifugation) for each coacervate system (an example for RP3/polyU is shown in Figure 6.6A). In addition, a reference experiment was performed without any droplets or soluble coacervate components. We note that studies on αSyn aggregation use various names and conditions for the control experiments. In our study, the reference experiment performed without any coacervate material reflects the *standard* aggregation kinetics of αSyn variants, and it can be used to obtain information about the general influence of the coacervate components (both in solution and in droplets) on the aggregation kinetics. The control experiments are performed with the coacervate components in solution at saturation concentrations, and they allow separating the influence of the coacervate droplets from the influence of the coacervate components present in the dilute phase (in solution) by comparing them to the kinetics obtained in the presence of coacervate droplets.
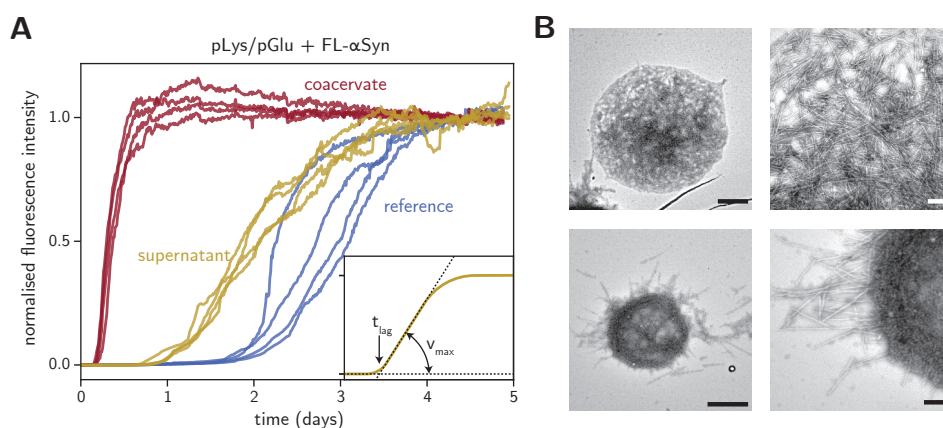

Figure 6.6: FL-αSyn aggregation in the presence of coacervates. (A) Aggregation traces for FL-αSyn: without coacervates (reference), with pLys/pGlu supernatant, and with pLys/pGlu coacervates. (B) TEM images of aggregates formed in the presence of RP3/polyU coacervates. Scale bars are 1 μm (images on the left side) and 200 nm (images on the right side).

Figure 6.6A shows a typical set of aggregation traces for one coacervate system and for one αSyn variant (FL-αSyn). It includes data for the reference sample without any coacervate material (blue traces), for the supernatant sample with diluted components shows faster aggregation (yellow traces) and for the sample with coacervate droplets (red traces). Before analysing the kinetics of aggregation further, we used TEM to determine whether the amyloid fibrils formed in the presence of droplets appear similar to the fibrils formed in solution. Figure 6.6B shows TEM images of FL-αSyn fibrils present in-

side and at the interface of coacervates droplets. The fibrils at the interface appear to be aligned parallel to the interface, forming an apparent aggregation shell that is not completely disordered. Some fibrils protrude into the surrounding solution. These results indicate that the fibrils can nucleate and grow in coacervate droplets. Moreover, analysis of the fibrils shown in Figure 6.6B revealed that there is no significant difference in thickness between these and fibrils formed in solution (Figure 6.7). Last, we also purified the incubated samples of αSyn with coacervates by dissolving the coacervates at high salt concentration, depositing the fibrils on a TEM grid and rinsing the grid with milliQ water. All combinations of αSyn variants and coacervates show the same fibril appearance as in samples without coacervates (Figure 6.6B and Figure 6.7).
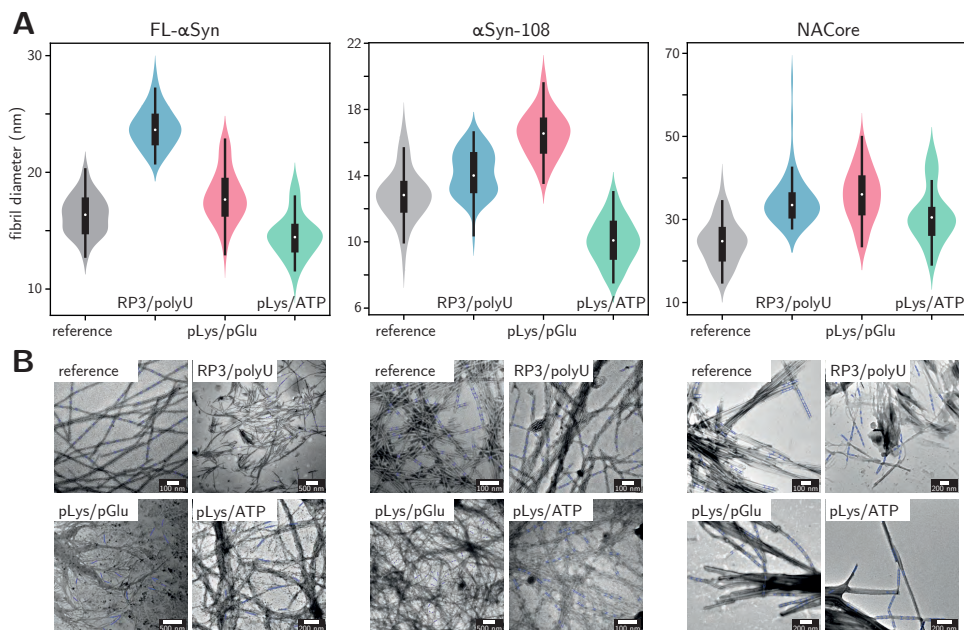

Figure 6.7: Characteristics of αSyn fibrils aggregated in the absence and presence of coacervates. (A) Distribution of fibril thickness formed by different αSyn variants in the absence (reference) or presence of coacervate systems (n=50). Violin plots were prepared using Gaussian kernels with bandwidth determined automatically using Scott's method. (B) TEM images of the fibrils formed by different αSyn variants in the absence (reference) or presence of coacervate systems. Blue marks indicate places where the diameter was measured.

To elucidate the role of condensates on the kinetics of aggregation, we plotted the distributions of both the lag times (t_{lag}, which is predominantly determined by the primary nucleation rate), and the maximum slopes of the ThT-based aggregation curves (v_{max}, which is mostly determined by the elongation and secondary nucleation rate). As can be seen in Figure 6.8, the presence of each of the coacervates resulted in faster aggregation for FL-αSyn with smaller spread of the nucleation times, even though the localisation of FL-αSyn in these coacervates is not identical: in the case of RP3/polyU we observed a

homogeneous distribution inside the droplets, while in the other two cases we observed strong interfacial adsorption (Figure 6.4).
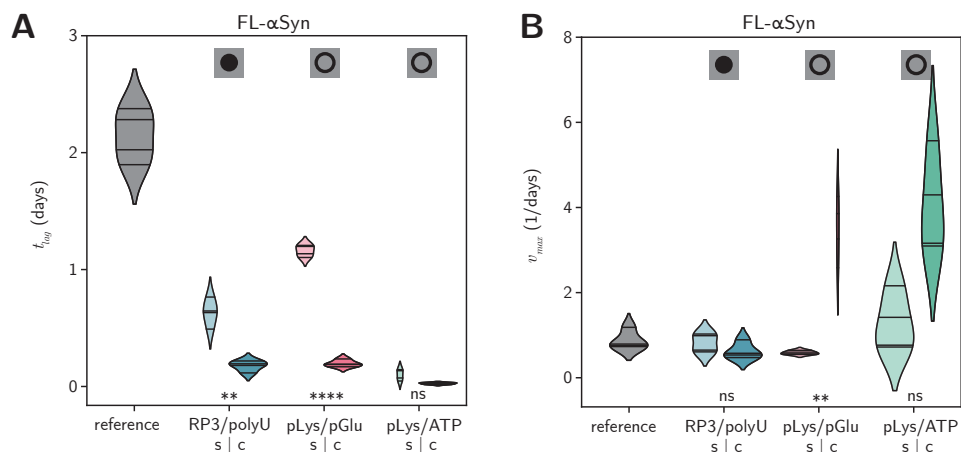

Figure 6.8: Analysis of FL-αSyn aggregation kinetics. (A) Distribution of the lag times (t_{lag}) for all coacervate systems (s - supernatant, c - coacervate) and for the reference sample. Symbols at the top indicate localisation of the corresponding variant as determined using fluorescence microscopy. Differences between samples were tested for statistical significance (Student's t test) in coacervate droplet–supernatant control pairs. *ns* indicates values above 0.05, single asterisk indicates $\alpha < 0.05$, double asterisk indicates $\alpha < 0.01$, triple asterisk indicates $\alpha < 0.001$, and quadruple asterisk indicates $\alpha < 0.0001$. Violin plots were prepared using Gaussian kernels with bandwidth determined automatically using the Scott's method; density plots were cut at two bandwidth units past the extreme data points; violins are scaled to have the same area in supernatant-coacervate pairs. (B) Distribution of the maximum aggregation rates (v_{max}) for all coacervate systems. Colours and symbols as in (A).

Presence of RP3/polyU droplets mostly affects the lag phase of αSyn aggregation. With these droplets the lag phase was four times shorter than in controls with only supernatant and ten times faster than in reference solution, indicating that the amyloid nucleation rate was enhanced by the droplets. On the other hand, the maximum αSyn aggregation rate in the presence of RP3/polyU droplets is comparable to the control samples with the RP3/polyU supernatant and to the reference sample without any coacervate material. Since these droplets concentrate FL-αSyn (Figure 6.4 and Figure 6.5), it was expected that the growth rate inside the droplets is enhanced, as we discuss below. A comparable growth rate despite higher local concentration indicates that FL-αSyn is less aggregation-prone inside RP3/polyU coacervates. Possibly, one of the coacervate components can bind weakly to FL-αSyn monomers, oligomers or short fibrils and slow down amyloid growth. Nevertheless, the presence of droplets accelerated aggregation overall, as the time to complete aggregation was reduced, due to a shorter lag phase.

Different behaviour was observed for FL-αSyn aggregating in the presence of pLys/pGlu and pLys/ATP coacervates. The FL-αSyn in both the supernatant and the coacervate sample showed a faster onset of aggregation. Unlike in the case of RP3/polyU, the growth
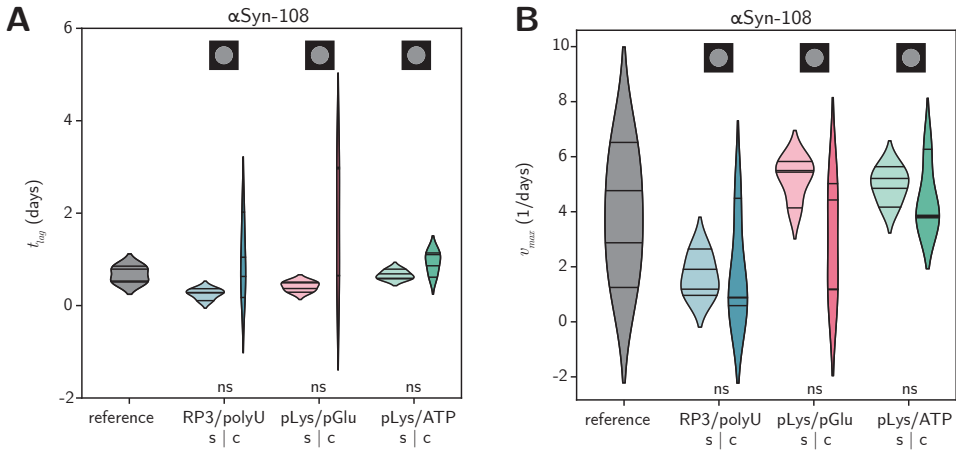
Figure 6.9: Analysis of αSyn-108 aggregation kinetics. (A) Distribution of the lag times (t_{lag}) for all coacervate systems. (B) Distribution of the maximum aggregation rates (v_{max}) for all coacervate systems (symbols and analysis as in Figure 6.8).
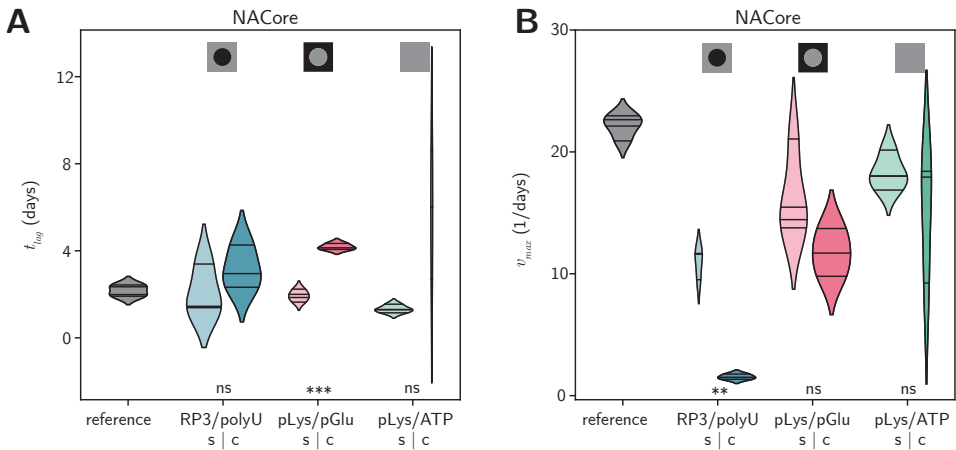
Figure 6.10: Analysis of NACore aggregation kinetics. (A) Distribution of the lag times (t_{lag}) for all coacervate systems. (B) Distribution of the maximum aggregation rates (v_{max}) for all coacervate systems (symbols and analysis as in Figure 6.8).

phase in the presence of pLys/pGlu and pLys/ATP droplets was significantly faster than in the reference sample, and also faster than in the presence of supernatant. This may be linked to the fact that pLys/pGlu and pLys/ATP systems seem to have a tendency to accumulate monomeric FL-αSyn at the interface of the droplets, thereby providing an alternative aggregation pathway, as we will discuss below. RP3/polyU system mostly accumulates FL-αSyn monomers inside and the increase in concentration and altered environment affects mostly the primary nucleation rate.

Figure 6.11: Interactions of coacervate systems with insulin. Confocal microscope images of coacervate systems with FAM-labelled insulin. Ratio of positive to negative charge of the co-acervate components is indicated in the brackets. Scale bars are 10 μm. Partition coefficient of FAM-labelled insulin dete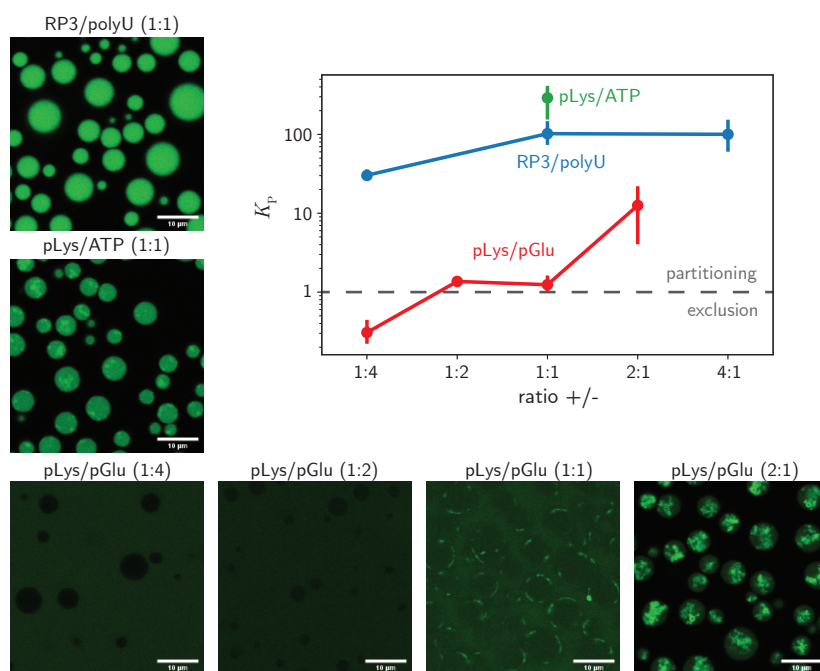rmined from microscopy experiments for different coacervate systems and different charge ratios of coacervate components.

The same experiments were performed for the αSyn-108 variant and the NACore peptide (Figure 6.9 and Figure 6.10). Interestingly, the aggregation behaviour of the shorter variants was fundamentally different from the FL-αSyn. While the samples incubated in supernatant aggregated at comparable rate to the references for both αSyn-108 and NACore, the presence of droplets resulted in slower aggregation. Large spread of the aggregation parameters for αSyn-108 made it difficult to assess the significance of the effect, but for NACore it was clear that the peptide in samples with coacervates aggregated significantly slower than peptide in both the supernatant and reference samples. Presence of all types of droplets resulted in lag times that were longer than in the corresponding supernatant sample, although the spread was typically very large, which made only the lag time of pLys/pGlu droplets statistically significant. The presence of RP3/polyU droplets also resulted in significantly slower maximum aggregation rates than in supernatant, suggesting that the NACore peptides sequestered inside these droplets are less aggregation prone, for reasons we discuss below.

Last, to show that the observed divergent influence of coacervate droplets on protein localisation and aggregation kinetics is not limited to αSyn (and its variants), we repeated these experiments with insulin, which is known to form amyloid-like aggregates upon

incubation. Interestingly, we found that insulin could also be sequestered inside some coacervate droplets (RP3/polyU and pLys/ATP), excluded from others (pLys/pGlu 1:4 and 1:2), and accumulated at the interface in one case (pLys/pGlu 1:1) (Figure 6.11). We observed that aggregation of insulin was enhanced in the presence of RP3/polyU and pLys/ATP coacervates, while for pLys/pGlu coacervates at all charge ratios aggregation was suppressed (Figure 6.12 and Figure 6.13).
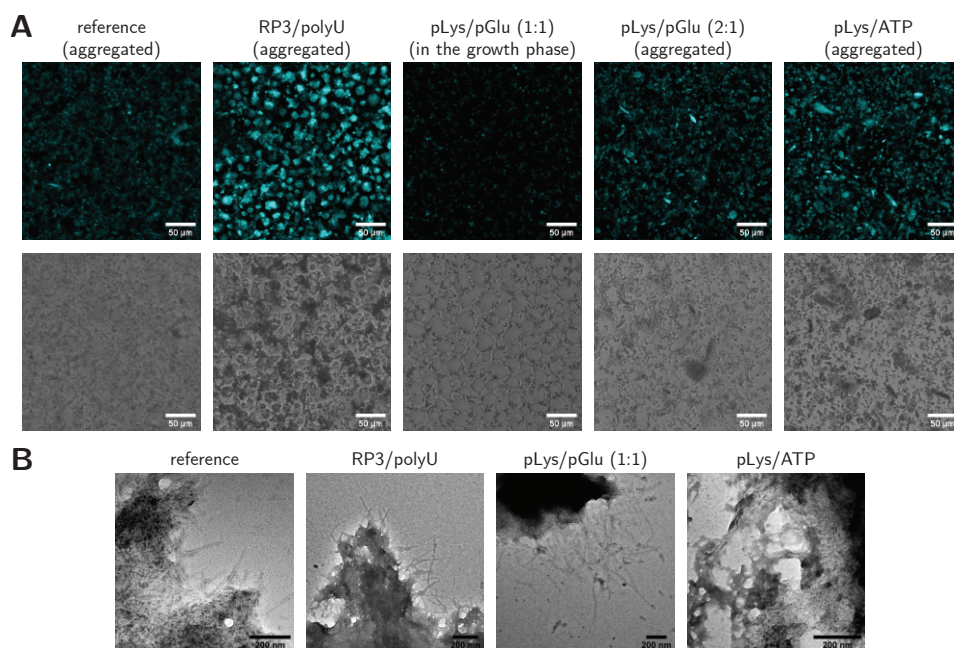
Figure 6.12: Characterisation of insulin aggregates formed in the absence and presence of coacervates. (A) Confocal microscope fluorescence images and transmission images collected at the end of the ThT aggregation assay. Apart from the image for pLys/pGlu at 1:1 charge ratio, which was still in the growth phase, images show samples that reached aggregation plateau or were in the final stage of the growth phase. Scale bars are 50 μm. (B) TEM images of insulin aggregates formed in the presence of different coacervate systems. Insulin aggregates appear as fine fibrils. Scale bars are 200 nm.

Figure 6.13: Analysis of insulin aggregation kinetics. (A) Distribution of the lag times (t_{lag}) and (B) distribution of the maximum aggregation rates (v_{max}) for insulin and all coacervate systems (supernatant – s, coacervate – c) and for the reference sample. Violin plots were prepared using Gaussian kernels with bandwidth determined automatically using Scott's method; density plots were cut at two bandwidth units past the extreme data points; violins are scaled to have the same area in supernatant–coacervate pairs.

6.5 Spatiotemporal mapping of the aggregation process

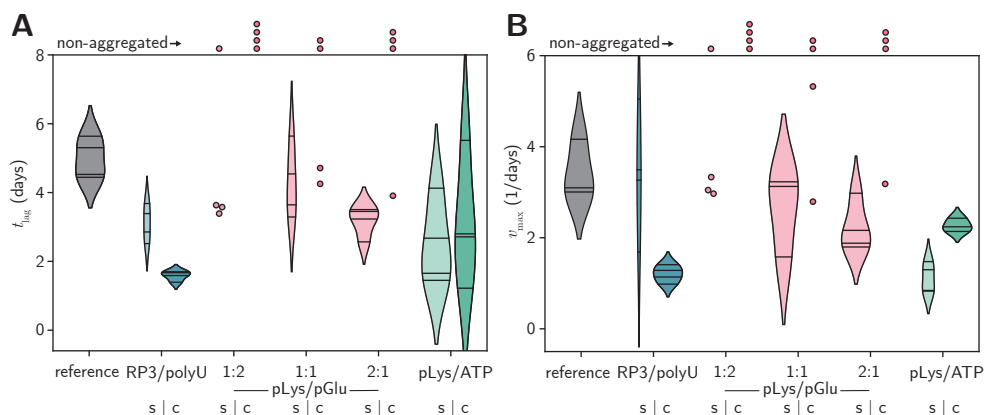To find out if the faster and slower aggregation is related to the location where aggregation takes place, as the partitioning data (Figure 6.4) seem to suggest, and to follow the spatiotemporal distribution of aggregates in the presence of coacervates, we developed an intramolecular FL-αSyn fluorescence resonance energy transfer (FRET) probe, similar to the probe used before to study conformations of αSyn at a single molecule level [26,27]. The probe includes two fluorescent dyes close to the region responsible for β-sheet formation: Alexa Fluor 546 and Alexa Fluor 647 (Figure 6.14A). Upon aggregation, the dye molecules become fixed close to each other, which results in enhanced energy transfer (Figure 6.14B). Experiments were performed in a similar fashion to the partitioning experiments, but the images were collected for several days and the samples were incubated at 37 °C. Collected fluorescence intensity images were used to create FRET efficiency maps, by calculating FRET efficiency for each pixel separately (Figure 6.15A).

We observed distinct behaviour for the different coacervates. In the case of RP3/polyU FRET signal increased throughout the entire coacervate droplet directly from the beginning, and was slightly enhanced at the interface, while it remained constant and low outside the droplets (Figure 6.15B and C). Please note that the FRET maps in Figure 6.15A combine both intensity and FRET signal, while Figure 6.15B and C are based on FRET signal only, so they reflect the conformation of the molecule but not the concentration. After 60 hours of incubation FRET signal increased inside the droplets, which suggests that the aggregates are formed inside the droplets, or at the interface and then
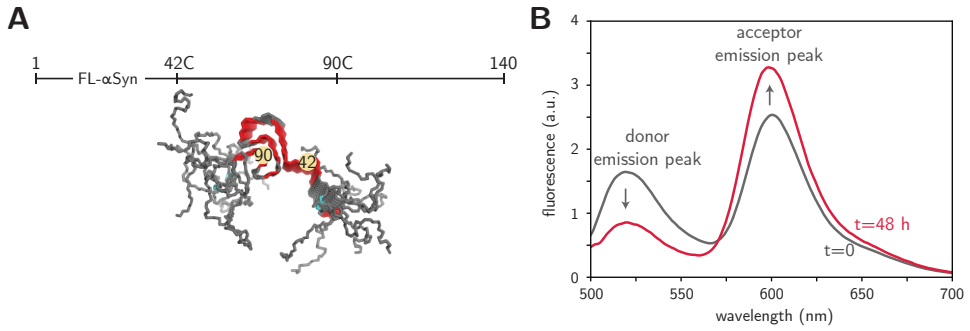
Figure 6.14: An intramolecular FL-αSyn FRET probe reports on fibril formation. (A) Positions of FRET labels in the FL-αSyn chain (PDB ID: 2N0A). (B) Fluorescence spectra of the FL-αSyn-based FRET probe in solution (in bulk), shortly after preparing the solution ($t=0$) and after 48 hours of incubation at 37 °C ($t=48$ h).
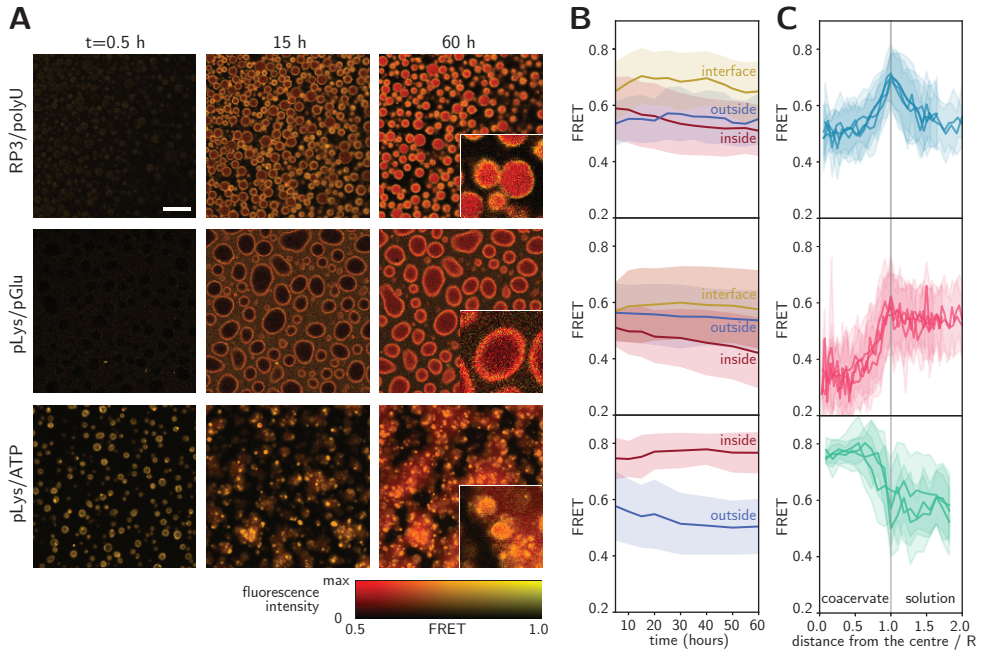
Figure 6.15: Aggregation monitored by FRET. (A) FRET maps of coacervate samples incubated with FRET-labelled FL-αSyn. Scale bar is 20 μm. Insets show three times enlarged part of the image at 60 hours; the experiment was performed in the presence of the FRET probe and 10 μM (RP3/polyU and pLys/ATP) or 40 μM (pLys/pGlu) concentration of nonlabelled FL-αSyn. (B) Changes in FRET intensity in different areas of the coacervate systems over time. (C) FRET intensity radial profiles for coacervate droplets after 60 hours of incubation (distance from the droplet center normalised by the droplet diameter, angular averaging).

127

move to the interior (Figure 6.15A). For pLys/pGlu, the FRET efficiency was higher at the interface than in the surrounding solution, and interestingly, also higher than inside the droplets, even after 60 h. This suggests a more compact conformation and high concentration of FL-αSyn at the interface, potentially promoting faster nucleation into fibrils, which form at the surface of the droplets, but do not move towards the interior. In the case of pLys/ATP, aggregation starts immediately, with practically no lag phase (as also observed in the kinetic experiments, Figure 6.8). The highest FRET efficiency was observed inside the coacervate droplets, and the droplets seem to mature over time, losing their liquid properties. Therefore, for the pLys/ATP system we also expect that the aggregates nucleate within the coacervate droplets, despite the enhanced concentration of monomeric αSyn at the interface, as observed in the partitioning experiments (Figure 6.4A). In FRET experiments, no accumulation of aggregated FL-αSyn could be observed at the interface of pLys/ATP coacervates. Presumably, even if aggregates nucleate at the interface, they immediately move to the interior of the droplets.
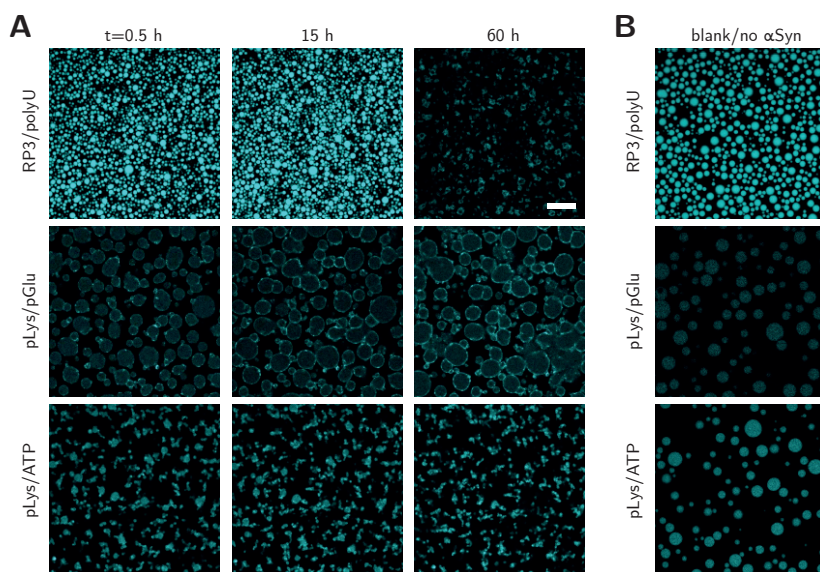
Figure 6.16: Coacervates with aggregated FL-αSyn show different ThT signal from empty coacervate droplets. (A) ThT aggregation assay under confocal microscope of FL-αSyn in presence of different coacervate systems. Scale bar is 20 µm. (B) Partitioning of ThT into coacervate systems (without added FL-αSyn).

Similar observations were made using unlabelled FL-αSyn and ThT as a dye to stain the fibrils under the microscope (Figure 6.16). In this case, presence of protein aggregates is simply indicated by high ThT fluorescence intensity. Direct analysis of the fluorescence intensities is complicated in this case, because free ThT also partitions into coacervates (Figure 6.16B). Nevertheless, we could observe significant increases in fluorescence intensity upon aggregation. In the presence of RP3/polyU and pLys/ATP droplets, aggregates were formed within the droplets resulting in irregular solid-like particles. In the presence of

pLys/pGlu coacervates, the highest fluorescence intensity was observed for the coacervate interface, suggesting that aggregation is promoted by droplet interface, as observed also for the FRET probe.

6.6 A kinetic model of protein aggregation accelerated or suppressed by condensates

Our microscopy experiments suggest that the presence of the coacervate droplets can affect the αSyn aggregation process either through partitioning of the protein into coacervate droplets or through αSyn–coacervate interface interactions. To prove that these interactions can be also the reason of differences observed in the kinetics of the aggregation process, we developed and fitted kinetic models to our experimental data (fits are presented in Figure 6.17). Two separate models were used to match the observations in Figure 6.4 and Figure 6.15: (i) αSyn is excluded from or sequestered by the droplets and aggregation can take place both inside and outside the coacervate droplets, (ii) αSyn is localised at the coacervate interface and heterogeneous nucleation followed by further aggregation can take place at the interface. These models were described in Chapter 5, so here we only present a brief explanation. The kinetic models are based on the three-step nucleation-elongation-secondary nucleation model proposed by Ferrone et al. [28]. Formation of protein amyloid fibrils (a) is initiated by nucleation, (b) the increase of aggregate mass is mostly caused by the elongation of fibrils, while (c) their presence also has an autocatalytic effect on the formation of new fibrils through secondary nucleation. In the simple case of aggregation in a homogeneous solution, it has been shown that these three processes (with three rate constants) are sufficient to describe the aggregation kinetics of various amyloidogenic proteins [29]. We developed two new models that describe fibril formation via the same three steps (a, b, c), but now: (i) taking place both outside and inside coacervate droplets, or (ii) taking place both outside and at the interface of coacervate droplets.

In the first case of exclusion or sequestration, we assumed that αSyn monomers are freely exchanged between the dilute phase (which we call supernatant hereafter) that surrounds the coacervate droplets and that the exchange of αSyn between the supernatant and the condensed phase is much faster than the aggregation process itself. Consequently, local αSyn concentrations are always equilibrated (i.e., the partition coefficient, as determined in Figure 6.5A, is constant). Aggregation of αSyn can occur both in the supernatant and in the coacervate droplets and the rate constants of each step of the aggregation process can be different in both phases (subsection 5.3.3), which makes our approach different from previous aggregation models. Kinetic rate constants for the data obtained for αSyn in the supernatant were determined by fitting a simple aggregation model (for a one-phase system) and were further used as input for the supernatant phase when fitting parameters for the coacervate-containing samples (Figure 6.17), thereby reducing the number of fit parameters. Last, the fibrils are assumed to be immobile, in accordance with previous models [30]: once formed they remain in the dilute or condensed phase.

Partitioning into the coacervate phase can accelerate aggregation because of increased local αSyn concentrations, but different rate constants for the aggregation process inside
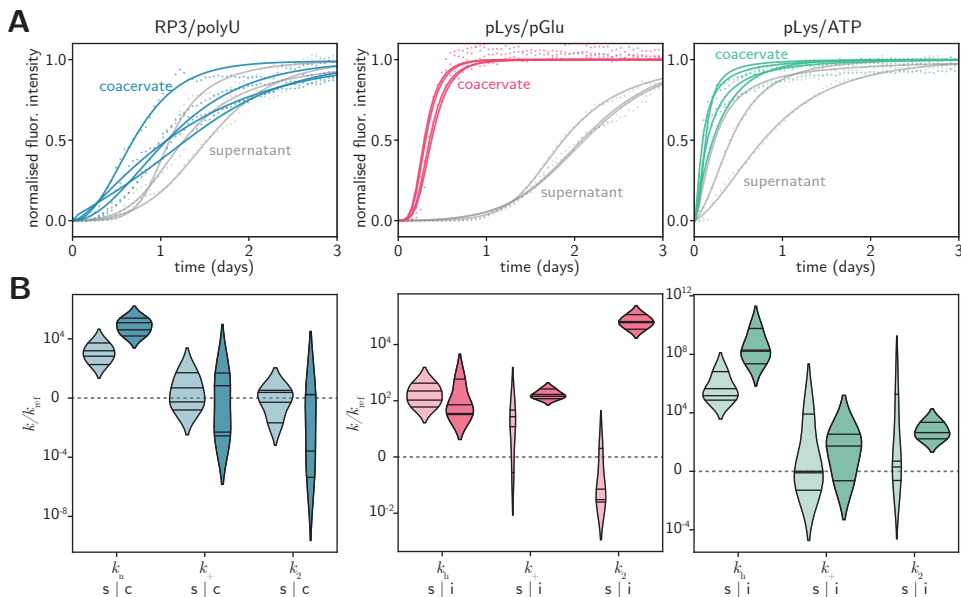
Figure 6.17: Fitting of the aggregation models. (A) Fits to the experimental data for RP3/polyU with FL-αSyn for the aggregation-in-droplets model and fits to the experimental data for pLys/p-Glu and pLys/ATP with FL-αSyn for the interface-aggregation model. (B) Resulting aggregation kinetic rate constants, for the dilute-supernatant phase (s) and for the coacervate/interface phase (c/i), normalised by values for the reference sample (without coacervate components). Violin plots were prepared analogously to plots in Figure 6.8.

the coacervate droplets might mask this effect or further enhance it. In our experiments, we know the local concentration of αSyn from partitioning studies (Figure 6.5A), and can therefore deduce the additional influence of the coacervate environment on the rate constants. We note that the fits can only be used to obtain an order-of-magnitude estimate of the rate constants, as it is difficult to determine the separate contributions of each step in the aggregation process from a fit without comparing data collected for different αSyn concentrations. Nevertheless, we found significant differences between the rate constants in the supernatant and the coacervate phase. The fitted aggregation curves for RP3/polyU suggest that the primary nucleation rate of FL-αSyn inside the droplets is higher than in the supernatant, while the elongation and secondary nucleation rates are slightly lower, implying that the RP3/polyU coacervate environment has a destabilising effect on monomeric FL-αSyn, but a stabilising effect on oligomers and fibrils, under the assumption that all steps in the aggregation process are not diffusion limited. For NACore, which was also sequestered in RP3/polyU coacervates, we found a similar trend, although the model is not able to capture the very sharp onset of aggregation in some cases.

The truncated αSyn-108 was excluded from all types of coacervates and, hence, we did not observe any significant difference in aggregation kinetics. Even in the presence of droplets, the aggregation process takes place predominantly in the supernatant, as

there is hardly any αSyn-108 present inside the droplets. Therefore, we could not reliably determine the rate constants of aggregation for αSyn-108 in the coacervates. The same is true for NACore in the presence of pLys/pGlu coacervates and pLys/ATP coacervates where we observed an overall suppressed aggregation, manifested in a longer lag time, but the monomers did not show significant sequestration. On the contrary, they are excluded from pLys/pGlu coacervates and indifferent to pLys/ATP coacervates. Therefore, a simple three-step model (as described in section 5.3) cannot explain the suppressed aggregation. It is possible that while free peptides were excluded, small oligomers, which form in early stages of the aggregation process, are sequestered by the droplets and prevented from further growth.

In other cases, we observed strong accumulation of the αSyn variants at the interface of coacervates, rather than inside, which suggests a different mechanism of aggregation. Therefore, we developed a kinetic model to describe binding of the protein to the interface and further heterogeneous nucleation and elongation. The simplest model involving only binding (dependent on the number of binding sites and the binding constant) and heterogeneous (primary) nucleation was not able to capture the very rapid aggregation observed in some cases. When we also allowed elongation and secondary nucleation to occur at the interface, we could capture the rapid global aggregation (Figure 6.17). Note that this model assumes that binding to the interface is an equilibrium process, governed by thermodynamics. Although it is known that interfaces can give rise to kinetic trapping of proteins, we expect that the fluid, low-tension interface of a coacervate droplet [31] does not lead to kinetic trapping, which is supported by the fact that αSyn remained mobile at the interface and we observed no significant difference in the interfacial accumulation of αSyn up to 48 hours after incubation. The (local) concentration of monomers at the interface, $[S]_{\text{int}}$, as estimated from partitioning experiments (Figure 6.4) to be roughly 200 and 300 µM for the pLys/pGlu and pLys/ATP systems, respectively, which is low compared to the local concentration of pLys/pGlu or pLys/ATP inside the coacervates. Therefore, the use of a binding model that assumes single-layer adsorption seems justified. For pLys/ATP coacervates the primary nucleation rate constant at the interface is several orders of magnitude higher than in the supernatant, while other rate constants appear the same. This can explain the very rapid onset of aggregation with virtually no lag time for pLys/ATP. For pLys/pGlu coacervates, primary nucleation and elongation seem unchanged, but the secondary nucleation rate constant is significantly faster at the interface, which explains the very rapid increase in ThT fluorescence after a lag phase (Figure 6.17A).

To confirm that the coacervate interface is crucial in enhancing the aggregation kinetics we have performed additional experiments in which we changed the amount of available surface area. In the first experiment, we varied the amount of droplets-forming material. In the second experiment, we centrifuged the coacervate dispersions before adding αSyn, causing the droplets to fuse (and thus reducing the available surface area). In both experiments we could observe that reducing the droplet surface area resulted in slower aggregation (Figure 6.18).
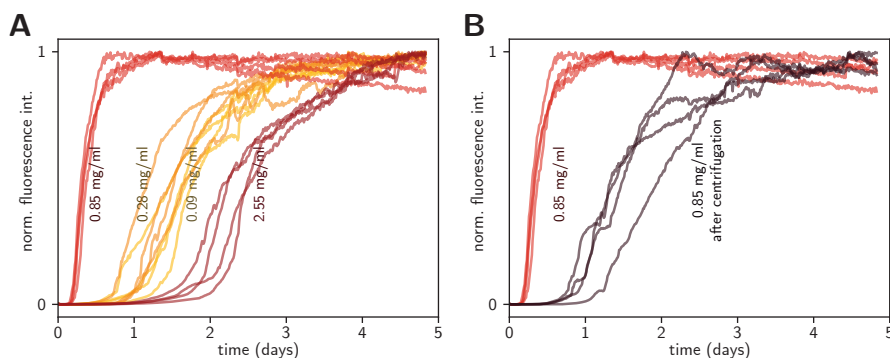
Figure 6.18: Coacervate surface area affects FL-αSyn aggregation kinetics in the presence pLys/p-Glu coacervates. (A) Aggregation traces of FL-αSyn in the presence of different amounts of pLys/pGlu coacervates. (B) Aggregation traces of FL-αSyn in the presence of coacervates dispersed in solution and fused at the bottom of the plate after centrifugation.

6.7 Conclusion

Our results show that condensates that are composed of non-aggregating material themselves can influence the aggregation of amyloidogenic proteins, such as αSyn and insulin, significantly and in a wide variety of ways. For FL-αSyn we observed an increase in overall aggregation propensity for all systems. As suggested before by Weber and co-workers[30], this influence can be at least partially caused by higher local concentration of the aggregating protein inside or at the surface of coacervates. However, partition coefficients determined for the studied systems do not seem to explain the difference in the aggregation kinetics, unless we assume different aggregation rate constants inside the coacervate droplets and in the surrounding solution. In particular, we find that the elongation and secondary nucleation rate constants are lower inside coacervates than in solution, indicating a partly stabilising effect of the coacervate environment and a suppressing role in part of the aggregation process. Such differences may be expected, as the more crowded and hydrophobic coacervate environment[32–34], which is rich in functional groups that can interact with αSyn, affects the protein conformation and its tendency to aggregate. By contrast, our partitioning data combined with FRET microscopy indicate a different mechanism of accelerated aggregation for pLys/ATP and pLys/pGlu coacervates, which both localised FL-αSyn at their interface giving rise to surface-bound enhanced primary nucleation (pLys/ATP) and secondary nucleation (pLys/pGlu).

We have thus observed for the first time that the coacervate droplet interface can serve as a nucleation site for protein aggregation. Relatively high apparent kinetic rate constants determined for FL-αSyn at the pLys/pGlu droplets interface may suggest that the coacervate droplets do not only serve as simple heterogeneous catalysis nucleation sites, but they also provide a distinct physicochemical environment or conformational arrangement, in which protein aggregation is substantially enhanced. It is interesting to note that very recently different behaviour has been observed for FL-αSyn under conditions

that promote phase separation of FL-αSyn itself (i.e., in the presence of PEG and at high concentrations). Under such conditions, FL-αSyn forms liquid droplets that undergo maturation (a transition into solid aggregates) and this transition was found to be initiated at the centre of the droplets, suggesting that FL-αSyn droplets also provide a distinct environment in which the kinetic parameters of aggregation are altered, just like in the case of our pLys/pGlu droplets[35].

Furthermore, our results show that the influence of the coacervate droplets on aggregation kinetics depends on both the coacervate composition and the sequence/length of the aggregating protein. While aggregation of the full-length variant was accelerated in the presence of all coacervate systems, aggregation of the truncated variant, αSyn-108, was not significantly affected. This can be attributed to a different affinity of the full-length and the truncated αSyn variants to the coacervate material, and particularly to the positively charged components. The absence of the negatively charged C-terminal part in αSyn-108 makes this variant slightly positively charged at neutral pH (pI = 9.16), while FL-αSyn is strongly negatively charged (pI = 4.67). FL-αSyn has been shown before to aggregate faster in the presence of polycations in solution, and similar acceleration may occur inside coacervates or at their interface[36].

Another interesting observation is that pLys/pGlu and pLys/ATP affect the aggregation process differently, although they both contain pLys. The reason for this difference is the binding strength of the counterions present in these coacervate droplets. ATP has fewer negative charges and binds less strongly to pLys than pGlu, which is evidenced by the lower critical salt concentration of pLys/ATP droplets. As a result, FL-αSyn can displace ATP more easily than pGlu and bind more strongly to pLys. We hypothesize that stronger binding of the negatively charged tail of αSyn makes the protein more prone to aggregation, similar to previous reports[37,38]. In addition, the weaker interaction of ATP compared to pGlu leads to a lower viscosity inside the pLys/ATP condensates, which facilitates movement of aggregates and FL-αSyn bound to pLys inside the droplets.

Last, coacervate droplets are also able to slow down aggregation, which was most prominent for NACore peptide (Figure 6.10) with RP3/polyU and pLys/pGlu coacervates. This may be explained by the sequestration of free peptides and small oligomers inside the coacervate (Figure 6.4), in a relatively stable conformation, not prone to rapid aggregation, an effect we also observed to a limited extent and were able to quantify for FL-αSyn in RP3/polyU coacervates (Figure 6.17B). In combination with lowered monomer concentration is the surrounding solution, this can result in overall aggregation inhibition (similarly to the sequestration of amyloid-β(1-42) described before[39]). Unexpetedly, in the case of pLys/pGlu droplets, where labelled NACore peptide remained excluded from the droplets, the aggregation was also slowed down. It is possible that while free peptides were excluded, small oligomers, which form in early stages of the aggregation process, are sequestered by the droplets and prevented from further growth. However, proving this is impracticable, because any action to separate the droplets from the supernatant will most likely disrupt such oligomers.

In conclusion, we show that pre-existing liquid condensates can affect protein amyloid formation in vitro, both accelerating and slowing down the reactions. We expect that the same process can happen in living cells, which contain multiple membraneless organelles, formed upon LLPS. By sequestering amyloidogenic proteins, such biological condensates

may prevent protein aggregation, but it is also possible that they can function as heterogeneous nucleation sites. This provides a new perspective on the early stages of amyloid formation by αSyn (and protein aggregation in general) in the complex cellular environment.

6.8 Experimental details

6.8.1 Materials

Poly-L-lysine hydrobromide (MW 15-30 kDa), adenosine 5'-triphosphate (ATP) disodium salt, polyuridylic acid potassium salt, buffers and thioflavin T (ThT) were purchased from Sigma-Aldrich. RP3 (RRASLRRASLRRASL-NH2), and NACore (GAVVTGVTAVA) peptides were purchased from CASLO ApS (Denmark). Labelled NACore peptide was synthesised on solid phase using standard Fmoc peptide synthesis strategy. Poly-D,L-lysine hydrobromide (MW = ca. 21 kDa) and poly-D,L-glutamic acid sodium salt (MW = ca. 15 kDa) were purchased from Alamanda Polymers (USA). Alexa Fluor maleimides were purchased from Thermo Fisher. Poly-L-lysine grafted with poly(ethylene glycol) (PLL-g-PEG) was purchased from SuSoS AG (Switzerland). Insulin (human, recombinant) was purchased from FujiFilm/Wako Pure Chemical Corporation. 5(6)-Carboxyfluorescein N-hydroxysuccinimide ester (FAM-NHS) and sodium bicarbonate were purchased from Sigma-Aldrich All aqueous solutions were filtered before use using Acrodisc 0.2 µm nylon syringe filters (Sigma-Aldrich) or Pierce cellulose acetate filter spin cups with 0.45 µm pore size (Thermo Fisher).

6.8.2 Protein preparation and labelling

Wild-type FL-αSyn, αSyn-108 and the cysteine mutants were expressed and purified as previously described (74). Purified proteins were stored at a concentration of 200 µM in 10 mM Tris-HCl, pH 7.4 at -80 °C, supplemented with 1 mM DTT for the cysteine mutants. Single-labelled proteins were labelled according to the dye manufacturer's procedures. For labelling of double-cysteine mutant (42C 90C), the first labelling step (with donor dye) was performed according to the dye manufacturer procedures, using 1:1 protein to dye ratio. Subsequently, the protein was incubated with pre-washed Activated Thiol–Sepharose 4B (Cytiva, USA) for 1 hour, rotating in the dark at 4 °C. Next, the resin was washed with several volumes of 10 mM Tris-HCl, pH 7.4, followed by elution of single and double labelled αSyn using a buffer containing 25 mM DTT. Eluted fractions were pooled, concentrated to about 0.5 ml and desalted. Triple excess of acceptor dye was added to the concentrated protein and the solution was incubated for 1 hour at room temperature. Unbound dye was removed using Amicon Ultra-4/15 centrifugal filters with suitable MWCO. Protein solutions were filtered using Pierce cellulose acetate filter spin cups (Thermo Fisher) before every aggregation kinetics assay and concentration was determined based on absorbance ($\epsilon = 5600$ M^{-1}cm^{-1} for wild-type αSyn and $\epsilon = 1400$ M^{-1}cm^{-1} for αSyn-108).

6.8.3   Preparation of modified glass slides

All glass slides used for microscopy were modified according to the following procedure. First, the slide was washed thoroughly with milliQ water. Subsequently, the surface intended to be modified was cleaned with oxygen plasma and 0.01 mg/ml solution of PLL-g-PEG in 10 mM HEPES buffer (pH 7.4) was applied on the glass immediately after plasma treatment. Glass was incubated with the PLL-g-PEG solution for 2 hours at room temperature. Subsequently it was rinsed 3 times with 10 mM HEPES buffer (pH 7.4), 3 times with milliQ water and dried with pressurised air. Modified slides were stored at room temperature and used within one week.

6.8.4   Coacervate systems

Unless specified otherwise, the coacervate systems were prepared in 50 mM HEPES buffer (pH 7.4) with 100 mM NaCl and 100 μM EDTA. All coacervate systems were prepared at 1:1 positive to negative charge ratio and 0.85 mg/ml total concentration of coacervate-forming material (0.53 mg/ml RP3 with 0.32 mg/ml polyU; 0.49 mg/ml pLys with 0.36 mg/ml pGlu; 0.23 mg/ml pLys with 0.62 mg/ml ATP).

6.8.5   Partitioning of labelled protein

Localisation of labelled proteins was studied using confocal microscopy. Leica SP8x confocal microscope equipped with a 40x magnification water-immersion objective was used. Samples were placed in 18-well chambered glass coverslips (Ibidi GmbH, Germany), previously modified with PLL-g-PEG. Partition coefficients were determined by calculating ratio of fluorescence intensity in the condensed phase to fluorescence intensity in the outer phase (average intensity values from at least 10 droplets and from the outer phase of a similar area was used). Background signal of the coacervate sample without labelled protein was subtracted separately for condensed and supernatant.

6.8.6   ThT aggregation kinetics assays

To estimate the aggregation kinetic parameters, we have performed standard thioflavin T (ThT) aggregation assays. Upon binding to β-sheets, ThT fluorescence intensity increases by several orders of magnitude and the changes of fluorescence in the solutions of aggregating protein are proportional to the amount of aggregate formed ($[M]$). Aggregation assays were performed under following conditions: 50 mM HEPES (pH 7.4), 100 mM NaCl, 100 μM EDTA, 20 μM ThT, and 40 μM FL-αSyn or αSyn-108, or 160 μM of NACore. All aggregation assays were performed in non-binding 384-well plates with black walls (Greiner Bio-One GmbH, Austria), at 37 ˚C. To prevent evaporation, wells in the two outer rows were always filled with water and the plate was sealed with film. Measurements were performed using Tecan Spark or Tecan Infinite M200 microplate reader. Fluorescence intensity was recorded every 12 min using bottom readout with continuous linear shaking in between. Excitation and emission wavelength range was controlled using monochromators for Tecan Infinite m200 (respectively 440 nm with 9 nm bandwidth and 480 nm with 20 nm bandwidth) or filters for Tecan Spark (respectively 430 nm with 20 nm

bandwidth and 460 nm with 20 nm bandwidth). To extract the basic kinetic parameters (t_{lag} and v_{max}) from the ThT fluorescence traces we fitted simple aggregation model and used the maximum slope of the curve as v_{max} and the intersection of line going through the max slope point and the baseline was used as t_{lag} (Figure 6.6).

6.8.7 Preparation of samples and transmission electron microscopy

Samples after the ThT aggregation kinetics assay in 384-well plates were used for electron microscopy experiments. In order to dissolve the coacervate material and separate the αSyn aggregates, sodium chloride solution was added to the selected wells, to final concentration of 300 mM sodium chloride. After incubation for 5 min at room temperature, plate was centrifuged for 10 min at 1000 rcf. Subsequently, solution was gently collected from the selected wells and 50 µl of milliQ water was added. The plate was centrifuged again with the same settings and again solution was gently collected from the selected wells. Any precipitate from the selected wells was resuspended in 20 µl of milliQ water, and subsequently 2 µl of the suspension was transferred onto a TEM grid (EM-Tec formvar carbon support film on copper, 300 square mesh, Micro to Nano, the Netherlands). Samples were blotted with filter paper, stained with 1.5 µl of 2% w/w sodium phosphotungstate solution (adjusted to pH 7.4), washed with 2 µl of water and left to dry overnight. Imagining was performed using JEOL JEM-1400 FLASH.

6.8.8 Intramolecular FRET experiments

FRET experiment was performed using a Leica SP8x confocal microscope equipped with 40x magnification water-immersion objective. Samples were placed in 18-well chambered glass coverslips (Ibidi GmbH, Germany), previously modified with PLL-g-PEG, and the whole setup was incubated at 37 °C during the experiment. FRET probe was added at 0.01 ratio to the nonlabelled FL-αSyn (0.1 or 0.4 µM and 10 or 40 µM, respectively), and other components remained the same as for the ThT aggregation kinetic assay. Samples were excited at 488 nm, and the emission was recorded at 515 to 530 nm for the donor and 590 to 610 nm for the acceptor. Fluorescence intensity images were saved in 8-bit 512 × 512 pixel format. FRET value was calculated for each pixel using the following formula:

$$\text{FRET} = \frac{\text{acceptor channel intensity}}{\text{donor channel intensity} + \text{acceptor channel intensity}}$$

The FRET value was not determined if intensities for both channels were lower than 2, which is close to the detector's dark count. A 512 × 512 array of FRET intensities was further converted into an 8-bit 512 × 512 image and visualised using a custom hue/brightness two-dimensional colour map. Hue corresponds to the FRET value scaled from 0.5 to 1 (pixels with values below 0.5 have the same hue as pixel with FRET equal 0.5). Brightness is proportional to the sum of fluorescence intensity for both channels, scaled from 0 to the value for the 95th percentile in the image collected after 60 hours (pixels with higher intensity have the same *max* brightness). The FRET experiment in

bulk (Figure 6.14) was performed using 0.4 µM concentration of the FRET probe and 40 µM concentration of nonlabelled FL-αSyn and incubated at 37 °C in an eppendorf tube. Fluorescence spectra were measured using a JASCO FP-8300ST spectrofluorometer.

6.8.9 ThT aggregation kinetics under confocal microscope

ThT aggregation kinetics under microscope experiment was performed using a Leica SP8x confocal microscope equipped with 40x magnification water-immersion objective. Samples were placed in 18-well chambered glass coverslips (Ibidi GmbH, Germany), previously modified with PLL-g-PEG and the whole setup was incubated at 37 °C during the experiment. Composition of samples was the same as for the plate-reader ThT aggregation kinetic assays. Samples were excited at 405 nm and the emission was recorded at 440-600 nm. Fluorescence intensity images were saved in 8-bit 512x512 pixels format.

6.8.10 Determination of critical salt concentration of coacervate systems with αSyn variants

Critical salt concentration was determined by titration in a plate reader. Samples of 50 µl with the same composition as for the ThT aggregation kinetic assay but without NaCl (50 mM HEPES, 100 µM EDTA, 20 µM ThT, and 40 µM FL-αSyn or αSyn-108, or 160 µM of NACore) were placed in wells of 384-well plate (non-binding, black walls, Greiner Bio-One GmbH, Austria) and titrated by adding stepwise 750 mM NaCl solution. Each step consisted of adding 2 µl of NaCl solution to each well, waiting 20 seconds and measuring absorbance at 600 nm. Experiment was repeated 3 times for each composition. Critical salt concentration was determined by reading x-coordinate of the intersection of the tangent of the absorbance vs. NaCl concentration curve at its maximal slope and the baseline.

6.8.11 Labelling of insulin

Insulin was labelled with FAM-NHS using the following method. Insulin was dissolved at 5 mg/ml concentration in sodium bicarbonate solution (0.1 M). FAM-NHS was dissolved in DMF at 10 mg/ml. Solution of FAM-NHS (54 µl) was added to the solution of insulin (1.32 ml) and the mixture was stirred gently at 4 °C overnight. Subsequently, insulin was separated from unbound dye using Amicon Ultra-15 centrifugal filters with 3 kDa MWCO, by washing with 0.1 M carbonate buffer (4 times) and then 0.005 M carbonate buffer (5 times).

6.8.12 Partitioning of FAM-labelled insulin

Partitioning of FAM-labelled insulin was studied the same way as described for labelled αSyn variants.

6.8.13 Statistical analysis

Microscopy images were analyzed using FIJI distribution of ImageJ. Error bars and error ranges of transfer energies and FRET plots were determined using SDs of pixel intensity values within the selected range. Plots in Figure 6.15B were prepared by manually selecting parts of the image. Plots in Figure 6.4B and Figure 6.15C were prepared using radial profile angle plugin for ImageJ. Violin plots were prepared according to the description under Figure 6.8. Fitting of the aggregation kinetic models in Figure 6.17 was performed using basinhopping function from scipy.optimize library in Python.

6.9 Contributions and acknowledgements

Bibliography

[1] W. M. Aumiller and C. D. Keating, "Phosphorylation-mediated RNA/peptide complex coacervation as a model for intracellular liquid organelles," *Nat. Chem.*, vol. 8, no. 2, pp. 129–137, 2016.

[2] T. Ukmar-Godec, S. Hutten, M. P. Grieshop, N. Rezaei-Ghaleh, M. S. Cima-Omori, J. Biernat, E. Mandelkow, J. Söding, D. Dormann, and M. Zweckstetter, "Lysine/RNA-interactions drive and regulate biomolecular condensation," *Nat. Commun.*, vol. 10, no. 1, p. 2909, 2019.

[3] I. Alshareedah, M. M. Moosa, M. Raju, D. A. Potoyan, and P. R. Banerjee, "Phase transition of RNA-protein complexes into ordered hollow condensates," *Proc. Natl. Acad. Sci. U. S. A.*, vol. 117, no. 27, pp. 15650–15658, 2020.

[4] S. L. Perry, L. Leon, K. Q. Hoffmann, M. J. Kade, D. Priftis, K. A. Black, D. Wong, R. A. Klein, C. F. Pierce, K. O. Margossian, J. K. Whitmer, J. Qin, J. J. De Pablo, and M. Tirrell, "Chirality-selected phase behaviour in ionic polypeptide complexes," *Nat. Commun.*, vol. 6, no. 1, p. 6052, 2015.

[5] S. Koga, D. S. Williams, A. W. Perriman, and S. Mann, "Peptide-nucleotide microdroplets as a step towards a membrane-free protocell model," *Nat. Chem.*, vol. 3, no. 9, pp. 720–724, 2011.

[6] K. K. Nakashima, J. F. Baaij, and E. Spruijt, "Reversible generation of coacervate droplets in an enzymatic network," *Soft Matter*, vol. 14, no. 3, pp. 361–367, 2018.

[7] T. Ishida and K. Kinoshita, "PrDOS: Prediction of disordered protein regions from amino acid sequence," *Nucleic Acids Res.*, vol. 35, no. SUPPL.2, pp. W460–W464, 2007.

[8] P. L. Onuchic, A. N. Milin, I. Alshareedah, A. A. Deniz, and P. R. Banerjee, "Divalent cations can control a switch-like behavior in heterotypic and homotypic RNA coacervates," *Sci. Rep.*, vol. 9, no. 1, p. 12161, 2019.

[9] K. K. Nakashima, M. H. van Haren, A. A. André, I. Robu, and E. Spruijt, "Active coacervate droplets are protocells that grow and resist Ostwald ripening," *Nat. Commun.*, vol. 12, no. 1, pp. 1–11, 2021.

[10] T. Lu and E. Spruijt, "Multiphase Complex Coacervate Droplets," *J. Am. Chem. Soc.*, vol. 142, no. 6, pp. 2905–2914, 2020.

[11] P. M. McCall, S. Srivastava, S. L. Perry, D. R. Kovar, M. L. Gardel, and M. V. Tirrell, "Partitioning and Enhanced Self-Assembly of Actin in Polypeptide Coacervates," *Biophys. J.*, vol. 114, no. 7, pp. 1636–1645, 2018.

[12] T. Kaur, M. Raju, I. Alshareedah, R. B. Davis, D. A. Potoyan, and P. R. Banerjee, "Sequence-encoded and composition-dependent protein-RNA interactions control multiphasic condensate morphologies," *Nat. Commun.*, vol. 12, no. 1, p. 872, 2021.

[13] T. Lu, S. Liese, L. Schoenmakers, C. A. Weber, H. Suzuki, W. T. Huck, and E. Spruijt, "Endocytosis of Coacervates into Liposomes," *J. Am. Chem. Soc.*, vol. 144, no. 30, pp. 13451–13455, 2022.

[14] T. J. Nott, T. D. Craggs, and A. J. Baldwin, "Membraneless organelles can melt nucleic acid duplexes and act as biomolecular filters," *Nat. Chem.*, vol. 8, no. 6, pp. 569–575, 2016.

[15] S. Elbaum-Garfinkle, Y. Kim, K. Szczepaniak, C. C. H. Chen, C. R. Eckmann, S. Myong, and C. P. Brangwynne, "The disordered P granule protein LAF-1 drives phase separation into droplets with tunable viscosity and dynamics," *Proc. Natl. Acad. Sci. U. S. A.*, vol. 112, no. 23, pp. 7189–7194, 2015.

[16] A. Patel, L. Malinovska, S. Saha, J. Wang, S. Alberti, Y. Krishnan, and A. A. Hyman, "Biochemistry: ATP as a biological hydrotrope," *Science*, vol. 356, no. 6339, pp. 753–756, 2017.

[17] T. H. Kim, B. J. Payliss, M. L. Nosella, I. T. Lee, Y. Toyama, J. D. Forman-Kay, and L. E. Kay, "Interaction hot spots for phase separation revealed by NMR studies of a CAPRIN1 condensed phase," *Proc. Natl. Acad. Sci. U. S. A.*, vol. 118, no. 23, p. e2104897118, 2021.

[18] N. A. Yewdall, A. A. André, M. H. van Haren, F. H. Nelissen, A. Jonker, and E. Spruijt, "ATP:Mg2+ shapes material properties of protein-RNA condensates and their partitioning of clients," *Biophys. J.*, vol. 121, no. 20, pp. 3962–3974, 2022.

[19] M. G. F. Last, S. Deshpande, and C. Dekker, "ph-controlled coacervate–membrane interactions within liposomes," *ACS Nano*, vol. 14, pp. 4487–4498, 4 2020.

[20] N. Martin, M. Li, and S. Mann, "Selective Uptake and Refolding of Globular Proteins in Coacervate Microdroplets," *Langmuir*, vol. 32, no. 23, pp. 5881–5889, 2016.

[21] S. Lindhoud, L. Voorhaar, R. D. Vries, R. Schweins, M. A. Stuart, and W. Norde, "Salt-induced disintegration of lysozyme-containing polyelectrolyte complex micelles," *Langmuir*, vol. 25, no. 19, pp. 11425–11430, 2009.

[22] W. C. Blocher McTigue and S. L. Perry, "Protein Encapsulation Using Complex Coacervates: What Nature Has to Teach Us," *Small*, vol. 16, no. 27, p. 1907671, 2020.

[23] N. A. Zervoudis and A. C. Obermeyer, "The effects of protein charge patterning on complex coacervation," *Soft Matter*, vol. 17, no. 27, pp. 6637–6645, 2021.

[24] H. Naiki, K. Higuchi, M. Hosokawa, and T. Takeda, "Fluorometric determination of amyloid fibrils in vitro using the fluorescent dye, thioflavine T," *Anal. Biochem.*, vol. 177, no. 2, pp. 244–249, 1989.

[25] H. Levine, "Thioflavine T interaction with synthetic Alzheimer's disease β-amyloid peptides: Detection of amyloid aggregation in solution," *Protein Sci.*, vol. 2, no. 3, pp. 404–410, 1993.

[26] M. A. Fakhree, I. S. Nolten, C. Blum, and M. M. Claessens, "Different Conformational Subensembles of the Intrinsically Disordered Protein α-Synuclein in Cells," *J. Phys. Chem. Lett.*, vol. 9, no. 6, pp. 1249–1253, 2018.

[27] G. Veldhuis, I. Segers-Nolten, E. Ferlemann, and V. Subramaniam, "Single-molecule FRET reveals structural heterogeneity of SDS-bound α-synuclein," *ChemBioChem*, vol. 10, no. 3, pp. 436–439, 2009.

[28] F. A. Ferrone, J. Hofrichter, and W. A. Eaton, "Kinetics of sickle hemoglobin polymerization. II. A double nucleation mechanism," *J. Mol. Biol.*, vol. 183, no. 4, pp. 611–631, 1985.

[29] G. Meisl, J. B. Kirkegaard, P. Arosio, T. C. Michaels, M. Vendruscolo, C. M. Dobson, S. Linse, and T. P. Knowles, "Molecular mechanisms of protein aggregation from global fitting of kinetic models," *Nat. Protoc.*, vol. 11, no. 2, pp. 252–272, 2016.

[30] C. Weber, T. Michaels, and L. Mahadevan, "Spatial control of irreversible protein aggregation," *eLife*, vol. 8, p. e42315, 2019.

[31] E. Spruijt, J. Sprakel, M. A. Cohen Stuart, and J. Van Der Gucht, "Interfacial tension between a complex coacervate phase and its coexisting aqueous phase," *Soft Matter*, vol. 6, no. 1, pp. 172–178, 2009.

[32] K. K. Nakashima, M. A. Vibhute, and E. Spruijt, "Biomolecular chemistry in liquid phase separated compartments," *Front. Mol. Biosci.*, vol. 6, p. 21, 2019.

[33] M. Abbas, W. P. Lipiński, K. K. Nakashima, W. T. Huck, and E. Spruijt, "A short peptide synthon for liquid–liquid phase separation," *Nat. Chem.*, vol. 13, no. 11, pp. 1046–1054, 2021.

[34] W. Peeples and M. K. Rosen, "Mechanistic dissection of increased enzymatic rate in a phase-separated compartment," *Nat. Chem. Biol.*, vol. 17, no. 6, pp. 693–702, 2021.

[35] S. Ray, D. Chatterjee, S. Mukherjee, K. Patel, and J. Mahato, "Spatiotemporal solidification of α-synuclein inside the liquid droplets," *bioRxiv*, 2021.

[36] V. N. Uversky, E. M. Cooper, K. S. Bower, J. Li, and A. L. Fink, "Accelerated α-synuclein fibrillation in crowded milieu," *FEBS Lett.*, vol. 515, no. 1-3, pp. 99–103, 2002.

[37] J. Goers, "Polycation-induced oligomerization and accelerated fibrillation of human alpha-synuclein in vitro," *Protein Sci.*, vol. 12, no. 4, pp. 702–707, 2003.

[38] T. Antony, W. Hoyer, D. Cherny, G. Heim, T. M. Jovin, and V. Subramaniam, "Cellular polyamines promote the aggregation of α-synuclein," *J. Biol. Chem.*, vol. 278, no. 5, pp. 3235–3240, 2003.

[39] A. M. Küffner, M. Linsenmeier, F. Grigolato, M. Prodan, R. Zuccarini, U. Capasso Palmiero, L. Faltova, and P. Arosio, "Sequestration within biomolecular condensates inhibits Aβ-42 amyloid formation," *Chem. Sci.*, vol. 12, no. 12, pp. 4373–4382, 2021.

7

General conclusions and future perspectives

7.1   To solid via liquid

The research area focused on the relations between protein liquid-liquid phase separation (LLPS) and amyloid formation emerged around 2015 with some pioneering works on disordered proteins and low complexity domains [1–3]. During the last 4 years we could observe the *maturation* of this scientific field, characterised not only by an increased number of publications about liquid-to-solid transition (LST) of liquid condensates, but also by the developments of new experimental methods and model systems to quantitatively monitor the process and new theories to describe and understand it. In the last chapter of this thesis, we will try to place our work within this field, identify the current limitations and propose further studies that may answer some of the remaining questions.

7.2   Phase separation of short peptide derivatives

In 2018 Hughes et al. published their work on LARKS, low-complexity, aromatic-rich, kinked segments, suggesting that reversible amyloid-like structures can be responsible for the membraneless organelle (MLO) formation [4]. While their work provided evidence that synthetic peptides inspired by natural low-complexity domains (LCDs) may reversibly form hydrogels, they could not show LLPS of their constructs. Inspired by these findings, we decided to search for short peptides that can undergo both LLPS and LST, in the hope that the availability of such simple models of protein phase separation will allow us to study the transitions in detail. At that time also new proteins were identified to potentially undergo aggregation via the condensed liquid phase, e.g. tau [5–8] and TDP-43 [9,10]. α-synuclein (αSyn) joined this group a bit later [11,12] and recently even amyloid-β oligomers were shown to undergo LLPS [13]. New findings about proteins undergoing LST further motivated the search for short peptides that could model this behaviour.

To our disappointment, we have not found small compounds with classical peptide structure that can undergo LLPS or LST. Instead, we studied LLPS and LST of small peptide derivatives that we describe in Chapter 2. We suggest that the dimers with two dipeptide moieties and a spacer can be used as a drastically simplified model of the sticker-and-spacer architecture characteristic for disordered proteins undergoing LLPS. We draw general conclusions that the balance between the hydrophobicity of the peptidic sticker motif and the hydrophilicity and flexibility of the spacer is essential for the ability to undergo LLPS. The derivatives that we study can be considered a simplistic representation of the sticker-and-spacer model suggested for phase-separating proteins - similar relation between the hydrophobicity of the sticker and the tendency to undergo LLPS has been shown e.g. for mutants of hnRNPA1 [14], for which interactions between tyrosine residues were stronger than interactions between phenylalanine residues Figure 7.1. The same article confirms also findings from other works [15,16], that charge-charge or cation-π interactions involving arginine are stronger than interactions involving lysine.
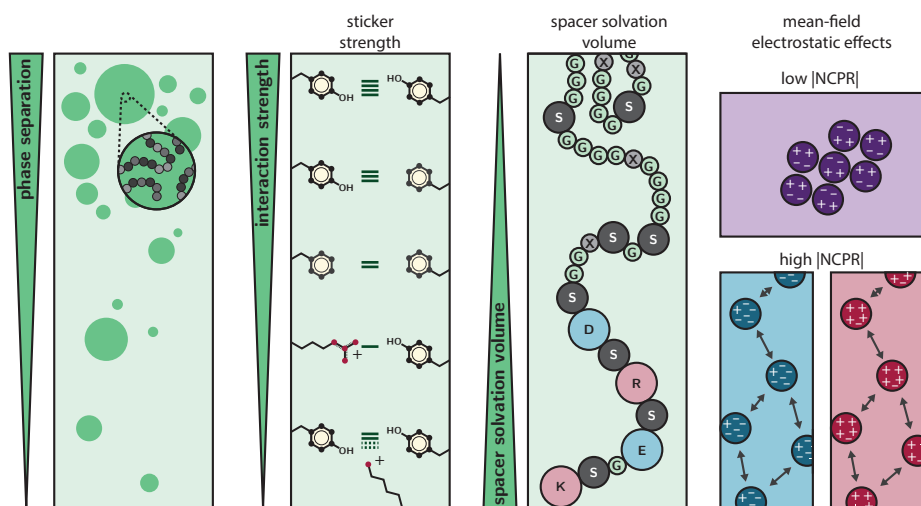
Figure 7.1: Hierarchy of physicochemical effects that underlie the driving force of phase separation of low-complexity domains. Cohesive interactions between disordered chains made up of sticker and spacer residues result in phase separation. Tyr–Tyr, Tyr–Phe and Phe–Phe interactions have respectively decreasing pairwise interaction strengths. Arg residues act as auxiliary stickers with aromatic residues if the net charge per residue (NCPR) is favourable. Lys residues weaken sticker–sticker interactions via three-body effects. Gly, Ser and charged residues are spacer residues that modulate the driving forces for phase separation through their effects on the effective solvation volume of spacers. The higher the effective solvation volume of spacers, the weaker the driving force for phase separation. NCPR of low-complexity domains affects phase separation via mean-field electrostatic effects, which modulate the saturation concentration by up to three orders of magnitude. NCPR values close to electroneutrality favour phase separation, whereas unbalanced charges increase solubility and weaken phase separation. Adapted from [14].

Two reasons make small phase-separating peptide derivatives particularly interesting: (i) they can serve as simplified model systems to study protein phase separation; (ii) they were potentially available prebiotically and could form primitive protocells. From both the biocondensate perspective and the protocell perspective, it could be beneficial to develop similar derivatives that do not include the non-peptidic disulphide linker, accessing the minimalist phase-separating peptide model. We tried synthesising different hexa- and heptapeptides with phenylalanyl-phenylalanine fragments on the N-terminus and on the C-terminus, but all these sequences formed aggregates. However, we still expect that certain short peptides can undergo LLPS.

7.3 Liquid-to-solid transition of short peptide derivatives

In the context of this thesis, the LST propensity of our small molecule-based model systems was particularly interesting. The sticker part in the original design of the simplistic

sticker-and-spacer architecture model was based on the phenylalanyl-phenylalanine (FF) moiety, a fragment well known for its ability to form aggregates. Therefore it comes with no surprise that its dimeric derivatives with a cystamine linker also shown propensities to form solid aggregates and various nanostructures[17–20]. Unlike previously described molecules featuring FF, FFssFF formed aggregates via metastable liquid phase. Knowing that FF was also proposed as the reductionist amyloid model[21], we expected that FFssFF molecule could be used as a simplistic model of the protein LST.

We expected the system to be simple enough to allow for detailed characterisation. In particular, it could be studied using NMR techniques that are recently gaining attention as a promising tool to investigate the protein structure in condensed liquid or aggregate[22,23], and combining this methods with simple model systems can substantially increase the amount and quality of structural information. In Chapter 3 we present a proof of concept that our model system expresses similar characteristics to proteins and suggest that while hydrophobic interactions drive LLPS, interactions between aromatic rings are probably mostly responsible for LST. This chapter presents also the potential of NMR in studying LLPS. In particular, NMR has been proven useful for studying the structure of proteins in the dilute and condensed phases[24,25], dynamics of proteins undergoing LLPS[26] and kinetics of phase transitions[27]. The advantage of simplified systems like FFssFF is that, even though they cannot completely represent the behaviour of proteins, their NMR characterisation is relatively easy allowing for combined studies of the structure, molecule dynamics and kinetics of LLPS.

Hopefully, this will allow us to understand better the LST process for small peptides but also proteins. To make our findings more universal, it would be beneficial to develop new model molecules that undergo LST, as at the moment we based our findings mostly on experiments with FFssFF. Furthermore, we did not investigate the kinetics of the LST process. This can be hopefully achieved by means of ssNMR and cryo-TEM.

7.4 Reaction-driven phase transitions of small peptide derivatives

While in Chapter 2 and Chapter 3 we investigate the properties of simple phase-separating peptide derivatives, their ability to undergo LLPS and LST, we only briefly mention the redox properties of the disulphide linker. In Chapter 4 we look closer at the potential of the disulphide linker in the formation of dynamic LLPS systems. It is particularly interesting in light of recent reports about the employment of phase-separation in product selection in dynamic combinatorial libraries on the one hand, and about the potential of liquid condensates to drive chemical reactions on the other.

We show that the disulphide exchange readily happens under basic conditions required for LLPS of the studied dimers and that forming more hydrophobic heterodimers can potentially drive LLPS and LST while forming more hydrophilic dimers can potentially drive solid-to-liquid transition and dissolution. It has been shown before that the formation of disulphide bonds can drive LLPS - we have described it for FFssFF in Chapter 2 but it can also work for other simple sticker-and-spacer models[28]. The reversibility of disulphide formation and the possibility to undergo disulphide exchange gives also access to transient

behaviours[29] and competition between products[30,31], which is particularly interesting from the protocell/synthetic cell perspective.

We anticipate that the disulphide-based phase-separating dimers are excellent candidates for dynamic libraries that can *evolve* to form derivatives able to form liquid condensates or aggregates. In the case of liquid condensates, it would be particularly interesting to study the kinetics of dimerisation/monomer exchange in the absence and presence of the liquid phase, as our simulation-based studies showed that the condensates may have a substantial effect on the reaction kinetics (autocatalytic characteristics). Apart from the local concentration effect, the influence of the condensate interface on the redox reactions is worth investigating as well, as very recently biomolecular condensates have been shown to modulate redox reactions[32].

7.5 Modelling protein aggregation in a two-phase system

Work described in Chapter 5 and Chapter 6 was largely inspired by the model suggested by Weber and coworkers[33], which, unlike previous attempts to explain the involvement of LLPS in the protein aggregation process, focuses on the host-guest interactions between inert condensates (as hosts) and aggregating protein (as a guest). The idea that liquid compartments can affect aggregation of guest proteins appeared relatively recently - the earliest work focusing on this aspect was probably the study done by McCall and coworkers on the assembly of actin filaments in poly-lysine/poly-glutamate coacervates[34]. Since then the idea of a host-guest interaction pathway has been considered in only a handful of publications. Partially in the works by Boyko and coworkers (where they look at the *dilution* of tau condensates with a non-aggregating mutant)[7,8,35]. Then, with more focus on the host-guest interaction and potential sequestration of aggregating protein by condensates, Küffner and coworkers[36] showed that various condensate-forming LCDs can hamper amyloid-β aggregation by partitioning-sequestration Figure 7.2A. Very recently, the group of Christoph Weber expanded the previous model by including complex viscoelastic properties of condensates[37].

Our aim was to provide a more complex understanding of the possible mechanisms via which liquid condensates can affect protein aggregation. In Chapter 5 we describe our computational approach to explaining the effects that host condensates can have on guest aggregating protein. We look at the influence of partitioning and accumulation at the interface using both differential equations-based models (to follow the kinetics of the aggregation process) and stochastic models (to follow the distribution of the kinetics parameters and of the fibril length). We provide a comprehensive overview of the protein aggregation mechanisms in phase-separated systems that so far were missing in the literature, including the involvement of the condensate interface, which was so far mostly omitted.
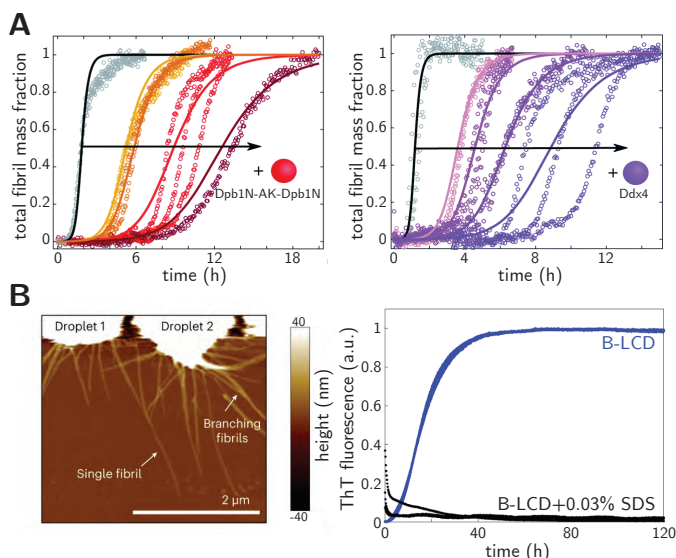
Figure 7.2: Sequestration of amyloid-β and interface aggregation of hnRNPA1 low complexity domain. (A) Condensates composed of different LCDs inhibit amyloid-β(1-42) fibril formation. Left: Aggregation profiles of 3.75 µM amyloid-β(1-42) solution in the absence (black) and presence of 1 µM, 2 µM, 5 µM and 10 µM DEAD-box ATPase Dpb1N-AK-Dpb1N (from left to right). Right: Aggregation profiles of 5 µM amyloid-β(1-42) solution in the absence (black) and presence of 1 µM, 5 µM, 10 µM and 20 µM (from left to right) Ddx4 LCD. (B) Amyloid formation from liquid condensates of the hnRNPA1-B LCD is promoted at the interface. Left: AFM of star-shaped aggregates formed by B-LCD after 1 h. Right: The addition of 0.03% SDS to a 30 µM B-LCD solution did not affect LLPS but prevented the increase of ThT signal over time. Panel (A) taken from [36], panel (B) taken from [38].

While we suggest multiple models that should cover various interaction modes between the monomers of the aggregating protein and the liquid condensates, we cannot say that our description is complete. One of the main limitations of our models is the assumption that the monomers and the aggregates do not affect the properties of the liquid phase, which should be true only for very low concentrations of the aggregating protein. A more robust model should take into account the volume change upon partitioning and the influence of the altered composition on the kinetic rate constants/activity coefficients. Furthermore, the models we used assume either instant or very fast diffusion of the monomers, always yielding the equilibrium concentration ratio between the dilute and the condensed phase. However, the transport rate may be dependent not only on the properties of the monomers/oligomers/fibrils, but also on the geometry of the condensates (which was not taken into account in the models described in this thesis).

7.6 Experimental investigation of the influence of the coacervate phase on the αSyn aggregation

Finally, in Chapter 6 we study the relations between the aggregation kinetics and the presence of condensates using a model experimental system. We compare the aggregation rates of three variants of αSyn in the presence and absence of different complex coacervates. As previously suggested by the models, liquid condensates may either accelerate or slow down the aggregation process. This provides an interesting perspective on the potential role of liquid condensates (or MLOs specifically) in the aggregation process in living cells.

While previous studies have suggested that the presence of liquid condensates can affect protein aggregation both by using simulations [33] and experimentally [36], the idea of interface-catalysed aggregation in the host-guest systems has not been investigated so far. Interfaces, mainly air-water and hydrophobic interfaces, have been proven to be of crucial importance in nucleating αSyn aggregation [39,40]. Very recently, it has been shown that the condensate-water interface is essential for nucleating aggregation of hnRNPA1 LCD condensates [38] (Figure 7.2B). Based on the previous findings and our results described in Chapter 6, we hypothesise that the condensate-interface nucleated aggregation can be more universal and have a more pronounced influence on the aggregation kinetics than the partitioning (increasing local concentration) in the host-guest systems. This idea is supported by simulations showing that conformations of molecules at the interface of condensates differ from conformations inside and in the dilute phase [41]. Interfaces can promote expanded conformations and in consequence, facilitate aggregation.

We provide a possible explanation of the accelerating and decelerating effect of liquid condensates on the aggregation process, however, the mechanistic understanding of the phenomena is still very limited. Similarly to the computational model, our experimental system focuses on the aggregation kinetics without taking into account the influence of the αSyn monomers and fibrils on the condensed phase. Understanding of the mutual influence of the aggregating protein and the condensate-forming polymers can be largely improved by the use of more advanced optical microscopy methods and electron microscopy methods. Furthermore, essential is a better characterisation of the viscoelastic properties of the condensates (and their changes during aggregation), which can be achieved by means of microrheology or optical tweezers.

7.7 Thesis outlook

While the scientific interest in the relation between LLPS and protein aggregation is constantly growing, as evidenced also by this thesis, multiple questions remain unanswered. In this final section, we suggest some future directions of the field, based on the recent findings and developments of experimental techniques.

Work presented in this thesis focused mostly on the influence of liquid condensates on the formation of protein aggregates. However, partitioning of aggregate fibrils into condensates or their accumulation at the interface can potentially change the dynamics of the condensed phase (Figure 7.3). Increasing the concentration of fibrils inside the con-

densed phase can increase its viscosity and in consequence slow down reactions, including aggregation reaction itself [37,42]. Changes in the interfacial tension can be also relevant biologically, as it determines the formation of multiphase compartments [16,43,44], or interactions between condensates and membranes and other surfaces [45–47]. It is therefore very relevant to understand the influence of protein aggregation on the dynamics of condensates. Several methods have been recently applied to study the viscoelastic properties of condensed liquid [48]. These include fluorescence recovery after photobleaching [49], fluorescence correlation spectroscopy [50], microfluidics [51], passive microrheology [52] (to measure diffusion and from this determine nanoviscosity or to measure macroviscosity directly); flicker spectroscopy [53] (to measure interfacial tension); and active microrheology [54,55], micropipette aspiration [56] or fusion dynamics [50,57] (to measure both viscosity and interfacial tension or their ratio). Some of these methods have been already used in the context of protein aggregation [42,58], but more emphasis should be put on the host-guest interactions rather than liquid-to-solid transition of phase-separating proteins and also on the influence of protein aggregates on the interfacial properties of condensates.
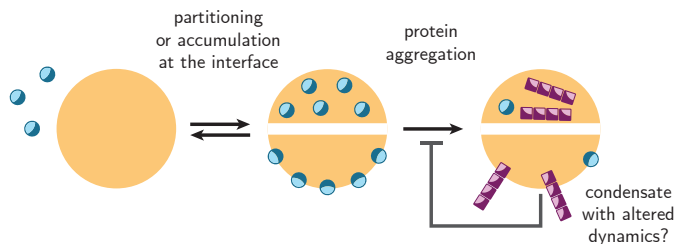

Figure 7.3: Formation of protein aggregates can potentially alter the condensate dynamics. Partitioning of monomers or the accumulation at the interface causes localised aggregation, potentially changing the viscoelastic properties of the condensates. Altered viscoelastic properties can affect the kinetics of reactions occurring within the condensate environment, including the aggregation reaction itself.

Another aspect that should be further investigated is the mechanism driving protein accumulation at the interface of condensates and further aggregation. We hypothesised that this accumulation is caused by the amphiphilic nature of the protein (αSyn in this case), however, we do not provide any evidence that the conformation of protein at the interface actually is amphiphilic. Recent advances in single-molecule fluorescence resonance energy transfer experiments should allow for a more detailed characterisation of proteins at the interface of condensates [59,60]. Understanding of the protein structure at the interface can not only explain the forces driving interfacial accumulation, but will also shed light on the aggregation mechanism (stabilisation of certain protein monomer conformations may either promote or hamper transition into aggregates and result in the formation of fibrils of altered morphology) [61,62].

Part of this detailed understanding of LST of proteins may come from the studies of simple systems, similar to FFssFF, which can be relatively easily characterised, e.g. by means of ssNMR. What we could not achieve so far but what should be achievable in the near future, is a detailed comparison of peptide conformations in the dilute phase,

in the condensed phase and in the solid phase. If also resolved spatially (separately for the interior and the interface of the condensates), and temporally (to follow the droplet maturation) this can also answer some of the questions stated in the previous paragraph. Before this simple model systems can be used to explain factors affecting LLPS of proteins and conformations of protein chains in condensed phases, new simple protein-mimicking molecules should be developed, preferably peptides composed of proteinogenic amino acids and without artificial components like the linkers present in FFssFF and similar derivatives. Search for these simple phase-separating peptides should be soon massively accelerated by the use of machine learning workflows in combination with simulations [63–66].

The scientific field of protein aggregation in the presence of biomolecular condensates has substantially grown in the last few years. LLPS is now generally recognised as one of the most important factors affecting the aggregation mechanism. We hope that with this thesis we make a useful contribution in this research area and that further progress will lead not only to a better understanding of pathological protein aggregation, but eventually also to the development of new therapies and methods to prevent aggregation-related diseases.

Bibliography

[1] A. Molliex, J. Temirov, J. Lee, M. Coughlin, A. P. Kanagaraj, H. J. Kim, T. Mittag, and J. P. Taylor, "Phase Separation by Low Complexity Domains Promotes Stress Granule Assembly and Drives Pathological Fibrillization," *Cell*, vol. 163, no. 1, pp. 123–133, 2015.

[2] A. Patel, H. O. Lee, L. Jawerth, S. Maharana, M. Jahnel, M. Y. Hein, S. Stoynov, J. Mahamid, S. Saha, T. M. Franzmann, A. Pozniakovski, I. Poser, N. Maghelli, L. A. Royer, M. Weigert, E. W. Myers, S. Grill, D. Drechsel, A. A. Hyman, and S. Alberti, "A Liquid-to-Solid Phase Transition of the ALS Protein FUS Accelerated by Disease Mutation," *Cell*, vol. 162, no. 5, pp. 1066–1077, 2015.

[3] Y. Lin, D. S. Protter, M. K. Rosen, and R. Parker, "Formation and Maturation of Phase-Separated Liquid Droplets by RNA-Binding Proteins," *Mol. Cell*, vol. 60, no. 2, pp. 208–219, 2015.

[4] M. P. Hughes, M. R. Sawaya, D. R. Boyer, L. Goldschmidt, J. A. Rodriguez, D. Cascio, L. Chong, T. Gonen, and D. S. Eisenberg, "Atomic structures of low-complexity protein segments reveal kinked b sheets that assemble networks," *Science*, vol. 359, no. 6376, pp. 698–701, 2018.

[5] S. Ambadipudi, J. Biernat, D. Riedel, E. Mandelkow, and M. Zweckstetter, "Liquid-liquid phase separation of the microtubule-binding repeats of the Alzheimer-related protein Tau," *Nat. Commun.*, vol. 8, no. 1, p. 275, 2017.

[6] S. Wegmann, B. Eftekharzadeh, K. Tepper, K. M. Zoltowska, R. E. Bennett, S. Dujardin, P. R. Laskowski, D. MacKenzie, T. Kamath, C. Commins, C. Vanderburg, A. D. Roe, Z. Fan, A. M. Molliex, A. Hernandez-Vega, D. Muller, A. A. Hyman, E. Mandelkow, J. P. Taylor, and B. T. Hyman, "Tau protein liquid–liquid phase separation can initiate tau aggregation," *EMBO J.*, vol. 37, no. 7, p. e98049, 2018.

[7] S. Boyko, X. Qi1, T. H. Chen, K. Surewicz, and W. K. Surewicz, "Liquid-liquid phase separation of tau protein: The crucial role of electrostatic interactions," *J. Biol. Chem.*, vol. 294, no. 29, pp. 11054–11059, 2019.

[8] S. Boyko, K. Surewicz, and W. K. Surewicz, "Regulatory mechanisms of tau protein fibrillation under the conditions of liquid-liquid phase separation," *Proc. Natl. Acad. Sci. U. S. A.*, vol. 117, no. 50, pp. 31882–31890, 2020.

[9] A. E. Conicella, G. H. Zerze, J. Mittal, and N. L. Fawzi, "ALS Mutations Disrupt Phase Separation Mediated by α-Helical Structure in the TDP-43 Low-Complexity C-Terminal Domain," *Structure*, vol. 24, no. 9, pp. 1537–1549, 2016.

[10] W. M. Babinchak, R. Haider, B. K. Dumm, P. Sarkar, K. Surewicz, J. K. Choi, and W. K. Surewicz, "The role of liquid-liquid phase separation in aggregation of the TDP-43 low-complexity domain," *J. Biol. Chem.*, vol. 294, no. 16, pp. 6306–6317, 2019.

[11] S. Ray, N. Singh, R. Kumar, K. Patel, S. Pandey, D. Datta, J. Mahato, R. Panigrahi, A. Navalkar,

S. Mehra, L. Gadhe, D. Chatterjee, A. S. Sawner, S. Maiti, S. Bhatia, J. A. Gerez, A. Chowdhury, A. Kumar, R. Padinhateeri, R. Riek, G. Krishnamoorthy, and S. K. Maji, "α-Synuclein aggregation nucleates through liquid–liquid phase separation," *Nat. Chem.*, vol. 12, no. 8, pp. 705–716, 2020.

[12] S. Ray, D. Chatterjee, S. Mukherjee, K. Patel, and J. Mahato, "Spatiotemporal solidification of α-synuclein inside the liquid droplets," *bioRxiv*, 2021.

[13] X. Gui, S. Feng, Z. Li, Y. Li, B. Reif, B. Shi, and Z. Niu, "Liquid–liquid phase separation of amyloid-β oligomers modulates amyloid fibrils formation," *J. Biol. Chem.*, vol. 299, no. 3, p. 102926, 2023.

[14] A. Bremer, M. Farag, W. M. Borcherds, I. Peran, E. W. Martin, R. V. Pappu, and T. Mittag, "Deciphering how naturally occurring sequence features impact the phase behaviours of disordered prion-like domains," *Nat. Chem.*, vol. 14, no. 2, pp. 196–207, 2022.

[15] Y. Hong, S. Najafi, T. Casey, J. E. Shea, S. I. Han, and D. S. Hwang, "Hydrophobicity of arginine leads to reentrant liquid-liquid phase separation behaviors of arginine-rich proteins," *Nat. Commun.*, vol. 13, no. 1, p. 7326, 2022.

[16] R. S. Fisher and S. Elbaum-Garfinkle, "Tunable multiphase dynamics of arginine and lysine liquid condensates," *Nat. Commun.*, vol. 11, no. 1, p. 4628, 2020.

[17] M. Reches and E. Gazit, "Casting metal nanowires within discrete self-assembled peptide nanotubes," *Science*, vol. 300, no. 5619, pp. 625–627, 2003.

[18] M. Reches and E. Gazit, "Formation of closed-cage nanostructures by self-assembly of aromatic dipeptides," *Nano Lett.*, vol. 4, no. 4, pp. 581–585, 2004.

[19] M. Reches and E. Gazit, "Controlled patterning of aligned self-assembled peptide nanotubes," *Nat. Nanotechnol.*, vol. 1, no. 3, pp. 195–200, 2006.

[20] I. Azuri, L. Adler-Abramovich, E. Gazit, O. Hod, and L. Kronik, "Why are diphenylalanine-based peptide nanostructures so rigid? Insights from first principles calculations," *J. Am. Chem. Soc.*, vol. 136, no. 3, pp. 963–969, 2014.

[21] S. Brahmachari, Z. A. Arnon, A. Frydman-Marom, E. Gazit, and L. Adler-Abramovich, "Diphenylalanine as a Reductionist Model for the Mechanistic Characterization of β-Amyloid Modulators," *ACS Nano*, vol. 11, no. 6, pp. 5960–5969, 2017.

[22] L. Emmanouilidis, L. Esteban-Hofer, F. F. Damberger, T. de Vries, C. K. Nguyen, L. F. Ibáñez, S. Mergenthal, E. Klotzsch, M. Yulikov, G. Jeschke, and F. H. Allain, "NMR and EPR reveal a compaction of the RNA-binding protein FUS upon droplet formation," *Nat. Chem. Biol.*, vol. 17, no. 5, pp. 608–614, 2021.

[23] L. Emmanouilidis, L. Esteban-Hofer, G. Jeschke, and F. H. Allain, "Structural biology of RNA-binding proteins in the context of phase separation: What NMR and EPR can bring?," *Curr. Opin. Struct. Biol.*, vol. 70, pp. 132–138, 2021.

[24] T. H. Kim, B. J. Payliss, M. L. Nosella, I. T. Lee, Y. Toyama, J. D. Forman-Kay, and L. E. Kay, "Interaction hot spots for phase separation revealed by NMR studies of a CAPRIN1 condensed phase," *Proc. Natl. Acad. Sci. U. S. A.*, vol. 118, no. 23, p. e2104897118, 2021.

[25] L. E. Wong, T. H. Kim, D. R. Muhandiram, J. D. Forman-Kay, and L. E. Kay, "NMR Experiments for Studies of Dilute and Condensed Protein Phases: Application to the Phase-Separating Protein CAPRIN1," *J. Am. Chem. Soc.*, vol. 142, no. 5, pp. 2471–2489, 2020.

[26] S. Guseva, V. Schnapka, W. Adamski, D. Maurin, R. W. Ruigrok, N. Salvi, and M. Blackledge, "Liquid-Liquid Phase Separation Modifies the Dynamic Properties of Intrinsically Disordered Proteins," *J. Am. Chem. Soc.*, vol. 145, no. 19, pp. 10548–10563, 2023.

[27] J. E. Bramham and A. P. Golovanov, "Temporal and spatial characterisation of protein liquid-liquid phase separation using NMR spectroscopy," *Nat. Commun.*, vol. 13, no. 1, p. 1767, 2022.

[28] S. Chowdhuri, S. Das, R. Kushwaha, T. Das, B. K. Das, and D. Das, "Cumulative Effect of pH and Redox Triggers on Highly Adaptive Transient Coacervates," *Chem. - A Eur. J.*, vol. 29, no. 24, 2023.

[29] S. M. Morrow, I. Colomer, and S. P. Fletcher, "A chemically fuelled self-replicator," *Nat. Commun.*, vol. 10, no. 1, p. 1011, 2019.

[30] M. Colomb-Delsuc, E. Mattia, J. W. Sadownik, and S. Otto, "Exponential self-replication enabled through a fibre elongation/breakage mechanism," *Nat. Commun.*, vol. 6, no. 1, p. 7427, 2015.

[31] B. Liu, J. Wu, M. Geerts, O. Markovitch, C. G. Pappas, K. Liu, and S. Otto, "Out-of-Equilibrium Self-Replication Allows Selection for Dynamic Kinetic Stability in a System of Competing Replicators," *Angew. Chemie - Int. Ed.*, vol. 61, no. 18, 2022.

[32] Y. Dai, C. F. Chamberlayne, M. S. Messina, C. J. Chang, R. N. Zare, L. You, and A. Chilkoti, "Interface of biomolecular condensates modulates redox reactions," *Chem*, vol. 9, no. 6, pp. 1594–

1609, 2023.

[33] C. Weber, T. Michaels, and L. Mahadevan, "Spatial control of irreversible protein aggregation," *eLife*, vol. 8, p. e42315, 2019.

[34] P. M. McCall, S. Srivastava, S. L. Perry, D. R. Kovar, M. L. Gardel, and M. V. Tirrell, "Partitioning and Enhanced Self-Assembly of Actin in Polypeptide Coacervates," *Biophys. J.*, vol. 114, no. 7, pp. 1636–1645, 2018.

[35] S. Boyko and W. K. Surewicz, "Tau liquid–liquid phase separation in neurodegenerative diseases," *Trends Cell Biol.*, vol. 32, no. 7, pp. 611–623, 2022.

[36] A. M. Küffner, M. Linsenmeier, F. Grigolato, M. Prodan, R. Zuccarini, U. Capasso Palmiero, L. Faltova, and P. Arosio, "Sequestration within biomolecular condensates inhibits Aβ-42 amyloid formation," *Chem. Sci.*, vol. 12, no. 12, pp. 4373–4382, 2021.

[37] W. Pönisch, T. C. Michaels, and C. A. Weber, "Aggregation controlled by condensate rheology," *Biophys. J.*, vol. 122, no. 1, pp. 197–214, 2023.

[38] M. Linsenmeier, L. Faltova, U. C. Palmiero, C. Seiffert, A. M. Küffner, D. Pinotsi, J. Zhou, R. Mezzenga, and P. Arosio, "The interface of condensates of the hnRNPA1 low-complexity domain promotes formation of amyloid fibrils," *Nat. Chem.*, vol. 15, no. 10, pp. 1340–1349, 2023.

[39] S. Campioni, G. Carret, S. Jordens, L. Nicoud, R. Mezzenga, and R. Riek, "The presence of an air-water interface affects formation and elongation of α-synuclein fibrils," *J. Am. Chem. Soc.*, vol. 136, no. 7, pp. 2866–2875, 2014.

[40] J. Pronchik, X. He, J. T. Giurleo, and D. S. Talaga, "In vitro formation of amyloid from α-synuclein is dominated by reactions at hydrophobic interfaces," *J. Am. Chem. Soc.*, vol. 132, no. 28, pp. 9797–9803, 2010.

[41] M. Farag, S. R. Cohen, W. M. Borcherds, A. Bremer, T. Mittag, and R. V. Pappu, "Condensates formed by prion-like low-complexity domains have small-world network structures and interfaces defined by expanded conformations," *Nat. Commun.*, vol. 13, no. 1, p. 7722, 2022.

[42] L. Jawerth, E. Fischer-Friedrich, S. Saha, J. Wang, T. Franzmann, X. Zhang, J. Sachweh, M. Ruer, M. Ijavi, S. Saha, J. Mahamid, A. A. Hyman, and F. Jülicher, "Protein condensates as aging Maxwell fluids," *Science*, vol. 370, no. 6522, pp. 1317–1323, 2020.

[43] T. Lu and E. Spruijt, "Multiphase Complex Coacervate Droplets," *J. Am. Chem. Soc.*, vol. 142, no. 6, pp. 2905–2914, 2020.

[44] H. Yu, S. Lu, K. Gasior, D. Singh, S. Vazquez-Sanchez, O. Tapia, D. Toprani, M. S. Beccari, J. R. Yates, S. Da Cruz, J. M. Newby, M. Lafarga, A. S. Gladfelter, E. Villa, and D. W. Cleveland, "HSP70 chaperones RNA-free TDP-43 into anisotropic intranuclear liquid spherical shells," *Science*, vol. 371, no. 6529, 2021.

[45] T. Lu, S. Liese, L. Schoenmakers, C. A. Weber, H. Suzuki, W. T. Huck, and E. Spruijt, "Endocytosis of Coacervates into Liposomes," *J. Am. Chem. Soc.*, vol. 144, no. 30, pp. 13451–13455, 2022.

[46] W. C. Su, J. C. Ho, D. L. Gettel, A. T. Rowland, C. D. Keating, and A. N. Parikh, "Kinetic control of shape deformations and membrane phase separation inside giant vesicles," *Nat. Chem.*, 2023.

[47] J. Agudo-Canalejo, S. W. Schultz, H. Chino, S. M. Migliano, C. Saito, I. Koyama-Honda, H. Stenmark, A. Brech, A. I. May, N. Mizushima, and R. L. Knorr, "Wetting regulates autophagy of phase-separated compartments and the cytosol," *Nature*, vol. 591, no. 7848, pp. 142–146, 2021.

[48] D. Michieletto and M. Marenda, "Rheology and Viscoelasticity of Proteins and Nucleic Acids Condensates," *JACS Au*, vol. 2, no. 7, pp. 1506–1521, 2022.

[49] N. O. Taylor, M. T. Wei, H. A. Stone, and C. P. Brangwynne, "Quantifying Dynamics in Phase-Separated Condensates Using Fluorescence Recovery after Photobleaching," *Biophys. J.*, vol. 117, no. 7, pp. 1285–1300, 2019.

[50] I. Alshareedah, G. M. Thurston, and P. R. Banerjee, "Quantifying viscosity and surface tension of multicomponent protein-nucleic acid condensates," *Biophys. J.*, vol. 120, no. 7, pp. 1161–1169, 2021.

[51] N. Taylor, S. Elbaum-Garfinkle, N. Vaidya, H. Zhang, H. A. Stone, and C. P. Brangwynne, "Biophysical characterization of organelle-based RNA/protein liquid phases using microfluidics," *Soft Matter*, vol. 12, no. 45, pp. 9142–9150, 2016.

[52] I. Alshareedah, M. M. Moosa, M. Pham, D. A. Potoyan, and P. R. Banerjee, "Programmable viscoelasticity in protein-RNA condensates with disordered sticker-spacer polypeptides," *Nat. Commun.*, vol. 12, no. 1, p. 6620, 2021.

[53] J. O. Law, C. M. Jones, T. Stevenson, T. A. Williamson, M. S. Turner, H. Kusumaatmaja, and S. N. Grellscheid, "A bending rigidity parameter for stress granule condensates," *Sci. Adv.*, vol. 9,

no. 20, p. eadg0432, 2023.

[54] A. Ghosh, D. Kota, and H. X. Zhou, "Shear relaxation governs fusion dynamics of biomolecular condensates," *Nat. Commun.*, vol. 12, no. 1, p. 5995, 2021.

[55] L. M. Jawerth, M. Ijavi, M. Ruer, S. Saha, M. Jahnel, A. A. Hyman, F. Jülicher, and E. Fischer-Friedrich, "Salt-Dependent Rheology and Surface Tension of Protein Condensates Using Optical Traps," *Phys. Rev. Lett.*, vol. 121, no. 25, p. 258101, 2018.

[56] H. Wang, F. M. Kelley, D. Milovanovic, B. S. Schuster, and Z. Shi, "Surface tension and viscosity of protein condensates quantified by micropipette aspiration," *Biophys. Reports*, vol. 1, no. 1, p. 100011, 2021.

[57] A. Ghosh and H. X. Zhou, "Determinants for Fusion Speed of Biomolecular Droplets," *Angew. Chemie - Int. Ed.*, vol. 59, no. 47, pp. 20837–20840, 2020.

[58] S. Jonchhe, W. Pan, P. Pokhrel, and H. Mao, "Small Molecules Modulate Liquid-to-Solid Transitions in Phase-Separated Tau Condensates," *Angew. Chemie - Int. Ed.*, vol. 61, no. 23, p. e202113156, 2022.

[59] G. Heesink, M. J. Marseille, M. A. Fakhree, M. D. Driver, K. A. van Leijenhorst-Groener, P. R. Onck, C. Blum, and M. M. Claessens, "Exploring Intra- and Inter-Regional Interactions in the IDP α-Synuclein Using smFRET and MD Simulations," *Biomacromolecules*, vol. 24, no. 8, pp. 3680–3688, 2023.

[60] M. A. Fakhree, I. S. Nolten, C. Blum, and M. M. Claessens, "Different Conformational Subensembles of the Intrinsically Disordered Protein α-Synuclein in Cells," *J. Phys. Chem. Lett.*, vol. 9, no. 6, pp. 1249–1253, 2018.

[61] M. Drescher, B. D. Van Rooijen, G. Veldhuis, V. Subramaniam, and M. Huber, "A stable lipid-induced aggregate of α-synuclein," *J. Am. Chem. Soc.*, vol. 132, no. 12, pp. 4080–4082, 2010.

[62] A. Carija, F. Pinheiro, J. Pujols, I. C. Brás, D. F. Lázaro, C. Santambrogio, R. Grandori, T. F. Outeiro, S. Navarro, and S. Ventura, "Biasing the native α-synuclein conformational ensemble towards compact states abolishes aggregation and neurotoxicity," *Redox Biol.*, vol. 22, p. 101135, 2019.

[63] R. Batra, T. D. Loeffler, H. Chan, S. Srinivasan, H. Cui, I. V. Korendovych, V. Nanda, L. C. Palmer, L. A. Solomon, H. C. Fry, and S. K. Sankaranarayanan, "Machine learning overcomes human bias in the discovery of self-assembling peptides," *Nat. Chem.*, vol. 14, no. 12, pp. 1427–1435, 2022.

[64] P. W. Frederix, G. G. Scott, Y. M. Abul-Haija, D. Kalafatovic, C. G. Pappas, N. Javid, N. T. Hunt, R. V. Ulijn, and T. Tuttle, "Exploring the sequence space for (tri-)peptide self-assembly to design and discover new hydrogels," *Nat. Chem.*, vol. 7, no. 1, pp. 30–37, 2015.

[65] P. W. Frederix, R. V. Ulijn, N. T. Hunt, and T. Tuttle, "Virtual screening for dipeptide aggregation: Toward predictive tools for peptide self-Assembly," *J. Phys. Chem. Lett.*, vol. 2, no. 19, pp. 2380–2384, 2011.

[66] X. Xiao, A. S. Robang, S. Sarma, J. V. Le, M. E. Helmicki, M. J. Lambert, R. Guerrero-Ferreira, J. Arboleda-Echavarria, A. K. Paravastu, and C. K. Hall, "Sequence patterns and signatures: Computational and experimental discovery of amyloid-forming peptides," *PNAS Nexus*, vol. 1, no. 5, 2022.

Research data management

This thesis research has been carried out in accordance with the research data management policy of the Institute for Molecules and Materials of Radboud University, the Netherlands*. The following datasets have been produced during this research:

- **Chapter 2:** Manzar Abbas, Wojciech P. Lipiński, Karina K. Nakashima, Wilhelm T. S. Huck and Evan Spruijt "A short peptide synthon for liquid–liquid phase separation" *Nature Chemistry* (2021) **13**, 1046-1054. doi.org/10.1038/s41557-021-00788-x. Data stored in: huckdfs-srv.science.ru.nl\huckdfs\Archive\Spruijt\Publications\009_2021_NatChem_Disulfide peptide coacervates, CNCZ, Radboud University.

- **Chapter 3:** Wojciech P. Lipiński, Johannes Zehnder, Manzar Abbas, Peter Güntert, Evan Spruijt and Thomas Wiegand "Fibrils Emerging from Droplets: Molecular Guiding Principles behind Phase Transitions of a Short Peptide-Based Condensate Studied by Solid-State NMR" *Chem. Eur. J.* (2023) e202301159. doi.org/10.1002/chem.202301159. Data stored in: huckdfs-srv.science.ru.nl\huckdfs\Archive\Spruijt\Publications\020_2022_ChemEurJ_Liquid to solid transition NMR, CNCZ, Radboud University.

- **Chapter 4:** Wojciech P. Lipiński. Data stored in: huckdfs-srv.science.ru.nl\huckdfs\Archive\Spruijt\Projects\DerailedPhaseTrans\Chapter4, CNCZ, Radboud University.

- **Chapters 5 and 6:** Wojciech P. Lipiński, Brent S. Visser, Irina Robu, Mohammad A. A. Fakhree, Saskia Lindhoud, Mireille M. A. E. Claessens and Evan Spruijt "Biomolecular condensates can both accelerate and suppress aggregation of α-synuclein" *Science Advances* (2022) eabq6495. doi.org/10.1126/sciadv.abq6495. Data stored in: doi.org/10.34973/km3n-bx28, Radboud Data Repository.

---

*www.ru.nl/rdm/vm/policy-documents/policy-imm/, last accessed on 01/11/2023.

Acknowledgements

Even though there is only one name on the cover of this book, completing a PhD thesis is a group project. I would like to acknowledge people who not only made finishing this work possible, but also made the process much easier and enjoyable.

W pierwszej kolejności chciałbym podziękować tym, którzy przygotowali mnie i dali mi motywację do rozpoczęcia studiów doktoranckich (First, I would like to thank people who prepared me and gave me the motivation to start my PhD project). Swoim rodzicom dziękuję za pełną wolność w wyborze kariery zawodowej oraz za ich akceptację i wsparcie, gdy zdecydowałem się pracować ponad 1000 km od domu. Mojej siostrze za bycie zawsze blisko, mimo dzielącej nas odległości. Mentorom z czasów szkolnych, Dorocie Taźbierskiej oraz Pawłowi Samulkiewiczowi, za rozbudzenie (i podtrzymanie) ciekawości do nauk chemicznych oraz ogromne zaangażowanie w kształcenie swoich uczniów również poza standardowymi godzinami pracy. Promotorce pracy inżynierskiej i magisterskiej, Beacie Kolesińskiej, za wprowadzenie do naukowej społeczności i za przekazane doświadczenie z zakresu chemii organicznej i chemii peptydów. Giuseppina Sabatino, Anna Maria Papini, Dennis Löwik and Oleksandr Savateev for my earlier, very positive experiences of doing science abroad.

Next, I want to thank Evan, my daily supervisor, a great mentor and an outstanding scientist. Thank you for giving me the chance (even twice) to join your exceptional team at Radboud, and for helping me stay on the right track while giving me a lot of freedom. I learned a lot from you during these 4 years and I am looking forward to our collaboration in the near future.

I am very grateful to Wilhelm, my main supervisor, for his critical and always constructive feedback. Thank you also for creating the interdisciplinary and very stimulating environment of the Physical Organic Chemistry Group.

Special thanks to the members of the oer-Spruijtgroup, for helping me set up in Nijmegen and in the lab. Karina, for showing me how to make coacervates, being a great deskmate and always being a voice of scientific reason; Alain for always knowing which people and papers are worth knowing and for laying the foundation of the biocondesate subgroup; Tiemei for always being in the lab when needed, providing both practical help and words of mental encouragement.

Over the years I had the pleasure to work with many more fantastic people who joined the Spruijtgroup later. I want to thank Merlijn for all his genuine kindness and true enthusiasm for all sorts of experiments, from synthesising peptides in a squeaky shaker from the 70s to testing the elasticity of HPLC vials. Haibin, for bringing Chopin to the lab and for being the best gym buddy. Iris, for her pragmatic approach and many language exchange sessions. Annemiek, for always being very cheerful and sharing the enthusiasm for analog. Brent, who should be mentioned on the cover of this thesis as a co-author, for his persistence in trying many high-risk-low-gain experiments, for motivating me to learn programming, and for being always chilled even when the DB train was delayed or when the synuclein labelling failed again. Zainab, who joined the group at the very end of my PhD journey, but quickly became my close friend, for always asking good questions and being excited about fun facts of all sorts. Manzar, for bringing FFssFF to Nijmegen

and for bringing our research work to the next level. Amy, for energising the group and for recognising the importance of Variomatic in the automotive history. Joep, for all the plasmids and for understanding my appreciation for Modern Talking. Irina, for making FRET work and for her persistence in completing the project. Stijn, for making sense of my vague research idea and for many unexpected hilarious jokes.

I am also grateful to many other members of the Physical Organic Chemistry department for numerous scientific discussions, help in the lab and fun lunch-table/evening-drinks talks: Aigars, Andrei, Anne, Bob, Britta, Carmen, Erik, Francesca, Hiroaki, James, Jeroen, Jessie, Jiahua, Jing, José, Kinga, Lena, Leonardo, Lía, Lina, Maaruthy, Mahesh, Malwina, Mart, Mathieu, Melde, Michael, Miglė, Mitch, Nikita, Oliver, Óscar, Pam, Peer, Pieter, Rianne, Roel, Sasha, Souvik, Stefan, Thijs, Will, Xinyu, Yaxun. And of course to our great PIs: Peter, Wim and Maike.

I want to express my gratitude to all collaborators from outside RU. Mireille, Saskia and Amin who made the synuclein aggregation project possible. Thomas, Johannes and Ettore for their incredible ssNMR expertise. Sijbren, Paul, Armin, Jim, and Guillermo for the work on encapsulating replicators in coacervates.

I thank the administrative and technical staff of Radboud University for all the support they provide. Desiree, for arranging all the formalities, which is often not easy with me. Theo, Peter, Jan and Samuel for always helping me find whatever I needed in the lab.

I am extremely grateful to the members of the manuscript committee, for reviewing the thesis and participating in the defence.

Last, but not least, special thanks to my paranymphs, Brent and Merlijn, for organising all the things around the defence. And for translating the summary to Dutch, which is a terrible language to translate summaries to.

About the author

Wojciech Paweł Lipiński was born on 07/05/1995 in the beautiful city of Łódź in Poland.

He obtained his magister inżynier title from Politechnika Łódzka (Lodz University of Technology) in 2018. His final project, performed under the supervision of prof. dr. Beata Kolesińska, focused on selective transport through biological membranes using cell-penetrating peptides. He also conducted internships in the labs of prof. dr. Anna Maria Papini at the University of Florence, dr. Dennis Löwik at Radboud University in Nijmegen and dr. Oleksandr Savateev at the Max Planck Institute of Colloids and Interfaces in Potsdam.

In 2018 he started his PhD project in the group of dr. Evan Spruijt. Results of his work, focused on protein aggregation in biomolecular condensates, are presented in this thesis.